Doctoral Dissertation
Doctoral Program in Chemical Engineering (36th Cycle)

Hydrothermal liquefaction of waste: understanding of reaction pathways and implementation

Edoardo Tito

* * * * * *

Supervisors
Prof. R. Pirone, Supervisor
Prof. S. Bensaid, Co-Supervisor
Prof. A. H. Monteverde, Co-Supervisor

Politecnico di Torino
June 1st, 2024

I hereby declare that, the contents and organisation of this dissertation constitute my own original work and does not compromise in any way the rights of third parties, including those relating to the security of personal data.

Edoardo Tito
Turin, June 1st, 2024

Summary

The production of advanced biofuels from waste biomass has gained much attention as a potential solution to the pressing issues of fossil fuel depletion and global warming. The hydrothermal liquefaction (HTL) reaction has exhibited intriguing capabilities in converting organic waste into oil under hydrothermal conditions (250-400 °C, 50-200 bar), with potential biofuel upgrading. Moreover, HTL has shown interesting preliminary results in the chemical and/or energy recycling of plastic waste. Although it has been observed that the nature of the feedstock significantly influences HTL performance, its impact on reaction mechanisms remains not fully understood. This thesis aims to enhance understanding of chemical reactions and interactions in HTL, enabling better tunability for diverse applications.

Initially, the study aimed to comprehend reaction mechanisms in hydrothermal liquefaction (HTL) of biomass. Experiments with synthetic mixtures of monomers, including glucose, glycine, and oleic acid representing complex carbohydrates, proteins, and lipids, were conducted in a batch reactor. The tests revealed a strong synergy between glucose and glycine, resulting in increased solids at low temperatures. At higher temperatures, this synergy led to an increased production of oil characterized by nitrogen-containing aromatics.

Subsequently, HTL of bio-polymers (cellulose, ovalbumin, and triolein) and real biomass was studied with a focus on the impact of heating rate. Understanding the heating rate is crucial for real biomass and bio-polymers, as it can influence overall reaction selectivity through different variations in the hydrolysis rate to

monomers and the decomposition rate of these monomers and intermediates to the final products. While long reaction times showed limited effects, significant changes were observed at shorter times. The variations in heating rate were explained by changes in the kinetic advancement of the reaction, with only minor differences attributed to a direct influence on reactive mechanisms.

Beyond biomass, synthetic polymers constitute a crucial waste category, given their global abundance and the imperative to address their mismanagement. A possible valorization pathways is represented by HTL, which could enable their chemical recycling or energy valorization.

PVC is a particularly important polymer due to the challenges it poses, given the corrosivity and toxicity of the hydrochloric acid and dioxin it generates. This hampers the effective valorization of mixed post-consumer plastic waste, as PVC is frequently present. To address this issue, the feasibility of generating a chlorine-free solid for subsequent valorization in a hydrothermal environment was assessed. Almost complete dechlorination of PVC occurred at 300 °C in just 20 minutes, resulting in a solid residue with a 94% carbon yield, 86% energy recovery, and a predominant aromatic structure. The dechlorinated solid was then tested as feedstock for a subsequent reaction under supercritical conditions, resulting in the production of hydrocarbons containing 30% of the initial PVC's carbon.

The conversion through HTL of multilayer plastics was also studied, as they are unsuitable for current recycling due to their composite nature. Subcritical experiments with PET-PE film recovered 94% of the monomer of the PET, leaving a solid residue constituted only by PE, later converted into paraffinic hydrocarbons by reaction in supercritical condition.

In the end, the industrial implementation of an HTL plant, coupled with an aqueous phase reforming section for residual aqueous phase valorization, was assessed from both techno-economic and life-cycle perspectives. APR catalytically converts the residual oxygenated compounds in the aqueous phase into hydrogen for in-situ upgrading of the oil into drop-in fuel. Two case studies were evaluated, based on two different lignocellulosic feedstocks, given their different distribution among the phases and oil properties after HTL. Resulting biofuel had a minimum selling price of 1.23-1.27 €/kg and a global warming potential of 41-47 g CO_2 eq/MJ, significantly reducing emissions compared to fossil diesel.

Acknowledgment

Chapter 4 as carried out within the ReFuel project – funded by European Union – Next Generation EU within the PRIN 2022 program (D.D. 104 - 02/02/2022 Ministero dell'Università e della Ricerca).

Chapters 5 and 6 have benefited from funding from the Independent Research Foundation Denmark project CatPol: Catalytic depolymerization of synthetic polymers, grant number 1032-00263B.

Prof. P. Biller is deeply acknowledged for tutoring the visiting period at Aarhus University and for having contributed to this work.

Chapter 7 has received funding from the European Union's Horizon 2020 research and innovation program under grant agreement N° 764675.

Contents

List of Tables

List of Figures

Chapter 1

Introduction

1.1 Global warming issue

Nowadays, natural phenomena of catastrophic magnitude are increasingly occurring around the globe. The explanation for this seems to be linked to global warming, which has therefore attracted more interest in recent years[1]. Since the pre-industrial era, the global average temperature has increased by 1°C and continues to rise inexorably. The cause is attributed to the anthropogenic contribution to the emission of greenhouse gases[2]. These gases accumulate in the atmosphere, where they absorb Earth's infrared radiation, leading to an increase in the net heat balance derived from solar radiation.

In 1992, an initial strong global response to this problem was attempted through the action of the United Nations, leading to the United Nations Framework Convention on Climate Change (UNFCCC), followed by the Kyoto Protocol in 1997. This legally binding treaty, signed (but not ratified) by over 160 countries, imposed a reduction on developed countries' greenhouse gas emissions (GHGs) by at least 5% during the period 2008-2012 from the levels recorded in 1990[3].

In the following years, initiatives were launched to broaden emission responsibilities to encompass developing and less developed countries, aiming for a more robust global effort. In 2010, at the sixteenth session of the Conference of the Parties (COP16), it was concluded that it was essential to limit the increase in the global average temperature, relative to the pre-industrial era, below 2°C, preferably below 1.5°C[4]. It was determined that failure to achieve this targe would result in severe climate changes, carrying dire consequences for the future of humanity. This process culminated in the United Nations Climate Change Conference in 2015 (COP21), at the end of which the Paris Agreement was signed. The signatory countries pledged to review their emission policies with the goal of transitioning towards a carbon-neutral economy, striving to remain below the 2°C threshold[5].

Among the main greenhouse gases are carbon dioxide, methane, nitrous oxide, and fluorinated gases. To ensure uniformity in calculating the impact on global warming, a factor called Global Warming Potential (GWP) is used. This factor relates the absorption of one ton of a greenhouse gas over a certain period to the absorption that would occur with one ton of carbon dioxide. Despite CO_2 having lower GWP than other compounds, its high quantity released into the atmosphere led it to account for 76% of the 42 Gt of CO_2 equivalent released in 2010[6]. It is hence evident that this molecule is identified as the main cause of the climate problem and consequently is the subject of numerous regulatory initiatives.

The primary source of greenhouse gas emissions is identified in energy production. Out of the 604 EJ of primary energy consumed globally annually, 82% is obtained through the use of fossil fuels[7]. The combustion of these sources leads to the release of CO_2 in the atmosphere that disrupts the natural carbon cycle. Fossil reserves are the result of biological processes lasting millions of years that led to the accumulation of carbon in the depths of the Earth. These reserves, following intensive exploitation over the last 150 years and concurrent uncontrolled deforestation, have been brought to the surface, resulting in a net accumulation in the normal natural cycle. The exploitation of fossil resources, along with uncontrolled deforestation, has led to a tangible increase in atmospheric CO_2 concentration from 296 ppm in 1900 to 419 ppm in October 2023[8].

In addition to the previously described issues, the current dependence on fossil resources poses another problem: their depletion. Given the high extraction rate since 1950, the world has questioned the dependency on these resources. Numerous models and predictions have been developed over the years to estimate the remaining time until the depletion of fossil reserves. Despite frequent contradictions, partly attributed to significant technological advances in extraction procedures, it is certain that the reserves will be depleted in the not-too-distant future. Through an immediate, albeit simplistic, relationship between current reserves and extraction rate (reserves-to-production ratio), it is estimated that as of 2021, there are 139 remaining years for coal, 54 years for oil, and 49 for gas[9].

1.2 Renewable energy and biofuel

In order to limit the increase in CO_2 emissions and transit away from fossil fuels, the use of renewable sources must be increased. Europe is leading the way in the shift from fossil to renewable energy. A first Renewable Energy Directive (RED) was approved by EU in 2009, setting a target for 20% of the overall final energy consumption in the EU to come from renewable sources by 2020[10]. In 2018, a revised version of the directive (RED II) was published[11]. The new target was fixed to a minimum of 32% of renewable energy by 2030. At the end of 2023, the 2030 target was further revised and increased to 42.5% by RED III[12]. This renewable-oriented policy contributed to raising the share of renewable energy in the EU from 12.5% in 2010 to 21.8% in 2021[13]. However, significant efforts are still required to meet the target.

Different renewable sources can be harnessed, with the most relevant being hydroelectric, wind, solar, geothermal, biomass and nuclear, although there is an ongoing debate about the latter's inclusion in this list. Three main final applications for energy are identified: electricity, heating & cooling, and transportation[11]. Hydroelectric, wind, solar and nuclear are primarily associated with the generation of renewable electricity, a sector experiencing significant growth[7]. However, special attention is given to the transportation sector. RED III has a specific sub-target for it, aiming for 29% renewable energy in transport, coupled with a 14.5% reduction in the carbon intensity of transport fuels[12]. Biomass and biofuels are potential means to achieve this target.

1.3 Bioeconomy and biorefinery concept

The concept behind a biomass economy is that the sustainable exploitation of biomass must allow for its regeneration, leading to synchronization between human activities and natural cycles. Plant organisms use photosynthesis, a biochemical process that harnesses energy from sunlight to convert CO_2 and H_2O into oxygen and primarily carbohydrates, to produce organic substances essential for their growth and sustenance. Sustainable exploitation of these organisms would not only provide greater independence from depleting fossil fuels but also achieve effective carbon neutrality in atmospheric emissions. For each molecule of CO_2 released during energetic valorization, a corresponding molecule of CO_2 would have been previously removed through photosynthesis, resulting in a net zero balance.

Besides being able to provide energy directly through combustion, biomass can be used as a primary source for generating energy carriers (biofuels) that can readily serve current infrastructures for use in the transportation sector. Originally, biofuels were produced from edible energy crops, specifically those based on sugar, starch, or oil. These biofuels, originating from such crops, are categorized as first-generation biofuel and are primarily comprised of bioethanol and biodiesel. However, ethical concerns have emerged as the cultivation of these crops for biofuel competes with the human food chain. Consequently, there is a growing trend toward limiting the use of these first-generation biofuels in preference for the conversion of lignocellulosic substrates and waste (second-generation fuels) and algae (third-generation fuels).

1.4 Biomass

The interpretation of biomass varies depending on the context in which it is discussed. Biomass holds particular significance in two distinct fields: ecology, where it symbolizes living organisms and their interactions with the environment, and renewable energy, where it serves as a biotic-origin energy source. When viewed in the latter context, biomass encompasses any material linked to carbon chemistry, specifically organic material derived from animals or plants. Its primary components include carbon, hydrogen, and oxygen, along with smaller proportions of nitrogen, phosphorus, potassium, chlorine, and other inorganic compounds found in ashes.

In order to precisely define biomass for energy purposes, the Renewable Energy Directive has characterized it as ‘the biodegradable fraction of products, waste and residues from biological origin from agriculture, including vegetal and animal substances, from forestry and related industries, fisheries and aquaculture, as well as the biodegradable fraction of waste, including industrial and municipal waste of biological origin’[10]. Due to the diverse sources eligible for biomass supply, such as plants, animals, or anthropogenic sources, there can be significant variations in chemical composition among different biomass types. Nevertheless, common organic macromolecules - carbohydrates, proteins, lipids, and lignin - can be identified across all biomass types.

1.4.1 Carbohydrates

Carbohydrates constitute the majority of biomass and are composed only of carbon, oxygen, and hydrogen. They predominantly exist as polysaccharides, high-molecular-weight polymer chains resulting from the linkage of monosaccharide units through glycosidic bonds. This linkage arises from the condensation reaction between the hemiacetal group of one monosaccharide and the hydroxyl group of another.

Common polysaccharides in biomass encompass cellulose, hemicellulose, starch, and glycogen. Cellulose is the predominant structural component in lignocellulosic materials, and consists of linear chains of cellulose units connected by β-(1-4) glycosidic bonds[14,15]. Hemicellulose, is the second most abundant in lignocellulosic biomass, and differs from cellulose with its highly branched structure and shorter length (around 500-3000 units), comprising not only glucose but also various pentose and hexose sugars[15,16]. Starch is the primary storage compound in tubers[17]. Starch is composed of approximately 80-90% amylopectin and 10-20% amylose. Amylopectin consists of branched chains of glucose linked by α-(1-4) and α-(1-6) bonds, while amylose consists of long linear helical chains of glucose linked by α-(1-4) bonds[18]. Glycogen is the polysaccharidic form by which animals store their energy[19]. It is a strongly branched polymer of glucose, with α-(1-4) bonds connecting the linear chain and α-(1-6) glycosidic bonds connecting later branches[20].

1.4.2 Proteins

Proteins constitute a significant proportion of various biomasses, including those derived from animals, algae, and human-generated waste such as the organic fraction of municipal solid waste (OFMSW) and sewage sludge[21,22]. Comprising carbon, hydrogen, oxygen, nitrogen, and sulfur, proteins are closely tied to the nitrogen content present in biomass[23]. These biological macromolecules form linear polymeric chains, connecting amino acids through peptide bonds, created by the condensation of an amino group from one amino acid with the carboxyl group of another[24]. Amino acids, serving as the monomeric units of proteins, possess distinctive structures featuring an amine group, a carboxylic acid group, and a unique side-chain for each type of amino acids[25]. Specifically, the prevalent α-amino acids have the amine and carboxylic acid groups attached to the same carbon[24]. Nature predominantly utilizes just 20 types of α-amino acids in the composition of proteins, distinguished by their side chains, which confer diverse properties like size, charge, and hydrophobicity. The order in which amino acids are polymerized contributes significantly to the overall structure, chemical attributes, and consequently, the function of each protein[24].

1.4.3 Lipids

Lipids, characterized by their non-polar and hydrophobic nature, share a structural similarity with hydrocarbons, making them particularly intriguing for fuel production. Lipids encompass several subcategories, including triglycerides, phospholipids, prenols, sterols, and polyketides[26]. Nevertheless, lipids are predominantly found as triglycerides.

Triglycerides are biomolecules formed through the esterification of glycerol with three fatty acids, which may be either identical or different. Nature boasts a spectrum of over 300 distinct fatty acids, distinguished mainly by variations in carbon chain length and the presence of unsaturations and their position[27]. Typically, these fatty acids comprise an even number of carbon atoms ranging from 12 to 24[27]. Fatty acids without double bonds along the chain are referred to as saturated fatty acids, predominant in the fat tissues of terrestrial animals[28]. In contrast, those with double bonds are termed unsaturated fatty acids and are commonly encountered in fish and vegetables oil[29].

1.4.4 Lignin

Lignin is a dense and intricate organic polymer, present in the cell walls of plants. Predominantly consisting of phenolic compounds, it falls within the category of phenylpropanoid compounds. Lignin is characterized by three monomeric units: hydroxyphenyl (H), guaiacyl (G), and syringyl (S)[30], , originating from paracoumaryl alcohol, coniferyl alcohol, and sinapyl alcohol, respectively[31]. These monomers, referred to as monolignols, form irregular couplings or additions through chemical linkages involving alkyl-alkyl, alkyl-aryl, and aryl-aryl groups, which form the irregular lignin structure[31]. The quantitative distribution of the three monolignols and the chemical bonds varies based on the biomass source of lignin[32].

1.5 Synthetic polymers (plastics)

The invention of plastic represented a major technological advance in human history, as it enabled the production of an inexpensive, lightweight, flexible material with easily tailorable properties. For these reasons, since the 1930s, when the first polymers were invented, the global plastic production has risen up to 359 Mt/yr in 2018[33]. Given the non-biodegradability of synthetic polymers, the amount of plastic waste has built up since then. As of 2015, 6300 Mt of plastic waste has been generated of which 12% incinerated, 79% disposed in landfills or spread into the environment, and only 9% recycled[34]. A great deal of efforts are directed towards improvements in recycling technologies to reduce the consumption of raw fossil sources and minimize the waste. However limitations are still present when dealing with mixed plastic waste[35,36]. Indeed, mechanical recycling, the cheapest and most common recycling technology, can be used only for pure streams containing only one type of polymer, typically pre-consumer waste or specific post-consumer stream of plastics (e.g. PET bottle)[35]. Moreover, mechanically recycled plastic is generally downgraded to lower-performing uses.

In alignment with the principles of a sustainable and circular economy, even though it does not originate biogenically, addressing and utilizing the pool of mixed plastic waste as a carbon and energy source is essential. A responsible waste management strategy advocates for prioritizing chemical recycling for mixed plastic waste, followed by energy valorization[37]. Chemical recycling enables the retrieval of materials in the form of chemicals, which can then be employed to manufacture virgin polymers possessing properties similar to those derived from fossil sources. Energy valorization, on the other hand, facilitates energy recovery while minimizing the volume of waste that requires disposal.

1.6 Hydrothermal liquefaction

1.6.1 Introduction to hydrothermal liquefaction

Among different technologies, hydrothermal liquefaction (HTL) has shown interesting performance for advanced biofuel production from organic waste. HTL is a thermochemical reaction performed in aqueous environment at subcritical temperature (250-374 °C), pressure high enough to avoid vaporization of the feed (4-25 MPa) and solid loading up to 20 wt.%[38,39]. The target product of HTL is an oily phase (referred to as biocrude when biomass is used as feedstock) that, after upgrading, can be used as a substitute for fossil fuels. Three other sub-products are obtained: a solid phase, a gas phase and an aqueous phase in which residual polar organics are mostly dissolved. The distribution among these phases is contingent on the operational range of the hydrothermal reaction, as depicted in Figure 1. Below 250 °C, the process is termed 'carbonization' due to the prevalence of the solid phase[40]. Between 250 °C and 350 °C, the peak in oil production characterizes the 'liquefaction' phase. Beyond the critical point of water, radical reactions dominate, leading to an escalation in gas formation, denoted as 'hydrothermal gasification'[41]. Notably, for recalcitrant feedstocks (polyolefin plastic-like), liquefaction occurs above the critical point of water, and the preferred term is 'supercritical liquefaction'.

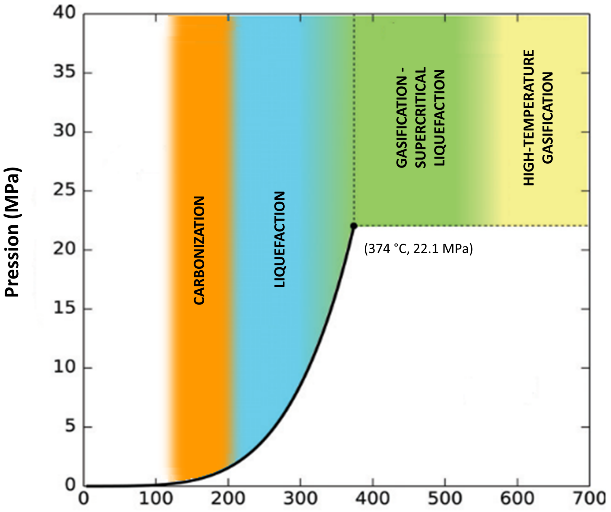

Figure 1: Operating conditions for hydrothermal reactions, adapted from [42].

HTL reactivity is strictly linked to the strong changes in water properties that take place near the critical conditions, where its dielectric constant decreases while its ionic product increases (Figure 2)[43]. The former allows better solubilization of the starting biomass and organic matter generated during the decomposition, by behaving as an apolar solvent. The latter increases H^+ and OH^- concentration favoring acid- and base-catalyzed reactions[44]. Furthermore, being performed in aqueous phase, HTL is particularly advantageous for the valorization of wet waste, as alternative and more established thermochemical technologies (combustion, pyrolysis and gasification) would require a significant amount of vaporization heat that would negatively affect the overall energy efficiency of the process[42].

Three major steps were identified during hydrothermal liquefaction: depolymerization, decomposition and recombination[45]. Initially, biologic and synthetic polymers undergo depolymerization, primarily through hydrolysis, into their smaller constituents. Subsequently, these small intermediates further decomposed into different compounds, distributing themselves between various phases based on their solubilities. Among the various possible reaction pathways, crucial reactions include decarboxylation, deamination, and dehydration[45]. During this stage, the amount of oxygen and nitrogen in the oil and solid phases decreases in favor of carbon-richer structures. Finally, as the reaction progresses, the hydrogen available in the system decreases, preventing the capping of free radicals. Consequently, repolymerization of these fragments occurs, ultimately leading to the production of a char-like structure[45].

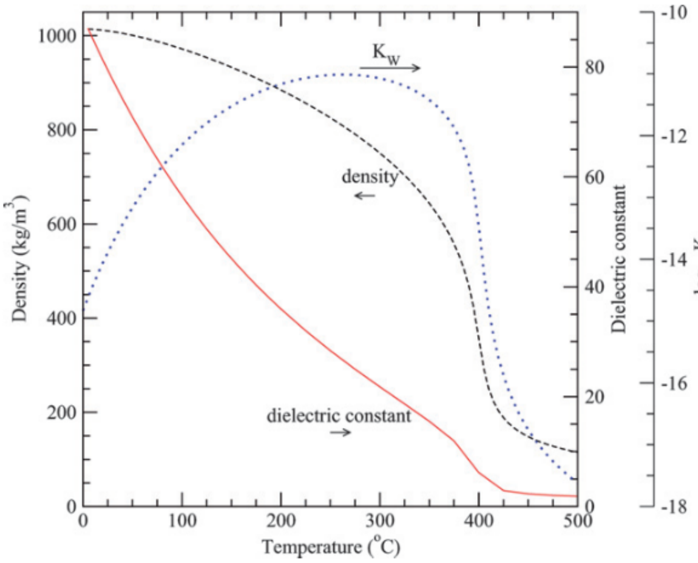

Figure 2: Density, dielectric constant and ionic dissociation constant at different temperatures of water at 30 MPa, as reported in [42].

1.6.2 History of hydrothermal liquefaction

On the scientific journal Science, in 1934-35 two letters signed by Prof. Ernst Berl from Carnegie Institute of Technology in Pittsburg (Pennsylvania), stated that it was possible to obtain liquid oil from plant in water at high temperature (230 °C) with a sufficient amount of alkaline additive[46,47]. The oily product contained 60% of the carbon of the plant and 75% of its energy[48]. These works of Prof. Berl initiated the study on hydrothermal liquefaction. However, the attention of the scientific community was limited since the fuel shortage and oil embargo of the 60-70s[49]. In that period, the pressing political need to find alternative fuel sources to imported fossil oil drove research into the development of various technologies, including HTL. Since then, the number of studies and publications on HTL grew, and from mid-2000s an extraordinary increase in attention took place (Figure 3).

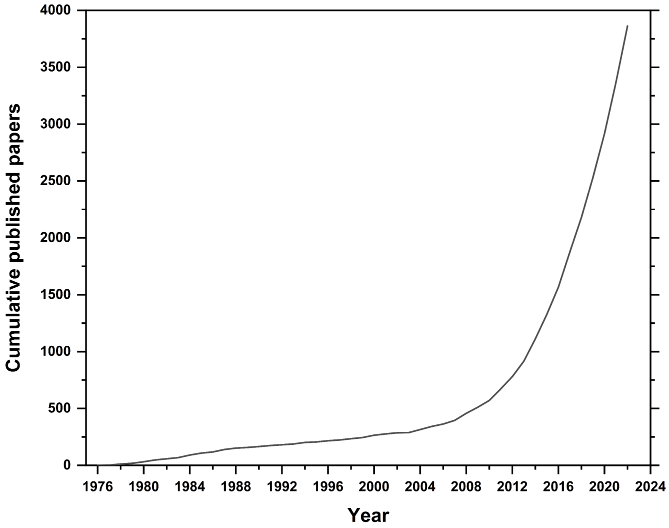

Figure 3: Cumulative published papers on hydrothermal liquefaction (source Scopus).

Figure 4 illustrates the distribution of published papers on HTL based on feedstock type. At the beginning, HTL mostly focused on lignocellulosic materials and sludge[50]. Then, in the mid-2000s, there was a significant surge in interest in HTL, primarily driven by the increasing popularity of algal biofuels. HTL demonstrated a competitive advantage in converting algae into biofuel[49], attributed to its hydrothermal environment. This environment allows algae to be cultivated in ponds and then directly converted after harvesting, without the need for a drying pretreatment that would otherwise reduce energetic efficiency. The advantage of using wet biomass was the same reason that initially drove interest in sludge. Concurrently, manure gained some attention, though to a lesser extent. In recent years, there has been growing interest in utilizing food waste and the organic fraction of municipal solid waste.

Since 2018, big attention has also being directed towards non-organic feedstock, specifically plastic waste. This development is a consequence of the current high momentum in plastic recycling[36]. The substantial global production of plastic waste presents both an exploitable resource and a challenge due to its high leakage rate into the environment[33,34]. Additionally, the imperative to transition away from fossil resources compels humanity to explore alternative methods for producing essential plastics. Consequently, among various technologies, HTL is currently under investigation as a potential method for chemically recycling plastics back into monomers and/or energetically valorizing them into oil.

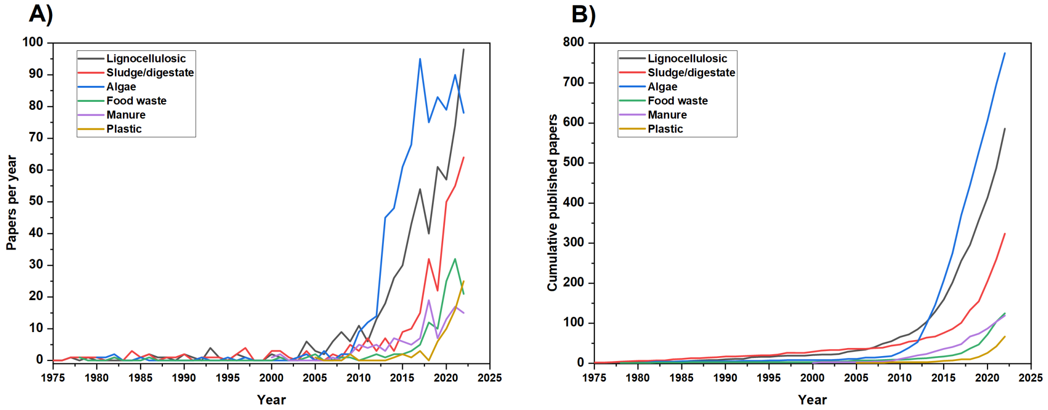

Figure 4: (A) Papers published per year and (B) Cumulative papers published per year, divided by feedstock type (source Scopus).

Different small pilot-plants were built in universities and research centers: Pacific Northwest National Laboratories (PNNL, USA)[51], Aarhus University (Denmark)[52], Aalborg University (Denmark)[53], University of Sidney (Australia)[54] and Iowa State University (USA)[55].

Despite all these studies, there are currently no commercial plants that have been operational for years. The first commercial HTL plants are currently under construction. Three major companies are trying to make HTL commercially available, namely Licella, Genifuel and Steeper Energy.

PNNL developed the ‘Modular Hydrothermal Liquefaction System’ (MHLS) that mostly focused on wastewater solids and is currently being patented by Genifuel Corporation. Two demonstrative pilot plants with a nominal capacity of 3 t/d of dry sludge from a wastewater plant are currently being building in Contra Cost County (USA) and Vancouver (Canada)[56].

In 2021, Steeper Energy concluded the construction of a commercial demo-plant in Tofte (Norway), having a nominal capacity of 30 barrels of oil per day[57]. There, their proprietary hydrothermal liquefaction technology (Hydrofaction™) was implemented. This technology is based on conversion of woody residues through HTL in supercritical conditions and with recirculation of both aqueous and oil phases[58]. If the commercial demo-plant will give positive results, a 2 000 barrels per day plant is expected to be built[57].

Licella Holdings Ltd. has developed a proprietary technology named Cat-HTR™, which is based on catalytic hydrothermal liquefaction. A commercial demonstration facility based on this technology has been operating for over 14 years in New South Wales (Australia)[59]. Currently, different commercial plants are under development worldwide (Australia, UK, Japan, South Korea, Canada) and a fullscale commercial Cat-HTR™ plant is expected to be built in Australia[59]. It is worth noting that some of these facilities are being built for processing biomass, while others are directed towards the use of plastic waste.

1.6.3 Main parameters affecting hydrothermal liquefaction

The primary objectives of hydrothermal liquefaction (HTL) involve minimizing by-products in both gaseous and solid forms, with a focus on optimizing the yield and quality of the resulting oil. However, findings from diverse research studies in the literature reveal substantial variations. These distinctions arise not only from the diverse types of biomass utilized, which significantly impact HTL performance, but also from the influence of various reaction parameters on the hydrothermal liquefaction process. Below a focus on the main operative parameters is reported.

Feedstock composition

The composition of the feedstock has been observed to strongly influence the yields of HTL products[45]. An important demonstration of this was firstly given by Biller and Ross[60]. They conducted an experimental campaign with model compounds showing that oil yield increases following the composition trend: lipids >> proteins > carbohydrates. Lipids inherently form an apolar phase; therefore, HTL simply facilitates the extraction of lipids from biomass, hydrolyzes them, and categorizes them as oil. Conversely, proteins tend to be hydrolyzed into amino acids, which mainly solubilize into the aqueous phase and partially are converted into oil phase. Carbohydrates on the other hand, mostly form a solid phase. Additionally, apart from the distinct behaviors of individual macroconstituents during HTL, strong interaction effects have also been observed between them[61]. Because of the strong dependency on the biochemical composition of biomass, the HTL performance can vary enormously starting from different biomasses, as shown in Figure 5.

The influence of feedstock properties on plastic hydrothermal liquefaction (HTL) was observed to be even more pronounced than in the case of biomass HTL. One advantage of plastic waste lies in its regular and well-defined starting composition, being of human-made origin. Consequently, understanding the types of polymers present in the waste allows for a highly predictable HTL outcome. For condensation polymers, the hydrolysis of monomers can be achieved through the action of water molecules[62]. This opens up the possibility of chemically recycling the monomer back into the chemical industry. However, precautions must be taken to prevent further degradation of the monomers, whether due to the hydrothermal environment or interaction with other intermediates. On the other hand, polymers devoid of heteroatoms, such as polyolefins or polystyrene, can undergo cracking through supercritical HTL to produce paraffinic-aromatic oil[63]. This oil can serve as feed for olefins production via steam cracking or as high-quality feedstock for fuel production[64].

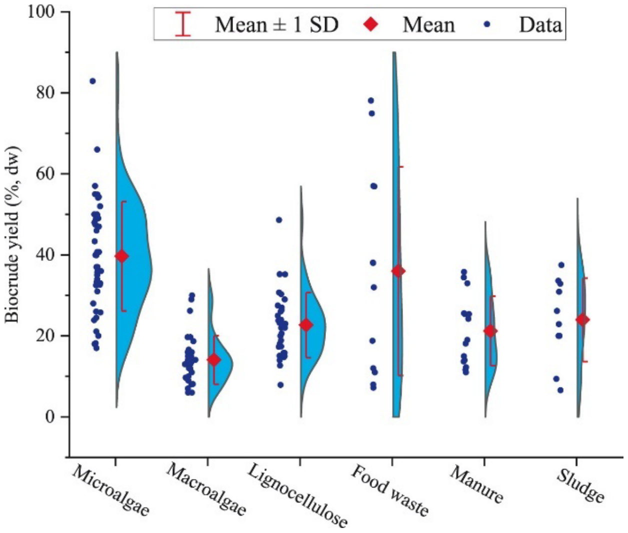

Figure 5: Oil yield obtained from HTL of different biomass sources, as reported in [65].

Temperature

Following the feedstock composition, temperature stands out as the second most critical parameter in HTL, exerting a substantial impact on oil yield and properties. Temperature not only affects water properties (Figure 2) but also indirectly influences the operating pressure, requiring it to surpass the vapor pressure of water under those specific conditions, and influences the selectivity between various reactive pathways. In subcritical conditions, the oil yield shows an optimum point with temperature[66]. However, the optimal temperature varies depending on the feedstock[38,66] (Figure 6), typically falling within the range of 280-350 °C for biomass HTL. This variation arises from the competition between the depolymerization of macromolecules, leading to the formation of intermediates, and the subsequent repolymerization of these intermediates[38]. The initial HTL step involving depolymerization is endothermic, and an increase in temperature facilitates overcoming the activation energy for bond breaking[38]. However, exceeding the optimal temperature leads to a prevalence of repolymerization reactions[67]. In lower temperatures, predominant hydrothermal reactions are ionic, transitioning to radical reactions as the critical point of water is approached. Consequently, unstable radical intermediates increase in concentration, ultimately recombining to form char and gas phases at the expense of oil[39].

In the case of plastics HTL, the effect of temperature is more pronounced. As showed by dos Passos et al.[62], heteroatom-containing plastics can effectively be converted in subcritical conditions. However, polyolefins and polystyrene, which does not contain heteroatoms, require supercritical conditions. This is because, in the absence of heteroatoms, carbon chains are not susceptible to ionic reactions but require radicals to be broken[68].

The properties of the oil are also significantly influenced by the reaction temperature. An increase in this variable generally leads to a higher calorific value of the bio-oil[69]. Primarily, this occurs because the presence of heteroatoms tends to diminish with rising temperature, mostly due to the increase in deoxygenation at higher reaction temperatures. For this reason, although produced in lower quantities, the biocrude produced at higher temperatures has better properties.

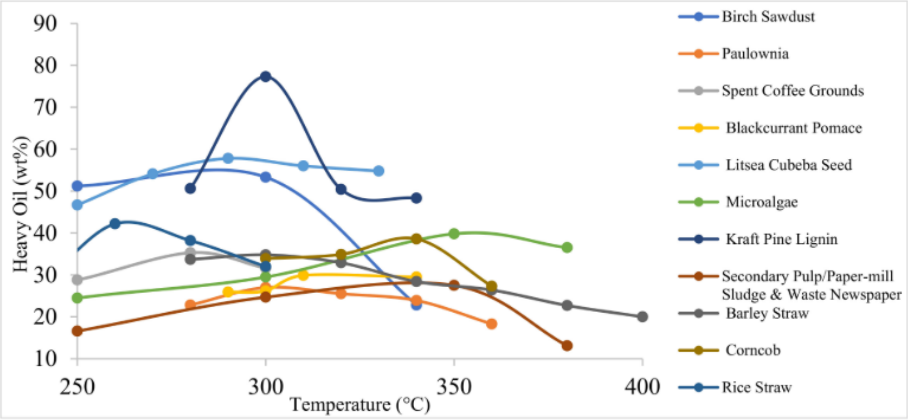

Figure 6: Effect of reaction temperatures on oil yield during the HTL of different feedstocks, as reported in [38].

Residence time

The residence time is defined as the time at a defined operating temperature, excluding heating and cooling times. The impact of this process variable has been extensively studied in the literature, and although less critical, it is correlated with the temperature. At a certain temperature, optimizing the residence time allows limiting the secondary recombination of intermediates and, consequently, optimizing oil production[66]. In the case of biomass, residence times are usually within 10-60 min[42]. The trend of oil yield with temperature depends on all the other variables, but often a slight maximum is present, and oil properties improve as time progresses[39]. However, above a certain residence time, no significant variations in yield are registered[70].

In recent years, fast HTL has been theorized[71]. It is characterized by fast heating rates (from 100 K/min to 100 K/s), high set-point temperatures (up to 600 °C), and limited residence times (less than 1 min)[71,72]. Fast HTL enabled the study of the effects of residence times in the order of seconds, and the results indicate a significant impact on HTL performance compared to isothermal HTL[71]. For example, Savage et al. obtained a 66 wt.% oil yield from *Nannochloropsis sp.* after fast HTL at a set-point temperature of 600 °C for 1 min, surpassing the performance achieved with isothermal HTL (a maximum of 52 wt.% at 300 °C for 20 min)[71]. Additionally, under the same fast HTL conditions, higher oil yields were also obtained from casein (23 wt.%) and potato starch (19 wt.%) compared to isothermal HTL (at 350 °C for 30 min), yielding 20 wt.% and 13 wt.%, respectively[73]. These high yields are associated with the fact that some intermediates formed in the first few seconds of HTL are apolar-like and can contribute to oil production. However, these oil-soluble molecules are more oxygenated and have lower stability, resulting in lower oil properties[74].

Pressure

Pressure plays a significant role in HTL from a technical perspective. A sufficiently high pressure is indeed required to prevent the vaporization of the water phase, enabling operating under hydrothermal conditions. Furthermore, the process achieves an enhanced energy balance by reducing the demand for vaporization enthalpy. Indeed, the amount of energy required to vaporize water at 25 °C and 1 bar is approximately the same required to bring it to 400 °C while remaining in the liquid state (225 bar). Since the majority of HTL research has been carried out in batch systems, adjustments to the operating pressure involve setting it before the reaction, considering the subsequent increase due to temperature rise. Conversely, in continuous systems, pressure can be directly controlled.

From a performance standpoint, in a subcritical environment, the dependence of oil yield on operating pressure is not yet well understood. Zhang et al. observed increased oil production from 2-3% to 33% at 300 °C for 15 min with corn straw after increasing the starting pressure from 20 to 40 bar[75]. However, the HTL performance did not change after further increasing the pressure to 60 bar. Mathanker et al. observed increased oil production with a higher starting pressure (21 bar vs 42 bar) at operating temperatures below 300 °C[76]. On the other hand, no variations were observed at 275 °C with spent coffee grounds at 5 and 20 bar of starting nitrogen[77]. Similar results were obtained by Tekin et al.[78].

The variations in performance in subcritical environment were explained by a decrease or increase in the density of the water phase, with an increase in water density associated with higher contact and penetration into the feedstock[67]. Conversely, variations in pressure in a supercritical environment seemed to not affect oil production[38]. Although there are contrasting opinions, it is believed that this is due to the fact that increasing the pressure introduces a 'cage effect,' which limits the breaking of C-C bonds[38,79].

Solid loading

The solid loading is expressed as the percentage of dry matter in the slurry fed to the HTL reactor, and alternatively can be expressed as a solid-water ratio. The presence of water in HTL is critical, as it releases the H^+ and OH^- that lead hydrolysis of the feedstock[38]. With higher solid loading, the amount of water available for dissociation decreases, limiting feedstock conversion. Moreover, water helps the dissolution of intermediates and the stabilization of free-radicals responsible for char and gas production[69]. Indeed, Singh et al. observed increasing conversion of water hyacinth and increasing oil yield from 6 to 16 and 18 wt.% with solid loading decreasing from 25% to 14% and 8%, respectively[80]. Although this trend was not always observed[81,82], there is a tendency not to operate with a low solid loading, as with the same amount of oil produced, in the presence of higher water content, pumping costs and, especially, the thermal demand of the plant would significantly increase, making the process less profitable. However, one of the main constraints for the industrial implementation of HTL is associated with feedstock pumpability, which limits the solid loading to 15-20 wt.%[83,84].

1.7 Aim and structure of the work

As described so far, hydrothermal liquefaction has proven to be a valuable technology for the production of fuel from wet biomass. Significant advances have been made since the beginning, enabling the current construction of the first commercial plants. Various feedstocks have been tested, ranging from lignocellulosic and sludge - studied since the outset - to more recent additions like manure, food waste, and even plastics. Despite the considerable attention and progress in recent years, little is still known about the mechanisms occurring during HTL, particularly concerning the more recently investigated feedstocks.

This work aims to enhance the understanding of the reaction mechanisms in HTL and explore potential applications. The focus was particularly directed towards two feedstocks, namely food waste and plastics, as they are the most recent and less studied. The study on the HTL of food waste examines how the initial biochemical composition influences reaction pathways and overall performance. Model compounds representing the three main biocomponents - carbohydrates, proteins, and lipids - along with real biomass were used. Monomers, such as glucose, glycine, and oleic acid, were tested individually and in mixtures at different temperatures to observe interaction effects. Additionally, consecutive reactions were employed to highlight the evolution between phases during HTL. Polymers - cellulose, albumin, glyceryl trioleate - and real biomass (canteen food waste) were used to investigate the effect of heating rate on HTL performance. Unlike monomers, polymers and real waste undergo hydrolysis before being converted into the final product. The hydrolysis reaction is typically fast and occurs during the heating process. Variations in heating rate can influence the relationship between hydrolysis and decomposition, with very high heating rates allowing for the degradation of polymers without prior hydrolysis. For this reason, the effect of the heating rate with bio-polymers and real waste was studied.

Very little is known about the HTL of plastic waste, which has garnered tremendous interest for its valorization, especially as chemical recycling. Despite being crucial for the packaging of many foods, multilayer plastic films pose a challenge as they cannot be mechanically recycled. This thesis explores the chemical recycling of multilayer plastic film made of PE-PET, aiming to recover the PET monomer, namely terephthalic acid (TPA), and convert the PE into paraffinic oil for recycling in the petrochemical industry as feed for the production of virgin polymers. Another significant challenge in plastic valorization is posed by PVC, given its corrosivity and toxicity issues. The dechlorination of PVC in a hydrothermal environment was studied, with a focus on understanding the reaction mechanisms. Subsequently, the dechlorinated solid was tested as feedstock for oil production through supercritical HTL.

Finally, given the low number of studies available, techno-economic (TEA) and life-cycle assessments (LCA) of an HTL plant were conducted. Within the HTL plant, an aqueous phase reforming section was designed to convert the residual oxygenates soluble in the aqueous phase into hydrogen for use in oil upgrading. The overall performance and the effectiveness of HTL-APR coupling were evaluated for two study cases differentiated by the feedstock used: lignin-rich stream and lignocellulosic residue.

Chapter 2 outlines the materials and methods employed throughout the thesis. The subsequent chapters present the obtained results. Chapter 3 focuses on the study of food waste HTL using monomers, while Chapter 4 delves into the study of heating rate during the food waste HTL using biopolymers. Chapters 5 and 6 are dedicated to the HTL of plastics. Chapter 5 details the campaign conducted to chemical recycle multilayer plastic film through HTL, while Chapter 6 describes the valorization of PVC via HTL. Finally, Chapter 7 provides a summary of both Techno-Economic Analysis (TEA) and Life Cycle Assessment (LCA).

Chapter 2

Materials and Methods

2.1 Materials

Various compounds were used to represent biomass composition. D-(+)-glucose (≥99.5% GC), glycine (ReagentPlus®) and oleic acid (90%, technical grade) were used as monomers. Cellulose (microcrystalline powder), albumin from chicken white (powder, 62-88%) and glyceryl trioleate (~ 65%) were used as polymers. All these compounds were purchased from Sigma-Aldrich. The albumin batch had a purity of 75%, with the remaining portion consisting of other proteins, namely conalbumin (10-15%), ovomucoid (10-15%), lysozyme (~2%), globulin, ovomucin and avidin. The glyceryl trioleate batch had a purity of 88%, based on fatty acid quantification. It was completely composed of triglycerides, and beside oleic acid, other fatty acids were palmitic and oleic. The actual biomass consisted of food waste collected from the university canteen after service. It was blended for homogenization and was then stored in a refrigerator until needed for the reaction.

For the plastic tests, a commercial multilayer film made of LLDPE-PET was employed as feedstock. This film, with a total thickness of 72 μm, where 12 μm of PET was on top of a 60 μm LLDPE layer, was cut into small pieces (~1 cm) before use. Pure LDPE powder from Sigma-Aldrich was used as feedstock to optimize the reaction conditions for the conversion of the PE layer. The PVC experiments employed PVC (low molecular weight) purchased from Sigma-Aldrich.

2.2 Methods

2.2.1 Hydrothermal liquefaction test (subcritical)

Biomass monomers (Chapter 3)

HTL tests were conducted in a batch reactor (Parr 4575A, 500 mL, Figure 7). In a typical experiment, the reactor was loaded with 200 g of solution of glucose or glycine with a concentration of 5 wt.% for the monocomponent solution, 10 wt.% for the binary solution (5 wt.% of each reagent) and 15 wt.% for the ternary solution (5 wt.% of each reagent). In this way, it was decided to keep the concentration of each reagent fixed rather than the overall solid concentration. Variations in the solid loading of the individual model compounds could affect HTL performance, so by keeping the individual solid loading constant, it was possible to exclude this effect in the analysis.

After loading, the reactor was purged with three cycles at 7 bar using He, and then was pressurized to 3 bar at ambient temperature. The reactions were carried out at different temperatures (200/250/300/350 °C), and the resulting heating rate was within 4-6 K/min according to the set point temperature. After reaching the set point temperature, a reaction time of 1 h preceded the activation of a cooling circuit inside the reactor, allowing the cooling to ambient temperature within 10 minutes.

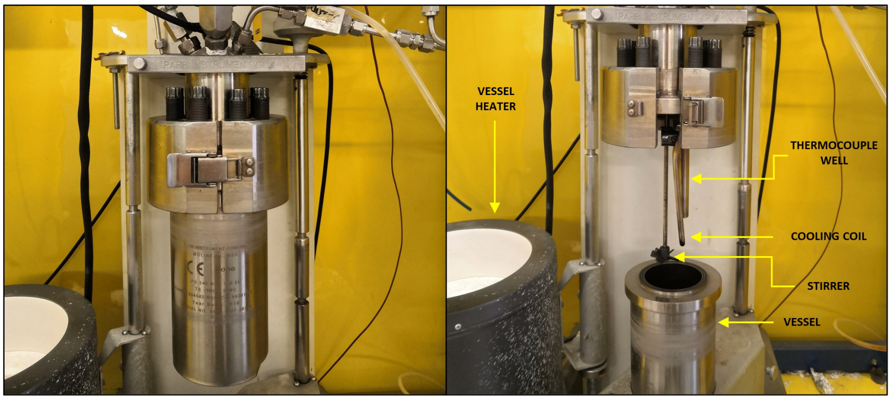

Figure 7: 4575A Parr reactor.

The liquid contained in the reactor was vacuum filtered to separate suspended solid. The permeate was extracted with diethyl ether in three steps (1:1 overall mass ratio); the raffinate was defined as aqueous phase (AP), while the extract phase was dehydrated and evaporated through a rotavapor (B-AP). The reactor, as well as the solid removed from the liquid, was cleaned by washing with ethyl acetate. The ethyl acetate solution was vacuum filtered. The solid removed by the filter was dried overnight at 105 °C and the resulting product constituted the solid. The ethyl acetate contained in the permeate was dehydrated and evaporated through a rotavapor. The resulting product was defined as B-S and the sum between B-S and B-AP represented the biocrude. An overview of the protocol is depicted in Figure 8.

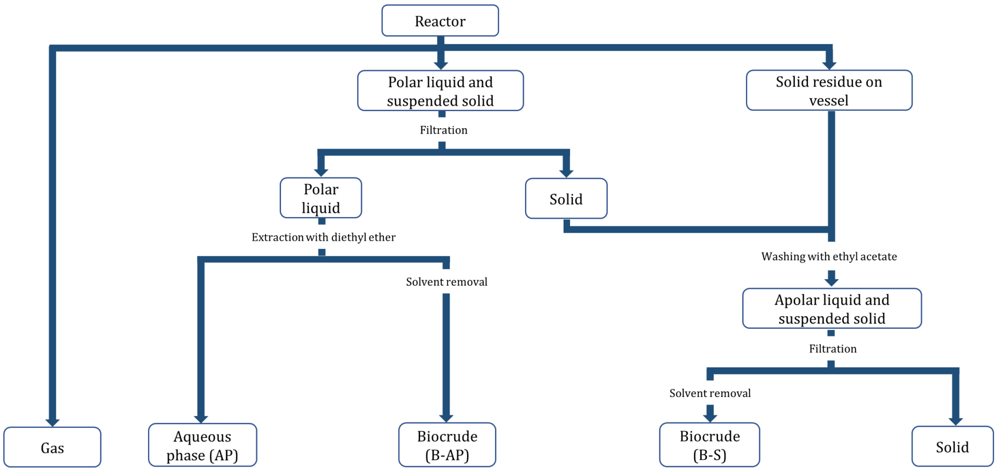

Figure 8: Work-up after HTL reactions with biomass monomers.

Effect of heating rate on biomass polymers (Chapter 4)

Experiments were conducted using bomb-type batch reactors with an internal volume of 20 mL (Figure 9). The reactors were assembled by closing off one end of a 316 stainless steel tube using a 3/4” cap. At the opposite end, a 3/4”-1/4” reducing union was positioned, with a 1/4” cap affixed to a 1-inch-long 1/4” tube. All fittings used were FITOK® and made of stainless steel.

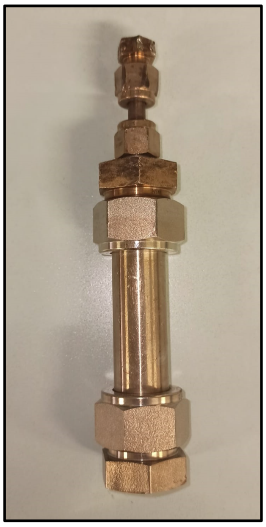

Figure 9: 20 mL bomb-type batch reactor.

Prior to reaction, the reactor was loaded with 1.8 g of feedstock and distilled water to achieve a total mass of 9 g. After loading, the reactor was then submerged into a sand bath (Techne© SBL-2D) equipped with a temperature controller (Techne© TC-9D). Four different heating rates were tested, and the submersion of the reactor was performed differently for each, as better described below. The operating temperature for all reactions was 325 °C, while two reaction times were used: 0 and 30 min. The 30-minute test was not performed for the highest heating rate used. After reaction, the reactor was removed from the sand bath and quenched in water at ambient temperature. Within less than 30 s, the internal temperature dropped below 50 °C. The reactor was left in water for further 5 minutes.

Heating rates

Different procedures were followed to obtain the four different heating rates:

- 5.2 K/min: the reactor was immersed in a sand bath at ambient temperature, operating in the bubbling fluidization regime. After immersion, the set-point temperature of the sand bath was raised to 325 °C. During the sand bath's heating process, the air's fluidization flow rate was adjusted to maintain the bubbling fluidization regime and prevent sand spillage;
- 29 K/min: the reactor was submerged into the sand bath while stable at the set-point temperature of 325 °C and within the bubbling fluidization regime. Immediately after submersion, the airflow for fluidization was halted, reducing the heat exchange coefficient. After 3 minutes, the sand bath was brought to the minimal fluidization velocity for 3 minutes long; after that the sand bath was returned to the bubbling fluidization regime;
- 77 K/min: the reactor was submerged into the sand bath while stable at the set-point temperature of 325 °C and within the bubbling fluidization regime;
- 115 K/min: the reactor was submerged into the sand bath while stable at a temperature of 360 °C and within the bubbling fluidization regime. This heating rate was exclusively used for a residence time of 0 minutes.

The heating rates were evaluated by using proxy reactors filled with 9 g of water and fitted with a 1/16” type K thermocouple, which enabled the plotting of the internal temperature over time. Heating rates were then calculated as the time required to reach 95% of the overall temperature change[85]. Accordingly, to reach 325 °C from the initial 25 °C, the heating rate was estimated based on the time needed to reach 310 °C. Figure 10 presents temperature profiles for the different cases, while the evaluated heating rate are reported in Table 1. Reactions conducted at 0 min were quenched upon reaching 310 °C, while reactions at 30 min were stopped 30 minutes after reaching 310 °C.

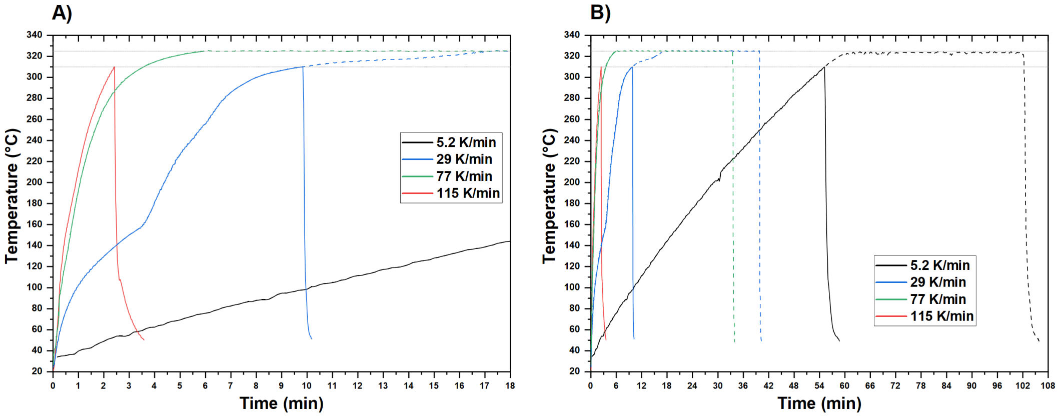

Figure 10: Temperature profiles for all the different reactions. (A) Zoomed in on the range of 0-18 min, and (B) covering the overall range of 0-108 min.

Reaction severity

Variations in HTL performance resulting from modifications in heating rate could be attributed to two causes. An 'indirect' cause is associated with higher or lower kinetic advancement of the reaction due to the fact that a slower/faster heating rate leads to longer/shorter heating times. On the other hand, another ('direct') cause could result from the fact that remaining at lower temperatures during the heating phase could lead to changes in the chemical mechanisms and formation pathways of the different phases. Indeed, reactions at lower temperatures typically result in increased production of the solid phase (hence it is indeed called 'hydrothermal carbonization' rather than 'hydrothermal liquefaction')[86], and prolonged exposure to lower temperatures could lead to irreversible formation of solid. To distinguish between these two causes, the kinetic severity factor (KSF, Eq. (1) was used. T(t) denotes the temperature (°C) at time t (min); t_0 corresponds to the starting time, while t_f represents the ending time of the reaction.

$$KSF = log_{10}(R^0) = \log_{10}\left(\int_{t_0}^{t_f} e^{\frac{T_{(t)}-100}{14.75}} dt\right) \qquad (1)$$

The kinetic severity factor was initially employed by Overend and Chornet to account for both the effects of temperature and reaction time during aqueous/stream pretreatments of lignocellulosic biomasses, expressing the severity through a single factor[87]. The KSF was derived from a first-order kinetic model, assuming a constant of 14.75 K, experimentally derived, and a reference temperature of 100 °C[88]. Currently, the KSF is widely applied in the study of HTL[71,89–92], as it is considered a reliable method for describing the kinetic severity of the process. Moreover, Prestigiacomo et al. recently observed that the KSF can be efficiently used as parameter to estimate the HTL performance[93].

The KSF was calculated for all the heating rates and residence times used. As shown in Table 1, increasing the heating rate at 0 min leads to a decrease in kinetic severity, while alterations in the heating rate at 30 min do not affect it. This difference can be explained by the fact that, at 0 min, the entire residence time was exclusively allocated to the heating time, being higher for lower heating rates to reach the reaction temperature, and resulting in a more significant advancement of the reaction. On the other hand, at 30 min, the time required for heating has minimal impact, as the reaction kinetics at the setpoint temperature dominate. Therefore, only variations observed in heating rates at 30 minutes can definitively confirm or refute a direct effect on HTL, which could be attributed to thermodynamically-driven changes in the reaction pathway during heating. Conversely, differences at time 0 can only provide an indication of the reaction's progression.

Table 1: Heating rates and kinetic severity factor for all the different cases.

Heating rate (K/min)	5.2	29	77	115
KSF at 0 min	6.8	6.4	6.0	5.7
KSF at 30 min	8.1	8.1	8.1	-

Work-up

After washing and drying with compressed air, the reactor was weighed. It was then opened to vent the produced gas, and weighed again. The difference in weight gave the mass of gas produced. The content of the reactor was poured into a 50 ml centrifuge tube. Diethyl ether was used to rinse the reactor and remove any possible solid and oil residues, along with mechanical action using a spatula. At least 36 mL of DEE were used, subdivided into multiple aliquots. If the cleaning solvent was not transparent, additional DEE was added until transparency was achieved. All the DEE used was added to the 50 ml centrifuge tube containing all the produced phases. The centrifuge tube was then shaken and placed in a vibro-mixer to ensure thorough mixing of all phases present. Subsequently, the tube was inserted into a centrifuge and spun for 8-10 min at 4500 rpm to fasten phase separation and solid sedimentation. The lightest apolar phase, which contained the biocrude, was collected using a Pasteur pipette and vacuum-filtered through a qualitative filter paper (Whatman grade 5). The resulting polar phase was then dried with sodium sulfate and evaporated in a rotavapor. The resulting biocrude was then weighed and stored for subsequent analysis. The aqueous phase was vacuum-filtered using the same filter employed for the apolar phase. Attention was paid to ensuring that all the solid in the tube was transferred onto the filter. Subsequently, the aqueous phase was then left for 36 h under a chemical hood to remove any residual DEE and then stored. The solid-containing filter was left overnight in oven at 105 °C to remove any residual moisture; it was then weighted and the solid collected. An overview of the protocol is depicted in Figure 11.

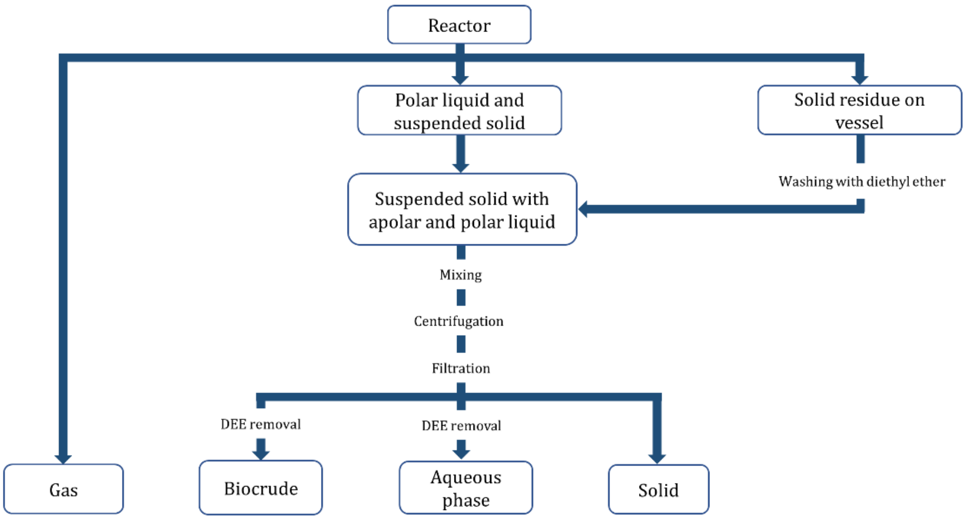

Figure 11: Work-up after HTL reactions with biomass polymers.

Blank tests were conducted with each feedstock to analyze their solubilities. The blanks were prepared by mixing each feedstock with an amount of water equal to that used in the reactions. Then, the previously described work-up was performed without conducting the reactions beforehand. The results are reported in Table 2.

All reactions at 0 min were performed at least on duplicate, while reactions at 30 min were performed at least on triplicate. Carbon balance resulted always higher than 77%.

Table 2: Feedstock moisture and distribution among the different phases after the blank tests.

Feedstock	Moisture (wt.%)	Ash (wt.%$_{db}$)	Solid (wt.%$_{db}$)	Biocrude (wt.%$_{db}$)	AP (wt.%$_{db}$)
Cellulose	0.0 ± 0.0	0.0 ± 0.0	94.3 ± 1.9	0.0 ± 0.0	5.7 ± 1.8
Albumin	5.4 ± 0.1	6.4 ± 0.2	12.1 ± 0.3	0.1 ± 0.0	87.8 ± 0.3
Triolein	0.0 ± 0.0	0.0 ± 0.0	0.0 ± 0.0	91.9 ± 2.5	8.1 ± 2.5
Simulated food waste	1.2 ± 0.0*	1.3 ± 0.0*	79.1 ± 0.9	2.6 ± 0.1	18.3 ± 0.9
Food waste	67.9 ± 0.5	2.9 ± 0.0	87.2 ± 0.2	4.2 ± 0.2	8.6 ± 0.4

**evaluated as average of the values obtained from cellulose, albumin and triolein.*

Multilayer film (Chapter 5)

Reactions were performed by loading 1.8 g of multilayer film and 7.2 g of distilled water (20 wt.% solid loading) into 20-mL bomb-type batch reactors described above. After loading, the reactor was submerged into a FTBL12 Fluidized Sand Bath (Accurate Thermal Systems LLC, USA) at 325 °C for 20 minutes of reaction time, including heating time. After reaction time, reactors were quenched in a water bath at ambient temperature.

After the reaction, the mass of gas produced was calculated by difference between the weight of the reactor before and after venting. The aqueous phase present in the reactor was removed by decanting. Then, the TPA phase was separated according to a solubilization-precipitation work-up, similar to what has been described in the literature[94]. Indeed, the solid phase, consisting mainly of a single block of melted polymers, was placed into a 30 mL test tube with 20 mL of NaOH solution (1.95 wt.%), which was previously used to collect any solid powder remaining in the reactor. The test tube was sonicated for 10 min in an ultrasonic bath, vacuum filtered and sonicated again for a further 10 minutes with 20 mL of fresh alkaline solution to ensure the neutralization of TPA and the solubilization of sodium terephthalate. The solid residue after alkali washing was left overnight in oven at 105 °C to remove residual moisture; it was then weighed and labelled PE-rich. The 40 mL of NaOH solution, containing the solubilized sodium terephthalate, was acidified with a few drops of H_2SO_4 until the pH was 1, ensuring precipitation of TPA. The liquid solution was vacuum filtered and the filter cake was dried in oven at 105 °C, then weighed and attributed to be TPA. Product mass yields are expressed as yields based on initial mass, while recoveries are defined as the quantity obtained based on available quantities.

Dechlorination of PVC (Chapters 6)

1.8 g of PVC were loaded in the 20-mL batch reactor along with sufficient distilled water to achieve an overall mass of 9 g. For reactions involving neutralization, 1.8 g of PVC was combined with 1.81 g of KOH (10% excess in molar basis), maintaining the total mass at 9 g. This ensured the neutralization of all HCl produced after complete PVC dechlorination. The reactor was then submerged into an FSB 3 Fluidized Sand Bath (Omega Engineering, USA), preheated at set point temperature. Six different temperatures were tested from 200 °C to 325 °C at a 25 °C interval in the case of non-neutralized reactions, and between 250 °C and 300 °C for neutralized reactions. The residence time was kept fixed at 20 min, after which the reactor was rapidly cooled in water. It is worth noting that corrosion was observed, also due to the high loading of PVC, and that reactors lasted for few experiments. Samples were labeled based on the operating temperature (e.g., 200, 225, 250, 275, 300, 325), and in the case of neutralized reactions, 'KOH' was appended to the name (e.g., 250-KOH, 275-KOH, 300-KOH).

The mass of gas was quantified by weight difference between the reactor before and after venting. After that, the liquid present in the reactor was poured in a centrifugal tube and centrifugated at 3500 rpm for 5 min. The separated liquid was collected. The solid remaining inside the reactor, as well as the solid in centrifugal tube, was removed by rinsing with distilled water and by mechanical action with a spatula. This aqueous solution was vacuum filtered with Buchner funnel and a pre-weighed paper filter. The filter was left overnight in oven at 105 °C to remove residual moisture; it was then weighed and the solid collected.

2.2.2 Hydrothermal liquefaction test (supercritical)

Reactions were performed in mini-batch reactors with an internal volume of 10 mL, made from a ¾ inch port connector (Hy-Lok ©) and two caps made of 316 stainless steel (Figure 12). The amount of distilled water was calculated in order to obtain an autogenous pressure of 225 bar at reaction temperature while the solid loading (solid/solid+water) was kept fixed at 33 wt.%. Water amount ranged within 0.832-1.084 g.

Figure 12: 10 mL bomb-type batch reactor.

Multilayer film (Chapter 5)

The PE-rich phase obtained after the subcritical treatment of the multilayer film was used as starting feedstock of the supercritical step. After loading, the reactor was submerged into a FTBL12 Fluidized Sand Bath (Accurate Thermal Systems LLC, USA) preheated at the desired temperature (425/450/475 °C). The reactor was left inside the sand bath for 60-120 minutes of reaction time, including heating time. After reaction time, reactors were quenched in a water bath at ambient temperature.

After reactions the liquid content of the reactor was recovered to a 1.5 mL Eppendorf tube using a Pasteur pipette. The Eppendorf tube was spun at 8000 rpm for 5 min, to separate the oil and aqueous phase. The supernatant oil phase was directly recovered using a glass Pasteur pipette, collected in a GC vial, and weighed. By not using any extraction solvent, the losses due to evaporation of the low-boiling oil portion were limited. However, some oil remained on the reactor's wall, and thus the reactor, as well as the Pasteur pipettes and the Eppendorf tube, were rinsed with acetone. The acetone solution was vacuum filtered and the solid residue was left overnight in oven at 105 °C, and weighed. The acetone was left in 30 mL amber bottles under nitrogen flow until the solvent was completely removed. The residual oil phase was then weighed. The oil yield is reported the sum of the oil directly collected and the one recovered with acetone. Approximately 90% of the overall oil was directly recovered from the reactor, and this directly recovered oil was used for the oil analysis.

Dechlorination of PVC (Chapter 6)

The dechlorinated solid obtained after the subcritical treatment of the PVC was used as starting feedstock of the supercritical step. After loading, the reactor was inserted in a pre-heated furnace (Carbolite GSM 11/8 8L) at set point temperature. Four different temperatures were tested from 420 °C to 480 °C with a 20 °C interval. After 60 minutes in the furnace, reactors were removed and let cool in air.

When room temperature was reached, reactors were weighed before and after venting, so gas yield could be determined by difference. The aqueous phase of the reactor was then poured into a beaker and vacuum filtered. The residue inside the reactor, as well as the solid retentate from the filtration, were washed with methanol. The organic solution was vacuum filtered to separate solid and the methanol phase. The filter containing the solid was dried overnight in an oven at 105 °C to remove residual moisture; it was then weighed and the solid collected. The solid-free methanol solution was collected in a 30 mL amber bottles and left under nitrogen flow until the solvent was completely removed. The residual oil phase was then weighed.

2.2.3 Analytical methods

Common methods

The mass yield of every phase was evaluated according to Eq. (2), except for the AP yield which was defined as complement to 100%. Carbon and nitrogen yields were calculated by dividing the masses of carbon and nitrogen in the products by the masses of carbon and hydrogen evaluated in the feedstock (Eq. (3) and Eq. (4)). An elemental analyzer (Elementar vario Macro Cube) was used to determine the elemental composition (CHNS) of feedstocks, solids, aqueous phases and biocrudes. Only samples of at least 20 mg were analyzed, each at least in triplicates. Higher heating values (HHVs) for solid and oil phases were evaluated from the elemental analysis (Eq. (5)), according to the work from Channiwala & Parikh[95]. Chemical energy recovery (ER) was calculated according to Eq. (6), where HHV values are given in MJ/kg.

$$Mass\ yield_{phase}\ (\%) = \frac{mass_{db,phase}}{\sum mass_{db,reagents}} \tag{2}$$

$$C\ yield_{phase}\ (\%) = \frac{C\ content\ phase\left(\frac{g\ C\ in\ phase}{g\ phase}\right) \cdot phase\ yield\ \left(\frac{g\ phase}{g\ feed}\right)}{C\ content\ feed\left(\frac{g\ C\ in\ feed}{g\ feed}\right)} \tag{3}$$

$$N\ yield_{phase}\ (\%) = \frac{N\ content\ phase\left(\frac{g\ N\ in\ phase}{g\ phase}\right)\cdot phase\ yield\ \left(\frac{g\ phase}{g\ feed}\right)}{C\ content\ feed\left(\frac{g\ N\ in\ feed}{g\ feed}\right)} \tag{4}$$

$$HHV\ \left(\frac{MJ}{kg}\right) = 0.3491\cdot C_{wt.\%}\ + 1.1783\cdot H_{wt.\%} + 0.1005\cdot S_{wt.\%}\ - 0.1034\cdot\ O_{wt.\%} - 0.0151\cdot\ N_{wt.\%} - 0.0211\cdot\ Ash_{wt.\%} + 0\cdot\ Cl_{wt.\%} \tag{5}$$

$$ER\ (\%) =\ Mass\ yield_{phase}\cdot\frac{HHV_{phase}(\frac{MJ}{kg})}{HHV_{feedstock}(\frac{MJ}{kg})} \tag{6}$$

Attenuated Total Reflectance Fourier-transform infrared spectroscopy (ATR-FTIR) was performed on a Bruker Alpha Platinum spectrometer. 24 spectra from 4000 to 400 cm^{-1} with resolution of 2 cm^{-1} were automatically collected and their average was given as result.

Analysis of organic acids, alcohols, aldehydes, ketones and sugars dissolved in the aqueous phase was performed through HPLC. HPLC analysis (Shimadzu) was performed with a Rezex ROA-Organic acid H+ (8%) column (300 mm · 7.8 mm). The mobile phase was 5 mM H_2SO_4 in water. The flow rate was fixed at 0.7 mL/min and the temperature of the column at 50 °C. The products were determined using a refractive index detector (RID) and quantified by external calibration using purchased standards.

Biomass monomers (Chapter 3)

Beside the mass yield reported in Eq. (2), an averaged yield (theoretical) was also defined to assess the synergistic/antagonistic behavior of the interactions (Eq. (7)). This value takes into account the experimental yields derived from the tests in which monomers were alone in the mixture. If a difference between the averaged yields and the experimental yields is present, an interaction between the constituents can be expected. Eq. (8) and Eq. (9) take account for this difference in absolute and relative form, respectively.

To better understand the correlation between the phases, a campaign of consecutive tests was also performed. The different phases (AP, B-AP, B-S, S) produced at 250 °C for 1 h with glucose, as well with glucose-glycine, were individually re-loaded in the reactor and heated up to 350 °C for 1 h and starting 3 bar of He. Before reaction, the solid and biocrude, which are insoluble in water, were loaded in the reactor by pouring them with fresh distilled water to obtain a total 200 g solution. On the other hand, the AP were left to mix overnight under chemical hood to ensure the removal of the residual diethyl ether and then were loaded without dilution.

$$Averaged\ value\ (\%) = \frac{\sum_{i=monomer} yield\ alone_i \cdot concentration\ in\ mixture_i}{\sum_{i=monomer} concentration\ in\ mixture_i} \quad (7)$$

$$Absolute\ difference\ (\%) = yield_{experimental} - yield_{averaged} \quad (8)$$

$$Relative\ difference\ (\%) = \frac{yield_{experimental} - yield_{averaged}}{yield_{experimental}} \quad (9)$$

The gas phases obtained from biomass and the model compounds were analyzed by a Micro-GC (SRA) equipped with Molsieve 5A and PoraPLOT U columns, and TCD detector. The quantification of the gas phase was based on the final concentration of He (used as internal standard), accordingly with the ideal gas law.

The oil phases were characterized using gas chromatography (Agilent Model 7890A) coupled to a mass spectrometer (Agilent Model 5975C). A DB-5ms column (30 m ·250 μm · 0.25 μm) and He as carrier was used. The injection volume was 0.5 μL, the injection port temperature was 290 °C with pulsed splitless mode. The temperature program used was as follows: 40 °C (2 min soak) // 15°C/min // 180 °C (10 min soak) // 3 °C/min // 230 °C (5 min soak)// 15 °C/min // 300 °C (2 min soak). After analysis the identified compounds were subdivided according to their functionality. In the case of molecules containing more than one functionality, their identification was assigned based on the following priority order: N-containing aromatics > phenol derivatives > benzene derivatives > furan derivatives > amines > cyclic oxygenates > cyclic ketones > esters > aldehydes > ketones > alcohols > ethers. The areas of all compounds belonging to a given group were summed and were presented as a percentage of the sum of the areas of all identified compounds.

Solid and biocrude properties were also evaluated through thermogravimetric analysis (TGA) and attenuated total reflectance-Fourier transform infrared spectroscopy (ATR-FTIR). TGA was carried out with a Mettler Toledo TGA/SDTA851 thermal gravimetric analyzer, from 25 °C to 800 °C at 10 °C/min heating rate and under nitrogen flow (50 mL/min).

Effect of heating rate on biomass polymers (Chapter 4)

To asses the gas composition, a slightly different reactor configuration was used compared to the one reported above (Paragraph 2.2.1). A 1/4"-1/8” reducing union was attached to one end of the 3/4”-1/4” reducing union, and a 50 cm-long 1/8” stainless steel tube was connected to it. This tube was sealed with a screwed bonnet needle valve. The extended length of the narrow tube was necessary to keep it clear of the sand bath, allowing the valve to remain outside of it. Simultaneously, due to its reduced inner diameter, its volume was only 0.77 mL compared to the 20 mL of the reactor immersed in the sand bath. Before the reaction, the reactor was loaded and then purged and pressurized with 9 bars of He. The resulting gas phase was then sampled and examined using a Micro-GC (SRA) equipped with Molsieve 5A and PoraPLOT U columns, along with a TCD detector. The average composition obtained at 30 min with the three different heating rates was used to evaluate the carbon content of the gas for all the tests at both 0 and 30 min.

To determine the compositions of the biocrudes, a GC-MS (Agilent 7890B GC-Agilent 5975C) was employed. A volume of 0.9 ml of the biocrude solution in acetone (ca. 10 mg/ml) in a glass vial was subjected to derivatization with 0.1 ml of BSTFA (+1% TCMS) for 1 h while being stirred over a magnetic plate at 70 °C. The derivatized sample was then injected in a DB-5ms column (dimensions 30 m × 0.25 mm × 25 µm) using a split ratio of 20:1 and an injection temperature of 280 °C. The helium flow in the column was kept constant at 1 mL/min, and the temperature was programmed as follows: 40 °C (5 min soak) // 10°C/min // 100 °C (0 min soak) // 4 °C/min // 280 °C (0 min soak) // 10 °C/min // 300 °C (0 min soak). Compound identification was carried out using the NIST 17 library and the subdivision between the different types of molecules was based on their functionalities. In the case of molecules containing more than one functionality, their identification was assigned based on the following priority order: S-containing molecules > DKPs > N-containing aromatics > imines/nitriles > cyclic amides/cyclic imides > amides > amines > long fatty esters > monoglycerides > long fatty acids > PAHs > O-containing aromatic rings > phenols > benzenes > furans > acid > oxygenated. In the case of biocrudes obtained from albumin at 0 minutes, the biocrude samples were injected into the GC-MS without prior derivatization. This was necessary due to the NIST library's inability to identify most of the peaks after derivatization of these samples.

To assess the biochemical content of the food waste, lipids, proteins and ashes were measured, while carbohydrates were calculated by difference. The protein content was calculated by multiplying the nitrogen content, which was evaluated through elemental analysis, by a factor of 6.25[96]. For lipid content determination, the biomass was dried overnight in an oven at 105°C. Subsequently, 7 g of dry biomass were subjected to extraction using a Soxhlet extractor with 200 ml of petroleum ether heated to 70 °C for 6 hours. The extracted material was then subjected to evaporation by rotavapor to remove the petroleum ether, and the remaining mass was accounted for as lipids. The ashes of the feedstock were measured by combustion at 550 °C for 3 hours in an oven. Alternatively, the ashes of the produced solids were measured via thermogravimetric analysis (TGA, Mettler Toledo SDTA851). A few milligrams of the sample in a 70 µl crucible were subjected to the following temperature program: 25 °C (0 min soak) // 30 °C/min // 900 °C (10 min soak) under an airflow of 50 ml/min.

Multilayer film (Chapter 5)

The feedstock composition and the distribution of the boiling points were performed by thermogravimetric analysis (TGA) with a Mettler Toledo TGA/DSC 3^+. For feedstock, a sample was loaded in a 70 µl crucible which was heated under nitrogen flow (50 ml/min) from 50 to 190 °C at 10 °C/min, from 190 to 470 °C at 1 °C/min and from 470 to 900 °C at 20 °C/min. At 900 °C the sample stayed for further 10 min under air flow (50 ml/min). The amount of PE and PET was evaluated by comparison with pure LDPE and PET. For oil boiling point distribution, ~ 8 mg liquid oil was loaded into a 70 µl crucible and covered with a perforated lid. The sample was heated under nitrogen flow (50 ml/min) from 25 to 900 °C at 10 °C/min.

Terephthalic acid (TPA) purity was evaluated by differential scanning calorimetry (DSC) with a Mettler Toledo TGA/DSC 3^+. The sample was loaded in a 70 µl crucible which was heated under nitrogen flow (50 ml/min) from 40 to 410 °C at 10 °C/min in duplicate. Triplicate TPA standards (98%, Sigma-Aldrich) were also run. The amount of TPA in the TPA-rich phase was calculated based on the heat of sublimation according to Eq. (10), as explained elsewhere[97].

$$TPA_{purity}\,(wt.\%) = \frac{(\Delta H_{subl.})_{TPA\text{-}rich\ phase}}{(\Delta H_{subl.})_{standard}} \tag{10}$$

The TPA recovery was calculated from the total amount of PET evaluated in the multilayer film. Based on stoichiometry of PET hydrolysis (Eq. (11)), the maximum amount of TPA is equal to 86.5 wt% of processed PET. The formula used is reported below (Eq. (12)).

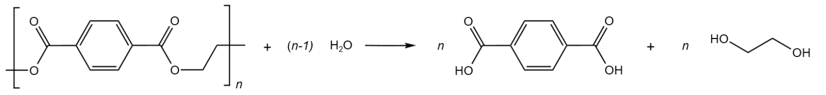

(11)

$$TPA_{yield}\,(wt.\%) = \frac{(Weight)_{TPA\text{-}rich\ phase}}{(Weight)_{multilayer}} \cdot \frac{(TPA_{purity,wt.\%})}{0.865 \cdot (PET_{wt.\%})_{multilayer}} \tag{12}$$

To evaluate the gas phase obtained in the supercritical conditions, selected reactions were also performed with 10 mL-reactors having a slightly modified setup. One of the two 3/4” port connector caps, was substituted with a 3/4”- 1/16” reducer to connect a 1/16” tube 42 cm long, connected to a needle valve. The hydrocarbons present in the gas phase were identified by GC-FID, adapting the method found in the literature[98]. An Agilent HP-PLOT/Q (dimensions 15 m × 0.32 mm × 20 µm) was used for hydrocarbon separation. 0.1 mL of gas sample was manually injected on the GC column; the temperature programming was 35 °C (10 min soak) // 5°C/min // 80 °C (1 min soak) // 5 °C/min // 200 °C (5 min soak). FID temperature was set at 250 °C. Identification of hydrocarbons was based on the elution order found in the literature[98], while their quantification with respect to methane was based on the carbon number according to Eq. (13). In order to quantify the concentration of methane, hydrogen and carbon dioxide, 0.2 mL of the gas sample was injected on a dedicated GC-TCD.

$$C_xH_y\ (vol.\%) = CH_4\ (vol.\%) \cdot \frac{(Area\ FID)_{C_xH_y}}{(Area\ FID)_{CH_4} \cdot x} \tag{13}$$

The oil compositions was analyzed using a GC (Agilent 7890B GC) coupled with MS (Agilent 5977A). Samples of liquid oil collected after centrifugation were syringe-filtered and diluted 1:100 v/v in acetone. 1 μL of diluted sample was injected on a VF-5ms column (dimensions 60 m × 0.25 mm × 25 μm) in split mode with a split ratio 20:1, injection temperature of 280 °C. The helium flow in the column was kept constant at 1 mL/min while the temperature programming was 40 °C (5 min) // 10°C/min // 100 °C (0 min) // 4 °C/min // 280 °C (0 min)// 10 °C/min // 300 °C (0 min). The identification of compounds was based on NIST 17 library and only compounds with a match factor greater than 80% and a peak area greater than 1% of the largest peak were considered. N-paraffins, PAHs and some aromatics were quantified through external calibration.

Dechlorination of PVC (Chapter 6)

Chlorine determination was performed by μ-XRF (Bruker-Tornado M4). Measurements were performed in duplicate for every sample analyzed. The chlorine recovery in the solids was computed according to Eq. (14). The correlation by Channiwala & Parikh (Eq. (5)) was used to estimate the Higher Heating Value (HHV) based on elemental composition, as it was checked to be applicable even for materials with high chlorine content like PVC[95].

$$Cl\ recovery\ (\%) = \frac{Cl\ content\ solid\ \left(\frac{g\ C\ in\ solid}{g\ solid}\right) \cdot solid\ yield\ \left(\frac{g\ solid}{g\ PVC}\right)}{Cl\ content\ PVC\ \left(\frac{g\ C\ in\ PVC}{g\ PVC}\right)} \tag{14}$$

Thermogravimetric analysis (TGA) was performed on a Mettler–Toledo analyzer (TGA/DSC 3^+). Samples were loaded in 70 μl crucibles which were heated under nitrogen flow (50 ml/min) from 50 to 900 °C with heating rate of 10 °C min^{-1}. Samples were then kept at 900 °C for 10 min under air flow (50 ml/min).

Py-GC-MS analyses were performed using a multi-shot pyrolyzer EGA/Py-3030D micro-furnace (Frontier Laboratories Ltd. Fukushima, Japan) interfaced to a gas chromatograph coupled with a mass spectrometer (7890B and 5977B Agilent Technologies, Palo Alto, USA). About 1 mg of each sample was placed into a clean stainless-steel cup, inserted into the micro-furnace and pyrolyzed at 600 °C for 1 min with helium as carrier gas (1 mL min^{-1}). The GC injector was operated at 280 °C, with 1:20 split ratio, and the interface temperature was kept at 280 °C. The pyrolysis products were eluted in constant flow mode at 1 mL min^{-1} (carrier gas helium) and separated by a HP-5MS fused silica capillary column (dimensions 30 m × 0.25 mm × 0.25 μm) with the following temperature program: 50 °C (2 min soak) // 10 °C min^{-1} // 280 °C (8 min soak). The MS was operated in EI positive mode (70eV, scanning 10–600 m/z) with transfer line temperature 250 °C, ion source temperature 230 °C and quadrupole temperature 150°C. Each sample was analyzed in triplicate and blanks were performed before each set of analysis.

The compositions of the oil obtained after the supercritical step was analyzed using a GC-MS (Agilent 7890B GC-Agilent 5977A). After removing the solvent from the oil phase, most of the light phase was lost. Therefore, the characterization of the oil phase was performed by directly injecting the oil-containing solvent without prior solvent removal. For this analysis, instead of using methanol as extracting agent, as done during the normal work-up, acetone was utilized. A volume of 1 μL of the acetone solution was directly injected into a VF-5ms column (dimensions 60 m × 0.25 mm × 25 μm), with a split ratio 20:1 and an injection temperature of 280 °C. The helium flow in the column was kept constant at 1 mL/min while the temperature programming was 40 °C (5 min soak) // 10°C/min // 100 °C (0 min soak) // 4 °C/min // 280 °C (0 min soak)// 10 °C/min // 300 °C (0 min soak). Compound identification was based on NIST 17 library.

The evaluation of the kinetic parameters was based on differential scanning calorimetry (DSC) performed on a Mettler–Toledo analyzer (TGA/DSC 3^{+}). PVC samples were loaded in sealed micro-reactors (30 μl) at 20% solid loading. Crucibles were then heated under nitrogen flow (50 ml/min) from 30 to 340 °C at 4 different heating rates 10-20-30-40 °C min^{-1}. At 340 °C the samples stayed for further 20 min. The Kissinger method was used for the determination of the kinetic parameters[99]. The apparent activation energy (E_A, J/mol) was evaluated based on the following equation (Eq. (15)):

$$ln\left(\frac{\beta}{{T_m}^2}\right) = ln\left(\frac{k_\infty \cdot R}{E_A}\right) - \frac{E_A}{RT_m} \tag{15}$$

where β (K/min) is the heating rates, T_m (K) is the reaction peak temperature, R (J mol/K) is the Arrhenius constant, k_∞ (min^{-1}) is the pre-exponential factor of the Arrhenius constant. Plotting $ln\left(\frac{\beta}{{T_m}^2}\right)$ vs $1/RT_m$ the apparent activation energy of the reaction can be determined by the slope of the line, while the pre-exponential can be determined by the intercept.

Chapter 3

Interaction between monomers of biomass

3.1 Introduction

Among the various types of biomasses that could be exploited, the utilization of food waste is particularly interesting. Food waste is generated in large quantities, especially in areas with high residential density, and it must be disposed of. Approximately one-third of the world's edible food is wasted, amounting to 1.3 billion tons of organic material, with nearly half of it occurring after the post-harvest stage and before retail[100,101]. Even if it were possible to drastically reduce all inefficiencies and losses along the supply chain, the production of food waste is inevitable, and its management must be addressed.

Due to the high moisture content in food waste, its valorization through hydrothermal liquefaction (HTL) is promising. Food waste is constituted by lipids, proteins and carbohydrates, and numerous studies have been conducted to study how the starting composition of biomass influences HTL performance[61,102–108]. However, most of these studies focused only on oil ('biocrude') yield, leaving the distribution of the remaining phases largely unexplored. Additionally, it remains unclear whether the different phases produced during HTL can interact and undergo conversion among themselves, and how the reaction conditions impact this phenomenon.

To address this knowledge gap, this chapter focuses on understanding the reaction mechanisms during HTL of glucose, glycine and oleic acid, serving as monomers of carbohydrates, proteins, and lipids, respectively. The study primarily aims to highlight the differences, both quantitative and qualitative, observed among all phases when reacting individually and in combination. Indeed, a comprehensive examination of all generated products is essential to delve into the underlying mechanisms. Temperature is widely acknowledged as one of the most crucial parameters in HTL (Paragraph 1.6.3); for this reason, the previous analyses were performed over a broad temperature range (200-350 °C) to observe whether and how they were affected.

The novelty of this chapter also lies in the approach used to detect the interactions among the different phases. The multiphase environment of HTL is often modeled and studied through a lump model based on the different phases produced (solid, gas, biocrude and aqueous phase)[109–111]. A typical reaction scheme is shown in Figure 13. According to this approach, each phase could be interconnected by exchange reactions. Although some hypotheses have been formulated in the literature, to the author's knowledge, no direct observation of interchange between the phases has been observed. To address this, 'consecutive' tests were performed in this chapter to experimentally confirm interchange between phases during HTL. In these tests, once separated during an initial test at low temperature, the oil, solid, and aqueous phases were individually subjected to subsequent HTL tests at high temperatures. This allowed for the direct observation of how and to what extent the production of each phase was linked to the others as the feedstock composition changed.

The findings presented in this chapter are derived from a published work[112].

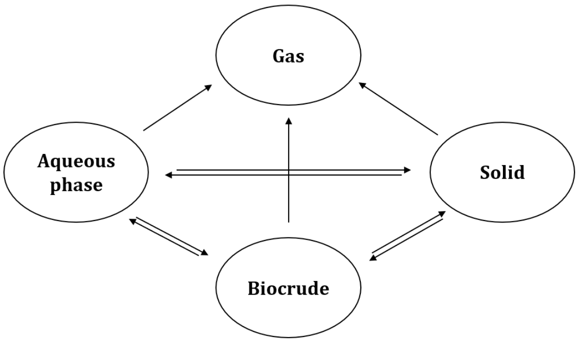

Figure 13: Possible interchange reactions between phases during HTL.

3.2 Results and discussion

3.2.1 Monomers

Glucose

In Figure 14-A the product distribution in terms of mass yields for glucose is reported at different temperatures. The gas yield showed an increasing trend with temperature, ending up being almost constant above 300 °C (10 wt.%). This trend is in accordance with tests performed by Minowa et al.[113]. As can be seen from Figure 14-B, the gas phase is mainly constituted by CO_2, with the increasing reaction temperature favoring the formation of H_2 and CO. However, despite the lower CO_2 concentration at high temperature, its partial pressure increased up to 300 °C and then remained constant; all the other compounds showed a stronger increase with temperature.

The differences in gas composition are attributed to the decomposition mechanisms occurring in the liquid and solid phase. Approaching the water critical conditions (T= 374 °C), radical-free reactions in the aqueous medium are favored over the ionic ones, enhancing the gas production through degradation of solid and liquid products[114]. In this way, the slight increase in small alkanes (C1-C3) observed at 350 °C could be explained by the presence of cracking reactions of oil and solid[38]. However, at lower temperatures, radical-free reactions are limited and the raise in CO and H_2 must be traced back to differences in the ratios of decarboxylation, dehydrogenation, and decarbonylation reactions that molecules in the other phases may undergo. In particular, the aqueous phase is usually of more interest in this regard because of molecules such as formic acid and acetic acid that are prone to H_2, CH_4 and CO formation[115].

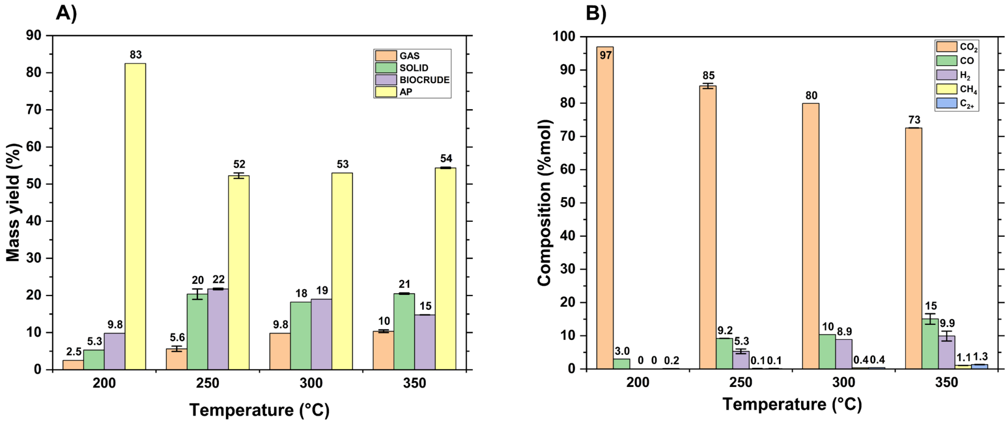

Figure 14: (A) mass yields and (B) gas compositions (vol.%) from HTL of glucose at different temperatures. With the term C2+ are identified ethane, ethylene and propane. Reaction conditions: 5 wt.% glucose, 60 min, 200 g total feed.

The compounds identified in the aqueous phase are given for every temperature in Figure 15, expressed as mass yield. At 200 °C, unconverted glucose is still detected, constituting 28% of the feedstock. A substantial amount of 5-HMF is observed, originating from glucose through an isomerization/dehydration pathway, with fructose as a reaction intermediate[113,116]. The latter was observed in preliminary tests at 150 °C, along with 92% unconverted glucose and 5-HMF (not shown). Above 200 °C, 5-HMF was barely detected in the aqueous phase, while levulinic acid (LA) was identified as the molecule with the highest mass yield. However, similar to 5-HMF, LA was also observed in the oil phase, as will be shown later on. Traces of 5-HMF and LA observed in the aqueous phase were hence attributed to an intermediate partition factor of these two molecules into to the polar solvents used[117,118]. LA is the dehydration product of 5-HMF and is produced in equimolar amounts with formic acid (FA)[119]. However, their molar ratio (FA/LA) is not constant and decreases from 3.0 to 0.03 as temperature increases from 200 °C to 350 °C. This trend could be attributed to the conversion of FA to H_2 at high temperatures, given its instability and hydrogen-donor nature.

It is worth noting that the sum of the compounds quantified via HPLC represents only 45.0 wt.% (200 °C), 7.4 wt.% (250 °C), 4.3 wt.% (300 °C), and 4.4 wt.% (350 °C) of the starting mass. The differences with respect to the mass yields for the aqueous phase reported in Figure 14 can be attributed to two reasons. First, it must be highlighted that the aqueous phase mass yields were evaluated by difference, so they can easily be overestimated. Second, only a limited fraction of the aqueous phase solubles can be identified via HPLC. This can be explained by the presence of other compounds that were not detected and/or separated (such as aromatics and heavier ketones) or compounds that were detected but could not be identified (such as positional isomers). Since a refractive index detector (RID) was used, identification was only possible by injecting specific standards.

With increasing temperature, the amount of missing aqueous phase solubles increased, which could be explained by an increase in the concentration of undetected/unseparable/unidentified molecules. This is corroborated by the fact at higher temperatures, the production of phenolic compounds increased, as discussed below.

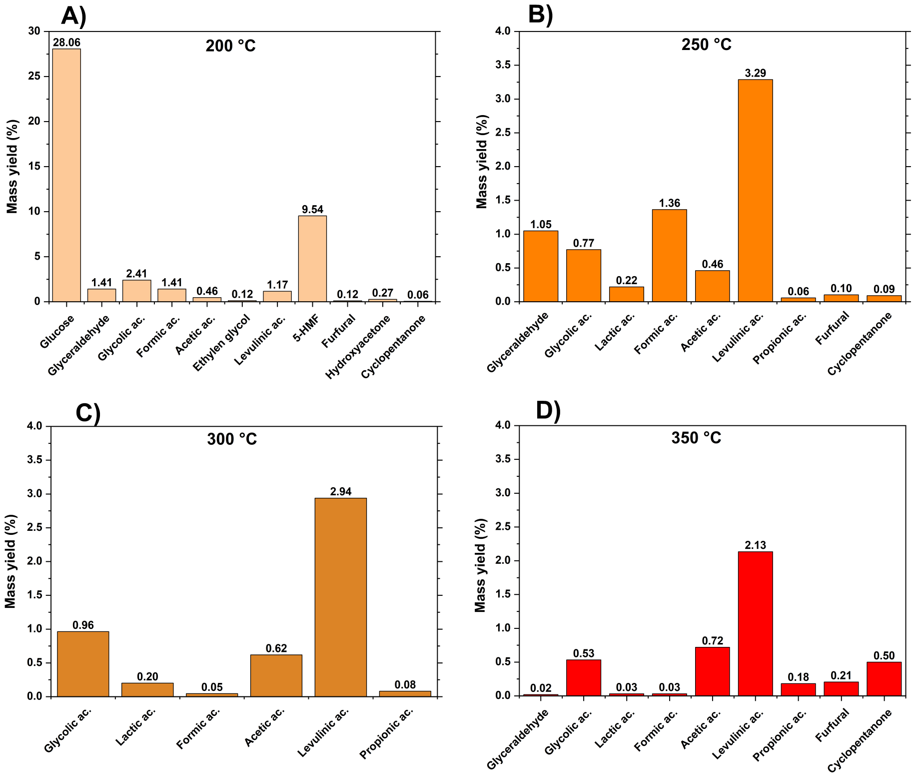

Figure 15: Mass yields of organic compounds identified in the aqueous phase from HTL of glucose at different temperatures: (A) 200 °C, (B) 250 °C, (C) 300 °C, (D) 350 °C.

Examining the solid phase (Figure 14-A), the mass yield showed an increase with the temperature rising up to 250 °C, after which it reached a plateau. The formation of the solid state is the result of the formation of intermediate compounds named humins. These are formed through condensation reactions of 5-HMF with glucose and/or a hydrated 5-HMF molecule[120]. The solid observed is hence not assimilable to a carbonaceous structure rich in carbon as char, but rather to a polymeric structure, water insoluble, still having a fair degree of oxygenation and a certain reactivity. Figure 16 reports the FTIR spectra for the solids obtained at 250 °C and 350 °C. The main peaks are attributable to carbonyl groups (1702 cm^{-1} and 1205 cm^{-1}), ether groups (1280 cm^{-1}) and aromatic structures (C=C at 1600 cm^{-1}, C=C-C at 1355 cm^{-1}, phenolic C-O at and aromatic C-O-C at)[121–125]. These spectra correspond to the furan-like and oxygenated structure observed by humins synthetized from different carbohydrates[121–124].

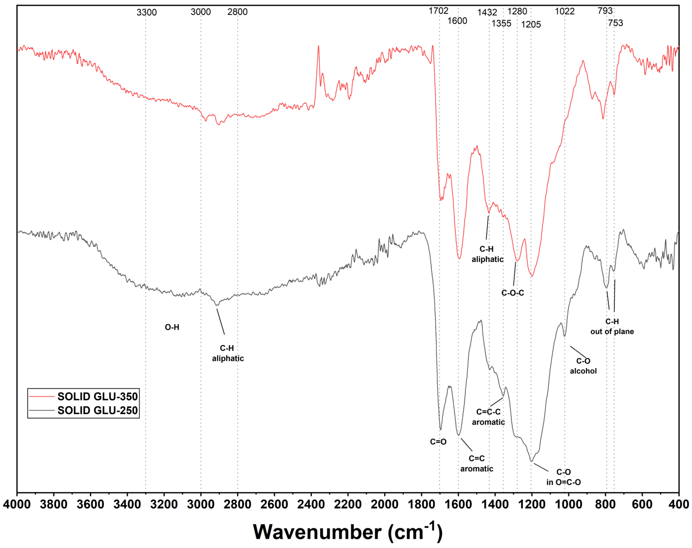

Figure 16: FTIR spectra of the solids obtained with 5wt.% glucose for 1 h at 250 °C (dark line) and 350 °C (red line).

The biocrude yield had a maximum at 250 °C, suggesting that its production from glucose was not favored at higher temperature. A maximum at 280 °C was also observed by Minowa et al.[113], which explained this behavior assuming the subsequent conversion of biocrude into gas and solid. In this study, however, biocrude yield was reduced simultaneously with an increase toward the gas phase but not toward the solid. The conversion of biocrude into other phases will be further deepen in Paragraph 3.2.4.

To better understand their nature, the biocrude extracted from the solid (B-S) and the biocrude extracted from the aqueous phase (B-AP) were separately analyzed through GC-MS (Figure 17).

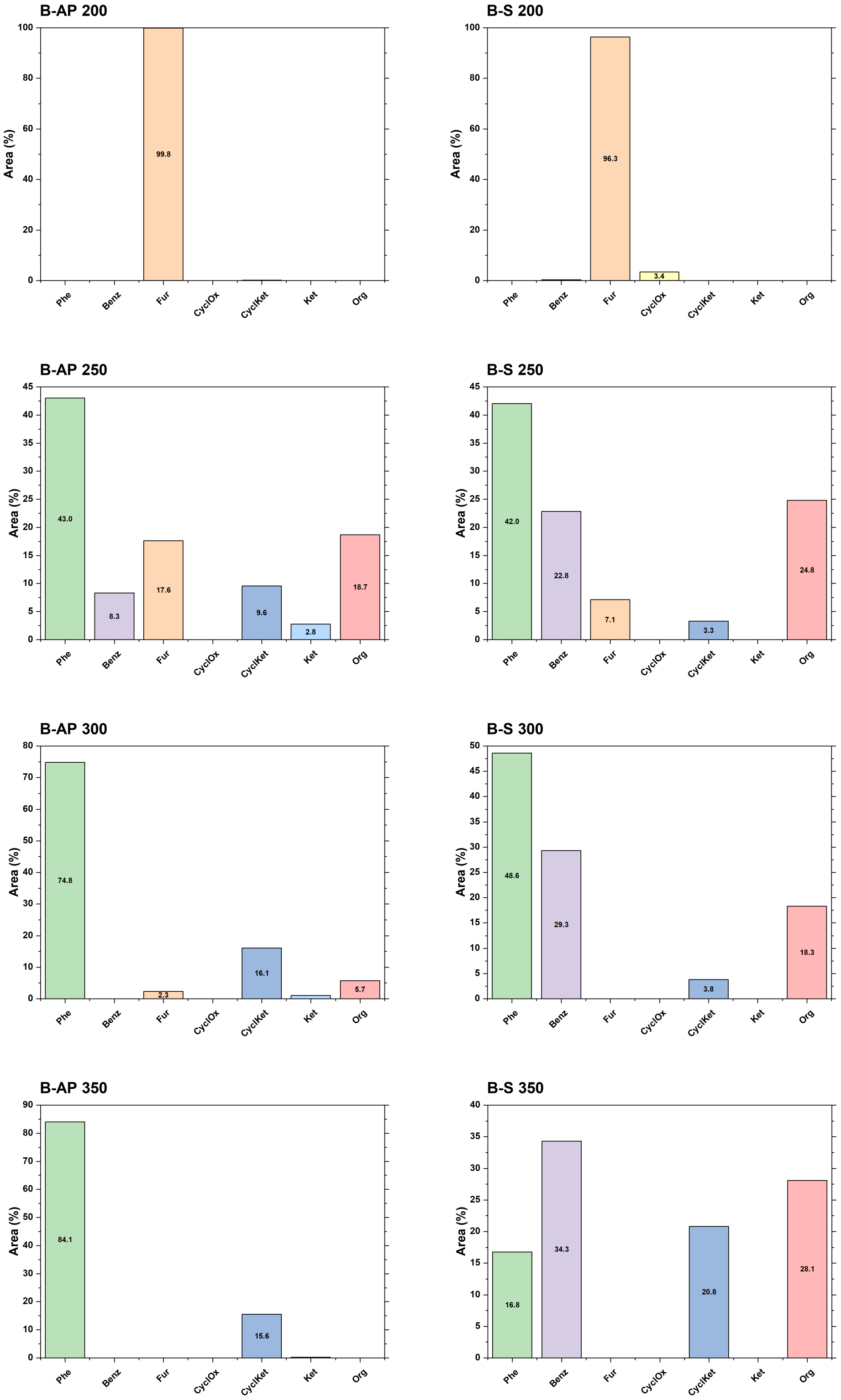

Figure 17: Family compounds identified in the B-S and B-AP obtained from glucose. Subdivision among: phenol derivatives (Phe), benzene derivatives (Benz), furanes (Fur), cyclic oxygenates (CyclOx), cyclic ketones (CyclKet), ketones (Ket), organic acids (Org).

At 200 °C B-S and B-AP were only constituted by furans derivatives (mostly in the form of 5-HMF and 2,5-furandicarboxaldehyde). Levuglucosan, a product of glucose dehydration[113], was also detected. As the temperature increases to 250 °C, the oil phases were enriched with new compounds. In particular, phenols represented the major group identified, while the portion of furanic groups decreased. The latter were no more represented by 5-HMF or similar but by benzofurans. Benzene derivatives and organic acids (levulinic acid) also appeared. At 300 °C the concentration of phenols and benzenes further increased, while furans were further reduced. Levulinic acid was detected. At 350 °C the portion of areas for benzenes and phenols additionally increased and, with respect to the other temperature, a high quantity of cyclic ketones was identified as cyclopentenones.

In general, at all temperatures the main differences recorded between the B-S and B-AP were due to a higher portion of phenolics in the latter, and a higher portion of benzenes in the former. This was attributed to a difference in polarity, and hence in water solubility, of these two classes of compounds. In addition, other families of compounds have been found in both oil products. TGA conducted over B-S and B-AP showed that the former had higher boiling point than the latter, while FTIR analysis showed fairly similar spectra for the two, with slightly higher intensity for the oxygenated bonds in B-AP.

Overall, the increase in temperature involves the increase in the oil products of aromatic compounds, cyclic ketones and the decrease of furans, mainly due to the reactivity of compounds such as 5-HMF, promoters of the solid phase. The presence of the previously listed compounds in oil produced by glucose liquefaction has been documented in the literature. These include ketones and furans[108], resulting from dehydration and isomerization of glucose, and phenols, in particular the molecule 1,2,4-benzentriol (detected in B-AP at 250 °C and 300 °C), resulting from the degradation of 5-HMF[126].

Glycine

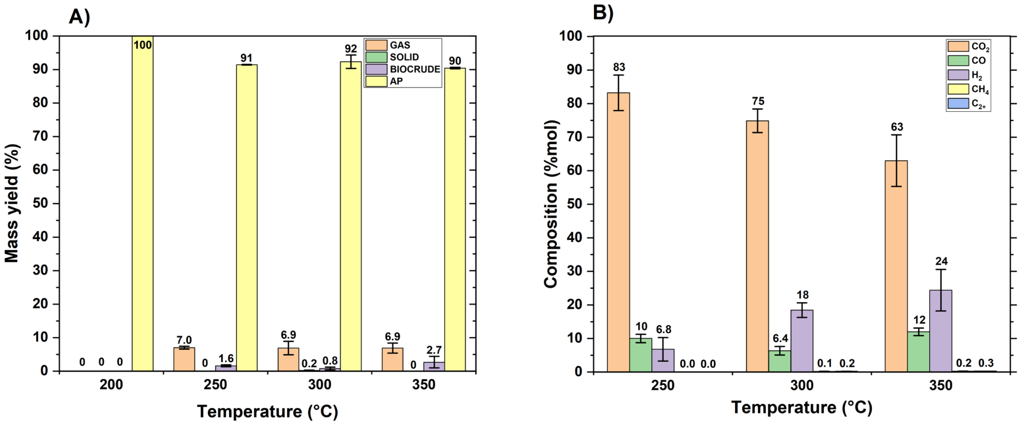

Figure 18: (A) mass yields and (B) gas compositions (vol.%) from HTL of glycine at different temperatures. With the term C2+ are identified ethane, ethylene and propane. Reaction conditions: 5 wt.% glycine, 60 min, 200 g total feed.

Figure 18-A shows the mass yields obtained with glycine alone. At 200 °C there was no production of phases other than the starting aqueous phase, which resulted predominant at every temperature. Except for the aqueous phase, at 250 °C and above, the highest mass yield was observed with the gas phase. In Figure 18-B the gas composition is reported. The gas consists mainly of CO_2 (at least 63 vol.% of the gas), in smaller amounts of CO and H_2, and in traces by CH_4 and longer alkanes. As observed with glucose alone, the CO_2 concentration decreases with temperature while the other compounds increase. However, for each gas, including CO_2, the partial pressure, and hence the amount produced, increased with temperature.

The possible reactions that occur in hydrothermal liquefaction of amino acids are mainly decarboxylation, deamination and dimerization[127,128]. The formulas for these three reactions with glycine are given in Eq. (16), Eq. (17) and Eq. (18), respectively. Decarboxylation leads to the production of CO_2 and methylamine, while deamination brings to the formation of NH_3 and acetic acid. The high CO_2 concentration was hence likely attributable to decarboxylation. However, the CO_2 yield from direct decarboxylation was limited. In fact, the CO_2 yields according to the stoichiometry reported in Eq. (16) were relatively low: from 11.0 % at 250 °C to 12.9% at 350 °C. Therefore, also because CO_2 could be produced by degradation of other molecules coming from the glycine decomposition, as probably happened for CO and H_2, only a reduced portion of the glycine took part to the decarboxylation reaction.

$$H_2N\text{-}CH_2\text{-}COOH \rightarrow H_2N\text{-}CH_2 + CO_2 \tag{16}$$

$$H_2N\text{-}CH_2\text{-}COOH \rightarrow CH_3\text{-}COOH + NH_3 \tag{17}$$

$$H_2N\text{-}CH_2\text{-}COOH \rightarrow H_2N\text{-}CH_2\text{-}COH_2\text{-}NH\text{-}CH_2 + H_2O \tag{18}$$

The solid yields were practically null while the biocrude yields were extremely low. The biocrude consisted exclusively of B-AP and Figure 19 shows its distributions among the different classes of compounds.

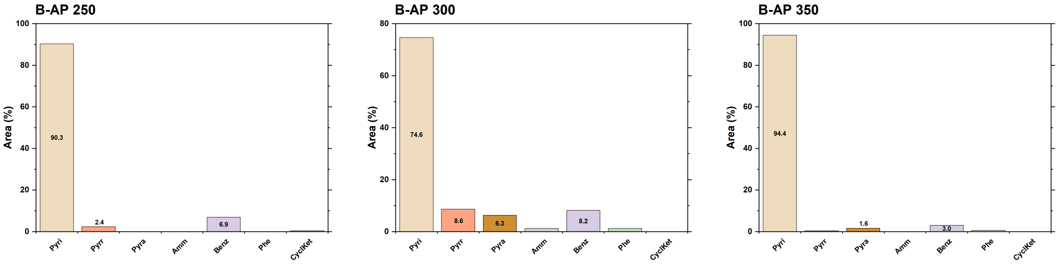

Figure 19: Family compounds identified in the B-AP with GLY. Subdivision among: pyridine derivatives (Pyri), pyrrole derivatives (Pyrr), pyrazole derivatives (Pyra), amines (Amm), benzene derivatives (Benz), phenol derivatives (Phe), cyclic ketones (CyclKet).

At every temperature the highest concentration of compounds belonged to the pyridine group. Specifically, the predominant compound identified was 5-ethyl-2-methylpyridine. Pyridines are aromatic compounds having one nitrogen within a six-atom ring, as depicted in Figure 20. Their formation has frequently observed as the result of the interaction between amino acids and decomposition products from sugars[129]. Therefore, it is probable that the formation of pyridine occurred due to its reaction with residual compounds resulting from its own degradation. In contrast, the formation of pyrazines was minimal. Pyrazines are aromatic compounds containing two nitrogen atoms, and their formation requires the interaction between two glycine molecules. This interaction occurs through dimerization and subsequent cyclization reaction with formation of diketopiperazines (DKPs)[106,129,130], which can ultimately undergo reduction to pyrazines[131]. However, the concentration of pyrazine was very low, and no DKPs were detected at any temperature. This result suggests a relative insignificance of this reactive pathway. Among other nitrogen-containing aromatics, a small amount of pyrroles was detected. Benzene and phenol derivatives were also registered, often containing amino groups attached to them.

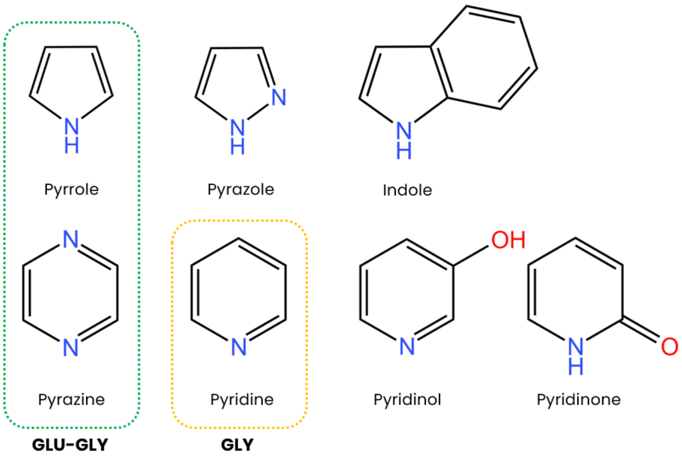

Figure 20: Nitrogen-containing aromatics identified in this chapter. The yellow and green dashed groups contain the most occurring molecules identified with glycine alone and glucose-glycine, respectively.

The low biocrude production from glycine alone seems to be inconsistent with what was stated by Biller et al.[60]. They observed a higher biocrude yield (18 wt.%) from real proteins (egg albumin and soy protein) than from carbohydrates (9 wt.% from starch). The same observation was made by Teri et al.[105]. Conversely, in this study, glycine exhibited a much lower biocrude yield than glucose when reacting alone (a 10-fold ratio difference). This difference is probably due to the very different behavior of glycine compared with real proteins. It partially derives from the fact that amino acids contained in real proteins have longer and more complex side chain that, although may not be reactive, can change the solubility of the generated molecules and hence the product distribution. Dote experimentally observed the different biocrude yields obtained from converting 19 amino acids in hydrothermal environment[132]. Glycine yielded the lowest biocrude yield (0.2 wt.%), while higher values were obtained with amino acids having big apolar side chain, namely serine (4.0 wt.%), iso-leucine (5.7 wt.%), leucine (7.7 wt.%), phenylalanine (9.6 wt.%) and tryptophan (66.4 wt.%). Moreover, protein depolymerization in hydrothermal environment is not as fast as carbohydrate depolymerization[133]. The partial depolymerization and decomposition of proteins would lead to shorter chains, which would be constituents of the biocrude phase, resulting in a different phase distribution compared with a feedstock composed of amino acids. In the same study reported above, Biller and coworkers observed that amino acids (asparagine and glutamine) yielded lower biocrude (both 9 wt.%) than proteins (both 18 wt.%)[60].

Oleic acid

Compared to glucose and glycine, oleic acid underwent minimal conversion. Reaction at 300 and 350 °C, gave a biocrude yield of 93-97 wt.%, with solid and gas phase negligible. It is hence likely that oleic acid gave only oil-soluble compounds, and the non-complete recovery of biocrude was attributed to the impossibility to reach a perfect collection efficiency after reaction.

While the mass yield was nearly complete in the oil phase, assessing its composition is crucial for understanding the conversion of oleic acid and the resulting products. Figure 21 presents GC-MS chromatograms for both the feed and the products. Apart from oleic acid, the feed contained minor amounts of elaidic acid (a trans-isomer of oleic acid) and stearic acid, along with traces of palmitic acid and fatty acid methyl esters. Shin et al.[134] observed that a temperature of 300 °C was necessary for the conversion of most fatty acids under hydrothermal conditions. In this work, following reactions above 300 °C, oleic acid remained the predominant compound, with conversion rates of 13% and 18% at 300 °C and 350 °C, respectively. Oleic acid was predominantly transformed into elaidic acid, the most prevalent product, through cis/trans isomerization. Additionally, the concentration of stearic acid, the saturated isomer of oleic acid, increased, suggesting a small hydrogenation of the feed. Similarly, Fu et al. observed a 4% yield of hydrogenation, converting oleic acid into stearic acid in subcritical water at 330 °C for 1 h[135].

As shown above (Paragraph 1.6.1), subcritical water at 300 °C has an ionic dissociation constant increased by four orders of magnitude compared to water at ambient temperature. This increased availability of hydrogen ions could explain the small hydrogenation observed above 300 °C, as well as the occurrence of cis-trans isomerization. In fact, it is well known that during hydrogenation of fatty acids, trans-isomerization is a recognized side reaction[136], attributed to partial hydrogenation[137].

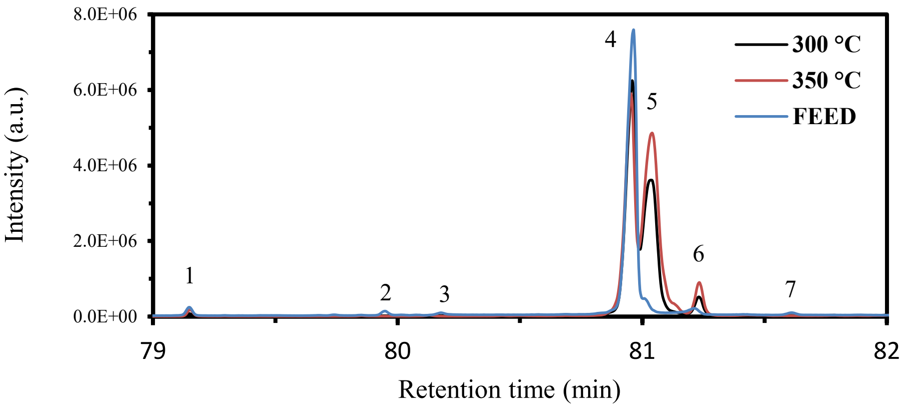

Figure 21: GC-MS chromatogram of feed and the oil phase obtained from HTL of oleic acid at 300 °C, 350 °C. (1) Palmitic acid, (2-3) FAME, (4) oleic acid, (5) elaidic acid, (6) stearic acid, (7) linoleic acid.

3.2.2 Binary mixture

Glucose-glycine

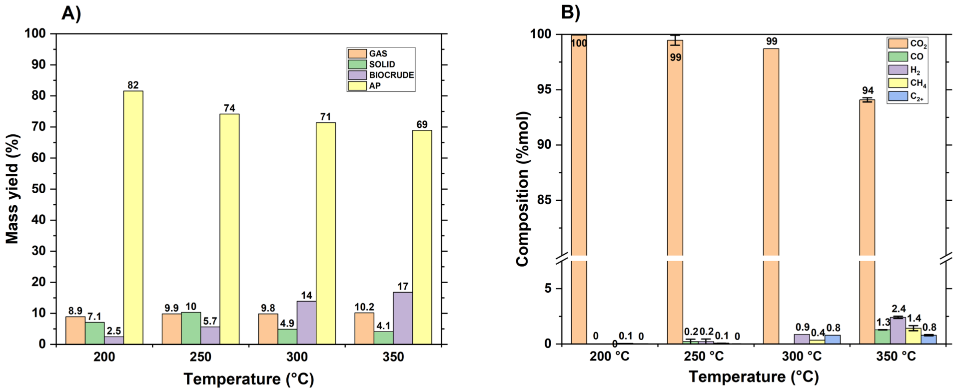

Figure 22: (A) mass yields and (B) gas compositions (vol.%) from HTL of glucose-glycine at different temperatures. With the term C2+ are identified ethane, ethylene and propane. Reaction conditions: 5 wt.% glucose-5 wt.% glycine, 60 min, 200 g total feed.

In Figure 22-A the mass yields for the glucose-glycine mixture are reported. The gas yield slightly increased passing from 200 °C to 250 °C and then resulted constant. Unlike the mono-component solutions, the gas phase is produced significantly already at low temperature and it is mostly constituted by CO_2 (Figure 22-B). Up to 300 °C, 99 vol.% of the gas is CO_2, and at 350 °C only traces of other gases were detected. Moreover, the partial pressure of CO_2 remains constant from 250 °C, confirming that all CO_2 is produced at low temperature. This can be can be attributed to the Strecker degradation[138], which leads to the decarboxylation of amino acids through the oxidizing action of some sugar-derived compounds (carbonyl compounds)[139]. The amino compounds formed from Strecker degradation are considered precursors of nitrogen-containing aromatics (pyrroles, pyrazines and pyridines, among others).

The mass yield of the solid surprisingly showed a maximum at 250 °C (Figure 22-A). At lower temperatures, the mass yield was notable, but with increasing temperature the solid seems to converted into biocrude; in fact, the biocrude yield monotonously increased with temperature. This hypothesis will be further investigated in Paragraph 3.2.4. In addition, the biocrude composition is drastically different from the one registered for glucose and glycine (Figure 23), suggesting a different behavior of the glucose-glycine mixture. At every temperature the most abundant products observed in the oil phase were nitrogen-containing aromatics. Among these, pyrazines were the most prevalent, followed by pyrroles (Figure 23). Interestingly, the former were observed both in the B-S and in the B-AP while the latter were registered almost exclusively in the B-S. This can be probably explained by a very low aqueous solubility of pyrroles, which determines their concentration in the biocrude extracted from the solid.

Pyrazines have recognized as a product of the degradation of intermediates of the Maillard reaction[140]. The Maillard reaction is an intricate set of reactions, including the Strecker degradation, initially ascribed to the interaction between amino groups (coming from ammonia, amino acids or amines) and carbonyl groups (coming from reductive sugars or their aldol-splitting derivatives)[104]. The products are called Amadori compounds, which in a second stage lead to the formation of melanoidins. These are high molecular weight compounds which are known for their characteristic brown color and for their solubility in water and insolubility in diethyl ether[141]. The glucose-amino acid system is known to be affected by this pathway[104,141,142] and the high presence of pyrazines, as well of pyrroles, confirmed this theory[143].

At low temperature, only pyrazines and pyrroles were detected, along with pyridinol (pyrazines with one oxydril group derived from the Maillard reaction[141]) and a few cyclic ketones. Upon increasing to 250 °C and 300 °C, additional compounds appeared, including indoles, amino groups, phenols and benzene derivatives. Indoles are usually identified in biocrude obtained from real protein-alone feedstock[105,144,145], but in this chapter they were not observed from glycine. Phenols and benzenes were almost always observed with amine groups attached, suggesting a different formation pathway with respect to benzenes and phenols registered for glucose alone. Finally, at 350 °C, cyclic ketones (mainly in the form of cyclopentenones), as well as indoles, pyridines and benzenes, increased further.

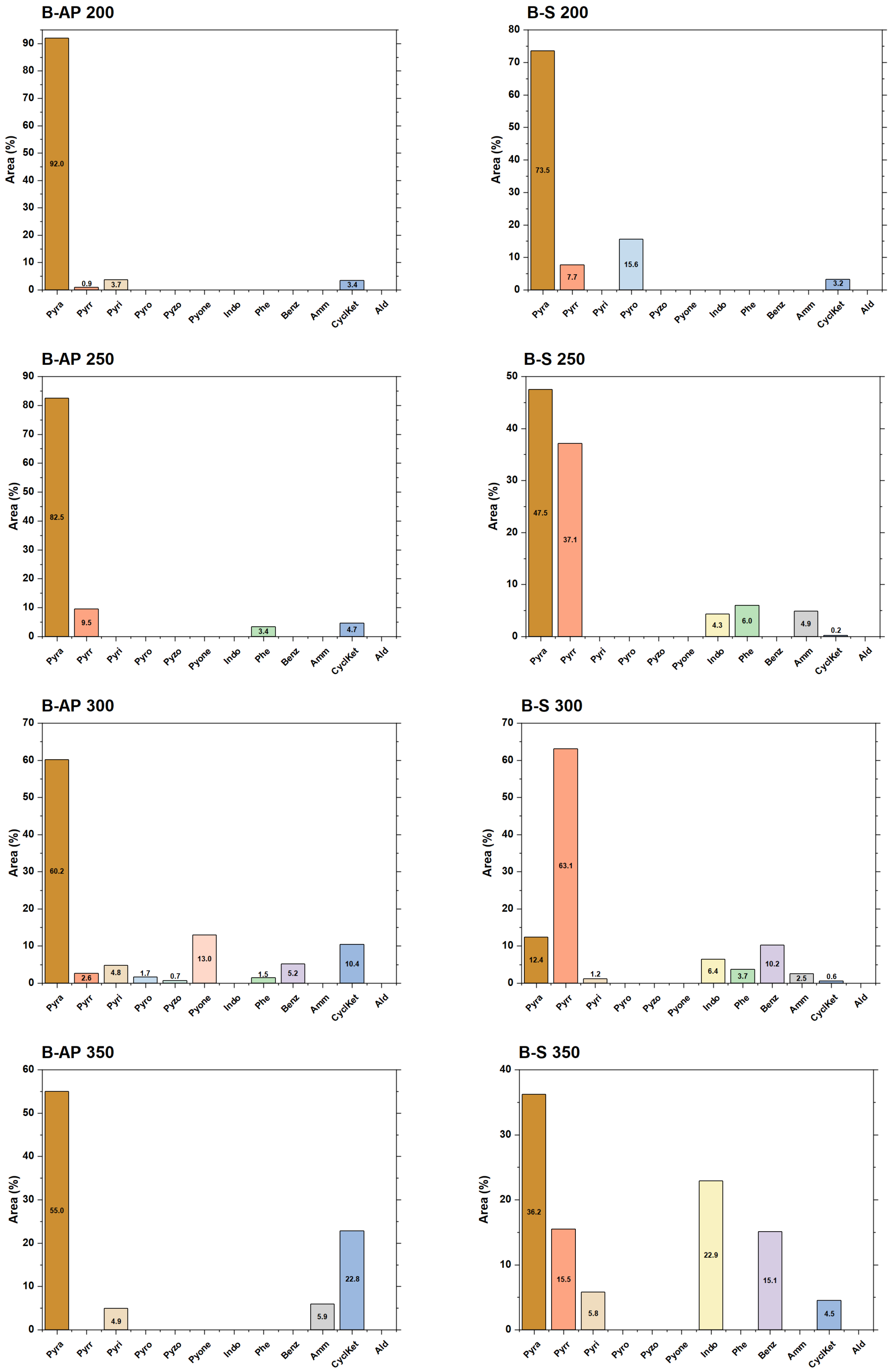

Figure 23: Family compounds identified in the B-S and B-AP obtained from glucose-glycine. Subdivision among: pyrazine derivatives (Pyra), pyrrole derivatives (Pyrr), pyridine derivatives (Pyri), pyridinol derivatives (Pyro), pyrazole derivatives (Pyzo), pyridinone derivatives (Pyone), indoles (Indo), amines (Amm), benzene derivatives (Benz), phenol derivatives (Phe), cyclic ketones (CyclKet), aldehydes (Ald).

The glucose-glycine interaction was further confirmed by the analysis of the aqueous phase composition (Figure 24). For clarity, it is reiterated that nitrogen-containing compounds are not reported. The main compounds identified were organic acids (mainly propionic and butanoic acid) as well as alcohols (methanol and ethanol) derived from acids dehydrolysis[129]. Acetic acid was observed at all temperatures in mass yields ranging from 2.4 to 3.0 % and its formation could be attributable to glycine deamination or glucose decomposition. Compounds such as levulinic acid, formic acid, and 5-HMF, which are products of glucose decomposition and were previously observed as predominant with glucose alone, showed lower carbon yields with glucose-glycine (considering the different carbon composition in the feedstock with glucose and glucose-glycine). This indicates a strong interaction of glycine with glucose degradation pathways, as previously observed by Peterson et al.[104].

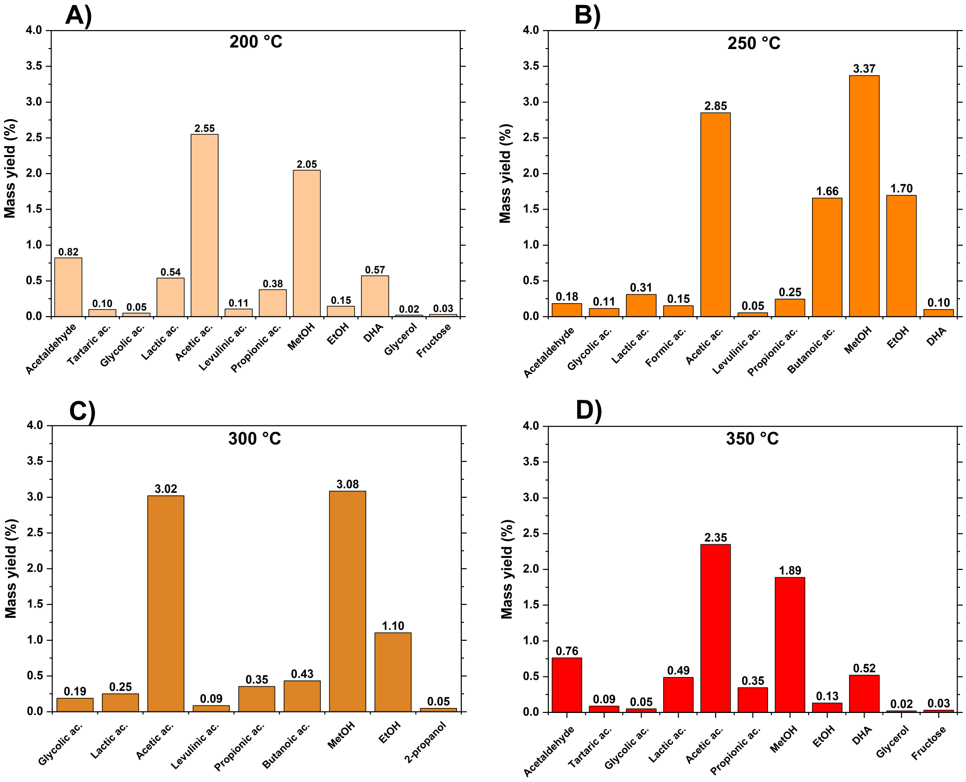

Figure 24: Mass yields of organic compounds identified in the aqueous phase obtained form glucose-glycine at different temperatures: (A) 200 °C, (B) 250 °C, (C) 300 °C, (D) 350 °C.

To better study the interaction between glucose and glycine, the absolute (Eq. (8)) and relative (Eq. (9)) differences between the experimentally obtained mass yields and those calculated as an average of the performance of the individual monomers (Eq. (7)) were evaluated. Figure 25 displays both the absolute (A) and relative (B) differences in mass yields. In both figures, a positive value represents an increase in mass yield with the co-presence of both molecules (synergy), while a negative value represents a decrease (antagonism).

At low temperature, the glucose-glycine system considerably favored gas yield compared to the monomers alone (Figure 25-B). Examining the differences between the partial pressure of glucose-glycine and the sum of those of glucose and glycine (Figure 26), it is evident that already at 200 °C the co-presence of the two led to the production of a high amount of CO_2, attributable to the Strecker degradation, as previously described. However, the synergy towards gas formation decreased with an increase in temperature. This is partially due to the increase in the gas production with the monomers alone, as well as a substantial non-variation of the gas from glucose-glycine at higher temperature (Figure 22-A). Additionally, at every temperature, glucose-glycine produced a lower amount of CO and H_2, and those differences were enlarged as temperature increased. These gases can be attributed to degradation mechanisms of unstable products at high temperatures, and the formation of these products appears to be limited for glucose-glycine.

The strong interaction between glucose and glycine is evident from the behaviors of solid and biocrude (Figure 25). The solid was favored at 200 °C, but became disfavored at higher temperatures. In contrast, biocrude formation showed an opposite trend: at 200 °C it was reduced, while at 350 °C it was increased by 93%. This suggests a strong correlation and interchange between biocrude and solid. At 200 °C, glucose and glycine are already reacting with each other, leading to the formation of a solid phase and the reduction of the already limited biocrude formation that would take place with glucose alone. The interaction between the two molecules can been traced back to the Maillard reaction[104,146] and Strecker degradation[138,139], with the latter that can be included within the former. The Maillard reaction involves the formation of melanoidins from which the biocrude is formed. However, melanoidins are water-soluble compounds which are present in the aqueous phase. They have been mainly studied in the literature after freeze-drying of the aqueous phase[138,141,147]. Fang et al.[138] saw that the solid fraction generated from glucose and glycine has similar ^{13}C and ^{15}N NMR spectra to those of the melanoidin fraction, suggesting a possible similar nature between solid and melanoidins. For this reason, the increase in temperature could have led to the degradation of the solid with a consequent increase of the biocrude formation. On the other hand, with glucose, the solid formation is ascribed to the humins formation, which showed more stability and did not seem to be precursors of the biocrude formation. These hypotheses were tested through consecutive tests presented in the next Paragraph 3.2.4.

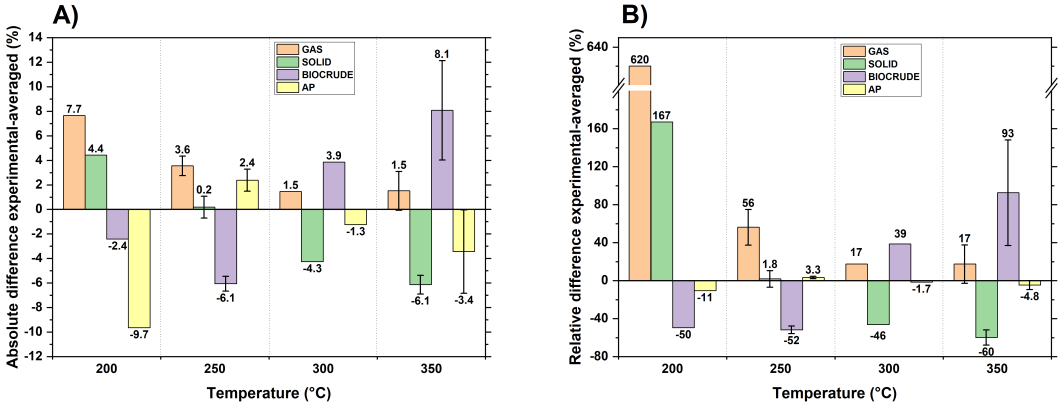

Figure 25: Absolute (A) and relative (B) differences between experimental mass yields obtained from glucose-glycine and mass-averaged yields from glucose and glycine.

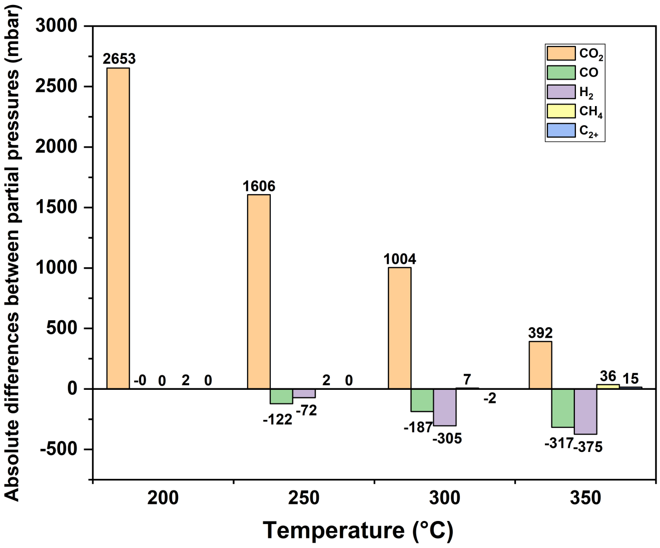

Figure 26: Differences between partial pressures of glucose-glycine and the linear combination of glucose alone and glycine alone. Data are reported in mbar at 25 °C.

Glucose-oleic acid

In Figure 27-A, the mass yields for the glucose-oleic acid mixture are reported. As expected, biocrude was the most produced phase due to the presence of oleic acid, but the other phases were also present. In descending order of magnitude, they were the aqueous phase, solid phase, and gas phase, mirroring the order obtained with glucose alone. Furthermore, the gas composition (Figure 27-B) closely resembled that of glucose reacting alone (Figure 14-B).

To better highlight potential interactions between glucose and oleic acid, Figure 27-C depicts the relative differences between the experimental yields obtained from the co-reaction of glucose and oleic acid and the linear combinations of the yields from the individual reactions, as calculated by Eq. (9). The plot indicates that, if present, interactions were weak, and more importantly, they appeared to slightly favor biocrude production. A similar observation was made at 300 °C with glucose and linoleic acid by Déniel et al.[61], who attributed this behavior to a reducing effect of glucose derivatives on the fatty acid, justified by the observation of an increase in unsaturated long-chain compounds.

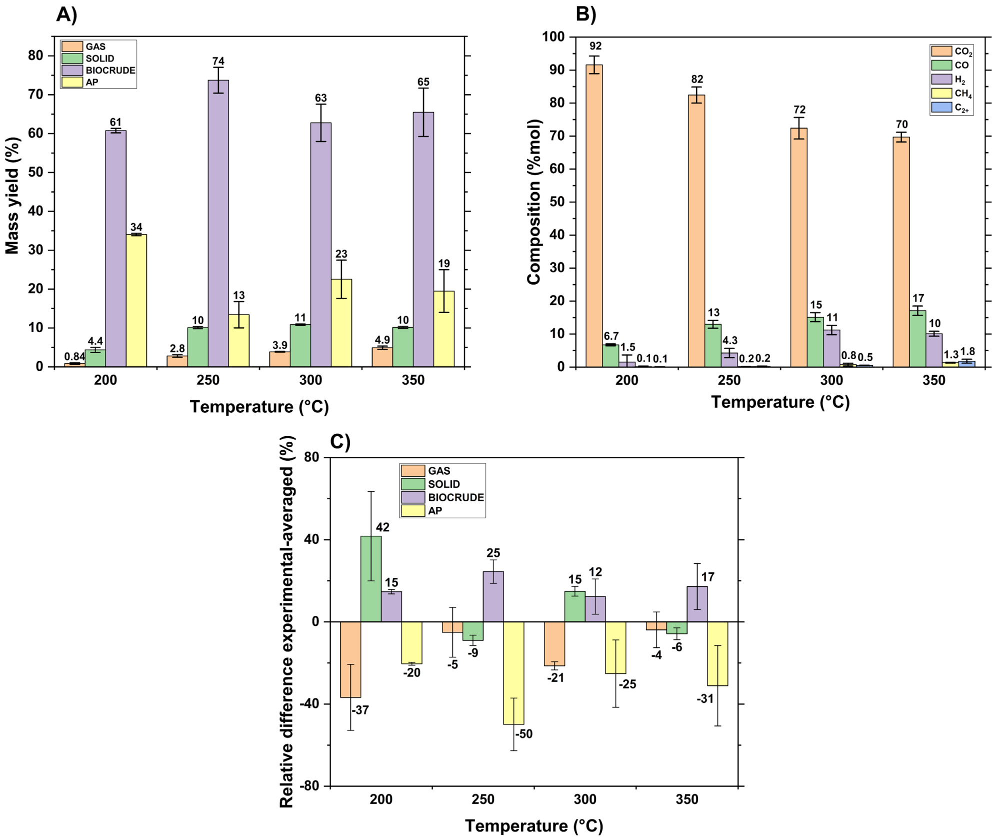

Figure 27: (A) mass yields with glucose-oleic acid at different temperatures. (B) Gas compositions (vol.%) with GLU-OLE at different temperatures. (C) relative differences between experimental mass yields obtained from glucose-oleic acid and mass-averaged yields from glucose and oleic acid. With the term C2+ are identified ethane, ethylene and propane. Reaction conditions: 5 wt.% glucose-5 wt.% oleic acid, 60 min, 200 g total feed.

In Figure 28, the GC-MS chromatogram of the biocrude is presented, revealing an increasing amount of elaidic and stearic acid with a rise in reaction temperature. The yields of these products were higher than those obtained using oleic acid as only reactant, particularly above 300 °C. Hence cis-trans isomerization and hydrogenation are favored in the co-presence of glucose and oleic acid. A possible explanation for this phenomenon could be the increased acidity of the aqueous environment resulting from the presence of glucose. The pH for the glucose-oleic acid experiment was in the range of 2.3-3.0, resembling quite well the values obtained from the experiments with glucose alone. It is hence likely that an increased availability of hydrogen ions favors the hydrogenation reaction leading to both an increase in saturated and isomerized products. However, even in the minor peaks, long-chain hydrocarbons were not identified, in contrast to the findings of Déniel et al.[61]. Instead, different acids (levulinic acid, glycolic acid, acetic acid) and phenols were detected, consistent with the portion of biocrude derived from the decomposition of glucose.

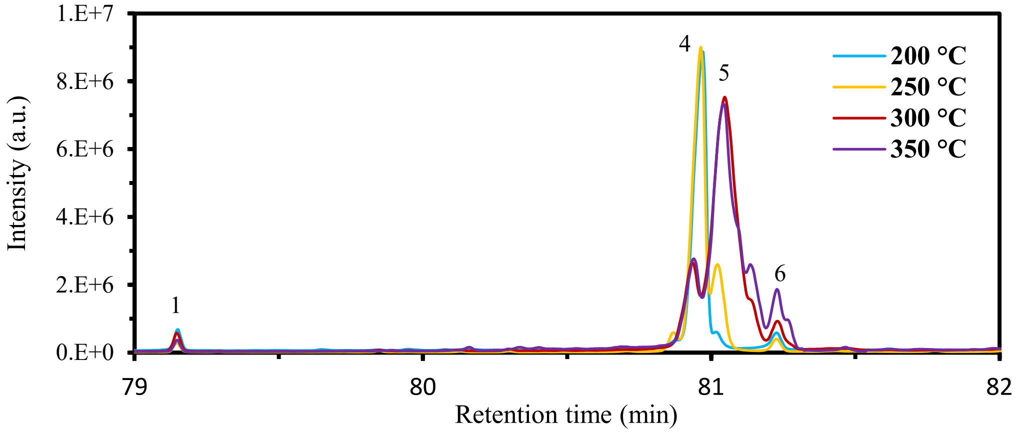

Figure 28: GC-MS chromatograms of the oil phase obtained from HTL of glucose-oleic acid at different temperatures. (1) Palmitic acid, (4) oleic acid, (5) elaidic acid, (6) stearic acid.

Glycine-oleic acid

In Figure 29-A, the mass yields for the glycine-oleic acid mixture are reported. Biocrude and aqueous phase largely represented the two most prominent phases, attributed to the tendency of oleic acid to favor the former and glycine to favor the latter. The solid phase was almost zero, while the gas phase was limited. The gas composition (Figure 29-B) was characterized by a consistent amount of CO_2, along with CO and H_2. It closely resembled the gas composition obtained with glycine alone (Figure 18-B), with the only exception of a decreased hydrogen production at 350 °C with glycine-oleic acid.

In Figure 29-C the relative differences between the mass yields obtained by glycine and oleic acid reacting together and the linear combination of the mass yields obtained by them reacting alone (Eq. (9)) are shown. No significant differences arose between the phases, suggesting that the co-presence of glycine and oleic acid did not affect the obtained mass yields. The most notable exception to this was represented by the solid phase at 300 °C. However, when glycine and oleic acid reacted together, the solid yield was always extremely limited, so this high relative difference was highly influenced by the very low denominator, which magnified small differences.

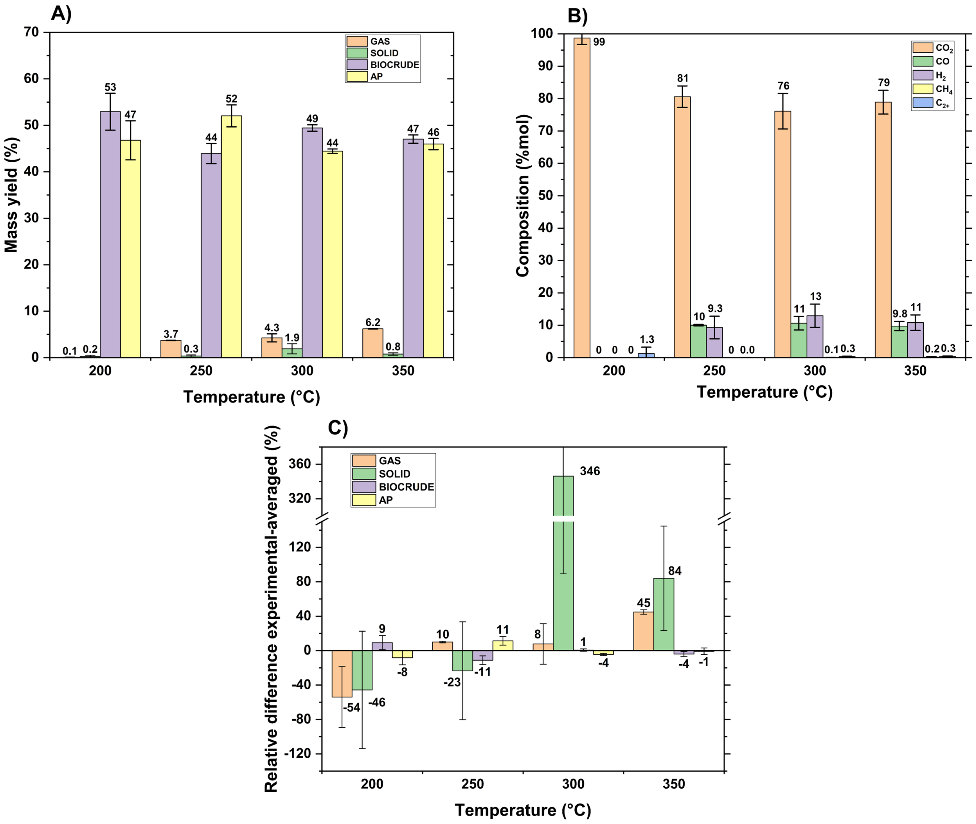

Figure 29: (A) mass yields with glucose-oleic acid at different temperatures. (B) Gas compositions (vol.%) with glycine-oleic acid at different temperatures. (C) relative differences between experimental mass yields obtained from glycine-oleic acid and mass-averaged yields from glycine and oleic acid. With the term C2+ are identified ethane, ethylene and propane. Reaction conditions: 5 wt.% glycine-5 wt.% oleic acid, 60 min, 200 g feed.

In Figure 30, the chromatogram of the biocrude obtained at 300 °C from glycine and oleic acid is presented. Notably, a consistent peak arose, attributable to N-methyl-oleamide. Amides were observed to form in hydrothermal environment between fatty acids and proteins, likely arising from the condensation of fatty acids with amino acid degradation products[148]. Specifically, N-methyl-oleamide likely derived from the interaction of oleic acid with methylamine, a result of glycine decarboxylation. Conversely, the production of oleamide, formed through oleic acid and ammonia interaction, was minimal, despite ammonia's consistent concentration in the aqueous phase post-reaction (30% yield from glycine). This suggests that the condensation reactivity of oleic acid with methylamine was significantly higher than that with ammonia. Additionally, traces of oleonitrile were detected, suggesting a possible conversion of amides into nitriles, as noted by Simoneit et al.[149]. Lastly, a notable finding is the disfavored conversion of oleic acid into its trans isomer (elaidic acid) compared to oleic acid reacting alone, indicating a preference for the formation of alkylated amide/amide formation.

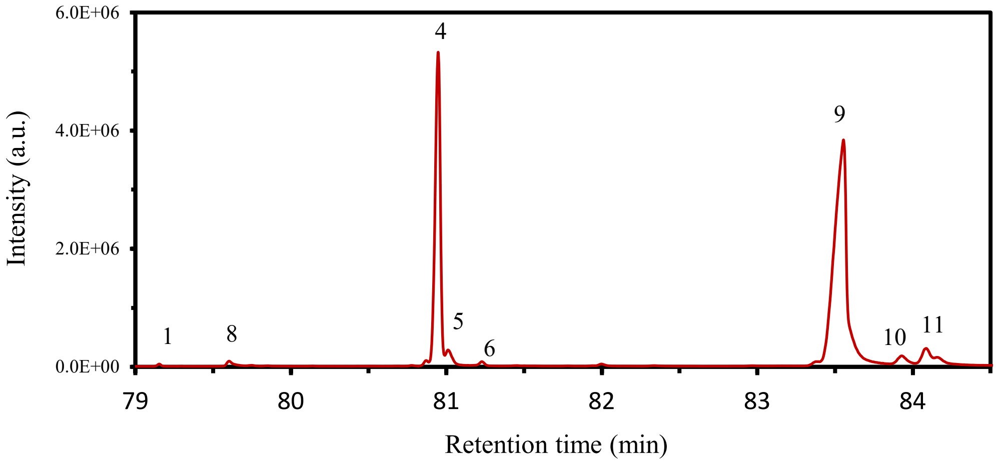

Figure 30: GC-MS chromatogram of the oil phase obtained after HTL of glycine-oleic acid at 300 °C. (1) Palmitic acid, (4) oleic acid, (5) elaidic acid, (6) stearic acid, (8) oleonitrile, (9) N-methyl-oleamide, (10) N-methyl-arachidamide, (11) N,N-dimethyl-oleamide.

With oleic acid being converted into N-methyl-amide, a heightened concentration of nitrogen was observed in the biocrude. The elemental composition of the biocrude obtained at 300 °C was 70.7 ± 1.1 wt.% carbon, 10.3 ± 0.1 wt.% hydrogen, 13.3 ± 1.1 wt.% oxygen and 6.3 ± 0.5 wt.% nitrogen. Interestingly, the theoretical nitrogen content for N-methyl-oleamide is 4.7 wt.%, hence the biocrude had an higher nitrogen content than the pure fatty amide. This could be due to the small contribution to biocrude from glycine-derived compounds that have a high concentration.

The presence of nitrogen atoms in the biocrude poses a well-known issue, as they are converted into NO_x during combustion. Consequently, the nitrogen concentration in the biocrude must be reduced through upgrading processes, typically hydrogenation[150]. However, unlike oxygen, nitrogen atoms are not easily removed[150]. Therefore, it would be advantageous to limit the nitrogen content in the biocrude during its formation. Consequently, the co-presence of glycine and oleic acid exacerbates this issue, as despite the biocrude yield remaining unaffected, its nitrogen content is significantly increased.

3.2.3 Ternary mixture

In Figure 31-A, the mass yields for the glucose-glycine-oleic acid mixture are reported. As observed with glucose-oleic and glycine-oleic acid, biocrude and aqueous phase largely represented the two most prominent phases. The solid phase decreased with increasing temperature, moving from a mass yield of 6.7 wt.% to 2.2 wt.%. The gas phase, on the other hand, slightly increased from 200 °C to 250 °C and then remained constant at higher temperatures, similar to what was observed with glucose-glycine. Moreover, the gas composition of the ternary solution (Figure 31-B) closely resembled the gas composition obtained with glucose-glycine (Figure 22-B), as it was composed only by CO_2.

In Figure 31-C, the relative differences between the mass yields obtained by glucose, glycine, and oleic acid reacting together and the linear combination of the mass yields obtained by them reacting alone (Eq. (9)) are shown. Interestingly, the phases' trends were similar to those observed with glucose-glycine (Figure 25-B). Specifically, the gas phase was strongly favored at 200 °C and then decreased at higher temperatures; the solid phase was strongly favored at 200 °C and then became disfavored at higher temperatures; biocrude became favored only at higher temperatures. In the case of biocrude, relative differences compared to the glucose-glycine reactions were less pronounced due to the high amount of oleic acid, which diminished the denominator. Nonetheless, all these observations suggest that in the case of ternary reactions (glucose-glycine-oleic acid), the strongest interaction taking place was the one involving glucose and glycine.

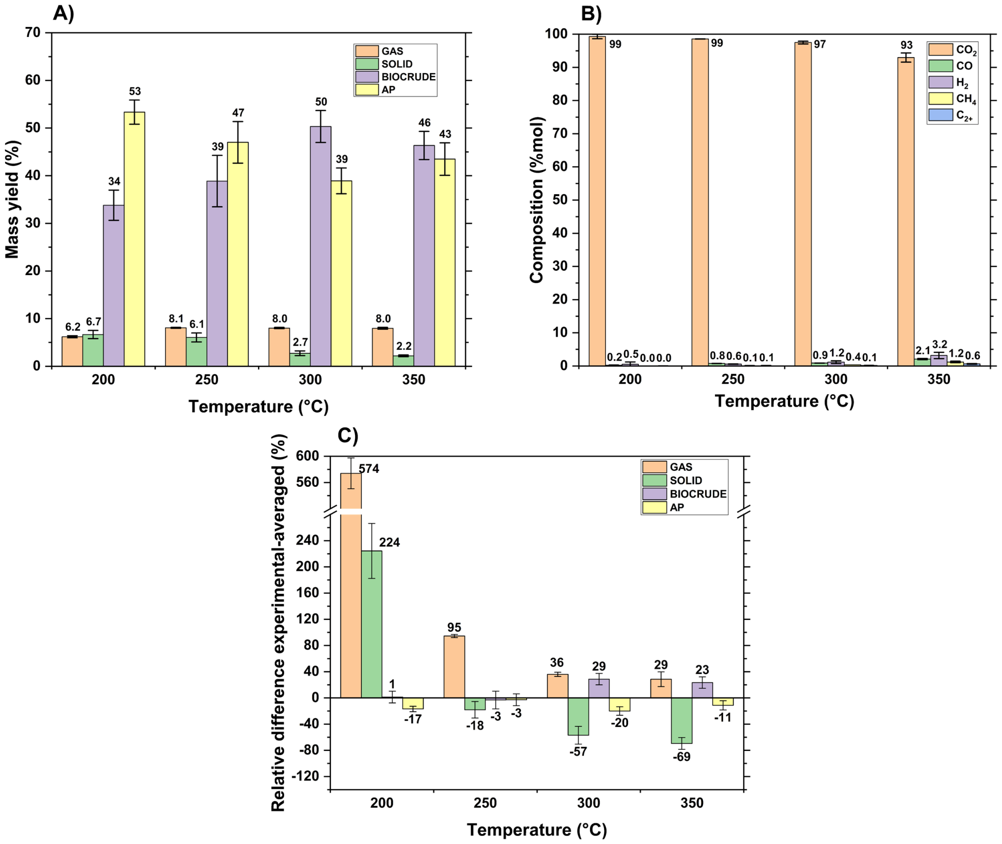

Figure 31: (A) mass yields with glucose-glycine-oleic acid at different temperatures. (B) Gas compositions (vol.%) with glucose-glycine-oleic acid at different temperatures. With the term C2+ are identified ethane, ethylene and propane. Reaction conditions: 5 wt.% glucose-5 wt.% glycine-5 wt.% oleic acid, 60 min, 200 g feed. (C) Relative differences between experimental mass yields obtained from glucose-glycine-oleic acid and mass-averaged yields from glucose, glycine and oleic acid.

In Figure 32, the chromatogram of the biocrude obtained at 300 °C from glucose, glycine and oleic acid is presented. It is worth noting that, although the observations of the variations in mass yields suggested the predominant presence of interactions between glucose and glycine, the products of their interactions had very low intensity in the chromatogram shown in Figure 32. This was attributed to the dilution effect caused by oleic acid, which rendered all other peaks less intense.

Besides oleic acid, a consistent amount of N-methyl-oleamide was also registered, along with smaller quantities of elaidic and stearic acid. The presence of fatty amides indicates the interaction between glycine intermediates and oleic acid, as observed with glycine-oleic acid. However, the N-methyl-oleamide content was lower than that registered with glycine-oleic acid (Figure 30). This could be explained by a lower amount of nitrogen containing molecules available due to the glucose-glycine interaction.

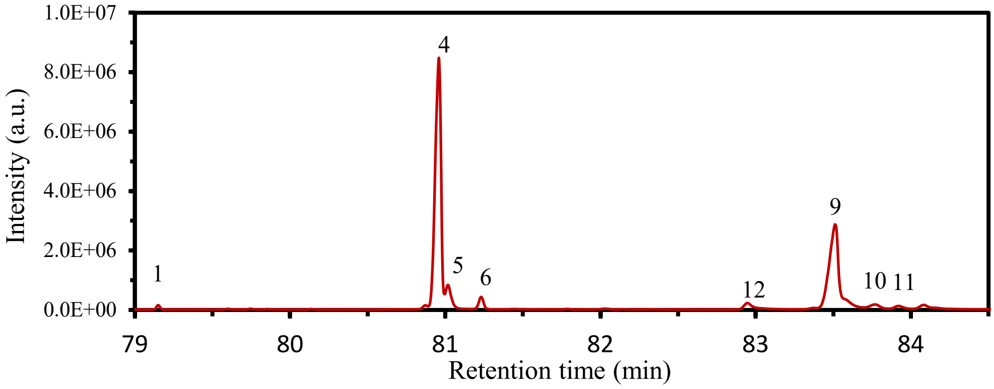

Figure 32: GC-MS chromatogram of the oil phase obtained after HTL of glucose-glycine-oleic acid at 300 °C. (1) Palmitic acid, (4) oleic acid, (5) elaidic acid, (6) stearic acid, (9) N-methyl-oleamide, (10) N-methyl-arachidamide, (11) N,N-dimethyl-oleamide, (12) N-methyl-oleamide.

In Figure 33, the organics detected in the aqueous phase via HPLC are detected. The compounds were the same observed with glucose-glycine and also the trends with temperature were the same. However, the yields were lower compared to the binary system. This can be partially explained by the fact that these molecules are generated from glucose and glycine but not oleic acid. Hence, as in the ternary feedstock, oleic acid is added to the binary system glucose-glycine, the resulting mass of aqueous-solubles is diluted by a 0.66 factor.

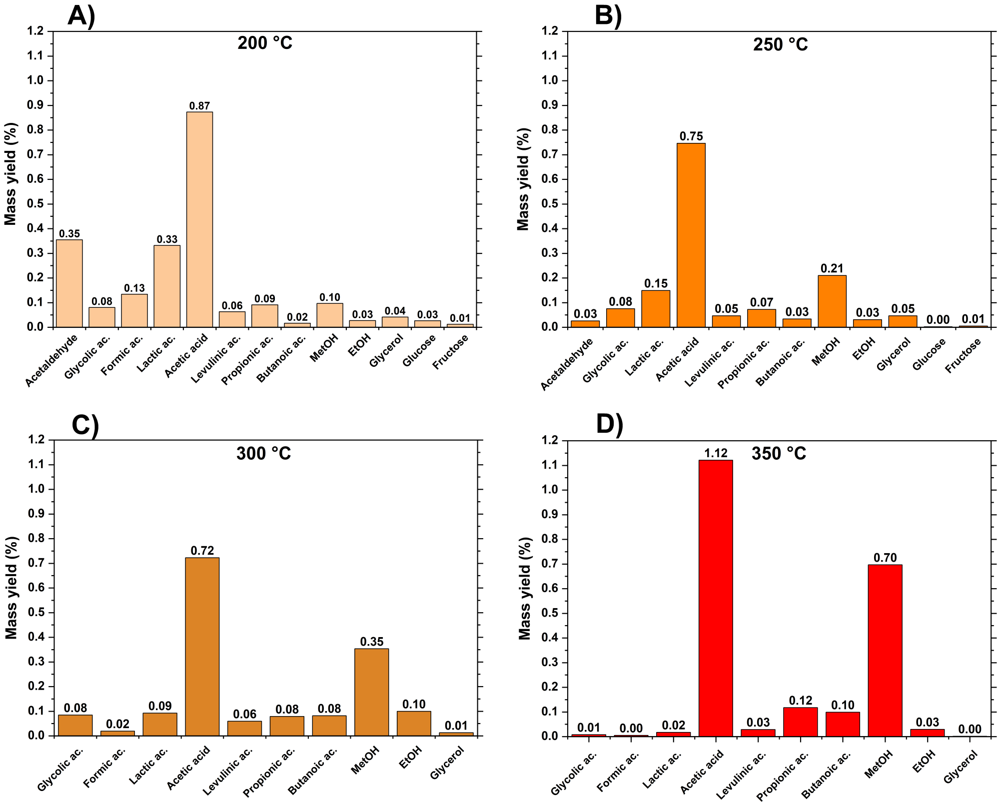

Figure 33: Mass yields of organic compounds identified in the aqueous phase obtained form glucose-glycine-oleic acid at different temperatures: (A) 200 °C, (B) 250 °C, (C) 300 °C, (D) 350 °C.

3.2.4 Consecutive reactions-evolution of the phases

As presented in the previous chapters, the interaction between glucose and glycine was predominant. To further investigate the relationships between the phases occurring in the co-presence of glucose and glycine, a campaign of consecutive tests was carried out. Except for the gas phase, the products generated from glucose and glucose-glycine obtained at 250 °C were separated and then used as reactants for a second reaction at 350 °C for 1 h, as depicted in Figure 34. Reactions with solid and biocrudes (B-AP and B-S separately) were prepared by adding distilled water to obtain a total 200 g solution. On the other hand, reactions with AP were prepared by leaving the AP overnight under a chemical hood to ensure the removal of the residual diethyl ether and then used as such as feedstock without any dilution.

The temperature of 250 °C was chosen for the first step because it led to the maximum yield in biocrude for glucose and the maximum yield in solid for glucose-glycine (Figure 22-A); analysis of the products generated by these phases could highlight how their formation is correlated. Consecutive reactions for glycine alone were not performed due it production of only the aqueous phase. In Figure 35 and Figure 36, the phase distribution for the consecutive test campaign is reported for glucose and glucose-glycine, respectively.

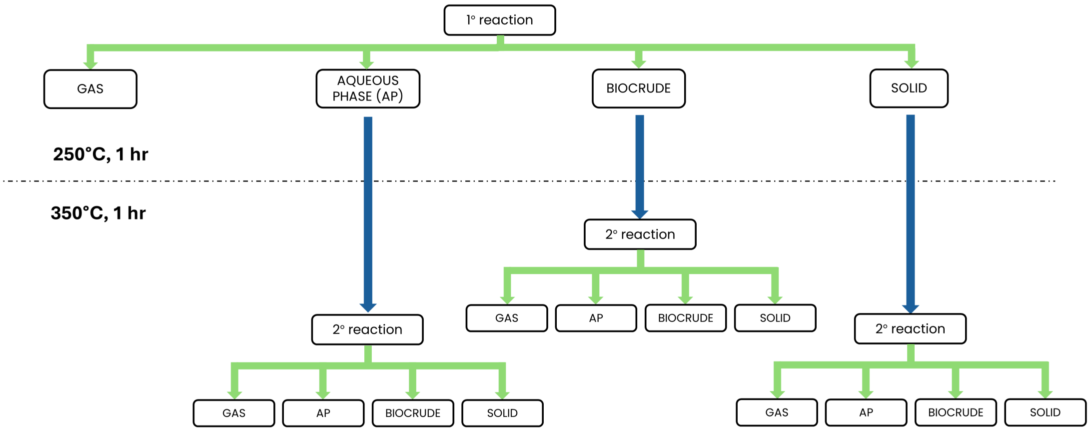

Figure 34: Consecutive reactions design.

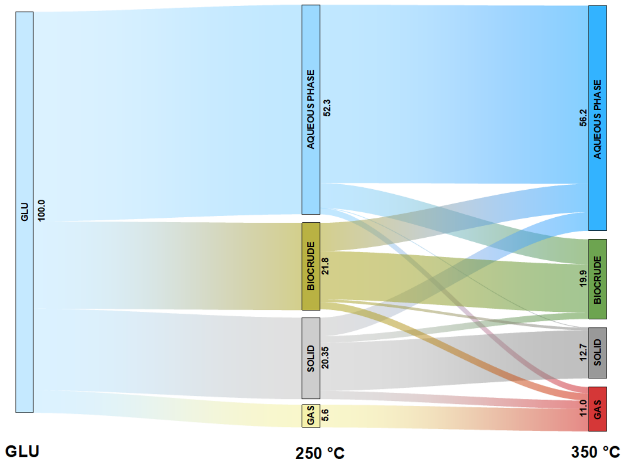

Figure 35: Sankey diagram with product distributions at 250 °C with glucose and for consecutive reactions of single phases reacting alone at 350 °C. All consecutive reactions were performed in duplicates.

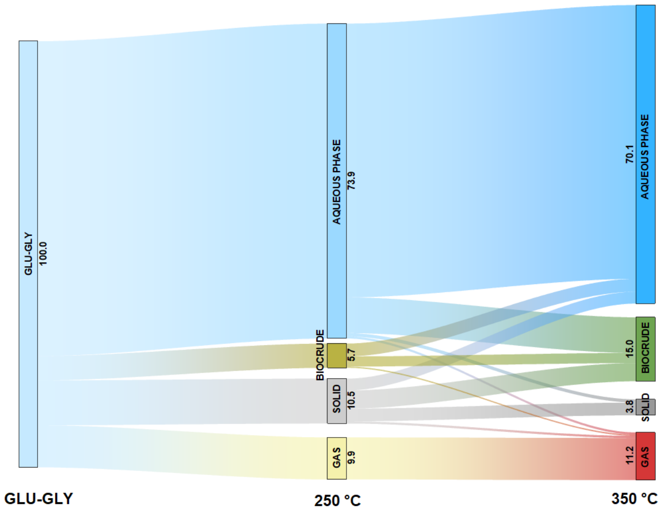

Figure 36: Sankey diagram with product distributions at 250 °C with glucose-glycine and for consecutive reactions of single phases reacting alone at 350 °C. All consecutive reactions were performed in duplicates.

Looking at the gas phase, although the mass yield is similar between glucose and glucose-glycine at 350 °C, it is easy to see that it derives from two different pathways (Figure 37 and Figure 38). With glucose at 350 °C, the gas clearly increased due to contributions from all phases, while with glucose-glycine, it remained similar to the yield at 250 °C. With glucose, the increase in gas was not attributable only to the organics in the aqueous phase, as would be excepted, but also to large contributions from solid and biocrude. These phases produced different gas compositions. Figure 37 shows the composition of the gas (averaged) at 350 °C, highlighting the contribution of each phase. The solid mainly produced CO_2, suggesting its decomposition through decarboxylation reactions; the aqueous phase contributed largely on the H_2 production, probably due to formic acid decomposition, as well as CO_2; the biocrude led to the formation of CO_2 and to a consistent amount of H_2 and CH_4. The formation of the latter two, therefore, occurs according to more complex mechanisms than just decarboxylation. In addition, the gas distribution appears to be slightly different from the products generated at 350 °C for 1 h, due to a decrease in CO in favor of H_2.

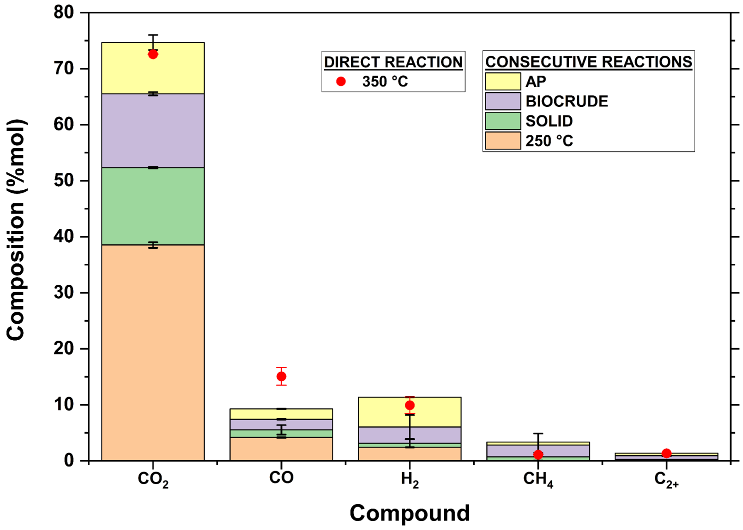

Figure 37: Gas composition for the consecutive reaction with glucose (5 wt.% glucose). Red dots show the gas composition obtained at 350 °C for 1 h. The cumulative composition obtained with the consecutive reactions is shown with bars. The contributions of each reaction step are highlighted.

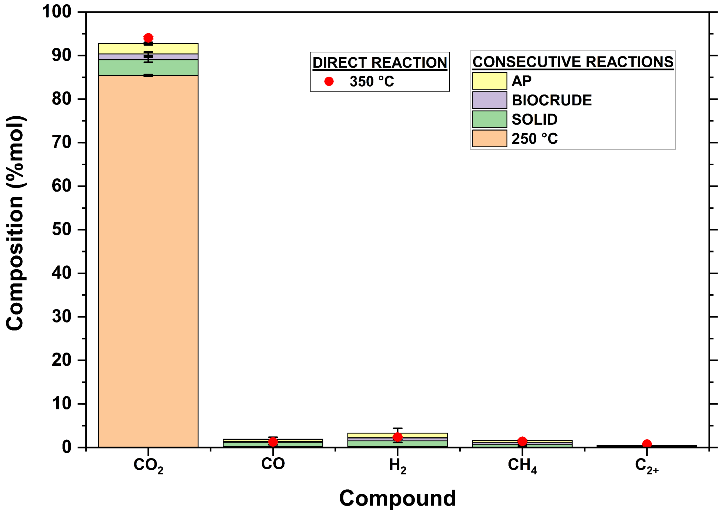

Figure 38: Gas composition for the consecutive reaction with glucose-glycine (5wt.% glucose-5wt.%glycine). Red dots show the gas composition obtained at 350 °C for 1 h. The cumulative composition obtained with the consecutive reactions is shown with bars. The contributions of each reaction step are highlighted.

The most significant differences between glucose and glucose-glycine were observed in the trends of formation of solid and biocrude phases. With glucose, the solid decreased from 250 °C to 350 °C, but most of the solid remained as such. A smaller portion was converted into water-soluble compounds and gas, while a negligible fraction was turned into biocrude, whose yield remained constant overall. The apparent stability of the biocrude resulted from the positive contribution (conversion of some aqueous-soluble compounds in biocrude) and negative contributions (conversion of biocrude into aqueous-soluble compounds, gas and solid). This interchange could also partially due to interchange between the phases of some molecules having intermediate polarity, such as levulinic acid.

Upon examining the composition of the biocrude formed at 350 °C from the biocrude generated at 250 °C with glucose, a higher concentration of benzene-derived compounds was observed. These were primarily in the form of benzofuranones, indanones, and indenones and a lower concentration of benzofurans, indicating their conversion into the aforementioned compounds. The water-soluble compounds contained in the aqueous phase produced a biocrude phase rich in benzenes (ca. 35%) and phenols (ca. 25%). Overall, the biocrudes obtained from the consecutive tests (from biocrude and aqueous phase) were found to be very similar to those obtained with glucose at 350 °C for 1 h (Figure 17). This corroborates that for glucose, biocrude formation also occurs from compounds present in the aqueous phase. Moreover, the solid production from biocrude was almost null, while the production of compounds released in the aqueous phase and gas was consistent. This suggests that biocrude does not undergo recombination reactions that promote char formation, but rather degradation mechanisms that lead to the formation of gas and aqueous phase products.

Examining the glucose-glycine system (Figure 36), it is evident that the mechanisms involved were distinct. Notably, it was observed a dramatic decrease in solid from 250°C to 350°C, as also seen in Figure 22. Confirming the hypothesis stated above, it is evident from Figure 36 that the majority of the solid phase (41 wt.% of the solid generated in the first step) was converted into biocrude. Analyzing the biocrude obtained from the solid, the identified compounds were mostly pyrazines-derivatives and indole-derivatives. The presence of the former confirms a composition similar to the biocrude obtained at 250 °C for 1 and 350° for 1 h. On the other hand, the latter were found in higher concentration compared to the biocrude obtained directly with glucose-glycine at 350 °C. Therefore, it is possible that the appearance of indoles at high temperature is due to the degradation of the solid. In general, these observations justify the assumption that the solid is an intermediate for biocrude production with glucose-glycine, contrary to the idea that the solid constitutes an end product of the HTL reaction[45,151]. The intermediate behavior herein observed can be attributed to the thermal instability of the solid phase, having a melanoidins-like structure with high molecular weight. To exclude a kinetic limitation for the conversion of the solid into biocrude, a longer test at 250 °C and 6 h was also performed. Compared with 250 °C for 1 h, the mass yield resulted higher for the solid (12 wt.%), for the biocrude (8.5 wt.%) but lower for the aqueous phase (70 wt.%). Solid decomposition was hence driven by the higher reaction temperature rather than the longer residence time used in the consecutive reactions.

The aqueous phase gave the highest contribution to the biocrude formation (8.4 wt.% of the starting feed). This is in agreement with the idea that melanoidins are formed in the presence of glucose and glycine and that these are intermediate in the formation of biocrude. As seen with glucose, also with glucose-glycine a fraction of the biocrude was converted to aqueous phase-soluble. As for glucose, it is worth noting that it could derive from exchange of some intermediate-polarity compounds. In the end, solid seemed not to be formed from biocrude, as assumed also from Minowa et al.[102], despite a carbonization process would be expected for long reaction time.

3.2.5 Consecutive reactions-interaction between the phases

The consecutive reactions were designed to understand the relationship between the phases produced at 250 °C (1 h) with glucose and glucose-glycine and those produced at 350 °C (1 h). In Figure 39, the mass yields obtained at 250 °C, 350 °C, and after the consecutive reactions (labelled as ‘isolated’) are reported (please note that the figure also contains data reported in the above paragraphs to facilitate the comparison). Regarding glucose (Figure 39-GLU), it is interesting to note that the yields obtained from the consecutive reactions (yellow bars) did not correspond with the yields obtained at 350 °C (cyan bars). In particular, the difference was significant for solid and biocrude. On the other hand, with glucose-glycine (Figure 39-GLU-GLY), the mass yields from the consecutive reactions were very similar to those at 350 °C for 1 h.

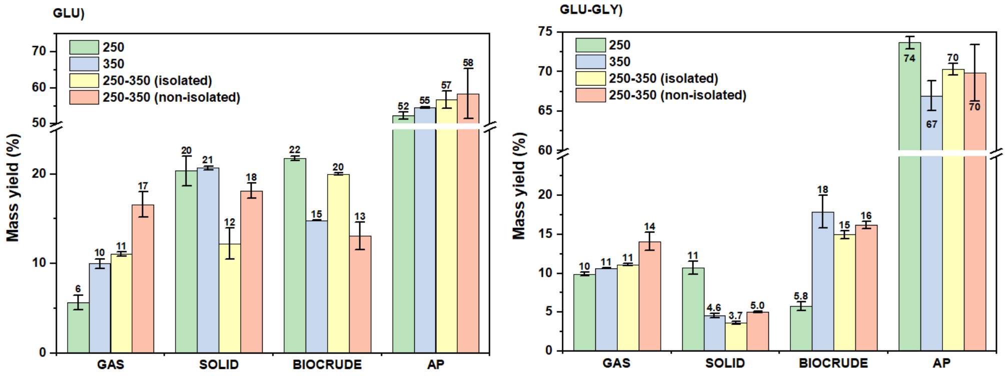

Figure 39: Mass yields at 250 °C for 1 h (green, 250), 350 °C for 1 h (cyan, 350), 250 °C for 1 h followed by 350 °C for 1 h with phases separated (yellow, 250-350 ('isolated')), and 250 °C for 1 h followed by 350 °C for 1 h without phases separated (orange, 250-350 (non-isolated)). Glucose on the left, glucose-glycine on the right. For 250-350 (isolated) and 250-350 (non-isolated), gas yield accounts for gas formed after the first step plus gas formed in the second step.

To understand whether the differences were either due to the different thermal profiles used (350 °C for 1 h versus 250 °C for 1 h +350 °C for 1 h) or to the hindrance of some phase interactions due to separation of the phases before the second step, an additional test was designed. That is, after an initial reaction at 250 °C for 1 h, the reactor was cooled down and the gas phase was removed without opening the reactor. Then the reactor was re-inerted, pressurized to 3 bar, and heated to 350 °C for 1 h without prior separation of the solid and liquid phases. The resulting mass yields are reported as 'non-isolated' in orange bars in Figure 39.

Comparing the non-isolated test (orange bars) with the results obtained at 350 °C for 1 h (cyan bars), it is evident that the mass yields were remarkably similar, except for the gas phase, with both glucose and glucose-glycine. This similarity suggests that the longer residence time used in the consecutive steps (1 h at 250 °C + 1 h at 350 °C) with respect to the reaction at 350 °C (1 h), did not significantly affect the final distribution among the phases. The difference observed in the gas phase can be attributed to the removal of the gas phase after the first step (1 hour at 250 °C), which likely promoted gas production in the second step. Therefore, it is possible that some equilibrium limitations for gas production exist.

Comparing the mass yields in the isolated tests (yellow bars) with those in the non-isolated test, glucose and glucose-glycine showed different behaviors. With the latter, the yields of solid, biocrude and AP were consistently similar, suggesting minimal phase interactions. On the other hand, with glucose, the co-presence of all phases favored solid production while disfavoring biocrude production. This suggests equilibrium-limited interactions among the different phases, wherein their separation results in a different distribution of final products. For example, Liu et al. proposed a solid formation mechanism from humins (i.e., the solid phase derived from hydrothermal conversion of glucose) involving an equilibrium between polymerization and depolymerization reactions[152]. Therefore, it may be suggested that the solid formed during the first step, upon contact with clean water in the second step, undergoes depolymerization, as the water lacks its precursors. Additional investigation is encouraged to better understand this phenomenon.

This interaction was further confirmed by testing the three phases recovered from the first step with glucose (solid, biocrude and aqueous phase) in combination with each other at 350 °C for 1 h (Figure 40). All the combinations tested (aqueous phase + solid, aqueous phase + biocrude and solid + biocrude in fresh water) showed synergy towards the solid and aqueous phase and an antagonism towards the biocrude. Moreover, observing the linear combinations of the mass yields obtained with the biphasic reaction (Figure 41, grey) calculated by Eq. (19), it is evident that solid and biocrude closely resembled the results obtained without isolation of the phases (Figure 41, orange). This further corroborated the hypothesis that strong interactions among phases characterize the final phase distribution with glucose.

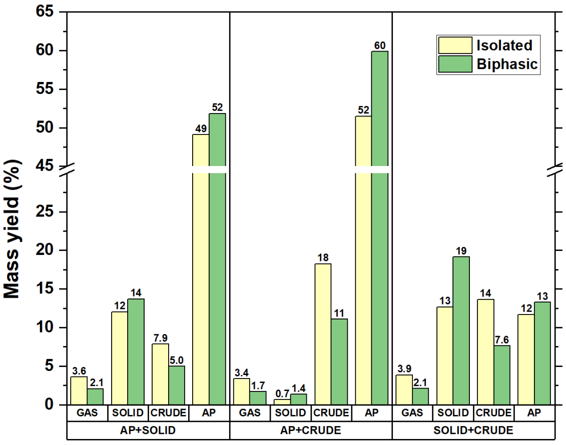

Figure 40: Mass yields obtained at 350 °C for 1 h from the combination of the solid, biocrude (B-S and B-AP) and aqueous phase recovered after glucose at 250 °C for 1 h (biphasic). Data are expressed as mass yields with respect to the amount of glucose in the first step. AP+SOLID and AP+BIOCRUDE were performed mixing the two products without further dilution, SOLID+BIOCRUDE was performed adding fresh water up to 200 g of total solution.

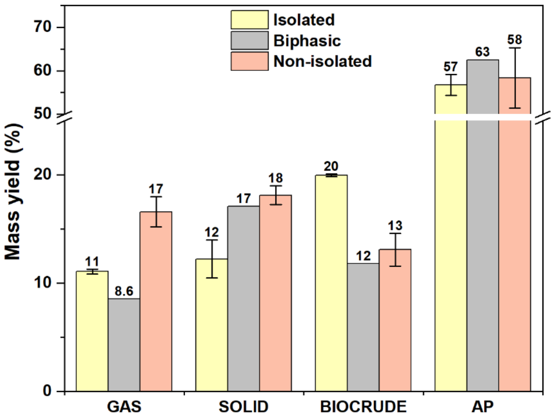

Figure 41: Linear combination of mass yields obtained at 350 °C for 1 h with isolation of the phases (yellow), with biphasic feedstock (grey) and mass yields obtained without isolating the phases. Data are expressed as mass yields with respect to the amount of glucose in the first step. Gas yield accounts for gas formed after the first step plus gas formed in the second step.

$$Biphasic\ yield = \frac{yield_{SOLID+AP} + yield_{SOLID+BIOCRUDE} + yield_{AP+BIOCRUDE}}{2} \tag{19}$$

3.2.6 Mechanisms description

Figure 42 depicts the relationships between the phases observed with glucose reacting alone. Glucose undergoes conversion into a plethora of organic compounds soluble in the aqueous phase. Among these, 5-HMF is formed through isomerization-dehydration and is the intermediate for the formation of both solid phase and biocrude. Even at low temperature, 5-HMF reacts with itself to produce an oligomeric structure (humins) that constituted the solid phase. Humins exist in a state of polymerization/depolymerization equilibrium with the aqueous compounds. Despite the presence of furanic groups in the chemical structure of humins, which might suggest their conversion into biocrude-soluble compounds, only a limited transformation of the solid into biocrude was observed. On the contrary, biocrude formation is likely to occur from 5-HMF, aldehydes, and ketones. The biocrude undergoes degradation at higher temperatures, resulting in water-soluble compounds. The gas phase is formed at both low and high temperatures and originates from all the other phases. CO_2 is the main gaseous product formed and derives from AP, solid and biocrude, probably mainly from decarboxylation reactions. CO and H_2 are also produced from the AP, the latter likely from formic acid, while a few CH_4 is formed from biocrude through demethylation.

Figure 43 displays the phase relationships observed for glucose and glycine reacting together (GLU-GLY). These two molecules show a strong interaction already at very low temperature due to the reaction between the amino group of the amino acid and the carbonyl group of the monosaccharide. This leads to the formation of Amadori compounds, which are intermediates in the Maillard reaction.

Among the various chemical pathways that occur during the Maillard reaction there is Strecker degradation, which results in the release of CO_2. The only gas formed in co-presence of glucose and glycine is CO_2 that is formed at low temperature through this mechanism. From the Maillard reaction, melanoidins are produced. Melanoidins are molecules known to have a very high molecular weight and to be water-soluble. Simultaneously with melanoidins, a solid phase with a structure similar to melanoidins is also produced. Both the melanoidins in the aqueous phase and the solid are precursors of the biocrude phase. At high temperature these structures are indeed thermically degraded into nitrogen-containing aromatics, mainly pyrazines and pyridines, which constitute the biocrude.

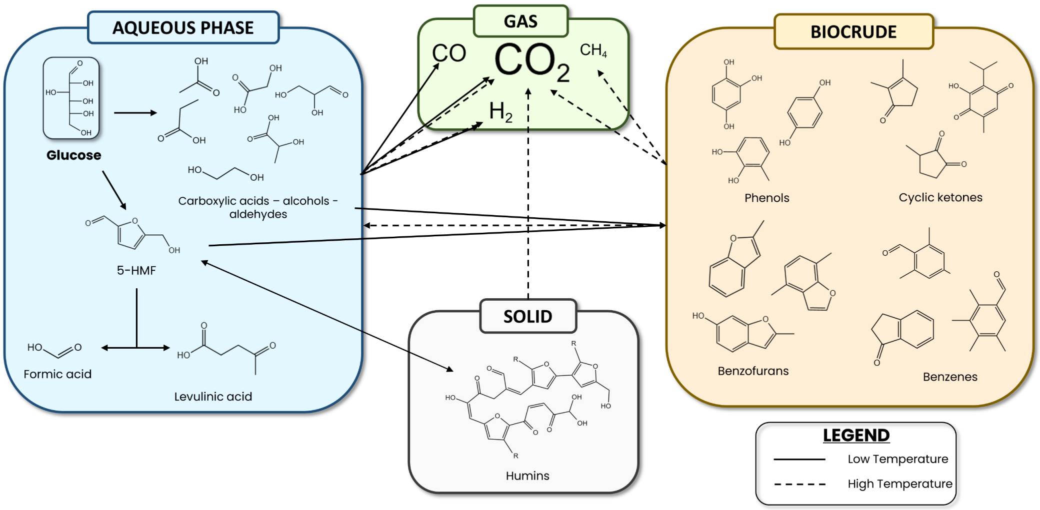

Figure 42: Suggested interchange mechanisms among phases with glucose (GLU).

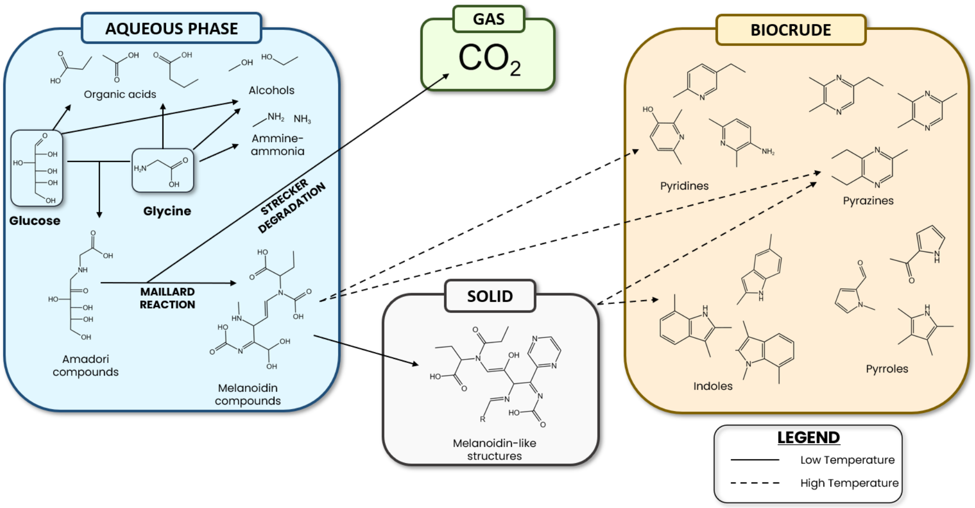

Figure 43: Suggested interchange mechanisms among phases with glucose and glycine (GLU-GLY).

3.3 Conclusions

The performance of carbohydrates, proteins and lipids during hydrothermal liquefaction has been investigated at different temperatures by experimental tests with glucose, glycine and oleic acid. The study was performed by comparing the reactivity of these molecules alone or in combination, as well as by observing the reaction pathways activated by each different phase produced in such HTL tests. The results have shown a strong interaction between glucose and glycine resulting in a set of products that differed significantly from the simple overlapping of the single monomer reactivities. In particular, solid and biocrude phases were strongly correlated. In contrast to the mechanisms occurring with glucose alone, the co-presence of glucose and glycine led to a higher solid and lower biocrude productions at low temperature (250 °C) and the opposite at higher temperature (350 °C). With remarkable novelty with respect to literature, consecutive reactions involving the generated phases have been performed to deepen the interchange phenomena. With glucose-glycine reacting together, solid and aqueous phase residues obtained at low temperature converted at high temperature into biocrude. Finally, with glucose alone the co-presence of solid and liquid phases (biocrude and aqueous residues) had a synergistic tendency towards the biocrude production at the expense of the gas and solid phase. Overall, this chapter strengthens the hypothesis that carbohydrates and proteins have a robust interaction during hydrothermal liquefaction, highlighting a central role for temperature in regulating such interaction. Furthermore, the experimental observations of interchange between the different phases of HTL allowed to understand the production/conversion of each phase and hence a better tuning of the reaction conditions towards the product of interest.

Chapter 4

Effect of heating rate and polymers in biomass

4.1 Introduction

As described above, the performance of HTL is known to be influenced by various operating parameters. Despite a wealth of knowledge about the impact of the aforementioned parameters, there is still limited understanding of the effect of heating rate on HTL performance[38]. To the best of the author's knowledge, the very few studies available have solely focused on the effect of heating rate on lignocellulosic feedstocks and, no studies on food waste have been performed. However, this is a key gap, since the biochemical composition of the feedstock strongly influences the reaction pathways[61,153]. According to the few studies on lignocellulosic feedstock, usually higher heating rates lead to an increase in the conversion of the feedstock and the production of biocrude. Brand et al. tested HTL of pine sawdust at temperatures ranging from 250 to 350 °C with two different heating rates: 2 and 20 K/min[154]. They observed that at reaction temperatures exceeding 280°C and with a residence time of 1 minute, there was an increase in biocrude yield and a decrease in the yield of residual solid as the heating rate increased. Specifically, at 320 °C, the biocrude yield increased from 15 wt.% to 24 wt.%, and the solid yield decreased from 28 wt.% to 14 wt.%. Similarly, at 350°C, the biocrude yield increased from 15 wt.% to 27 wt.%, and the solid yield decreased from 28 wt.% to 12 wt.%. Similarly, Tran et al. observed an increased biocrude production (from 19 wt.% to 36 wt.%) at the expenses of solids (from 43 wt.% to

27 wt.%) and aqueous-solubles (from 4 wt.% to 8 wt.%) when they increased the heating rate from 66 to 169 K/min during HTL of wood at 350 °C for 15 minutes[155]. However, the 15-minute duration included the heating time, so lower heating rates resulted in a shorter effective reaction time.

Except for the study on cellulose by Kamio et al.[156], all the aforementioned studies used real biomass as feedstock. While the use of real biomass enables the direct observation of how the heating rate affects the actual implementation of the HTL, a more in-depth understanding of the chemical mechanisms leading to variations in performance could be achieved by employing model compounds. Hence, this would enable to generalize the obtained results to all types of biomass. Furthermore, focusing only on short residence times, it is impossible distinguishing between a direct influence of the heating rate, linked to variations in chemical pathways during the heating period, and any indirect effects, associated with a different kinetic advancement of the reaction. In recent years, the use of the fast HTL has gained interest as an alternative to isothermal HTL[71,72,85]. The former requires very fast heating rates (from 100 K/min to 100 K/s), high set-point temperatures (up to 600 °C), and limited residence times (less than 1 min)[71,72]. This is in contrast to isothermal HTL, which involves longer residence times (>15 min) at lower temperatures (250-350 °C)[38]. Because these two techniques have significantly different residence times, the effect of the heating rate can have varied implications in each case.

This chapter aims to address this knowledge gap by systematically investigating the effect of heating rate on HTL of food waste. Real food waste from the university canteen was used as feedstock, as well as monomer compounds - cellulose, albumin, and triolein – chosen to mimic the essential components representing carbohydrates, proteins, and lipids, respectively. This approach enabled to investigate how varying heating rates affect both real biomass and its constituent parts, thereby enhancing the comprehension of the chemistry involved during the HTL reaction. Experiments were conducted for each feedstock by keeping all operating parameters fixed while varying only the heating rates and reaction times to exclude other influences. Additionally, to improve the understanding of any kinetic implications arising from the varied heating rates employed, a kinetic severity factor was utilized.

The findings presented in this chapter are derived from a published work[157].

4.2 Results and discussion

4.2.1 Cellulose

Figure 44 depicts the mass yields obtained after HTL of cellulose. With the exception of the compounds soluble in the aqueous phase (not reported), the most abundant phase was the solid one, as observed from glucose in Chapter 3.2. However, despite being completely insoluble in water (Table 2), cellulose yielded only 18 wt.% as a solid at 0 min and 115 K/min. The mass yield of glucose was 21 wt.% at 115 K/min, 2 wt.% at 77 K/min and zero for lower heating rates. Cellulose hydrolysis takes place in few seconds in hydrothermal environment[158] and the heating time was likely long enough to allow for glucose formation and its further conversion.

At 0 min, with decreasing heating rate, the amount of solid produced continuously increased. AP-soluble compounds formed from cellulose, in particular furanic compounds, are prone to repolymerization into solid humins[120]. Their formation is likely kinetically limited, and the increase in KSF with lower heating rate could explain the increase in solid. After waiting for an additional 30 min at set-point temperature, the differences between the heating rates became less pronounced, despite the same trend was still visible. Increasing the residence time from 0 to 30 min, the solid yield at 77 K/min increased, as humins did not have enough time to be formed during the heating time, while at 5.2 K/min it slightly decreased, likely due to a partial degradation of the excessively formed solid.

An increasing yield with decreasing heating rate was also observed for the gas phase at 0 min, as expected since gaseous compounds are end-products[45]. A higher extent of the reaction would result in their increased production, as observed after further 30 min. At 30 min the gas phase was composed by CO_2 (80-83 vol.%) and CO (15-18 vol.%).

Biocrude production showed an opposite trend. Biocrude-forming compounds were hence likely formed directly from cellulose degradation and are intermediate in the formation of other compounds, as confirmed also by the slight decrease in yield after 30 min of reactions. This aspect will be deepened by GC-MS analysis reported below.

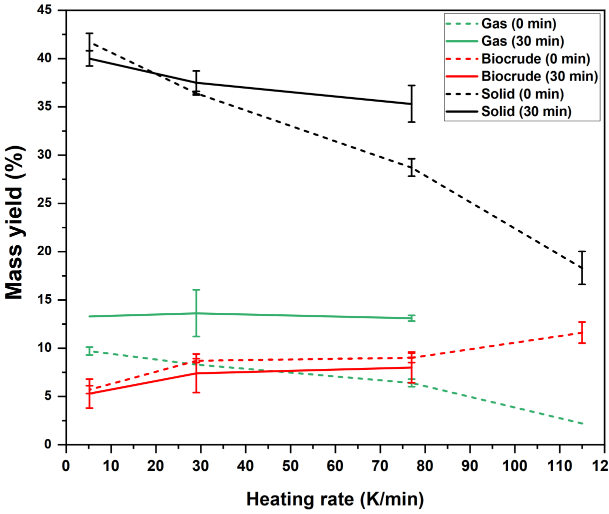

Figure 44: Mass yields obtained from cellulose. Reaction conditions: 1.8 g cellulose, 9 g total, 325 °C, 0 and 30 min.

The elemental compositions of solids and biocrudes are reported in Figure 45-A. After reaction, the elemental composition of the solid drastically changed from cellulose, with carbon increasing significantly at the expense of oxygen. However, except at 115 K/min run and 0 min, the elemental composition of the solid did not change significantly with different heating rates. Additionally, an increase in the reaction time did not significantly affect the solid composition. Therefore, it is likely that the solid observed after reaction at 0 min and 115 K/min was actually a mixture of unconverted cellulose and solid product. That run, in fact, lasted just the few minutes necessary for heating, and it is probable that cellulose hydrolysis was not completed. However, already at 0 min and 77 K/min the elemental composition was the same observed in all the other runs. Despite minimal changes in the elemental composition, the carbon yield in the solid (Figure 45-C) strongly increased with lower heating rates at 0 min. Hence, solid humins are formed by the condensation of compounds soluble in the aqueous phase within a time frame comparable to the heating duration.

At 0 min, the biocrude elemental composition (Figure 45-B) mostly showed an increase in hydrogen content with decreasing heating rate. After 30 min, the carbon content slightly increased, while oxygen and hydrogen decreased. However, no differences were registered between the different heating rates. The breakdown of compounds present in the biocrudes is depicted in Figure 45-D. At low KSFs, a consistent amount of furanic molecules and oxygenates were identified. In particular, the former are known to be prone to polymerize into solid humins[112,159], thus explaining the opposite trends of furanic compounds and biocrude yield in relation to solid formation. Despite solid formation cannot be explained solely by the conversion of biocrude-soluble compounds, as the biocrude content remained low under all conditions, the presence of these compounds in the biocrude is indicative of similar compounds in the aqueous phase, as their polarity and solubility are intermediate[118]. With increased KSF, the amount of acids and phenols increased. Phenolic compounds are known to be the final product during HTL of saccharides[160] and levulinic acid, identified as the most prevalent acid, results from dehydration of 5-HMF, which was also identified in the aqueous phase through HPLC.

As for the mass yield, the majority of the carbon yield was directed towards the solid phase (Figure 45-C). At 30 min, a slight effect of the heating rate was observed, with solid favored and biocrude disfavored at lower heating rates. The AP carbon yield was consistent at low KSF due to hydrolysis of cellulose into glucose and subsequent formation of oxygenated intermediates that subsequently converted into solid.

Overall, after 0 min of reaction, the heating rate had a strong effect on the HTL of cellulose, both quantitatively and qualitatively. At higher heating rates, the heating time was not sufficient to complete the conversion of furans and aqueous-soluble compounds into solid humins, aromatics, and levulinic acid. Conversely, after 30 min of reaction, the heating rate appeared to have a minor impact on mass yields, favoring a slightly higher biocrude yield over solid yield at elevated heating rates. This could be attributed to humins formation occurring at low temperatures[112], and thus, a shorter stay at lower temperatures during the heating time limited the amount of solid formed, which may not be completely recovered. On the other hand, from a qualitative perspective, the differences at 30 minutes were almost negligible.

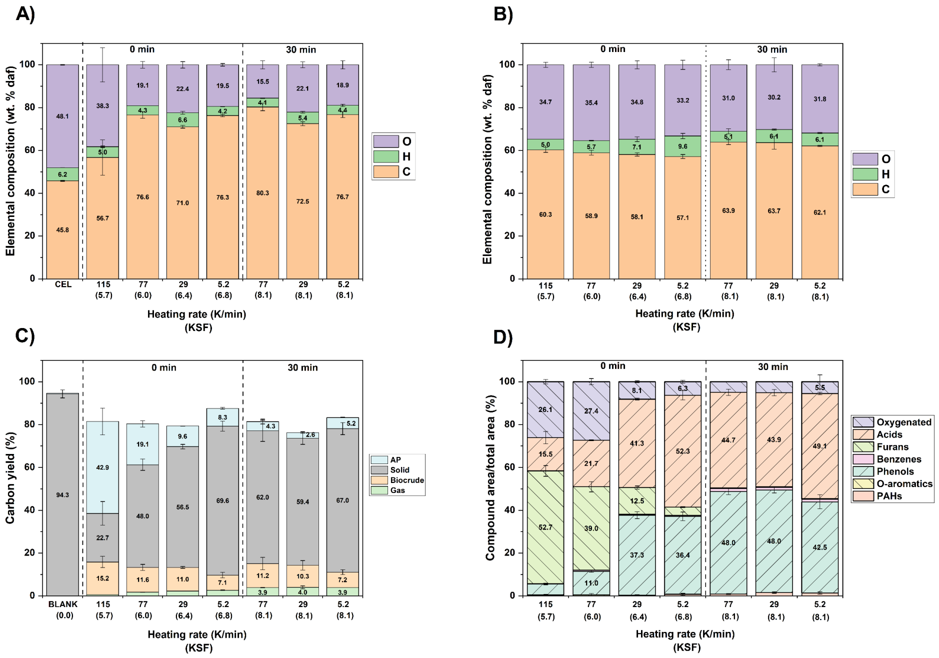

Figure 45: (A) Elemental composition of solids and feedstock (CEL); (B) elemental composition of biocrudes; (C) carbon yields of all the phases; (D) families of compounds identified in the biocrudes by GC-MS. Data refer to products obtained from cellulose at 325 °C with different heating rates and with two residence times (0 min, 30 min).

4.2.2 Albumin

Figure 46 depicts the mass yields obtained after HTL of albumin. 88 wt.% of albumin was soluble in the aqueous phase at room temperature, as reported in Table 2, and after every reaction, the aqueous phase yield was within 64-74 wt.% (not reported). Hence, the fraction of albumin soluble in the aqueous phase was converted into the other phases.

At 0 minutes, the solid phase decreased with a decreasing heating rate, hence increasing KSF, in contrast to what happened with cellulose. However, at 77 K/min and above, the solid yield was consistently higher than the solid fraction of albumin. As already observed after fast HTL of bovine serum albumin[109], above 78-86 °C ovalbumin is denatured into a more stable and hydrophobic structure that results in an increased solid yield[161]. With increasing KSF, the denatured structure is then slowly converted, resulting in a 4.7 wt.% of solid yield. After further 30 minutes at

325 °C, the solid phase further decreased up to 1.4-1.9 wt.%, likely attributable to the ashes present in albumin, as 6 wt.% of the albumin constituted ash (Table 2). The remaining portion of ashes was likely solubilized in the aqueous phase[162–164].

Unlike the solid, biocrude increased with a decreasing heating rate at 0 minutes of reaction time and further increased after 30 minutes at 325 °C. This increase implies the occurrence of secondary reactions contributing to biocrude production. One possible explanation for this phenomenon is the conversion of the solid phase into biocrude, as indicated by the opposing trends observed between the two phases. During HTL, proteins are hydrolyzed to smaller peptides with a decreasing molecular weight as the residence time increase[165]. Most of the degradation products of peptides are amines and aqueous phase soluble[109]. HTL experiments conducted with glycine showed a limited biocrude production (Paragraph 3.2.1), hence suggesting that biocrude production from proteins takes place from the degradation of the solid polypeptides.

As observed with cellulose, gas yield increased with decreasing heating rate at 0 minutes and increased after further 30 minutes, confirming the increased production as KSF increases. At 30 minutes, 96-98 vol.% of the gas phase was composed by CO_2.

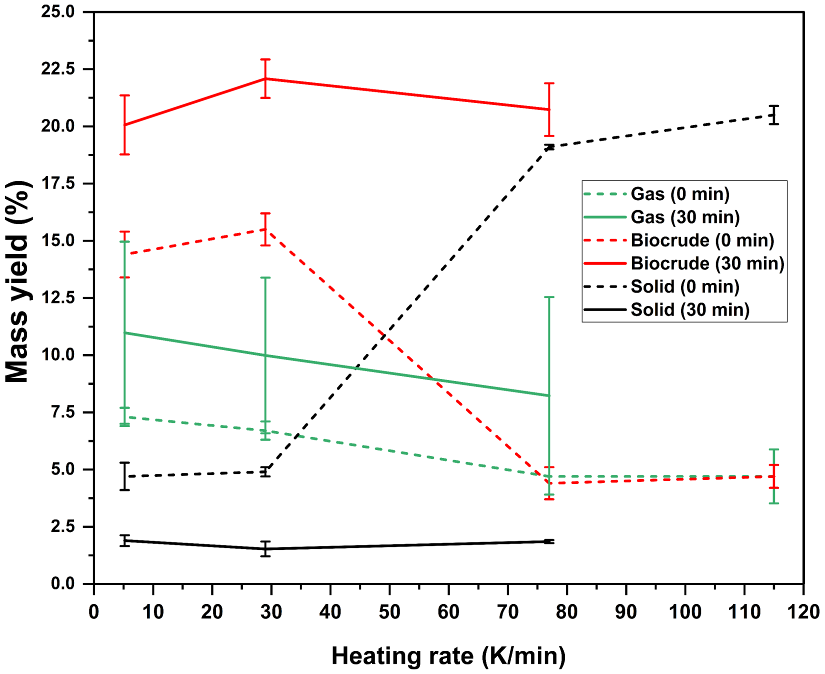

Figure 46: Mass yields obtained from albumin. Reaction conditions: 1.8 g albumin, 9 g total, 325 °C, 0 and 30 min.

The elemental composition of the solids and biocrudes is depicted in Figure 47-A/B. In addition to carbon, hydrogen and oxygen, albumin contains a noteworthy amount of nitrogen and a small sulfur fraction, leading to the classic sulfur odor after the HTL reaction. The solid fraction of unconverted albumin exhibited lower oxygen levels compared to the overall albumin composition, and following a reaction at 0 minutes, the oxygen content in the residual solid further decreased. However, decreasing the heating rate, and consequently increasing the KSF, the elemental composition of the solid did not change significantly. It is hence possible that degradation of the albumin solid phase may occur through a random scission mechanism that does not occur on precise portions of molecules, as speculated by Aida et al.[165], until complete conversion.

Regarding the biocrudes (Figure 47-B), it was not possible to obtain the elemental composition at high heating rates at 0 min due to their low mass yields, which made it difficult to identify a trend. However, by increasing the reaction time from 0 to 30 minutes, carbon and hydrogen increased at the expenses of oxygen and nitrogen. That is an interesting result that confirms that with longer residence times, the amount of heteroatoms in the biocrude decreases, providing a higher-quality product that can be more easily upgraded to biofuel.

The molecular compositions of biocrudes are reported in Figure 47-E/F. It is worth noting that the results of Figure 47-E and Figure 47-F are not directly comparable due to the different derivatization method used, as explained Paragraph 2.2.3. At 0 minutes most of the compounds identified by GC-MS were amides (amides, cyclic amides/imides and diketopiperazines), which accounted for 60-72% of the overall area (Figure 47-E). Among these, the most abundant molecules were diketopiperazines (DKPs) derivatives, which are associated with hydrolysis of proteins. DKPs were observed to be formed through cyclization of amino acids[106,130,166] and were inferred to be hydrolysis products resulting from progressive cyclization, forming smaller and smaller cyclic peptides until they became DKPs[143]. As the heating rate decreased, the relative area of DKPs decreased in favor of other amides (cyclic amides/imides and linear amides), suggesting that their formation occurred through degradation of DKPs[106]. With decreasing heating rate even the nitrogen-containing aromatics increased, with indole derivatives being the most abundant, along with benzenes and phenols. Indoles are likely the result of interactions between phenols and amino acids[167], while phenols and benzenes could be produced by interactions and recombination of oxygenated molecules[129,168].

After 30 min of reaction time, the differences at various heating rates were negligible (Figure 47-F). Most of the identified molecules were amides, followed by aromatics (phenols, nitrogen-containing and benzenes) and amines. Among the nitrogen-containing aromatics, indoles were the most present ones. Amines are formed after the complete hydrolysis of proteins into amino acids, and residual amino groups can persist after recombination of amino acids into other molecules. In fact, many of the amines identified in this chapter also contained other functional groups, primarily aromatic rings. Finally, the presence of sulfur-containing molecules was very limited after both 0 and 30 minutes of reaction time.

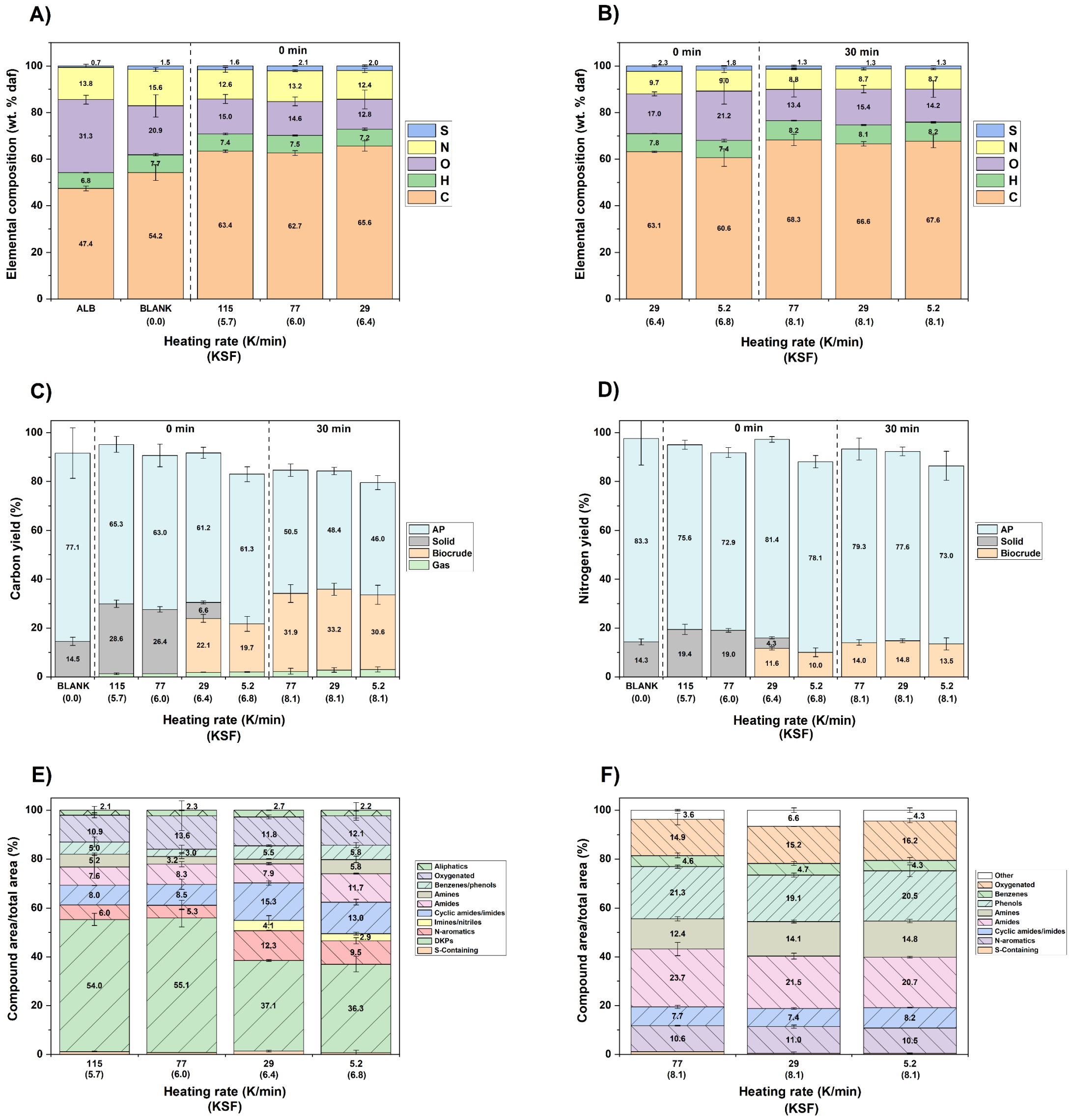

Figure 47: (A) Elemental composition of solids, feedstock (ALB) and its solid fraction (BLANK); (B) elemental composition of biocrudes; (C) carbon yields of all the phases; (D) nitrogen yields of all the phases; (E) families of compounds identified in the biocrudes obtained at 0 minutes by GC-MS without derivatization with BSTFA; (F) families of compounds identified in the biocrudes obtained at 30 minutes by GC-MS after derivatization with BSTFA. Data refer to products obtained from albumin at 325 °C with different heating rates and with two residence times (0 min, 30 min).

The carbon distribution among the different phases (Figure 47-C) confirmed the observations made based on the mass yields (Figure 46). Specifically, it revealed a decrease in the solid phase and an increase in biocrude with the increasing KSF. Moreover, Figure 47-C provides confirmation that, prior to the reaction, most of the carbon in the albumin feedstock was present in the aqueous phase. During the heating time, a portion of the aqueous-soluble fraction became entrapped in the solid phase due to the denaturation. In addition to this, another portion of the aqueous soluble was converted into the biocrude phase.

As for the nitrogen distribution (Figure 47-D), the trends closely resembled those observed for carbon distribution. However, compared to the carbon yields, the nitrogen yields in both the solid and biocrudes were significantly lower, with a preference for the aqueous phase. This was expected as nitrogen is more polar than carbon, and nitrogen-containing functional groups tend to have higher aqueous solubility.

Overall, as observed with cellulose, the heating rate strongly affects the HTL performance of albumin, both quantitatively and qualitatively, at 0 min. However, after 30 min of reaction time, the effects of heating rate were not observable.

4.2.3 Triolein

During HTL of triglycerides, the oil phase is the predominant product, as depicted in Figure 48. This is due to the fact that triglycerides are insoluble in the aqueous phase, and the main reaction they undergo is hydrolysis[145], resulting in the formation of free fatty acids, which remain insoluble in the aqueous phase, and glycerol, which is soluble in water. Stoichiometrically, complete hydrolysis of triolein would yield 95.7 wt.% as biocrude and 10.4 wt.% as aqueous phase (due to glycerol) on a mass base. The average biocrude mass yield was 91.5 wt.% at 0 minutes and 87.8 wt.% at 30 minutes. The difference between the expected 100 wt.% and the recorded 91.5 wt.% at 0 min was likely due to an incomplete recovery of triolein during the work-up, as confirmed by the blank experiment (Table 2). Conversely, the 87.8 wt.% observed at 30 minutes represents 96.0% of the biocrude yield at 0 minutes, closely aligning with the theoretically expected 95.7% reduction. This alignment suggests that hydrolysis primarily occurred after 30 minutes at 325 °C. This assumption was confirmed by the assessment of the hydrolysis yield (Figure 48), according to Eq. (20). This equation is analogous to the glycerol yield, and its application is substantiated by an experimental test involving glycerol alone, which demonstrated that after 30 minutes at 325°C, 97% of glycerol remains unconverted. The hydrolysis yield was minimal at 0 minutes (0-1.4 %), but almost complete at 30 minutes (87-90%). Based on these results, it is reasonable to assume that the kinetics of triglycerides are slow enough that significant hydrolysis does not occur during the initial heating phase, eliminating the influence of heating rate on the final product distribution.

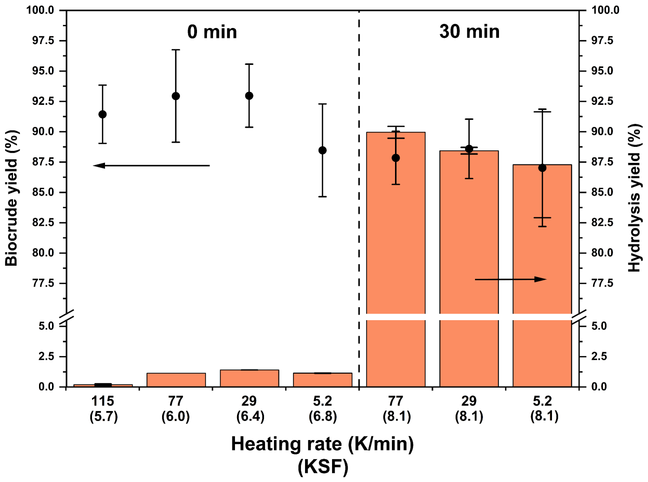

Figure 48: Biocrude yields (scatter) and hydrolysis yields (bars) from triolein. KSFs are reported inside brackets. Reaction conditions: 1.8 g triolein, 9 g total, 325 °C, 0 and 30 min.

$$Hydrolysis\ yield\ (\%) = \frac{glycerol\ concentration\ in\ the\ AP\ (\frac{g_{glycerol}}{g_{AP}}) \cdot 7.2\ g_{AP}}{0.104\ (\frac{g_{glycerol}}{g_{feed}}) \cdot 1.8\ g_{feed}} \tag{20}$$

4.2.4 Food waste

The biochemical composition of the food waste collected from the university canteen was 19.6 ± 0.7 wt.% proteins, 2.9 ± 1.2 wt.% lipids and 77.5 ± 1.9 wt.% carbohydrates, based on a dry and ash-free basis. A synthetic mixture of cellulose, albumin and triolein was used to mimic the food waste during the HTL reaction, referred to as ‘simulated food waste’ hereafter. The resulting mass yields are reported in Figure 49-A, while the linear combination of the mass yields obtained from singular biopolymers was calculated using Eq. (21), and the results are presented in Figure 49-B. Interestingly, the linear combination of the mass yields strongly differs with the actual results obtained from the simulated food waste. To further highlight the discrepancies, in Figure 50-A/B, the absolute and relative differences between the experimental results and the averaged values are plotted. The biggest difference can be observed for the solid phase at 0 min, which showed a big increase in mass yield at fast heating rates in the case of simulated food waste. With increasing KSFs, the difference in solid production decreased up to be unfavored at higher values. The biocrude yield showed an opposite trend, as it was slightly unfavored at low KSFs and ended up being slightly favored at higher KSFs. The differences between the simulated food waste and the linear combination of the biopolymers reacting alone must be explained by synergistic/antagonistic behaviors between the biopolymers. The strongest interaction between biochemical compounds during HTL takes place between carbohydrates and proteins[107]. As observed in the previous chapter, the interaction between monomers of carbohydrates and proteins led to an increased production of solid phase at low temperature (KSFs of 4.8 and 6.3 at 200 °C and 250 °C) due to the formation of melanoidin-like compounds that at higher temperatures (KSFs of 7.8 and 9.3 at 300 °C and 350 °C) were converted into biocrude[112]. Due to the similar trends observed in this chapter with biocrude and solid with increasing KSF, the synergistic/antagonistic behavior is likely explained by the presence of the Maillard reaction. Moreover, also the gas yield was increased in the case of the simulated food waste (Figure 50-A/B). This can be explained by the presence of the Strecker degradation that, during the Maillard reaction, leads to the production of carbon dioxide already at low temperatures[112,138,139].

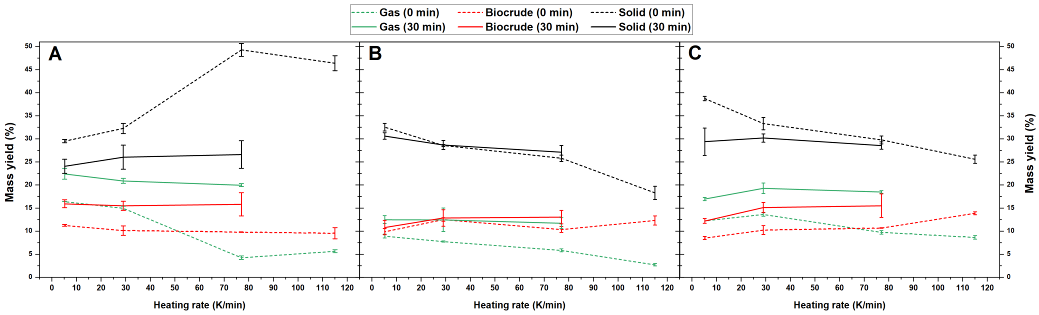

Figure 49: (A) Mass yields obtained from the simulated food waste. Reaction conditions: 1.36 g cellulose, 0.39 g albumin, 0.05 g triolein, 9 g total, 325 °C, 0 and 30 min. (B) Mass yields obtained as linear combination of cellulose, albumin and triolein reacting alone evaluated according to Eq. (21). (C) Mass yields obtained from the real food waste. Reaction conditions: 5.6 g food waste (1.8 g dry based), 9 g total, 325 °C, 0 and 30 min.

The mass yields obtained from the HTL experiments with real food waste are reported in Figure 49-C. The mass yields obtained at 30 min after the HTL of real food waste (Figure 49-C) were relatively similar to those obtained after the HTL of simulated biomass (Figure 49-A). Any minor differences could be attributed to the structural distinctions between the constituents of real biomass and the model macromolecules used to mimic it (cellulose, albumin and triolein). However, the trend of the solid phase with varying heating rate significantly differed at 0 min. Specifically, the mass yield decreased with decreasing heating rates in the case of simulated food waste but increased with actual food waste. Before the reaction, both actual and simulated food waste consisted mainly of the solid phase (87 wt.% and 79wt.%, respectively, as reported in Table 2), which was converted over time. Simultaneously, another solid phase was produced as a result of interactions between molecules in the other phases, such as the formation of insoluble melanoidins[112]. Consequently, the resulting solid yield was the outcome of a balance between the conversion of solid food waste and the production of solid intermediates. Therefore, the disparities between real and simulated food waste could arise from the different kinetics of hydrolysis and intermediate formation, which tend to minimize over longer reaction times.

The solid phase decreased after increasing the reaction time from 0 to 30 min, while biocrude increased (Figure 49-C). This trend confirmed the instability of the intermediate solid at higher temperatures and suggests its conversion into biocrude.

It is important to note that the biocrude yield slightly decreased with a decreasing heating rate, even at 30 min. The same trend at 30 min was observed during the HTL of cellulose (Figure 44), along with an increase in the solid. Although the increase in the solid phase is not clearly visible in Figure 49, it is likely that the heating rate has a subtle effect on the performances of carbohydrate-containing feedstock, even at higher residence times.

It is worth noting that the biocrude yields reported herein from actual food waste were lower than those reported in the literature[169,170]. For example, Motavaf and Savage obtained approximately a 28 wt.% yield with similar operating conditions of pressure, temperature and residence time[169]. This difference could be explained by the fact that the lipid content of the food waste used as feedstock in this chapter was extremely low (2.9 wt.%$_{daf}$ vs 16.6 wt.%$_{daf}$). This is corroborated by works performed with similar biochemical content to the one used herein, obtaining comparable values[170].

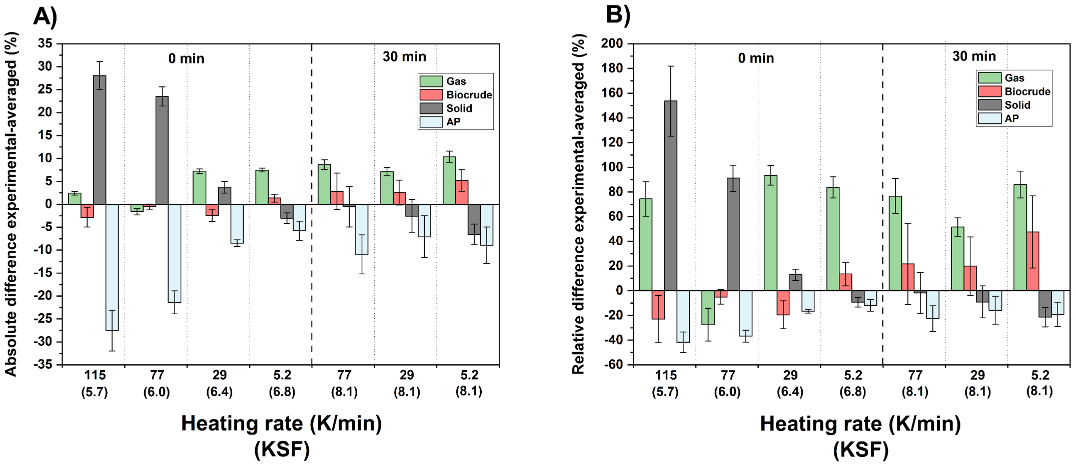

Figure 50: (A) Absolute differences and (B) relative differences between the mass yields obtained from the 'simulated' food waste and the linear combination of cellulose, albumin and triolein, weighed according to their quantities used for the simulated food waste (as per Eq. (21)). For each phase (gas, biocrude, solid and aqueous phase), the absolute difference was calculated using Eq. (8), while the relative difference was calculated using Eq. (9).

$$Yield_{averaged}\ (\%) = \frac{yield_{cellulose} \cdot mass_{cellulose} + yield_{albumin} \cdot mass_{albumin} + yield_{triolein} \cdot mass_{triolein}}{mass_{cellulose} + mass_{albumin} + mass_{triolein}} \tag{21}$$

Figure 52-A/B depict the elemental composition of solids and biocrudes, respectively. Even at 0 min and 115 K/min, the elemental compositions of the solid and the biocrude were similar to those obtained after 30 min of reaction time. In the case of solids, carbon ranged within 66-74 wt.%, hydrogen within 5.1-5.6 wt.%, oxygen within 16-24 wt.% and nitrogen within 4.5-5.0 wt.%. Similarly, for biocrudes, carbon ranged within 64-73 wt.%, hydrogen within 7.0-9.2 wt.%,

oxygen within 15-27 wt.% and nitrogen within 2.2-3.8 wt.%. For both solids and biocrudes, at 0 min, the carbon content increased with decreasing rate, at the expense of oxygen. In contrast, at 30 min, the elemental composition of the biocrudes did not vary significantly, while the solids decreased the carbon content in favor of oxygen with decreasing heating rate.

Figure 52-C/D depict the carbon and nitrogen yields in the different phases, respectively. While the carbon and nitrogen were initially exclusively present in the solid fraction of the food waste, after the reaction, both the carbon and nitrogen content increased at 0 minutes with decreasing heating rate. However, at 30 minutes, these values decreased compared to those obtained at 0 minutes, coherently with the mass yields of Figure 49. On the other hand, biocrudes increased their nitrogen and carbon content as the reaction time increased from 0 to 30 min. Moreover, the carbon yield in the biocrude exhibited a decreasing trend at 30 min with decreasing heating rate, confirming a certain effect of the heating rate even with the same KSFs. As for the aqueous phase, the carbon yield decreased from 28% to 19% with decreasing heating rate at 0 min, and equaled 13-14% at 30 min. On the other hand, nitrogen showed a higher distribution in the aqueous phase (36-52%).

Figure 52-E presents the most prevalent families of molecules identified by GC-MS in the biocrudes. At 0 min and 115 K/min, the majority of the identified molecules were furans, followed by organic acids, aromatics (benzenes/phenols), long fatty acids, and oxygenated compounds. Apart from fatty acids, this composition closely resembled the biocrude obtained from pure cellulose (Figure 45-D), coherently with the carbohydrate-rich composition of the food waste. The presence of long fatty acids is attributable to the lipids present in the food waste. While GC-MS cannot identify triglycerides due to their high boiling point, it can detect fatty acids. Consequently, at 0 minutes with a decreasing heating rate, the content of long fatty acids increased in the GC-MS, eventually constituting the majority of the integrated area at 30 minutes. This increase is a result of the hydrolysis of fatty acids, as observed with triolein (Figure 48). However, only the vaporized fraction of the biocrude is analyzed with GC-MS. Figure 51 illustrates that approximately 48% of the biocrude evaporates prior to reaching 280 °C, which is the injection temperature of the GC-MS. Consequently, the composition depicted in Figure 52-E solely represents this 48%. This observation may elucidate why Figure 52-E indicates that 68% of the biocrude consists of fatty acids, particularly when considering that, at the 30-minute mark, about 15 wt.% of the biocrude was generated, while the biomass waste contained only 3 wt.% of lipids. In addition to long fatty acids, monoglycerides and long fatty esters were detected, particularly at 0 min, as products of the partial hydrolysis of triglycerides and degradation of monoglycerides[73].

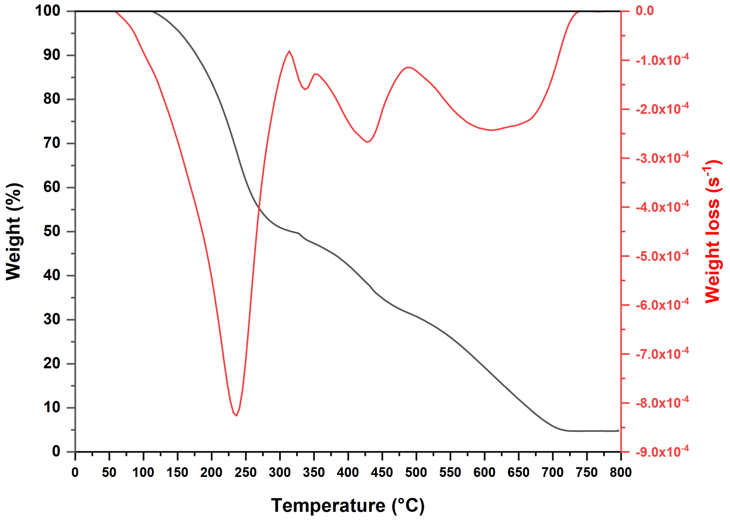

Figure 51: TGA of biocrude obtained after HTL of food waste at 77 K/min and 30 min. TGA conditions: 25 °C - 800 °C (10K/min) in 50mL/min Argon.

By excluding the area attributed to long fatty acids, the area associated with furans decreased as the heating rate decreased at 0 minutes. In its place, it was observed an increase in the presence of acids, phenols, and nitrogen-containing aromatics, ultimately becoming the three most abundant compound families after 30 minutes of the reactions. The significant presence of acids and phenols aligns with the carbohydrate-rich content, while the presence of nitrogen-containing aromatics is due to the proteinaceous content of the food waste. Notably, in contrast to the composition of the biocrude derived from albumin, this case revealed that pyridines, rather than indoles, constituted the majority of the nitrogen-containing aromatics, suggesting a different mechanism of formation[141]. Furthermore, the GC-MS results for the simulated food (Figure 53) closely resembled those of Figure 52-E, indicating a chemical resemblance between biocrude from real waste and model macromolecules. Interestingly, no fatty amides were detected in both Figure 52-E and Figure 53, unlike what was observed in the case of monomers (Figure 32). The variation in behavior may be attributed to triglycerides undergoing hydrolysis over an extended period of exposure to high reaction times. Consequently, there is a depletion of reactive amine groups through interactions with other functional groups. Another explanation could be linked to the intricate nature of proteins, resulting in more pronounced degradation and a reduced availability of amino groups for reacting with fatty acids.

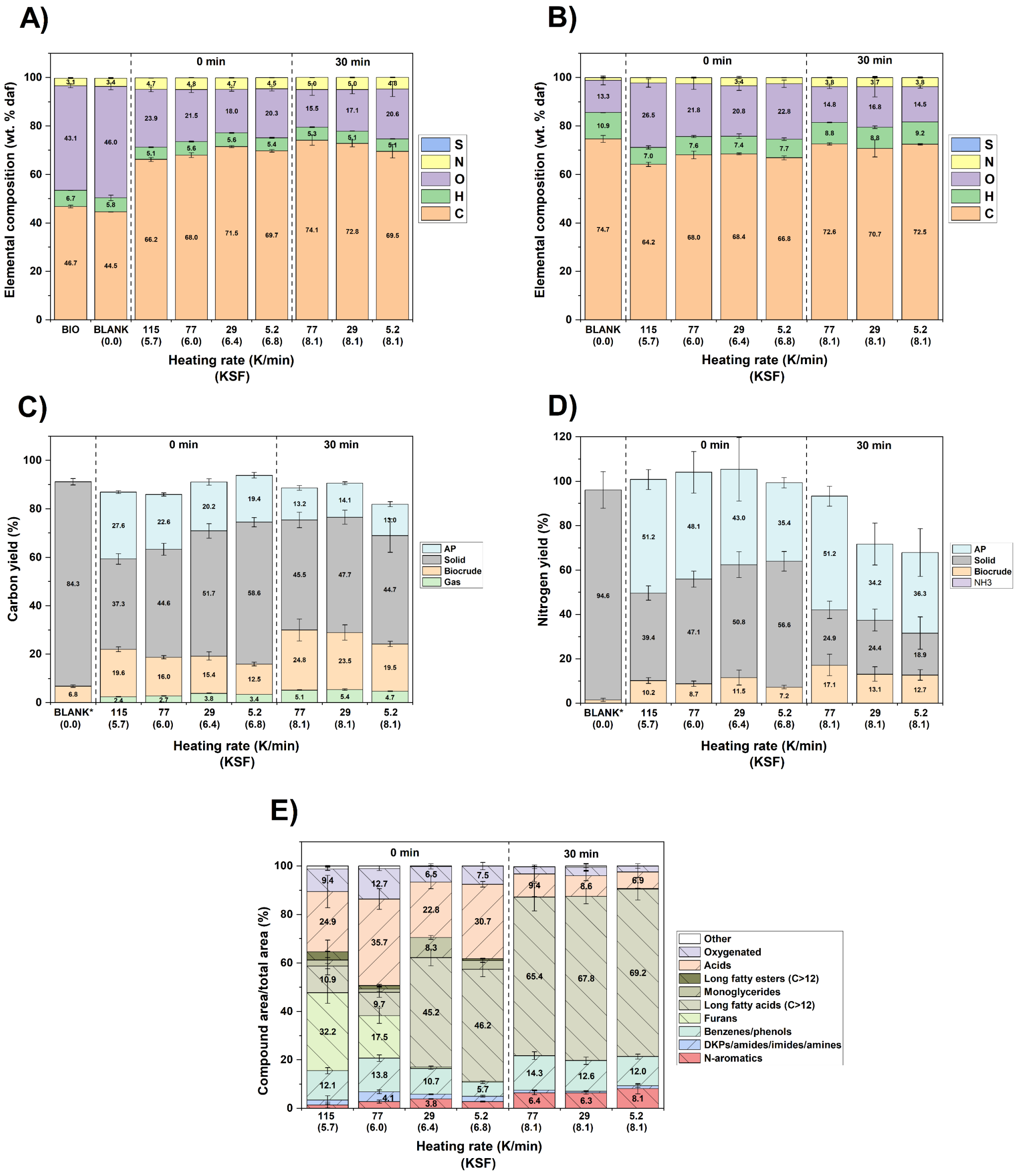

Figure 52: (A) Elemental composition of solids, feedstock (BIO) and its solid fraction (BLANK); (B) elemental composition of biocrudes and the oil fraction of the feedstock (BLANK); (C) carbon yields of all the phases and of fraction of the feedstock (BLANK); (D) nitrogen yields of all the phases and of fraction of the feedstock (BLANK); (E) families of compounds identified in the biocrudes. Data refer to products obtained from real food waste at 325 °C with different heating rates and with two residence times (0 min, 30 min). *AP not quantified.

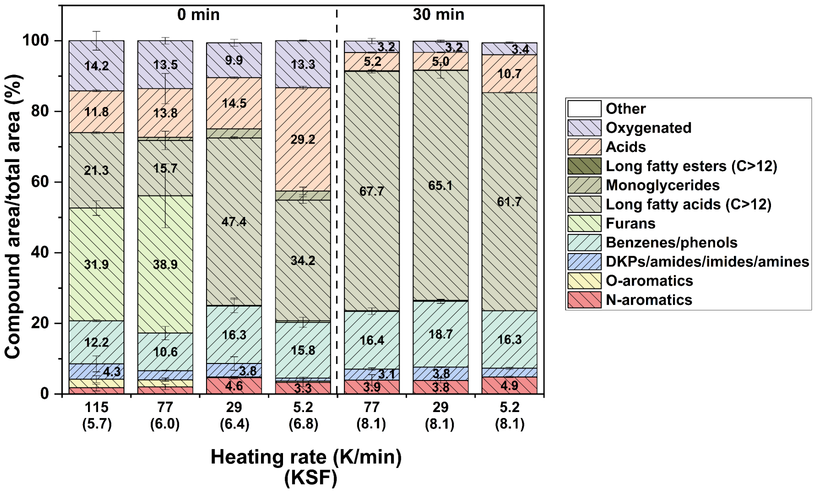

Figure 53: Families of compounds identified in the biocrudes obtained from simulated food waste at the different heating rates and with the two residence times (0 min, 30 min).

4.3 General considerations

With the exception of triolein, which requires a long residence time at a higher temperature to undergo hydrolysis into fatty acids, cellulose, albumin, real and simulated food waste showed significant variations in performance when the heating rate was changed at 0 min. These differences were both quantitative (e.g., mass, carbon and nitrogen yields) and qualitative (e.g., biocrude composition). This behavior can be explained by an 'indirect' effect of the heating rate on reaction kinetics, represented by the kinetic severity factor (KSF). Specifically, at short reaction times, decreases in the heating rate lead to an increased heating time, resulting in a higher KSF and hence a higher advancement of the reaction.

Conversely, after an additional 30 min at the set-point temperature, the differences in both quantitative and qualitative aspects due to variations in the heating rate became less evident. Because of this, it can be assumed that any 'direct' effects during the heating time - associated to the fact that a prolonged permanence at lower temperatures during heating time could induce changes in mechanisms and, consequently, overall selectivity - are limited. Furthermore, notably, any potential intermediate product produced by varying the heating rate with short reaction time is further converted when the test is extended for 30 minutes. Therefore, the primary effect associated with the heating rate is kinetic.

To further reinforce this concept, Figure 54 plots biocrude and solid yield against the KSF. With short reaction times (KSF < 7), some trends of the mass yields were clearly visible with the KSF. Conversely, for the experiments lasting 30 min, having the same KSF of 8.1, the mass yields were similar. Notably, some differences outside the standard deviations arose for solid in the case of cellulose and for biocrude in the case of cellulose and food waste. In these cases, biocrude production was favored at the expense of solid when using faster heating rates. Nevertheless, in contrast to the variances noted with diverse KSFs, these distinctions were negligible. Additionally, while there were slight variations in yields for these two types of feedstocks under different heating rates, there were no qualitative changes observed in the composition of the biocrude.

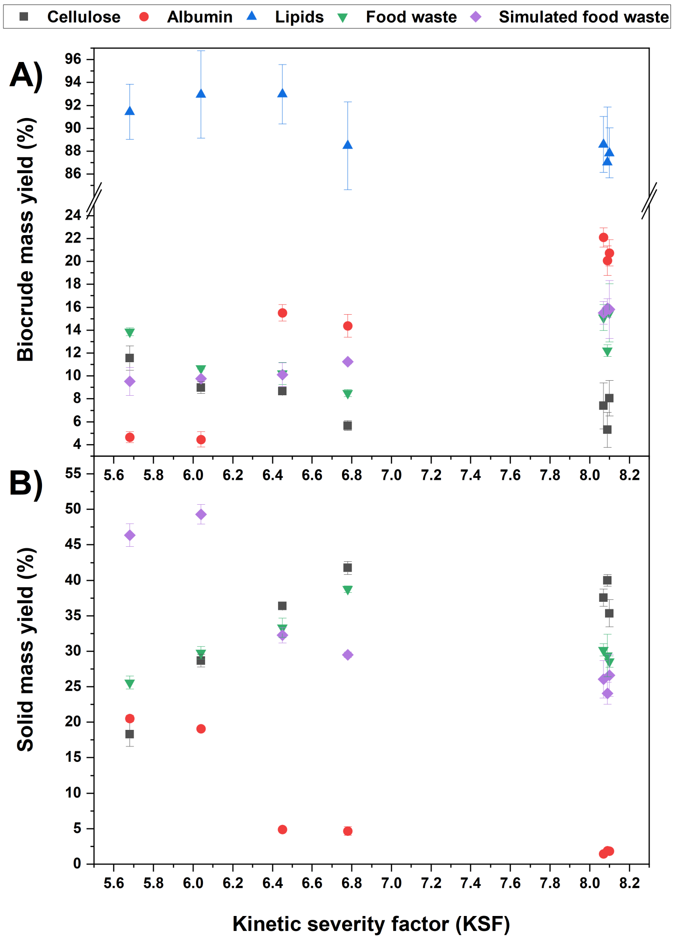

Figure 54: (A) Biocrude and (B) solid phase obtained from the HTL of cellulose, albumin, lipids, food waste and simulated food waste according to the KSF of the test.

4.4 Conclusions

In this chapter, the effect of the heating rate on the HTL performance was investigated, as it could affect the HTL performance of bio-polymers and real waste. Actual waste and model compounds - cellulose, albumin, triolein - were tested at different heating rates and residence times. Cellulose and triolein showed similar behavior compared to their respective monomers, glucose and oleic acid. Conversely, albumin presented different results compared to glycine, suggesting the different degradation mechanisms during HTL of proteins and amino acids.

Only a limited effect was observed after heating variation at longer reaction times, but significant changes were noted at shorter reaction times. According to these results, the significant differences in HTL performance observed when varying the heating rate are indirectly caused by changes in the kinetic advancement of the reaction, while only minor differences can be attributed to a direct influence of the heating rate on reactive mechanisms. Carbohydrate-rich feedstocks, in particular, showed the highest discrepancies, albeit limited, with varying heating rates at longer times.

In conclusion, the kinetic severity factor (KSF) proved to be a useful parameter for explaining the differences in performance observed with different heating rates. Indeed, the variations in performance are not directly attributed to the heating rate, but rather to differences in the kinetic advancement of the reaction. The KSF, which is based on the Arrhenius law, has been shown to effectively explain HTL behavior. Although the heating rate is not explicitly present in the KSF formula (Eq. (1)), it does influence the time spent at a certain temperature during heating. This relationship is elucidated by Eq. (22), where the KSF is subdivided into a first term dependent on the heating rate (HR), and a second term dependent on the set-point temperature (T_f) and the residence time (RT) at that temperature. If the residence time at the set-point temperature is short, the second term is limited, and the KSF closely resembles its value during heating. Conversely, with increasing residence time, the second term significantly increases, rendering the first term negligible and reducing the kinetic dependence on the heating rate. Thus, from this chapter, it can be concluded that the KSF can serve as the sole parameter, encapsulating temperature, residence time, and indirectly, the heating rate.

$$KSF = KSF_{heating} + KSF_{setpoint} = \log\left(\int_0^{t_{setpoint}} e^{\frac{HR\cdot t-100}{14.75}} dt\right) + \log\left(e^{\frac{T_f-100}{14.75}} \Delta RT\right) \tag{22}$$

From this work, it can also be stated that the value of KSF for obtaining the maximum amount of biocrude changes according to the feedstock used (Figure 54). Proteins require a higher KSF due to their lower kinetics. Lipids do not significantly alter the resulting biocrude mass, but only at higher KSFs can triglycerides be hydrolyzed to fatty acids. Carbohydrates maximize biocrude yields at lower KSFs. Real biomass, on the other hand, exhibited a curve with a minimum at intermediate KSF levels. Further investigations are hence needed to understand if this trend could be due to some interactions between the biochemical families.

For all the reasons mentioned above, the use of 'fast HTL' is suggested for those feedstock (likely carbohydrate-rich ones) that show better performance at lower KSFs. Fast heating rates with high set-point temperatures and short residence times can indeed result in small KSFs and at a sufficiently high temperatures to maximize biocrude. On the other hand, 'isothermal HTL' could be more appropriate for feedstock requiring higher KSFs (protein-rich ones).

Chapter 5

Chemical recycling of multilayer plastic film

5.1 Introduction

The plastic packaging sector is the largest contributor to plastic waste generation, responsible for almost half of all plastic waste[34]. Plastics are well suited for the packaging industry due to their lightweight, reducing transportation cost and the amount of end-of-life waste[171]. Up to 84% of synthetic polymers used in the packaging market are thermoplastics[172]. The most common types are high-density and low-density polyethylene (HDPE and LDPE), polypropylene (PP), polystyrene (PS), polyvinylchloride (PVC), and polyethylene terephthalate (PET)[171]. The different polymers are used due to the different properties of packaging, e.g. to protect/preserve food, and merchandise, ease of transport and handling, etc.[173].

Multilayer materials are estimated to constitute 26% of all flexible plastic packaging and 10% of the total plastic packaging market by weight[174]. The great advantage of using multi-material multilayer is the possibility to combine different functionalities required for the correct conservation and transport of sensitive products, usually foodstuffs, in very thin films. Multi-material films are typically formed by two to nine layers[175] depending on the required properties. These usually include food compatibility, mechanical strength, heat sealability, gas/aroma and moisture barrier[176]. Together with versatility, the intrinsic characteristic of having multiple layers leads to an increased difficulty to apply common mechanical recycling techniques, which in practice hinders almost entirely their recyclability. Possible solutions to multilayer plastic recycling that have been suggested include chemical recycling via pyrolysis[177] and solvent based dissolution processes followed by mechanical recycling[178]. Both of these entail serious difficulties. Dissolution uses vast amounts of often toxic solvents, making large scale implementation difficult[35]. Pyrolysis is not recommended for PET valorization due to the fact that gas prevails among the generated phases, ranging between 50-75 wt.% and mostly constituted by CO and CO_2[179–182]. Moreover, the biggest issue associated to PET pyrolysis is severe clogging issues. Terephthalic acid and other similar generated molecules have a condensation temperature low enough to clogging inside the pipes[35]. Clogging issues were also observed with plastic mixtures containing PET[182]. For this reason, typically, the maximum fraction of PET in the feedstock that pyrolizers can withstand is 5%[183].

HTL could be a promising technology for valorizing this waste, and HTL performance strongly depends on the polymeric chains[62]. It is known that polymers with no heteroatoms in the carbon chain, such as polyolefins (LDPE, HDPE, PP) or PS, are inert in subcritical water condition (below 374 °C and 22.1 MPa) due to the absence of active sites for hydrolysis[63]. Under supercritical HTL conditions (>374°C) however, they can be converted into oil with high yields[63,184,185]. On the other hand, condensation polymers (e.g. PET, nylon, polyurethane) containing heteroatoms are easily hydrolyzed in subcritical conditions to their starting monomers[186]. However, if supercritical conditions are approached, monomer recovery could be affected due to their degradation[187].

To maximize the value of the recovered products, a two-stage HTL process for the chemical recycling of mixed plastic waste is proposed in this chapter. To this end, a case study using a real PET-LLDPE film was conducted, as PE and PET represent the two polymers most commonly found in multi-material multilayer films[188]. In the first stage, a subcritical step is used to recover monomers from condensation polymers, namely ethylene glycol (EG) and terephthalic acid (TPA) from the PET layer, while the recalcitrant PE are left unconverted. The aim of the second stage was then the conversion of the PE into oily and gas hydrocarbons. Different operating conditions (425-475 °C, 60-120 min) were tested to optimize the conversion of PE by using pure LDPE as feedstock. A basic block diagram depicting the overall work flow is shown in Figure 55.

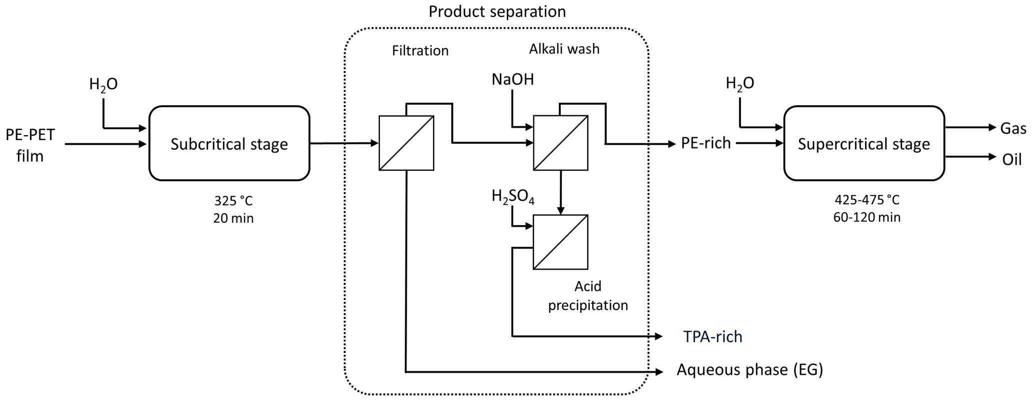

Figure 55: Block diagram for the two-stage HTL.

The results reported in this chapter are based on a published work[189].

5.2 Results and discussion

5.2.1 Feedstock composition

FTIR spectra of the feedstock showed that one side of the film was made of PE while the other side was made of PET (Figure 56).

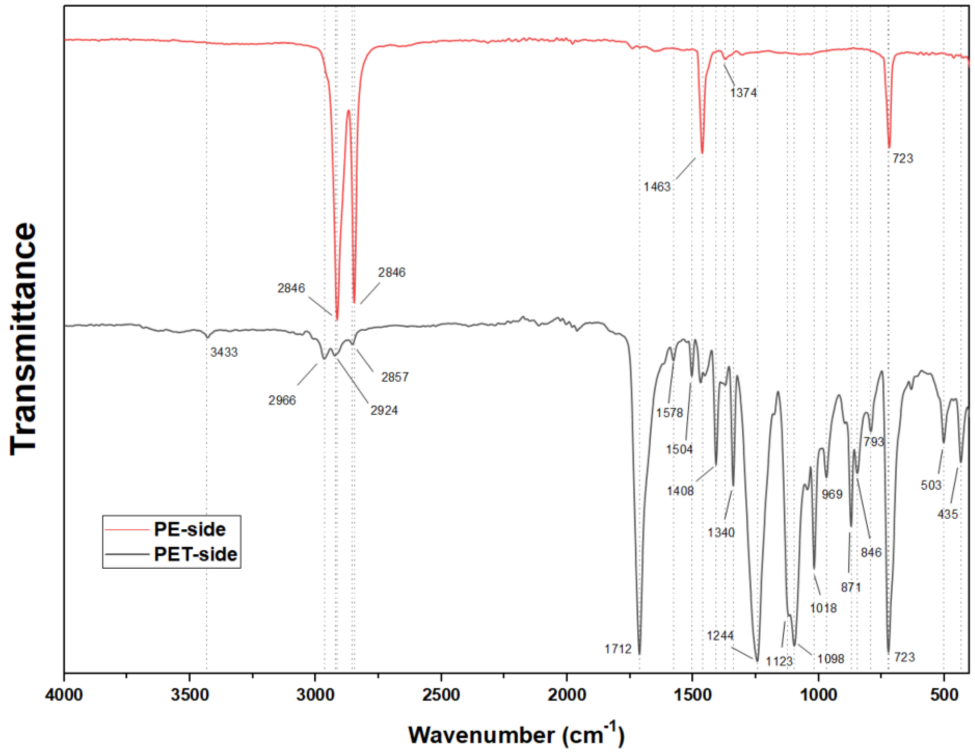

Figure 56: FTIR spectra of both sides of the multilayer film.

In Figure 57 the TGA and DSC of the PE-PET feedstock are shown. The lower shoulder around 392 °C is due to PET decomposition while the big peak at 441 °C is due to LLDPE decomposition. Compared to literature[190,191] these peaks resulted at lower temperature due to the much lower heating rate used in this work. The weight composition based on TGA analysis of the multilayer film is shown in Table 3. The ashes could be attributed to pigments used as dyes, while the remainder could be attributed to other additives or adhesives[35].

Table 3: Multilayer composition evaluated by TGA.

	PET	**PE**	**Other**	**Ash**
Composition (wt.%)	17.2	73.0	8.3	1.5

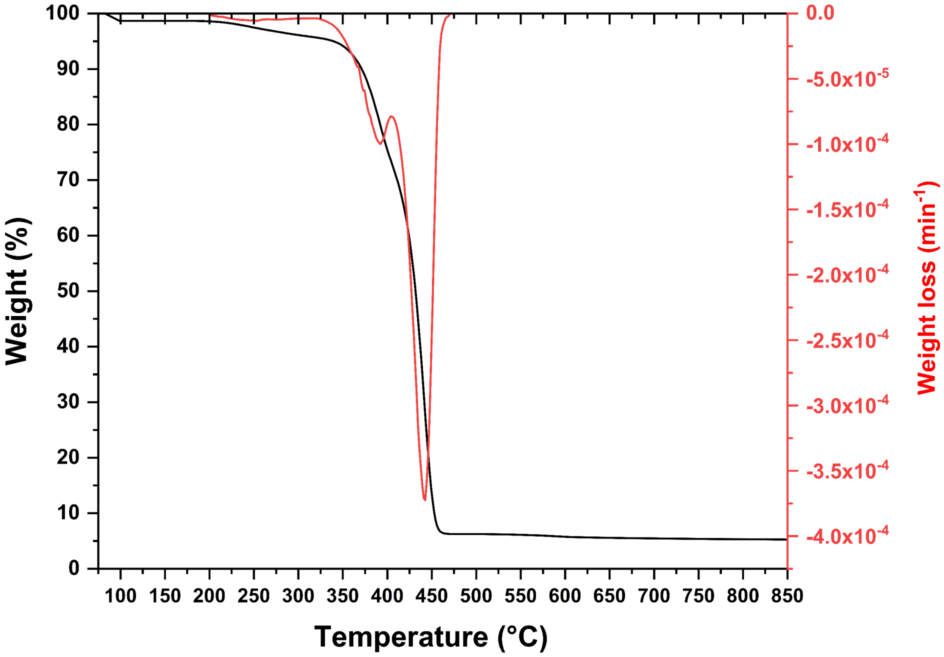

Figure 57: TGA (black line) and DTG (red line) of the PE-PET feed.

5.2.2 Subcritical stage

Mass yields

Figure 58 shows the yields obtained after the subcritical stage at 325 °C for 20 min while in Figure 59 the two solid products, as well as the feedstock, are shown as photographs.

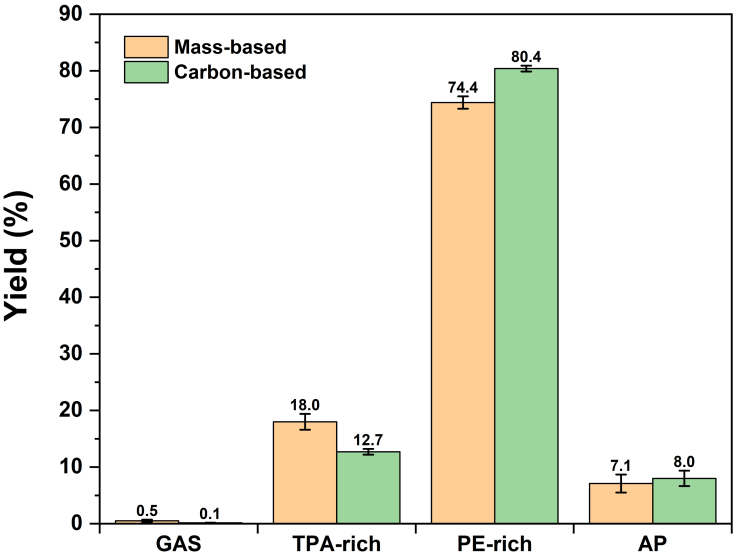

Figure 58: Mass yields obtained from the PE-PET multilayer after the subcritical stage. Orange bars refer to mass-based yields, while green bars refer to carbon-based yields. Reaction conditions: 1.8 g PE-PET film, total mass of 9 g, 325 °C, 20 min.

The PE-rich phase was the most produced product due to its higher initial amount compared to the other constituents. It is noteworthy that the yield of PE-rich phase was comparable to the initial amount of PE (Table 3). Its color shifted from blue of the starting film (Figure 59-A) to green-like (Figure 59-B); this change in color suggested a degradation of the colorant additives present in the starting feedstock. Almost all PE input in the first step was recovered in the PE-rich (98%) with high purity (96%) (Table 4). Polyolefins are well known to be recalcitrant in subcritical HTL due to the absence of heteroatoms in the structure[62]. The same is observed here, as the PE melted under subcritical conditions and resolidified into a plastic cluster at room temperature.

The TPA-rich phase was recovered with a TPA purity of 78% and a TPA recovery of 94%. Some of the impurities present in the TPA-rich phase could be attributable to residual organics, as only 7% of the ash was detected in the TPA-rich phase by TGA. The TPA-rich phase showed a yellowish color (Figure 59-C) that differed from the white color of pure TPA. A difference in color was also observed by Mancini & Zanin between commercial TPA and TPA recovered after HTL treatment of post-consumer PET waste[192].

Simultaneously with the formation of TPA there should be an equimolar production of ethylene glycol (EG) from PET hydrolysis. However, the EG recovery in the aqueous phase was equal only to 47%. Yamamoto et al. were able to recover up to 70% of EG from PET with operating temperature between 250 °C and 300 °C[193]. Only 53% of the carbon registered in the AP was attributable to EG. The presence of other carbon in the AP other than the EG and the lower yields of EG compared with TPA is likely due to the fact that the EG is prone to be further degraded, forming mainly acetaldehyde, followed by 1,4-dioxane and diethylene glycol[186,187]. 1,4-dioxane, acetaldehyde, benzoic acid and acetic acid concentration in the aqueous phase after reaction were estimated through GC-FID. However, apart from 1,4-dioxane (1.4 ± 0.2 %), their carbon yields were negligible (<0.25%).

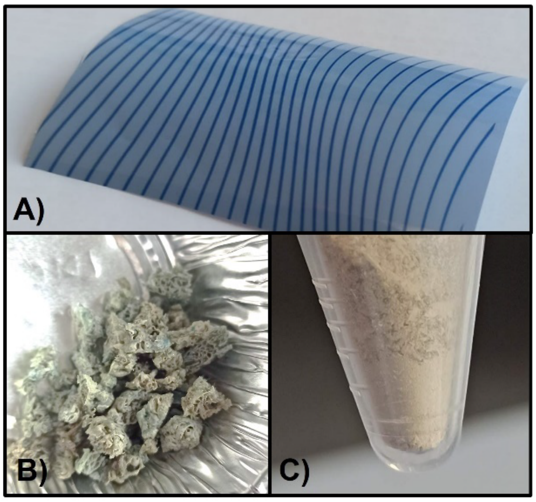

Figure 59: (A) Multilayer film, (B) PE-rich phase and (C) TPA-rich phase.

Table 4: Purity and yields for TPA-rich, PE-rich and AP obtained after the subcritical stage. Reaction conditions: 1.8 g PE-PET film, total mass of 9 g, 325 °C, 20 min. *EG quantified in the AP.

	TPA-rich	**PE-rich**	**EG***
Purity (wt.%)	77.6 ± 4.5	96.1 ± 0.4	53.2 ± 16.9
Recovery (%)	94.1 ± 12.6	98.0 ± 1.8	47.3 ± 7.0

Elemental composition

In Figure 60 the elemental analysis of feedstock, PE-rich and TPA-rich phases are reported. The multi-material multilayer film has a carbon-rich structure, comprising 78% carbon. This composition is quite similar to the theoretical elemental composition of a polymer consisting of 81 wt.% PE and 19 wt.% PET. The PE/PET ratio of 81/19 is the same that was evaluated for the multilayer film (73/17) in Table 3, without accounting for the remaining 10 wt.%. It follows that the discrepancies between the actual film and a theoretical film made only of PE and PET in the ratio 81/19 (PE81%-PET19%) are attributable to the 8.3 wt.% additives in the film. They consist of materials with a low carbon content and a higher oxygen content. The PE-rich phase had an elemental composition very close to the theoretical one of PE (Pure PE in Figure 60) as suggested by its very high purity and yield (Table 4). However, it contained a slightly higher hydrogen concentration, resulting in a H/C molar ratio comparable with the theorical value (2.3 instead of 2.0), and not oxygenated. The absence of oxygen is interesting as it indicated that no residues from PET or TPA were left in the solid residue after alkali wash, and no oxygenation of PE took place during subcritical HTL. The elemental composition of the TPA-rich phase slightly differed from values obtained in previous studies from PET alone[62,94], which were similar to the theoretical value for TPA (Pure TPA in Figure 60). In this chapter, the hydrolysis of PET by HTL was carried out in the presence of polyolefins, which did not convert. For this reason, the solid TPA was present in the solid blob of melted polyolefins and had to be extracted through alkaline washings and then precipitate with a change in pH. On the other hand, previous studies[62,94] working with isolated PET, were able to obtain the purified TPA directly as a reaction product. It is therefore possible that the added stage used here slightly affected the elemental composition of the TPA-rich solid. It is worth noting that the alkaline wash used in this chapter to recover TPA was due to laboratory-scale experiments. In fact, the concept here propose would involve separation under subcritical conditions to recover TPA. On an industrial scale, hot water at about 250 °C is usually used to solubilize TPA[194,195], so a separation step under subcritical conditions would allow separation of the PE-rich solid phase from the purified TPA without the need for an alkali wash. The TPA-rich phase targeted during the subcritical step is similar to what is called crude TPA in petrochemistry[195], which requires an additional purification step prior to polymerization in PET. This step is usually performed according to the AMOCO process, which involves the solubilization of crude TPA in water at high temperatures (> 260 °C), hydrogenation of impurities over Pd catalyst, and the crystallization of purified TPA in a series of crystallizers[196].

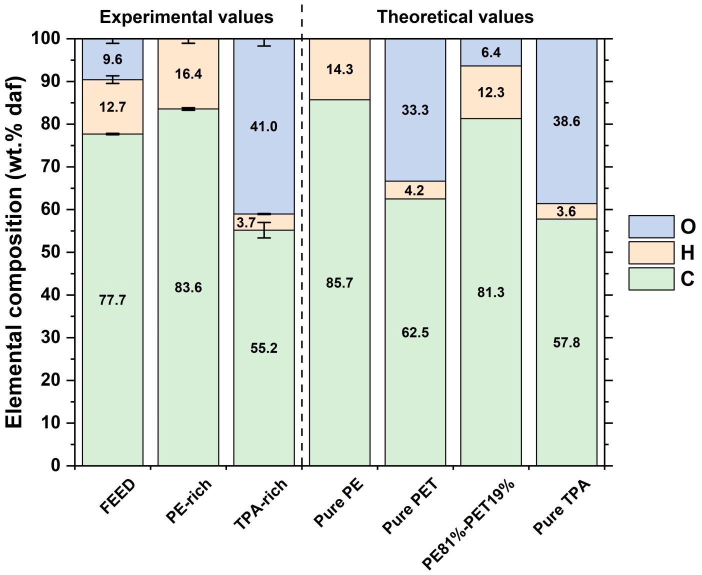

Figure 60: Elemental analysis (daf basis) of feedstock and products after the subcritical stage (FEED, PE-rich, TPA-rich) and pure compounds used for comparison purposes (Pure PE, Pure PET, PE81%-PET19%, Pure TPA). Reaction conditions: 1.8 g PE-PET film, total mass of 9 g, 325 °C, 20 min.

FTIR

The FTIR spectra of the PE-rich and TPA-rich solid are shown in Figure 61. Looking at the PE-rich phase, some differences are evident compared with the PE-layer spectra. A new prominent peak appeared at 1430 cm^{-1} attributable to C-H bending vibration of -CH_3 groups, which usually has a medium intensity; it proves a consistent increase of methyl groups in the PE-rich phase that corroborates the higher H/C registered; it could be due to the hydrolysis of the chemical bonds present on the contact surface of the multilayer film. Another peak occurred at 880 cm^{-1}, attributed to geminal C-H bending vibration of alkenes[197]. This peak is usually of strong intensity, while the other peaks generally attributed to alkenes were not visible, so it is possible that few alkene groups were formed within the solid. As observed from the elemental analysis, no oxygen-containing groups were detected. This result is in contrast to the previous work by dos Passos et al.[62], which observed the signal of carbonyl groups and no peak at 1430 cm^{-1} and 880 cm^{-1} in the solid obtained after HTL of pure HDPE and LDPE at 20 min at 350 °C. The absence of oxygen could be ascribed to the lower temperature (325 °C) used in this work, while the presence of methyl and olefinic groups could be attributed to the higher reactivity of the contact surface within the multilayer film requiring the recombination of the chemical bonds. The FTIR spectrum (Figure 61) of TPA corresponds well to those reported in literature with pure TPA[94,198], as well to the TPA standard analyzed for comparison purposes. This result seems to contradict the 78% purity evaluated by DSC. Thermogravimetrically, a value similar to the one obtained by DSC was recorded (82%). For this reason, the purity determined by DSC can be considered reliable. The high resemblance between the TPA-rich phase and the TPA standard can be attributed to the limited depth of analysis by ATR-FTIR, which only examines a few micrometers, rendering it not fully representative of the entire sample. Additionally, impurities with comparable functional groups (such as carboxylic acids or esters) may coexist in the TPA-rich phase without significantly altering the overall spectra.

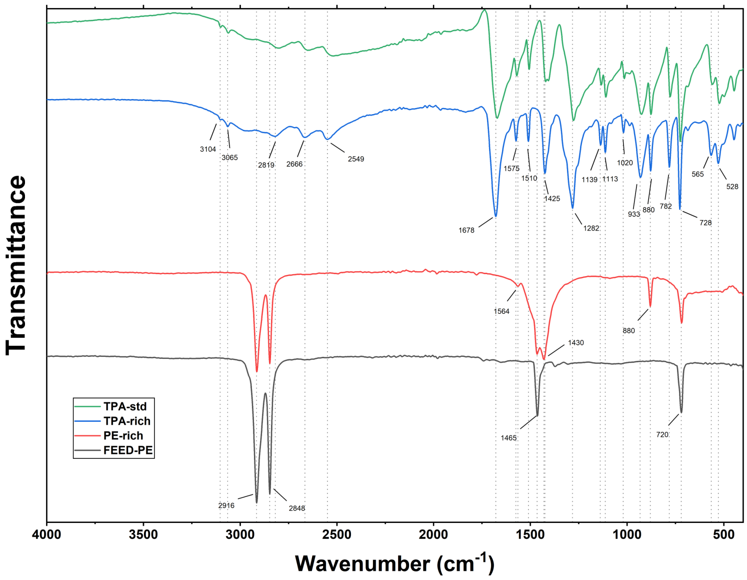

Figure 61: ATR-FTIR spectra of TPA-standard (green), TPA-rich phase (blue), PE-rich phase (red) and starting PE layer (black).

5.2.3 Screening of optimal conditions for PE conversion

Before performing the supercritical stage with the PE-rich sample recovered from the subcritical stage, a preliminary assessment with pure LDPE was carried out to find the optimal conditions of residence time (60-120 min) and temperature (425-475 °C). A face-centered central composite design (α=1) with 2 factors and 3 levels was designed for response surface methodology (RSM). The star and factorial points were run in duplicate, while the central point was run five times, resulting in 21 different tests. Predictive models for oil and gas yields as a function of temperature (T, °C) and residence time (t, min) were derived on Design Expert®, based on Eq. (23). The predictive models for oil and gas phase are given in Eq. (24) and Eq. (25). The analysis of variance (ANOVA) for oil and gas phase showed that the models were highly capable of predicting yields with a relatively low bias.

$$Yield_{wt.\%}\,(T,t) = a + \sum_{i=1}^{2} b_i \cdot T^i + \sum_{i=1}^{2} c_i \cdot t^i + d \cdot Tt \tag{23}$$

The contour plots resulting from the response surface methodology (RSM) are shown in Figure 62. The oil yield showed a maximum with varying temperature and residence time (Figure 62-A); in particular, temperature variations had the biggest influence on the oil yield, while the effect of residence time was most easily observed for higher temperatures (T > 450 °C). The strong dependence of HTL performances on temperature was expected, as it is well-known that temperature is the most important parameter for HTL[38,67]. The maximum oil yield was predicted to be around 456 °C and 83 min, with an expected oil yield of 54%. Differences between experimental oil yields obtained at 450 °C, 90 min and 456 °C, 83 min were within the experimental errors (Table 5).

$$Oil\ yield\ (wt.\%) = -9.120 \cdot 10^3 + 3.9583 \cdot 10^1\,T + 3.5148\,t - 5.883 \cdot 10^{-3}\,tT - 4.2847 \cdot 10^{-2}\,T^2 - 5.144 \cdot 10^{-3}\,t^2 \tag{24}$$

$$Gas\ yield\ (wt.\%) = -9.0955 \cdot 10^2 + 3.7789\,T - 1.6157\,t + 2.967 \cdot 10^{-3}\,tT - 3.724 \cdot 10^{-3}\,T^2 + 2.025 \cdot 10^{-3}\,t^2 \tag{25}$$

Table 5: Experimental yields obtained with pure LDPE.

	450 °C, 90 min	456 °C, 83 min
Oil yield (wt.%)	52.2 ± 4.1	49.1 ± 0.4
Gas yield (wt.%)	27.8 ± 0.9	34.0 ± 2.0
Solid yield (wt.%)	2.1 ± 0.2	0.3 ± 0.2

At low temperatures (~ 425 °C), oil production was limited due to low conversion of LDPE, as observable from the high solid residue (Figure 62-C). With increasing temperature, depolymerization was favored, resulting in increased oil. However, at the same time as the oil, the gas phase was also increased. Depolymerization of LDPE in supercritical water occurs through free-radical random chain scission that leads to the formation of shorter hydrocarbon-like structures[63]. Depending on the ultimate length, these molecules under ambient conditions form solids, waxes (C_n >25), liquids (25 >C_n >5) or gases (C_n<5). At more severe conditions, the decomposition of hydrocarbons increasingly pronounced, leading to an increment of gaseous compounds that do not repolymerize. For this reason, the gas yield showed a constant upward trend with temperature (Figure 62-B). Around 450-455 °C, the solid yield was almost zero while the yield in oil was highest, due to the trade-off between the decomposition of starting PE into oil and the further degradation of oil into gas. Residence time showed to have an effect only at temperatures higher than 450 °C. Under these conditions, an increase in reaction time strongly favored the conversion of oil primarily to gas.

Based on the RSM here discussed, the conditions of 450 °C and 90 min were chosen for the supercritical stage with the PE-rich phase.

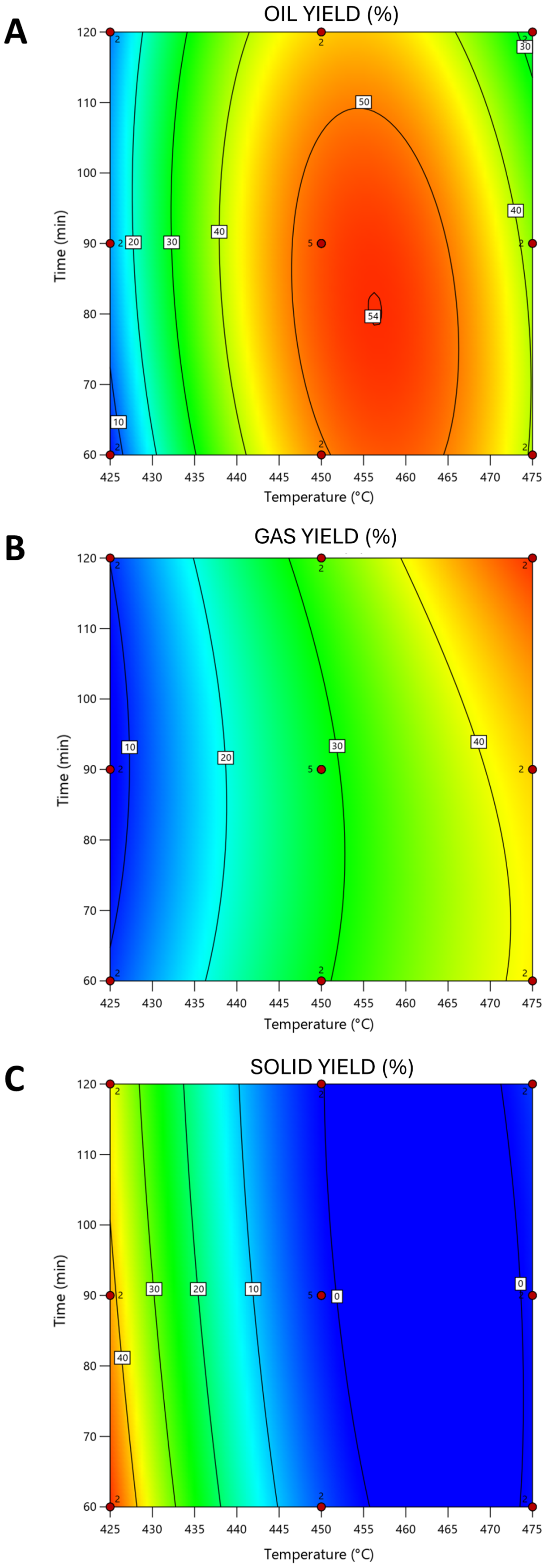

Figure 62: Contour plots for oil (top), gas (center) and solid yield (bottom).

5.2.4 Supercritical stage

Mass and carbon yields

The mass and carbon yields obtained under supercritical conditions (450 °C, 90 min) from the PE-rich phase are reported in Table 6. Yields using the PE-rich phase were similar to the ones obtained from pure LDPE (Table 5). It follows that the previous presence of PET in the multilayer did not have an impact on the reactivity of PE during the subsequent supercritical step. Surprisingly, the solid yield also closely matched the yield obtained from the pure sample. In fact, the real sample had an ash content of 1.9 ± 0.5 wt.%, which is probably the main reason for solid yields; hence a slightly higher solid yield was expected. Alternatively, the ash could be solubilized in the aqueous phase or in the oil, as observed for Na, Ca, Mg[162–164], some of the most common inorganic elements found in post-consumer plastic waste[94]. Due to the very low amount of solid produced, it was not possible to quantify the amount of ash present in the solid sample and its elemental composition. However, TGA analysis confirmed a limited ash content in the oil (lower than 400 ppm).

The carbon yield in the oil and gas phases during the PE-rich HTL were consistent with the mass yields. The sum of the carbon yields of gas and oil phases was found to be 76.2% (Table 6) while the remaining 23.8% was distributed among the other phases and losses during the work-up. As reported by Colnik et al.[185], the carbon yield in the aqueous phase for PE processing at similar conditions was less than 0.6%, and the carbon yield in the solid phase was also low due to the low mass yield reported here. Hence, it is likely that the missing portion was due to losses during the work-up, as volatile hydrocarbons found in oil and gas phases were easily lost due to very low boiling points.

Table 6: Mass and carbon yields obtained from the PE-rich phase after the supercritical stage. The difference between 100 and the sum of the phases is also represented. Reaction conditions: 464 mg PE obtained from subcritical stage, total mass of 1.39 g, 450 °C, 90 min.

	Gas	**Oil**	**Solid**	**Difference**
Mass yield (wt.%)	28.9 ± 2.0	46.8 ± 4.7	2.1 ± 1.5	22.1 ± 8.2
Carbon yield (C%)	27.3 ± 6.3	48.9 ± 5.5	NQ	23.8 ± 11.8

Gas composition

The gas phase was composed of short hydrocarbons, as can be seen from the gas composition reported in Table 7. Methane was the most abundant gas, accounting for almost a third of the total gas, while 79% of the total composition was made up of normal linear saturated alkanes. In addition, 6.5 vol.% of H_2 and 2.0 vol.% of CO_2 were identified. The presence of CO_2 was connected to the fact that the atmosphere inside the reactor was not inert before the reaction, resulting in oxidation of hydrocarbons by the residual oxygen. This can be further substantiated by the fact that the amount of CO_2 produced after reaction corresponds to the molar amount of oxygen left in the reactor before the reaction. It is hence possible to conclude that in the industrial implementation of this concept, there will be no CO_2 and that the higher heating value of the generated gas would be slightly higher than the 50.2 MJ/kg (60.8 MJ/Nm^3) calculated here.

Table 7: Compositions obtained after HTL at 450 °C for 90 min of the PE-rich phase.

Composition	%vol.	±
H_2	6.5	1.2
CO_2	2.0	0.6
Methane	30.7	2.9
Ethene	2.2	0.5
Ethane	27.4	3.4
Propene	6.3	1.2
Propane	16.0	2.1
Butane	3.8	0.6
Other C4s	2.8	0.5
Pentane	1.0	0.6
Other C5s	0.4	0.2
Hexane	0.2	0.2
Other C6s	0.1	0.2
TOT	**99.5**	**14.2**

Oil elemental composition

The oil phase was the highest yielding product, reaching 47 wt.% of the starting feedstock. Most of the oil (~90%) was recovered directly after the centrifugation of the liquid contained in the reactor (Figure 63), while the rest was collected through extraction with acetone. The oil was a very dark-brown liquid, with low viscosity and high volatility (Figure 63). The elemental composition was 87.3 ± 0.7 wt.% C and 12.7 ± 0.2 wt.% H, resulting in the empirical formula $C_nH_{1.7n}$. No oxygen was found, meaning that no oxygen from water was incorporated in the oil, as would be expected from the thermal decomposition through free-radical chain scission of polyethylene[199]. However, the oxygen content was evaluated by difference from the carbon and hydrogen contents and an uncertainty of ± 1% was associated to its quantification. Slightly higher values were estimated by Lu et al. (2022), obtaining an oil with 2.3 wt.% oxygen after HTL at 450 °C for 4 h from HDPE[200], while Chen et al. converted polypropylene at the same conditions used in this chapter obtaining an oil with less than 0.6 wt.% of oxygen[201]. The HHV of the oil was evaluated as 45.4 MJ/kg, hence in the range of diesel. As also observed in literature[63,200,201], the oil produced from supercritical HTL of polyolefins has a very high heating value that makes it suitable not only as fuel but also as a feedstock for chemical production. The advantage in HTL oil quality from polyolefins stands out when comparing the HHV with HTL oils obtained from biomass[45].

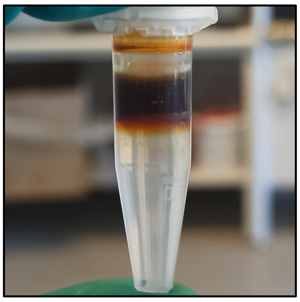

Figure 63: Aqueous phase (bottom) and oil (top) obtained after HTL at 450 °C for 90 min of the PE-rich phase.

Boiling point

The boiling point distribution of the oil assessed by TGA is shown in Figure 64. The boiling points were divided into light naphtha (30-90 °C), gasoline (90-200 °C), kerosene (200-270 °C), diesel (270-320 °C) and heavy oil (>320 °C). Most of it was in the naphtha-gasoline range, making it suitable as a steam cracker feedstock, since this is the predominant feedstock used for steam cracking in Europe and Asia[202]. The high gas yield registered in Table 6 is hence explained by the fact that the PE was cracked down into small molecules with carbon number lower than 12 and that, according to their boiling points, ended up as part of the gas or oil phase. However, it is very likely that the amount of naphtha was underestimated due to losses during work-up, favored by the low amount of feedstock used for the reaction, which led to the missing mass in Figure 64, and during the TGA, as the high volatility was clearly visible, leading to the underestimation of light naphtha. A similar boiling point distribution was also observed by Lu et al. after supercritical HTL of HDPE-based plastic waste at 450 °C for 4 h[200].

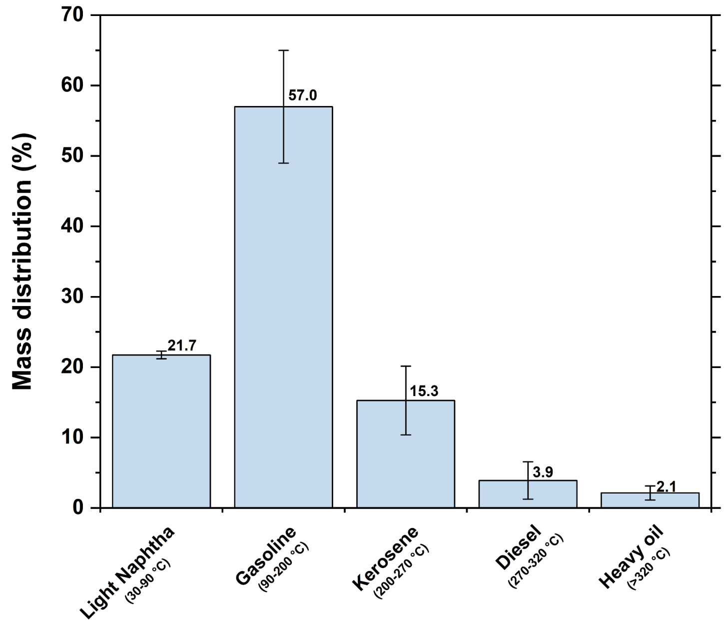

Figure 64: Boiling point distribution of the oil. Boiling points range: light naphtha 30-90 °C, gasoline 90-200 °C, kerosene 200-270 °C, diesel 270-320 °C and heavy oil >320 °C. Reaction conditions: 464 mg PE obtained from subcritical stage, total mass of 1.39 g, 450 °C, 90 min.

FTIR and GC-MS

FTIR of the oil phase is reported in Figure 65. The main peaks are attributable to a linear paraffinic structure. That is, alkane C-H stretching within 2955-2854 cm^{-1}, methylene C-H bending at 1455 cm^{-1}, methyl C-H bending at 1377 cm^{-1}, methylene C-H rocking at 725 cm^{-1} [203,204].

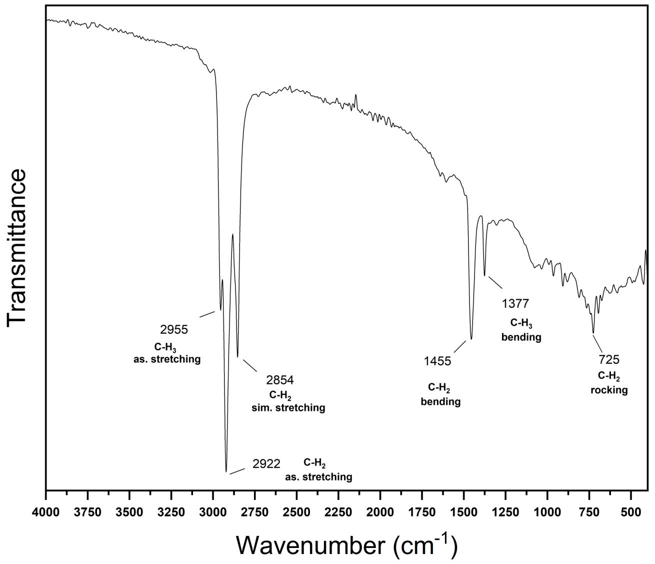

Figure 65: FTIR of the oil phase obtained after HTL at 450 °C for 90 min from the PE-rich phase.

The GC-MS spectrum of the oil is shown in Figure 66 while the chemical composition of the oil phase, expressed as the ratio of peak area to total integrated area, and differentiated by carbon number, is reported in Figure 67.

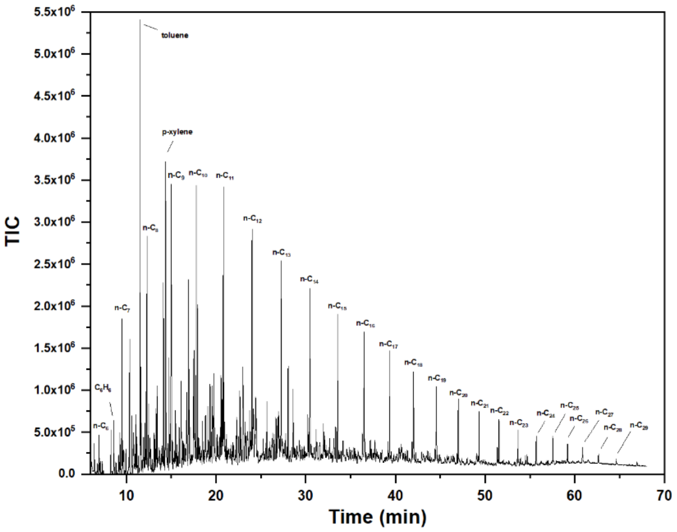

Figure 66: GC-MS chromatogram of the oil obtained from the PE-rich phase at 450 °C for 90 min.

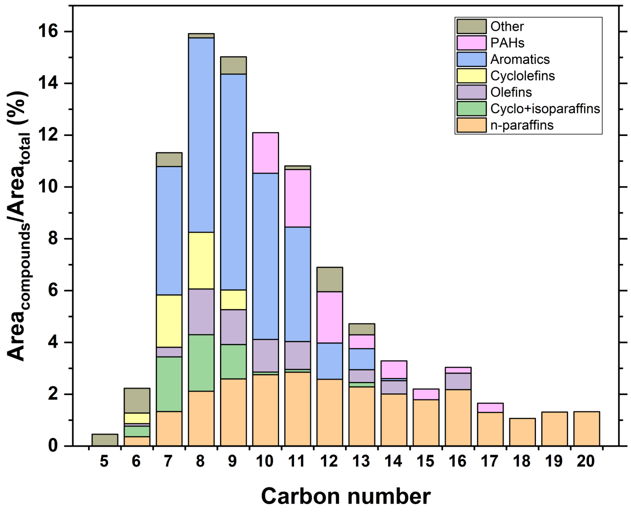

Figure 67: Composition of oil obtained after HTL at 450 °C for 90 min from the PE-rich phase. Data are expressed as a percentage of the area of each compound compared to the total integrated area.

The highest peak was associated to C8 compounds and 79% of the total chromatogram area was related to compounds with carbon number ranging from 7 to 12. The concentration of these compounds was mainly related to the large amount of aromatics recorded in this range. Most of them were alkylbenzenes, while a smaller part at higher carbon numbers was due to indane derivatives. Overall aromatics and n-paraffins represented the two most present group of molecules. Polycyclic aromatic hydrocarbons (PAHs) were mostly observed as alkylated derivatives of naphthalene, the simplest PAH. Cyclic paraffins were most favored at low carbon number, while iso-paraffins were very low. Olefins and cyclic olefins were recorded in smaller quantities than paraffins.

Although the ratio of peak area to total integrated area is usually used in literature to study the composition of oil from HTL, a quantification of the present compounds should be performed through external calibrations. From the calibrations, the overall concentration of n-paraffins (C6-C31), aromatics (BTEX and some isomers) and PAHs amounted to 30.9 ± 2.5, 9.4 ± 2.2 and 3.0 ± 0.7 wt.%. n-paraffins confirmed to be present in a high extent in the oil but, as can be seen from Figure 68, the carbon distribution was shifted towards lower values than those shown in Figure 67. The amount of aromatics appeared limited compared to Figure 67, also due to the limited amount of compounds tested, especially indane-derivatives.

The conversion of PE during supercritical HTL occurs through a random chain scission that converts the polymer into linear radical chains[199]. These free-radical fragments are subsequently converted via β-scission into olefins plus smaller radicals, which can react with other radical fragments to form linear paraffins[184]. The formation of olefins by β-scission was confirmed in this chapter by the fact that almost all olefins identified by GC-MS were α-olefins. Paraffins can then be further reduced in size through the same mechanisms, up to the point of forming gaseous compounds; olefins, on the other hand, tend to polymerize forming cyclic structure that eventually can produce more stable aromatics through dehydrogenation[199]. The occurrence of these pathways was confirmed by the high amount of linear alkanes, the low concentration of iso-alkanes, the presence of olefins, cyclic compounds and aromatics. Moreover, the high amount of aromatics, along with the limited amount of olefins in both oil and gas phase, and the low boiling point of the oil confirmed a high progress within the pathway.

The paraffinic-rich composition of the oil, together with a higher amount of n-paraffins than iso-paraffins and a naphtha-like boiling point, makes it an interesting feedstock for steam cracking, as well as the paraffinic gas phase[64]. Thus, olefins needed for virgin polymer production could be produced from this recycled oil phase. Kusenberg et al. tested the use of pyrolysis oil obtained from PE film as feedstock to steam cracking in co-feeding with fossil naphtha[205]. Ethylene production and char formation were higher than those obtained from fossil naphtha alone. However, compared to the HTL-derived oil obtained in this chapter, the pyrolysis-derived oil from PE had a higher boiling point that gave it a wax-like appearance[205,206]. Kusenberg et al. hence also proved the possibility of using the naphtha fraction obtained after the distillation of pyrolysis oil from real plastic waste as the sole feedstock for steam cracking[207]. Despite some differences in the composition of the oils, in particular the higher presence of unsaturated compounds in pyrolysis oil, the naphtha fraction obtained from pyrolysis oil should be closer to the oil obtained in this work. For this reason, good performance in steam cracking is likely with the oil produced through HTL.

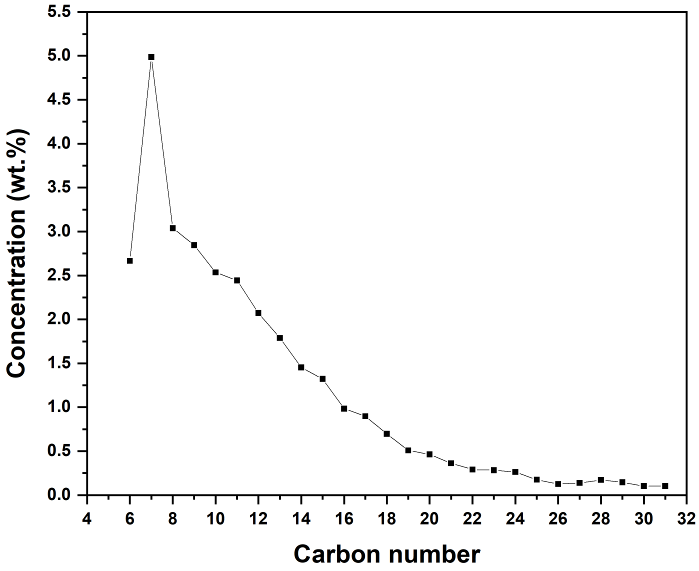

Figure 68: n-paraffins concentration (wt.%) in the oil obtained after HTL at 450 °C for 90 min from the PE-rich phase.

5.2.5 Overall performances

Figure 69 shows the mass distribution to the different phases after the subcritical and supercritical stages. As described earlier in Paragraph 5.2.2, following the subcritical stage, the mass yields among the phases quite accurately reflected the initial composition of the multilayer film. Therefore, it is reasonable to assume that changing the feedstock to a film with different proportions of PE-PET would alter the mass distribution accordingly. After conversion of the PE-rich in the supercritical stage, a gas phase, an oil and a low amount of residual solid were obtained.

The overall yields from the starting feedstock were 21.5 wt.% and 34.8 wt.% for the gas and oil phase, respectively, while their overall energy recoveries were 26.8 % and 39.2%. Moreover, the losses in the Sankey diagram, were more than likely light hydrocarbons lost during the sample work-up procedure, as discussed previously. For this reason, it is likely that up to 72.8% of the mass of the starting feedstock ended up as gaseous/oily hydrocarbons. In terms of chemical recycling, these streams could be used in the petrochemical industry as feedstock for a steam cracker to produce new olefins. Indeed, 63 wt.% of the light hydrocarbons forming the gas phase were alkanes, excluding CH_4, which are suitable for conversion into olefins. On the other hand, the lighter portion of the gas phase could be separated to have a stream of CH_4 and H_2 that could be burned (2 MJ/kg film) to partially meet the thermal energy demand of the plant. The separation between light hydrocarbons and the CH_4-H_2 stream could be performed through a train of distillation columns similar to those necessary for downstream separation of hydrocarbons produced after steam cracking of naphtha[202]. Therefore, if the HTL plant was built next door to a steam cracking unit, it would be possible to exploit its separation units for separating these two streams. Concerning the oil, at least 31 wt.% of it was formed by n-paraffins (mainly C6-C15), making it an interesting feedstock for the steam cracking unit.

From the subcritical step, 18 wt.% of the multilayer film was converted into a TPA-rich phase. It is worth emphasizing that, while in this chapter an alkali wash was necessary to separate the TPA-rich phase from the melted PE-rich phase, given the lab scale, in an industrial implementation of this process the separation would be engineered to be performed directly under subcritical conditions. Indeed, TPA is soluble in subcritical water[208], and a separation under these conditions would be more efficient, economical, and environmentally friendly. However, the subcritical separation process needs to be further studied and optimized in-depth. For this reason, although the TPA purity in the TPA-rich phase was 78 wt.%, this value could be affected by the separation technology used. The TPA-rich product can be then used by the petrochemical industry has a raw material for the production of TPA, limiting the use of fossil sources. Besides TPA, EG, PET's other monomer, was also produced by the HTL sequential process. However, EG was found in the aqueous phase obtained after the subcritical stage at a concentration close to 1 wt.% together with other water-soluble compounds. Although recycling EG back to the PET industry would be as interesting as recycling TPA, its low concentration might pose challenges from an economic perspective. However, if the starting feedstock has a higher PET concentration, the EG concentration is expected to be higher, thus making recovery feasible. One potential method of recovery could be reactive distillation with acetaldehyde, which produces acetals with boiling points lower than water, facilitating their separation by distillation and reducing energy costs[209].

In the event that the recovery of EG is not economically feasible, a potential valorization pathway could involve its catalytic reforming directly in the aqueous phase, following the aqueous phase reforming (APR) process. Indeed, APR of EG showed 100% conversion and hydrogen yield of 85% at 270 °C over Pt/Al_2O_3[210]. In this scenario, the advantage could stem from conducting APR immediately after the separation of phases while maintaining the temperature, thus avoiding thermal expenditures.

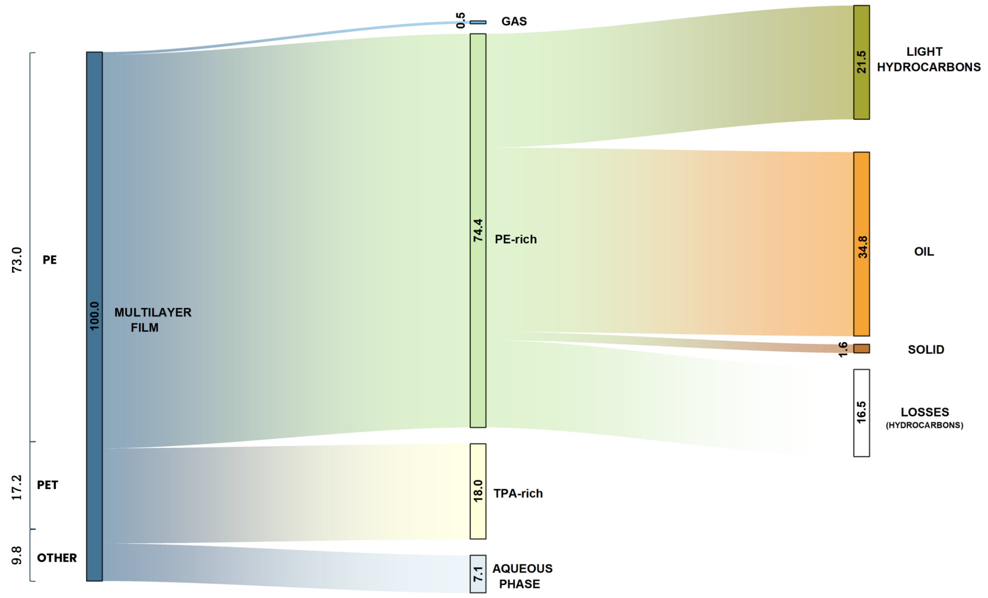

Figure 69: Mass distribution between the different phases after subcritical (325 °C, 20 min) and supercritical stages (450 °C, 90 min).

5.3 Conclusions

This chapter presented a two-stage HTL process for chemical recycling of multi-material multilayer plastic films. The study was carried out using a LLDPE-PET film but the concept can likely be expanded to many if not most multi-material plastic films. Through the first subcritical stage, it was possible to completely hydrolyze PET and recover its monomers, namely terephthalic acid (TPA) and ethylene glycol. The residual polyolefin did not show any substantial degradation after the first stage, it just melted and resolidified after cooling. The residual PE can be valorized by the second HTL stage under supercritical conditions. At the optimized operating conditions of 450 °C and 90 min it was possible to completely convert all the PE by obtaining a gas and oil phase. The gas phase consisted mostly of saturated alkanes, and can be used as feedstock for steam cracking to produce olefins required by the plastics industry. In this way, a chemical recycling loop would be created. The oil phase had a boiling point distribution comparable to light naphtha-gasoline, a composition rich in n-paraffins and aromatics and no oxygenation. For the technical implementation of this technology, further research should be conducted for the integration of the two stages (subcritical and supercritical) from a thermal and product separation perspective.

Chapter 6

Valorization of polyvinyl chloride

6.1 Introduction

Poly (vinyl chloride) (PVC) is currently the third most produced polymer worldwide[211], and in 2015 the PVC waste reached 15 Mt/y, mainly linked to the building and construction sector, which requires 69% of the overall PVC produced[34]. Furthermore, PVC is typically the third most present plastic in the organic fraction of municipal waste[212] and in mixed waste for incineration plants[213]. Given its pervasive presence, addressing PVC waste has become imperative.

As previously described, plastic recycling through chemical pathways is currently gaining interest. However, in the case of thermochemical technologies, dealing with even a small quantity of PVC within the plastic mix poses significant technical challenges[35]. Indeed, PVC is a halogenated polymer, consisting of a carbon chain containing chlorine side groups that account 57 wt.% of the overall mass. The release of chlorine during the recycling process results in a substantial increase in acidity, making the reaction environment highly corrosive. This corrosiveness can significantly reduce the operational lifespan of facilities[188], especially under the demanding conditions of incineration and pyrolysis and supercritical HTL, due to the so-called high temperature chlorine corrosion[214]. Additionally, the presence of chlorine-containing compounds in the resulting oil hampers its subsequent utilization[215]. Hence, the prospect of employing a preliminary treatment step to eliminate chlorine from mixed plastic waste emerges as a compelling avenue. This approach could facilitate the subsequent chemical recycling of the waste using a more intensive process.

The pretreatment step could be performed in subcritical environment. As heteroatoms-containing polymers (e.g. PET, nylon, polyurethane) can be easily hydrolyzed already in subcritical conditions[186,189], it has been observed that PVC at low loadings (~0.15 wt.%) can achieve complete dechlorination in water at around 240 °C[216], resulting in a solid phase with low residual chlorine and an acidic aqueous phase rich in HCl[62,217]. The high acidity of the aqueous medium, besides posing a threat to the material used for the construction of the reactor[218,219], could also be the reason why the production of solid from PVC is predominant in hydrothermal environment and no oil is recovered[62]. Indeed, acidity is well recognized in HTL for increasing the solid yield due to dehydration and repolymerization reactions[220]. For this reason, alkali additives (NaOH, KOH, K_2CO_3) were tested during subcritical dechlorination of PVC[219,221,222]. The results showed that the use of a basic additive could be beneficial for the dechlorination efficiency especially at low reaction temperature. Nevertheless, it was observed that an excessive amount of alkali diminished the positive effect[222]. However, these observations were performed with sub-stoichiometric amounts of additive, and very limited information exists regarding reaction kinetics when employing stoichiometric amounts of base to neutralize all chlorine-derived acidity. Moreover, it would be beneficial to have a neutralizing agent that could decrease the corrosivity of the aqueous media through pH control, and that the chlorine salt of the base used could be easily recovered downstream of the reaction process.

In this chapter, a two-stage hydrothermal process to valorize plastic waste with a high concentration of PVC is proposed. This innovative process involves a first step in subcritical conditions, taking advantage of PVC's propensity for dechlorination in hydrothermal environment, targeting in a dechlorinated solid and an aqueous phase containing HCl. Experiments were conducted with pure PVC at high loadings (20 wt.%) with and without the addition of an equimolar amount of KOH. The effects of temperature and the use of KOH were studied, focusing on mass yields, residual chlorine, as well as solid properties. The reaction mechanism during the subcritical stage were investigated, emphasizing the differences in reaction pathways between the presence and absence of a basic additive. In particular, the activation energy for both the neutralized and non-neutralized cases was evaluated.

After the subcritical stage, the valorization of the chlorine-free solid was tested through the more severe supercritical HTL. Pyrolysis of the dechlorinated was also investigated by Py-GC/MS to better characterize the structure of the dechlorinated solid, as well as to compare it with supercritical HTL and elucidate the role of water in solid degradation. During supercritical HTL, thermal breakdown of the dechlorinated solid was hypothesized to lead to the formation of lower molecular weight compounds forming an oil phase. This way, the two-stage hydrothermal process would enable the production of oil from PVC-containing waste.

The findings presented in this chapter are derived from a published work[223].

6.2 Results and discussion

6.2.1 Mass yields

In Figure 70 the yields of solid residue obtained after the subcritical stage are depicted. With the non-neutralized reactions, a decrease in the solid yield was observed with increasing temperature. At 200 °C almost all the solid remained unconverted, while most of the mass was lost between 225-250 °C. Hydrothermal dechlorination of PVC was already observed to take place below 250 °C[216,224], hence the solid loss in this range was attributed to this. By further increasing the operating temperature, the solid yield further decreased to 42 wt.% at 300 °C. This value corresponds to the theoretical solid yield obtained if a complete dechlorination was reached through the chlorine elimination pathway (Eq. (26)). For this reason, complete dechlorination was expected close to 300 °C. Moreover, the color of the solid shifted from the white of the virgin PVC, to yellowish at 200 °C, brownish at 225 °C and black from 250 °C and higher. This change in color is attributed to the formation of polyenes in the solid structure, as reported in literature[225] and according to Eq. (26).

$$-(CH_2 - CHCl)_n -\!\!\rightarrow -(CH = CH)_n - + n\,HCl \qquad (26)$$

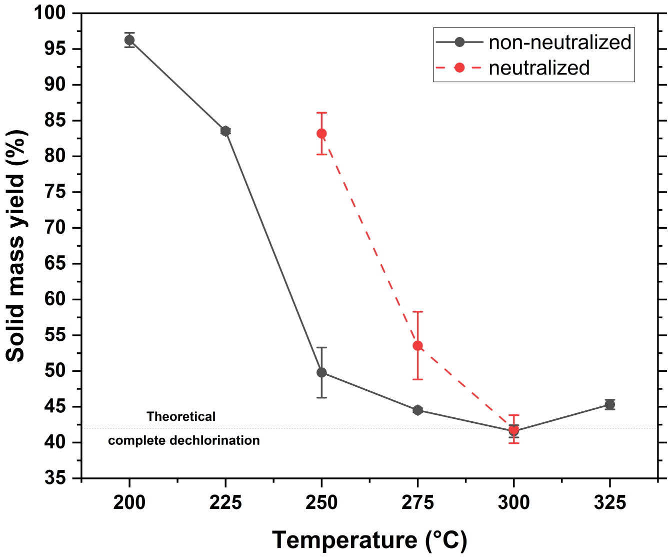

Figure 70: Solid mass yields obtained at different temperatures. Black solid line refers to non-neutralized reactions, red dotted line refers to neutralized reactions. Reaction conditions: 1.8 g PVC, 1.81 g KOH as basic additive in the case of neutralized reaction, total mass of 9 g, 20 min.

After the addiction of the basic additive (red line, Figure 70), the solid residue yield was higher than without at 250 °C and 275 °C. These differences are attributed to changes in the dechlorination mechanism, which could either decrease the efficiency of dechlorination or increase the incorporation of oxygen into the solid. However, at 300 °C the solid mass yield was equal to that of the non-neutralized reaction, representing the value that would be expected in the case of complete dechlorination via chloride elimination.

6.2.2 Elemental analysis

The elemental compositions of the solids obtained after the subcritical step are depicted in Figure 71. Already at low reaction temperatures, the presence of chlorine diminished significantly, being replaced by oxygen. This observation highlights chlorine's susceptibility to removal within hydrothermal media and underlines the crucial role of water molecules, which are responsible for the incorporation of oxygen atoms into the solid's structure. With increasing operating temperature, the chlorine content was further reduced, reaching 1.5 wt.% at 300 °C. Conversely, the carbon content increased from 39 wt.% in PVC to approximately 85-86 wt.% beyond 300 °C, aligning with expectations of a carbonized and aromatic solid, supported by its dark appearance. Upon introducing KOH, the carbon and hydrogen contents were reduced while oxygen and chlorine contents were higher compared to the non-alkali experiments. These differences were less pronounced with increasing temperature, but they validate a deterioration in the dechlorination reaction following the introduction of the base.

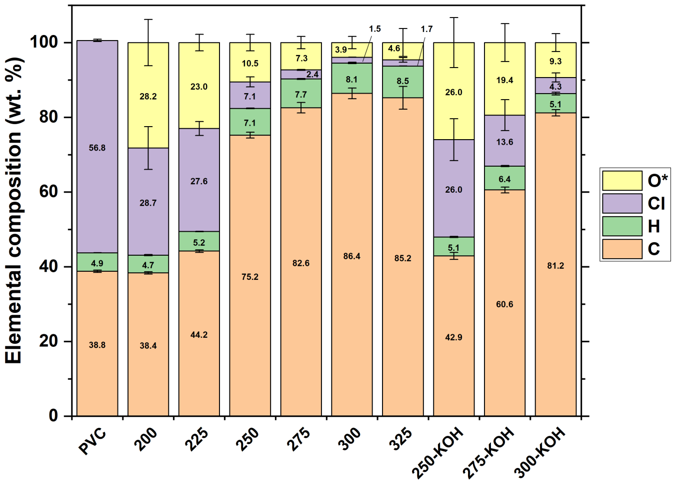

Figure 71: Elemental composition of the solids obtained after subcritical step. Reaction conditions: 1.8 g PVC, 1.81 g KOH as basic additive in the case of neutralized reaction, total mass of 9 g, 20 min. *Oxygen has been evaluated by difference. Each sample is named after the operating temperature at which it was produced. 'KOH' was added to the name of neutralized reactions.

Focusing on the elemental recoveries in the solids presented in Table 8, it is remarkable that carbon exhibited nearly complete retrieval across all tested temperatures. Specifically, carbon recovery spanned from 94% to 99% for non-neutralized reactions, and from 84% to 92% for neutralized reactions. Conversely, chlorine recovery decreased with increasing temperatures, resulting in notably low values: 1.1% at 300 °C without KOH and 3.1% with KOH. Consequently, the dechlorination efficiencies, which complement the chlorine recovery in the solid, were high and amounted to 98.9% and 96.9%, respectively. These outcomes were quite satisfactory due to the substantial limitation of carbon losses to other phases, most likely the aqueous phases, and the nearly complete elimination of undesired chlorine from the solid residue.

The higher heating value (HHV) of the solid samples increased with increasing temperature. For instance, the HHV progressed from 19 MJ/kg for PVC to 39 MJ/kg at 300°C without KOH, and 33 MJ/kg with KOH (as detailed in Table 8). This enhancement is attributed to the carbon-rich structure and the relatively low presence of heteroatoms. On the other hand, at lower temperatures, the incorporation of oxygen atoms into the solid structure resulted in a decrease in calorific properties compared to virgin PVC. The fixed carbon also increased as the reaction temperature increased, moving from 8% of virgin PVC up to 54% at 300 °C, explaining the increasing carbon content of the solid.

The favorable HHV values led to an impressively high energy recovery (ER) within the solid materials. Without KOH, ER ranged from 80% to 92%, while with KOH, it ranged from 72% to 78%. Considering these findings, the dechlorination step exhibited promise by effectively eliminating nearly all chlorine, which would otherwise render the solid material unsuitable for various applications, while simultaneously preserving the majority of carbon and embedded energy from the original PVC in a solid form with a higher energy density.

Table 8: Elemental recovery of solids after subcritical step.

	PVC	**200**	**225**	**250**	**275**	**300**	**325**	**250-KOH**	**275-KOH**	**300-KOH**
Carbon recovery (%)	-	95.2 ± 1.7	95.1 ± 1.0	96.5 ± 7.7	94.8 ± 2.1	94.2 ± 3.8	99.5 ± 4.9	92.0 ± 5.1	83.6 ± 8.4	87.6 ± 4.9
Chlorine recovery (%)	-	48.6 ± 10.2	40.5 ± 2.8	6.2 ± 1.6	1.9 ± 0.1	1.1 ± 0.1	1.3 ± 0.5	38.1 ± 9.5	12.8 ± 5.0	3.2 ± 1.0
Fixed carbon (wt.%)	8	13	20	47	53	54	53	11	25	29
HHV (MJ/kg)	19.4 ± 0.1	16.1 ± 0.9	19.2 ± 0.4	33.6 ± 0.6	37.1 ± 0.8	39.3 ± 0.9	39.3 ± 1.5	18.3 ± 1.2	26.6 ± 1.0	33.4 ± 1.0
ER (%)	-	79.9 ± 6.0	82.9 ± 2.6	86.4 ± 8.2	85.4 ± 3.0	85.9 ± 4.6	91.9 ± 5.5	78.4 ± 8.5	73.7 ± 9.7	72.3 ± 5.9

To better understand the chemical mechanisms by which the dechlorination occurs, it is useful to observe the elemental molar ratios of the solids depicted as van Krevelen diagrams in Figure 72-A/B. In fact, two reaction mechanisms have been inferred as possible routes for the dechlorination of PVC in hydrothermal environment: elimination and substitution (Scheme 1)[222,225,226]. The elimination reaction occurs through the removal (E2 elimination) of a chloride ion from the PVC backbone, simultaneously removing an adjacent hydrogen to form a double bond[218,227,228]. Due to this elimination pathway, when a chlorine atom is removed, a hydrogen atom is also removed (pathway I in Scheme 1). On the other hand, the substitution pathway involves a Sn2 nucleophilic mechanism: an OH^- ion is attracted to the carbon in the α-position, causing the release of the chloride ion [218,227,228]. With the substitution pathway, for every chlorine atom removed, one oxygen and one hydrogen atom are added to the solid (pathway IIa in Scheme 1, ‘substitution-1’ in Figure 72). In addition to this, an alternative substitution mechanism has also been observed[219,229,230], involving the simultaneous replacement of a chlorine atom and the hydrogen attached to the same carbon atom, in favor of two hydroxyl groups (pathway IIb in Scheme 1, ‘substitution-2’ in Figure 72). According to this latter mechanism, with an equal number of removed chlorine atoms, the clustered oxygen atoms result in being double.

As clearly shown in Figure 72 , at low temperatures, the primary pathway for dechlorination involves substitution. Indeed, alongside the reduction in chlorine content, there was an increase in oxygen, yielding an O/C ratio rising to 0.55 at 200 °C. In particular, the substitution-2 was likely the predominant pathway, as the ratio between oxygen atoms added and the chlorine atoms removed was 2.2 and 1.5 at 200 °C and 225 °C, respectively. As temperatures rose, the O/C, H/C, and Cl/C ratios all declined. At elevated temperatures, the predominant mechanism became elimination. Ultimately, the resultant solids exhibited an H/C ratio close to 1, implying a predominantly aromatic structure. The Cl/C ratio is below 0.01, and some residual oxygen was registered (O/C approximately 0.05), indicating a minor presence of the substitution reaction. In the case of addition of KOH as neutralizing additive, a lower degree of dechlorination and a higher amount of oxygen were observed at lower operating temperature. Interestingly, at 300 °C, O/C and Cl/C ratios similar to the non-neutralized reaction were obtained, whereas the H/C was consistently lower (0.75). This suggests a difference in the dechlorination mechanism, which will be deepened below (Paragraph 6.2.5). To summarize, it is evident that to achieve nearly complete chlorine elimination, the primary mechanism required was elimination.

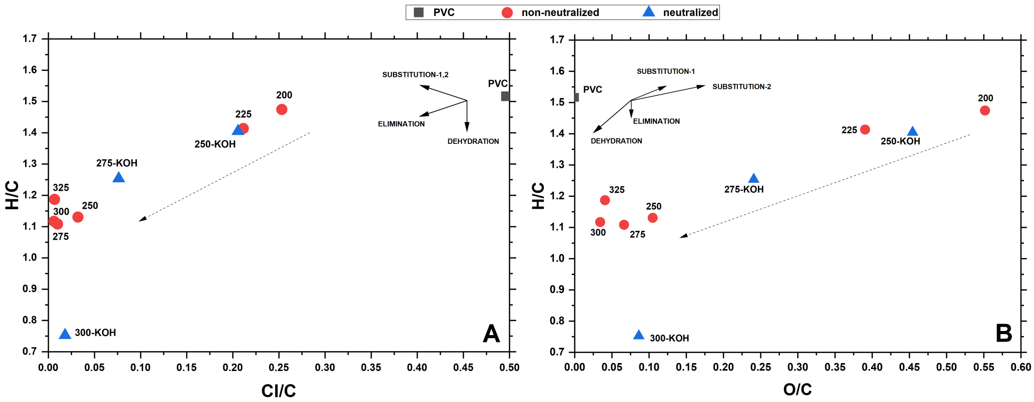

Figure 72: Van Krevelen diagram for solids obtained after the subcritical step (A) H/C versus Cl/C and (B) H/C versus O/C. Reaction conditions: 1.8 g PVC, 1.81 g KOH as basic additive in the case of neutralized reaction, total mass of 9 g, 20 min.

6.2.3 FTIR

Figure 73 presents the ATR-FTIR spectra of PVC and solids. Functional groups were identified based on values reported in the literature[231,232]. Looking at the virgin PVC spectrum, various peaks are associated with the presence of chlorine within the structure, namely at 1250, 834, 679 and 610 cm^{-1}. The last one is linked to the stretching of the C-Cl bond and is the most intense peak. At low temperatures (200 °C and 250 °C), the resulting spectra closely resembled that of virgin PVC. Despite the removal of chlorine from the structure, it appears that the overall structure did not change significantly. However, as indicated by the elemental analysis, substitution was likely the main mechanism occurring at low temperatures, leading to an increase in the oxygen content of the solids. Due to this reason, the presence of peaks associated with bonded oxygen was expected, particularly for the solid obtained at 200 °C, given that oxygen accounted for 28 wt.% of its total mass. However, in the region around 3300-3400 cm^{-1}, where the stretching of the O-H bond absorbs, the signal intensity was low. This low signal intensity can be attributed, in part, to the sharpness of the peaks at low wavelengths, which tends to overshadow broader peaks like that of the hydroxyl group. Additionally, since PVA (polyvinyl alcohol) is prone to undergo cross-linking when exposed to heat[233], it is plausible that during the drying phase (overnight at 105 °C), some hydroxyl groups in the chain underwent cross-linking, diminishing their vibration and, consequently, their intensity in the FTIR spectrum. Moreover, Yao et al. also did not register a significant difference in intensity at 3300 cm^{-1} between PVC and the solid obtained after hydrothermal treatment of PVC at 200 °C for 60 min, even though the latter contained 13 wt.% of oxygen[229]. At 250 °C, the signal at 610 cm^{-1} was weak and above 250 °C it became invisible, suggesting that FTIR was not sensitive to chlorine concentrations below 5 wt.%. On the other hand, signals at 1698 and 1600 cm^{-1} emerged at temperatures above 250 °C. The former is associated with C=O stretching, likely of an aromatic or unsaturated nature, due to its lower frequency (<1700 cm^{-1})[234]. The formation of C=O could result from substitution of chlorine with two hydroxyl groups (pathway IIb in Scheme 1), their intramolecular dehydration (pathway III in Scheme 1) and subsequent keto-enol tautomerization (pathway IV in Scheme 1)[219,229]. The peak at 1600 cm^{-1} is attributed to the aromatic C=C bond and, and its presence, coupled with the H/C ratio nearing 1, supports the formation of an aromatic structure as the reaction temperature rises. However, no peaks were visible at wavelengths above 3000 cm^{-1}, the region of the spectrum associated to the presence of double bonds. Some char and biochar standards were tested as references, and in both cases no signals were recorded above 3000 cm^{-1}, confirming that even though double bonds may be present, their corresponding signals are not detected in the spectra.

In the case of KOH addition, at 250 °C, the peaks associated with C-Cl (1250 and 610 cm^{-1}) remained the most intense; at 275 °C further decreased, and at 300 °C they were no longer visible. This was consistent with the chlorine content estimated by µ-XRF. As seen without KOH, at 250 °C the peak associated to C=O emerges, along with a peak shoulder for the C=C bond. Although there was a baseline drift towards lower wavelengths for the solid obtained at 300 °C with KOH, the peaks resembled those observed without the addition of KOH.

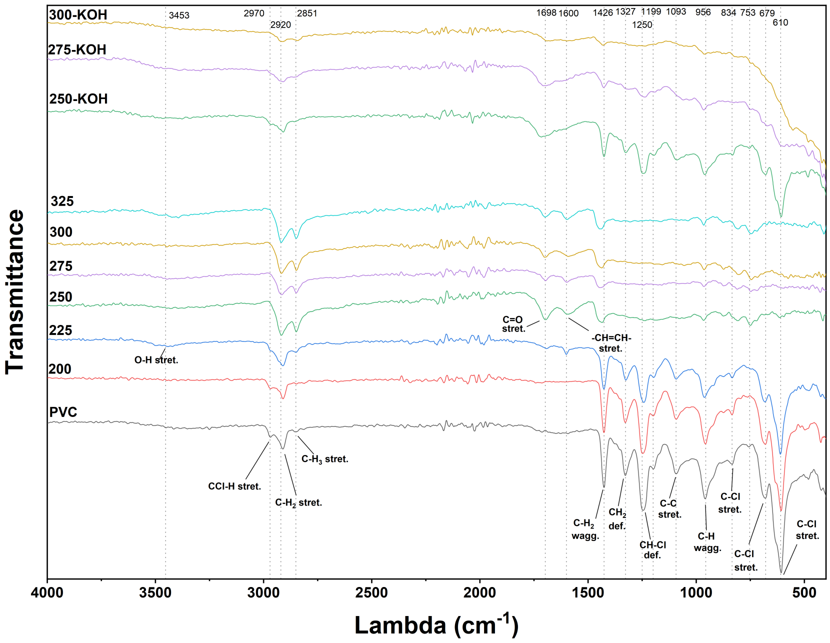

Figure 73: ATR-FTIR of the solids obtained after the subcritical step. Reaction conditions: 1.8 g PVC, 1.81 g KOH as basic additive in the case of neutralized reaction, total mass of 9 g, 20 min.

6.2.4 TGA and Pyro-GC-MS

TGA and DTGs for the virgin PVC and for the solids obtained after the first hydrothermal step are reported in Figure 74. Two main peaks were discernible: the first was centered at 290-311 °C, while the second peak at 446-465°C. As widely acknowledged, the initial weight loss attributed to dechlorination in the case of PVC during dry and inert conditions (pyrolysis-like) is characterized by the removal of chlorine as HCl[235]. As registered in hydrothermal environment, during TGA, the dechlorination reaction started at around 250 °C and led to a mass decrease in PVC of 63% by 380 °C. As the temperature at which the solid material was generated increased, the reduction in mass yield associated with the dechlorination reaction decreased, as detailed in Table 9. This was coherent with μ-XRF results. Moreover, as described above, the residual chlorine was increased in the case of the neutralized reactions (depicted in Figure 74-C/D), resulting in an increased mass loss associated with the first peak with respect to that of non-neutralized reactions (Figure 74-A/B) at the same operating temperature.

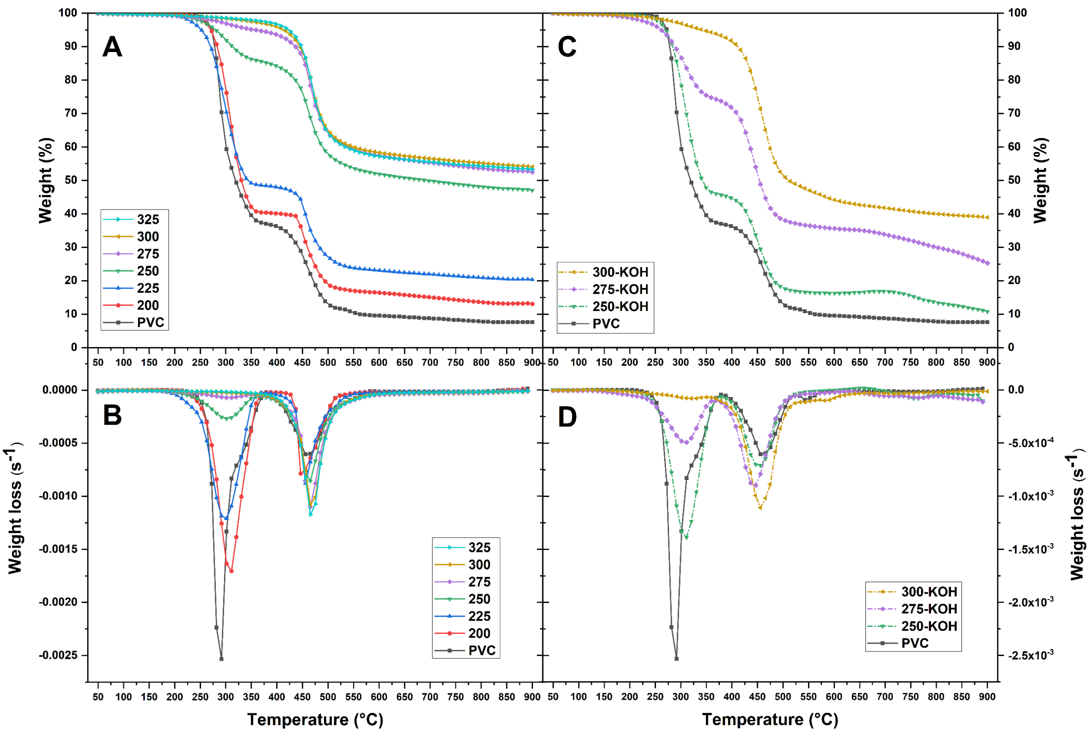

Figure 74: TGAs and DTGs of virgin PVC and solids obtained after the subcritical step. (A) TGA and (B) DTG of solid produced through non- neutralized reaction. (C) TGA and (D) DTG of solid produced through neutralized reaction. Reaction conditions: 1.8 g PVC, 1.81 g KOH as basic additive in the case of neutralized reaction, total mass of 9 g, 20 min.

At temperatures above 380 °C, the samples experienced a second mass loss, which is commonly associated with the breakdown of the structure formed after dechlorination[235,236]. The reduction in mass at this stage was more pronounced at higher operating temperatures (Table 9, Figure 74-B-D). However, as depicted in Figure 70, elevated operating temperatures led to a greater weight reduction. In order to establish a connection between the loss of mass and the initial quantity of PVC, the mass loss normalized by the solid yield achieved after the subcritical process was calculated (Eq. (27)). As detailed in Table 9, the normalized data showed an opposite pattern, indicating that, in comparison to the solid formed after the initial PVC dechlorination peak in TGA, the hydrothermal-derived solids were less susceptible to decomposition through pyrolysis. This suggests that the first hydrothermal step might have induced chemical modifications in the PVC structure, differentiating it from the pyrolysis favored behavior of untreated PVC at 380 °C and beyond. Moreover, the addition of the basic additive increased the normalized mass loss (Table 9, Figure 74-D), suggesting that the solid structure formed during the neutralized dechlorination was more susceptible to further conversion.

Table 9: Mass losses calculated from DTG. *The normalized mass loss is calculated according to Eq. (27).

	PVC	200	225	250	275	300	325	250-KOH	275-KOH	300-KOH

1st mass loss (204°C-379 °C)	62.8%	59.5%	50.7%	13.9%	4.8%	2.6%	1.9%	53.9%	24.7%	4.9%
2nd mass loss (379°C-550 °C)	25.4%	22.8%	23.6%	30.0%	33.2%	35.0%	36.5%	29.2%	37.3%	40.5%
Normalized* 2nd mass loss (379°C-550 °C)	25.4%	21.9%	19.7%	14.9%	14.8%	14.8%	16.6%	24.3%	20.0%	22.3%

$$\mathit{Normalized\ TGA\ mass\ loss}\left(\frac{g\ lost\ during\ TGA}{g\ starting\ PVC}\right)=\mathit{TGA\ mass\ loss}\left(\frac{g\ lost\ during\ TGA}{g\ dechlorinated\ solid}\right)\cdot \mathit{solid\ mass\ yield}\left(\frac{g\ dechlorinated\ solid}{g\ starting\ PVC}\right) \qquad (27)$$

Py-GC-MS was conducted at a pyrolysis temperature of 600 °C using the solid obtained after the subcritical step, aiming at a better understanding of its structure. The semiquantitative analysis of the volatile compounds is reported in Figure 75. It is evident that a substantial quantity of aliphatic hydrocarbons (including linear/cyclic alkanes, linear/cyclic monounsaturated alkenes and dienes/trienes) was present. This is noteworthy considering that Py-GC-MS converts many aliphatic hydrocarbons into aromatics during pyrolysis[237,238], and that the amount of aliphatic hydrocarbons observed in this chapter was higher than typical values obtained from biochar[239].

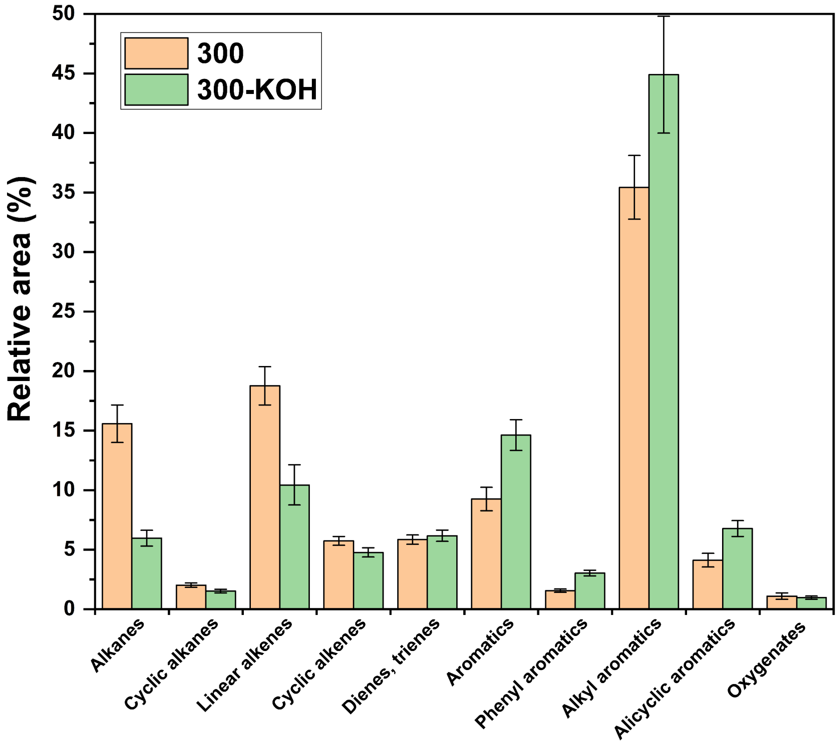

Figure 75: Products distribution from Py-GC-MS at the pyrolysis temperature of 600 °C of the solids produced in subcritical water at 300 °C without KOH (orange) and with KOH (green). Subdivision was performed based on substitution groups. 'Phenyl,' 'alkyl,' and 'alicyclic' indicate the nature of the substituents. As dienes and trienes were accounted both aliphatic and alicyclic structures. Data are expressed as relative area with respect to all identified peaks.

Py-GC-MS of virgin PVC results in the formation of low alkanes and high amount of aromatics[240]. This is explained by the fact that the pyrolysis of PVC appears to proceed through free-radical reactions that lead to the release of chlorine, forming radicals that subsequently convert into monocyclic aromatics and PAHs (polycyclic aromatic hydrocarbons)[240]. Interestingly, literature reports that long-chain aliphatics (ranging from C7 to C22) were almost absent in the Py-GC-MS of virgin PVC[240]. In contrast, after Py-GC-MS analysis of the dechlorinated samples, long-chain aliphatic hydrocarbons accounted for 11% and 24% of the total integrated area in solids obtained with and without KOH, respectively. Therefore, it is probable that these saturated hydrocarbons found in the dechlorinated solid originate from the degradation of extended aliphatic chains already present in the solid structure. However, it is essential to stress that during Py-GC-MS, as indicated by TGA in Figure 74, only 42 wt.% (without KOH) and 58 wt.% (with KOH) of the solids were converted into volatiles and, therefore, were subject to analysis. For this reason, it is reasonable to assume that the remaining portion was composed of a more heavily condensed, charred phase, which would explain the elemental H/C close to 1.

The addition of KOH during the subcritical step led to a higher share of aromatics at the expense of aliphatic hydrocarbons. This shift in product distribution made it resemble pure PVC more closely. This change can be related to a lower abundance of aliphatic branches or to a higher amount of unsaturation within the solid. Moreover, the signal associated with HCl was too weak to be identified, confirming the low level of chlorine remaining in the solids. Additionally, the only chlorine-containing compound detected was chlorobenzene, but it was found with negligible intensities. This finding suggests the potential to obtain a chlorine-free product after pyrolysis of the dechlorinated solid. However, it is worth noting that even in the Py-GC-MS analysis of virgin PVC, no chlorinated compounds were observed at pyrolysis temperatures exceeding 600 °C[240], implying a limited sensitivity of Py-GC-MS in detecting such compounds. The intensity of oxygen-containing molecules was also very low, comprising approximately 1% of the overall identified area.

6.2.5 Kinetic evaluation and dechlorination mechanism

Figure 76-A depicts the points obtained by the DSC using the Kissinger method, as described in Paragraph 2.2.3. These data were subjected to linear interpolation using Eq. (15), allowing for the calculation of apparent activation energies and pre-exponential factors, which are summarized in Table 10. For the hydrothermal dechlorination of PVC without neutralization, the apparent activation energy was determined to be 185.9 ± 6.8 kJ/mol, and the pre-exponential factor was found to be $1.42 \cdot 10^{17}$ min^{-1}. The calculated activation energy value aligned closely with the activation energies of 187 kJ/mol and 190 kJ/mol reported for hydrothermal dechlorination of PVC powder by Hashimoto et al.[241] and Li et al.[242], respectively. Notably, this agreement is significant since this study is the first to

employ the Kissinger method for evaluating these hydrothermal kinetic parameters. The values reported for the pre-exponential factor by Hashimoto et al. and Li et al. were $5.23 \cdot 10^{16}$ min^{-1} and $1.86 \cdot 10^{16}$ min^{-1} [241,242]. The former value falls within the confidence interval of this work, while the latter is slightly lower. Based on these apparent activation energy values, it can be inferred that the dechlorination reaction is primarily controlled by chemical reactions[227]. Additionally, prior literature has indicated that the dechlorination process adheres to first-order kinetic behavior[227,242–244].

In the case of addition of KOH, the apparent activation energy decreased from 185.9 ± 6.8 kJ/mol to 119.8 ± 7.0 kJ/mol and the pre-exponential factor decreased from $1.42 \cdot 10^{17}$ min^{-1} to $6.14 \cdot 10^{10}$ min^{-1}. Based on these results, it can be inferred that the addition of KOH kinetically favors the dechlorination reaction at lower temperatures while becoming unfavored at higher temperatures. This is confirmed by Figure 76-B, which shows the plot of the reaction velocity of dechlorination ($\ln k$) versus the inverse of the reaction temperature (1/T). It can be observed that below ca. 270 °C the neutralized reaction has higher dechlorination rates while at higher temperatures the non-neutralized reaction favors the dechlorination rate. Similar kinetic results were observed also in the literature. Hashimoto et al. observed a decrease in both activation energy (120 vs 187 kJ/mol) and pre-exponential factor ($3.0 \cdot 10^{11}$ vs $5.2 \cdot 10^{16}$ min^{-1}) when a 0.6 M solution of ammonia was used instead of water for hydrothermal dechlorination of PVC powder[241]. Shin et al. registered apparent activation energies within 92-146 kJ/mol in 1–7M NaOH solution for flexible PVC pellets[243]. From the same feedstock, the same group evaluated the activation energy as low as 89-103 kJ/mol using a 1.0 M NaOH in ethylene glycol instead of water as solvent[227]. However, unlike literature, in this chapter the dechlorination efficiency decreased at low temperatures if KOH was added in the reactor.

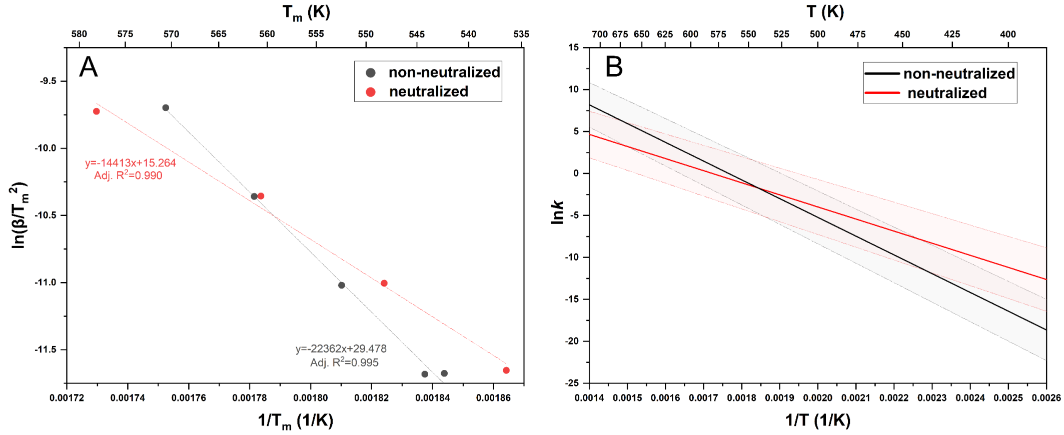

Figure 76: (A) linear interpolation of data obtained after DSC by KAS method, (B) lnk versus 1/T for the dechlorination reaction. Shadows represent the confidence interval.

Table 10: Kinetic parameters for neutralized and non-neutralized dechlorination of PVC in subcritical water.

		non-neutralized	neutralized
E_a, activation energy (kJ/mol)	Mean value	185.9	119.8

	Confidence interval	179.1-192.7	112.8-126.8
k_∞, pre-exponential factor (min^{-1})	Mean value	$1.42\cdot10^{17}$	$6.14\cdot10^{10}$
	Confidence interval	$3.11\cdot10^{16}$- $6.45\cdot10^{17}$	$1.26\cdot10^{10}$- $2.98\cdot10^{11}$

As documented in various sources[217,227,245], it was noted that incorporating a basic additive during the dechlorination of PVC can encourage the presence of hydroxyl ions (OH^-). These ions play a role in promoting the substitution mechanism (pathway IIa and pathway IIb in Scheme 1). By employing the Kissinger method via DSC analysis, the determined apparent activation energy in the case of neutralized reactions was likely associated with this pathway. Therefore, in addition to its neutralization role, KOH acts as a catalyst. This assumption is supported by the fact that at 250 °C the O/C molar ratio was increased with addition of KOH (Figure 72). Nevertheless, achieving a high degree of chlorine removal efficiency may require the utilization of the elimination mechanism (pathway I in Scheme 1), as discussed above (Paragraph 6.2.2). This mechanism is associated with the activation energy of 186 kJ/mol and is not only thermally favored but also self-propagating due to the ‘zipper mechanism’ (pathway V in Scheme 1): the formation of a double bond following the removal of a HCl molecule from the PVC structure triggers the adjacent chlorine atom's activation, facilitating the spread of the chlorine removal process throughout the PVC structure[246–248].

By giving preference to the substitution of chloride ions with hydroxyl ions, the effectiveness of the zipper mechanism is hindered. This is further exacerbated by the high amount of KOH introduced in this study, which elevates the solution's pH to a highly basic level. Consequently, this high basicity could deter the dehydration reaction (pathway III in Scheme 1), as it is known to be acid-catalyzed[218,249]. As a result, the hydroxyl groups produced after the substitution process are unable to transform into the polyene structure, ultimately limiting the effectiveness of chlorine removal in the presence of KOH. This theory may also elucidate why existing literature indicates that the addition of basic additives initially enhances chlorine removal but eventually reaches a point where further increases in alkali concentration leads to diminishing returns[221,243]. Indeed, a moderate amount of alkali can aid the dechlorination by substitution, resulting in the formation of a carbon backbone with hydroxyl groups. The basicity of the solution is limited and as the reaction proceeds, the aqueous phase ends up being acidic due to the high amount of chlorine released. This shift in conditions could facilitate intramolecular dehydration, forming the polyene structure which can then initiate the ‘zipper mechanism’. The polyenes are prone to instability and easily tend to react. They engage in intramolecular reactions, leading to cyclization, aromatization, polymerization, and cross-linking[224,235,250,251]. Consequently, the resulting solid likely comprises a substantial quantity of polyaromatic structures, along with aliphatic branches and hydrogenated aromatics (pathway VI in Scheme 1).

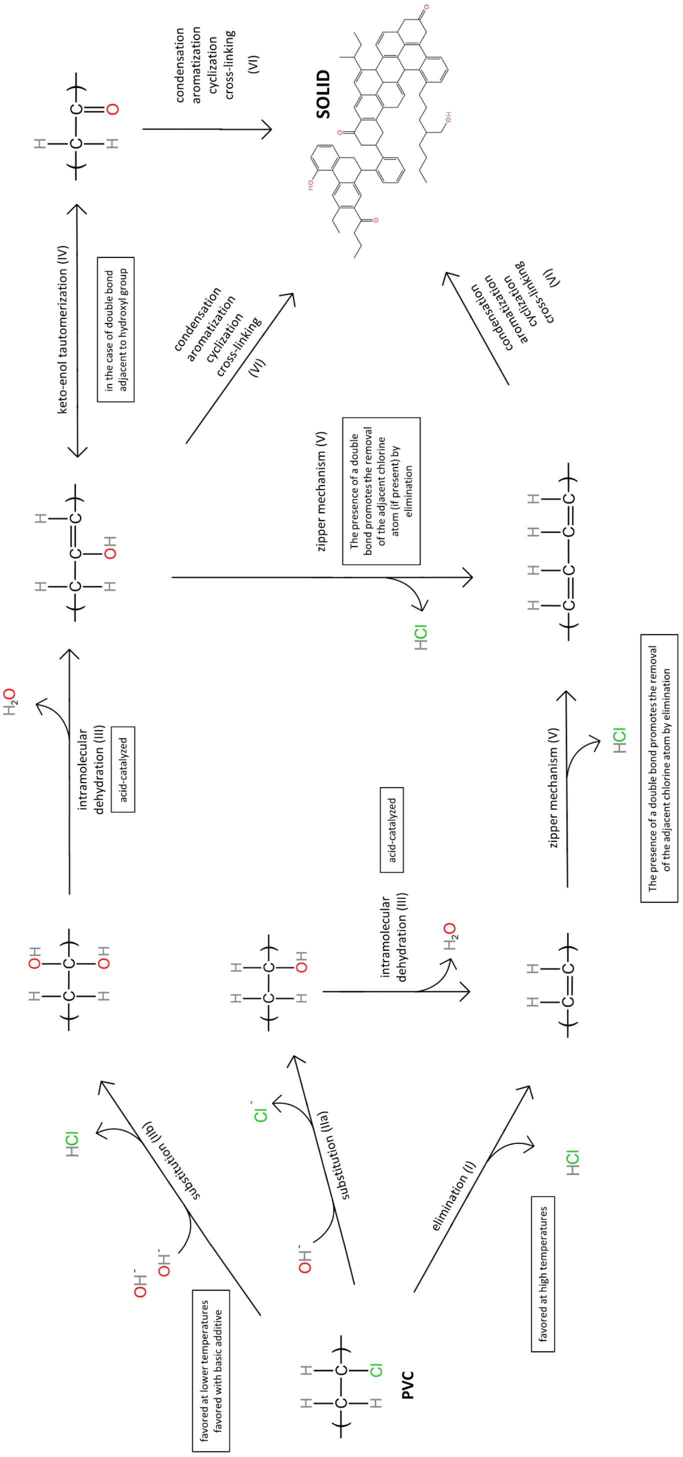

Scheme 1: Proposed reaction pathways for dechlorination of PVC in hydrothermal environment.

6.2.6 Supercritical step

Figure 77 presents the mass yields of the products obtained after supercritical HTL at varying temperatures. As the reaction temperature increased, the amount of produced gas also rose from 6.5 wt.% to 19.7 wt.%. This trend was anticipated, considering that gas production is known to escalate with reaction temperature in hydrothermal liquefaction[112,189]. The gas composition is predominantly composed of aliphatic compounds, as observed by Takeshita et al. from the hydrothermal decomposition of PVC at 400 °C[224].

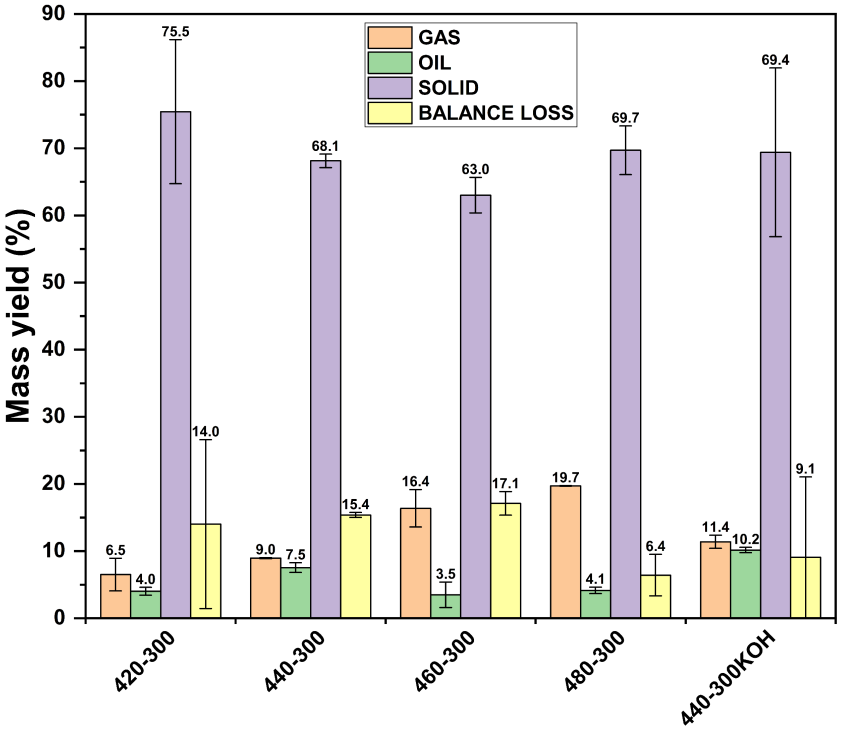

Figure 77: Mass yields obtained after the supercritical step of the solids obtained from the subcritical step. Reaction conditions: 0.832-1.084 g of dechlorinated solid (depending on the temperature), solid/water ratio of 1/2, 60 min, 225 bar. The first number in the experiment denotes the temperature of the supercritical step, while the second number pertains to the sample used as the feedstock for the supercritical step.

The oil formation after the supercritical step was rather limited. The maximum production was registered at 440 °C, yielding 7.5 wt.% and 10.2 wt.% using the solid produced in the absence and presence of KOH, respectively. The sum of oil and gas was in fact increasing with increasing temperature, suggesting that higher temperatures led to degradation of the oil phase into gaseous hydrocarbons. Moreover, a portion of the oil was lost after evaporation of the extraction solvent, as shown in Figure 79. This hypothesis was confirmed by the fact that the amount of carbon missed in the aqueous phase was quantified as 0.1% of the carbon present in the dechlorinated solid used as the feedstock for the supercritical step. It is hence reasonable to assume that the missing mass (yellow columns in Figure 77) was actually low-boiling oil compounds. For this reason, the composition of the oil was studied prior to drying; the results are depicted in Figure 78, along with the results obtained from Py-GC-MS, in order to highlight the differences between fast pyrolysis and supercritical HTL as the processing step.

The products obtained after supercritical HTL at 440 °C were mainly aromatics. In particular, PAHs largely outnumbered other compounds, accounting for ca. 50% of the overall area of the chromatograms. Among these, the naphthalene derivatives were the most prevalent, with the remaining PAHs following in sequence from lightest to heaviest (Figure 78-A). Moreover, some partially hydrogenated derivatives of PAHs ('alicyclic aromatics' in Figure 78-B) were also present, in particular indanes and tetralins (Figure 78-A). Other than these, the most abundant molecules were alkanes and benzene derivatives. Interestingly, the distribution between these two families was the biggest difference observable between the use of solids obtained with KOH and without KOH. Without KOH a higher share of alkanes and lower production of benzene derivatives was registered with respect to the addition of KOH. As previously discussed for fast pyrolysis, this may be symptomatic of a higher quantity of saturated aliphatic chains in the absence of basic additive.

Although a consistent amount of alkanes was also registered after supercritical HTL, few alkenes were identified. This is interesting, as more alkenes than alkanes resulted after fast pyrolysis. Moreover, with respect to supercritical HTL, fast pyrolysis favored the production of monoaromatics (benzenes) at the expenses of PAHs, and increased the presence of unsubstituted aromatics at the expenses of alkylated and alicyclic aromatics (Figure 78-B). These observations suggest that pyrolysis results in higher cracking of the dechlorinated solid, increasing dealkylation and unsaturation of the product.

After supercritical HTL, the amount of chlorinated compounds identified in the chromatograms was very low, amounting to 0.34 ± 0.30 % and to 0.74 ± 0.35 % of the overall identified area, in the case of 440-300 and 440-300KOH, respectively. This is an improvement with respect to the production of oil directly from PVC, as many chlorinated compounds were found in the oil[246]. On the other hand, the presence of oxygen was not irrelevant. Indeed, 4.4 ± 0.7 % and 10.0 ± 1.0 % of the overall identified area was constituted by oxygen-containing molecules, in the case of 440-300 and 440-300KOH, respectively (Figure 78-B). The higher amount of oxygenated compounds compared to fast pyrolysis suggests the active role of water molecules during the supercritical reaction.

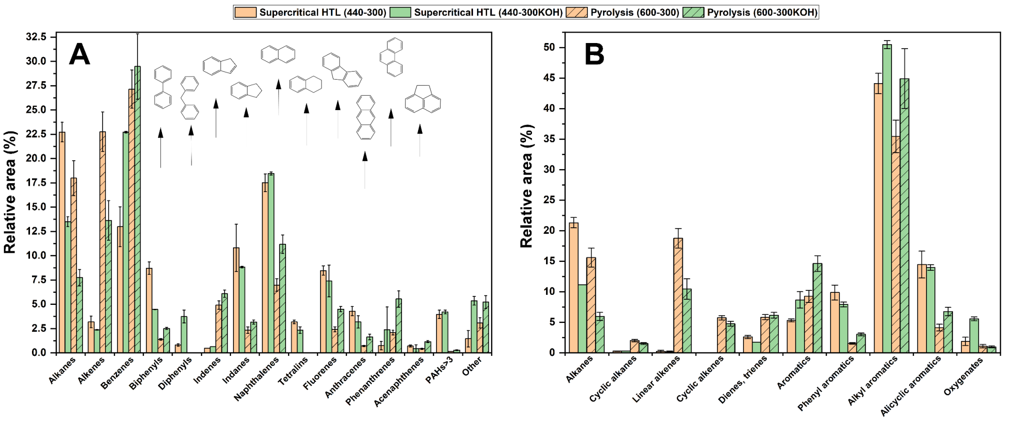

Figure 78: GC-MS chromatograms of the oil obtained after the supercritical step at 440 °C (bars without pattern) and chromatogram obtained from Py-GC-MS for comparison purposes (hatched bars). The

compounds in the chromatograms are categorized in two ways: (A) based on their aromatic structure or (B) based on their functionalities. 'Phenyl,' 'alkyl,' and 'alicyclic' indicate the nature of the substituent groups. Orange bars refer to the oil obtained using as feedstock the solid produced at 300 °C without KOH; green bars refer to the oil obtained using as feedstock the solid produced at 300 °C with KOH. Data are expressed as relative area with respect to all identified peaks.

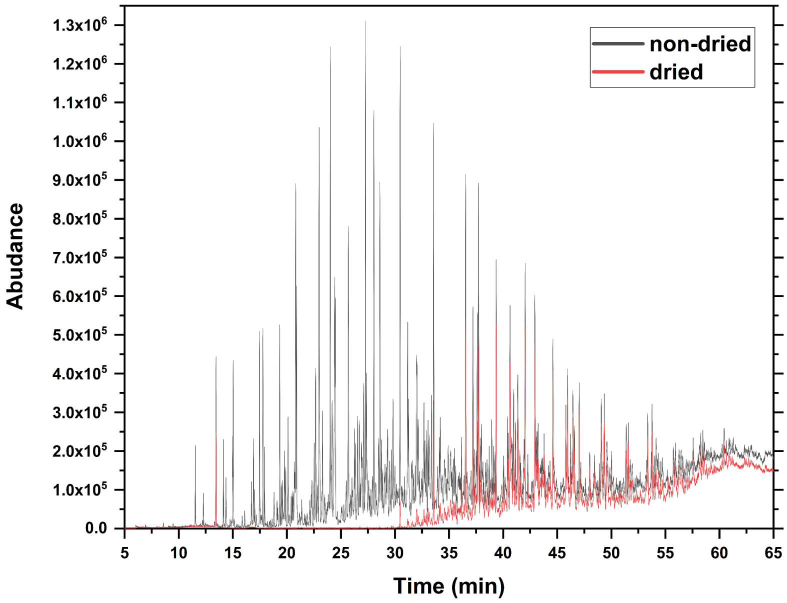

Figure 79: Chromatograms from GC-MS of oils produced after the supercritical step from the solid obtained at 300 °C without KOH. The black line represents the oil directly injected after extraction with acetone. The red line represents the same oil injected after evaporation of the solvent and subsequent resolubilization.

After the supercritical step, most of the solid remained as such. In fact, the solid yield ranged between 63-76 wt.%, corresponding to a conversion of 24-37 wt.%. Interestingly, the conversion of the solid material did not consistently rise with temperature; instead, it reached a peak at 440°C. The introduction of KOH during the subcritical phase did not affect the solid conversion, but slightly increased the production of oil and gas. With respect to supercritical HTL, with fast pyrolysis at 600 °C (Figure 74), solid conversion would be increased from 31 to 56 wt.% and from 32 to 42 wt.%, in the case of dechlorinated solid obtained at 300 °C with and without KOH, respectively.

Similar to the mass yield, the carbon yield within the solid phase ranged between 57% and 79% after the supercritical step (as outlined in Table 11). The carbon content remained similar to that registered prior to the supercritical step (around 90%). On the other hand, hydrogen decreased as the operating temperature increased. Consequently, the H/C molar ratio dropped from a starting 1.1 after the subcritical step to 0.29 after the supercritical step at 480 °C. The solid hence moved towards a heavier anthracite-like structure, as confirmed also by the higher fixed carbon. Furthermore, the chlorine content diminished even further, reaching approximately 1 wt.%, while the O/C ratio experienced a slight increase, confirming the incorporation of oxygen from water. Due to the reduced hydrogen content and increased oxygen content, the energy content of the solid material decreased after the supercritical step.

Table 11: Elemental compositions, carbon recovery and HHV for solids obtained after the supercritical step.

		420-300	**440-300**	**460-300**	**480-300**	**440-300KOH**
Elemental composition (wt.%)	**C**	90.3 ± 0.3	86.5 ± 5.8	87.7 ± 1.9	86.4 ± 1.8	92.2 ± 2.4
	H	6.1 ± 0.3	3.1 ± 0.2	2.5 ± 0.2	2.1 ± 0.2	3.9 ± 0.2
	Cl	1.0 ± 0.3	0.7 ± 0.3	1.1 ± 0.1	1.0 ± 0.1	1.1 ± 0.1
	O	2.6 ± 0.9	9.7 ± 6.2	8.7 ± 2.2	10.6 ± 2.1	2.7 ± 2.5
Elemental molar ratio	**H/C**	0.81 ± 0.05	0.42 ± 0.05	0.34 ± 0.04	0.29 ± 0.04	0.51 ± 0.04
	Cl/C	0.004 ± 0.001	0.003 ± 0.001	0.004 ± 0.001	0.004 ± 0.000	0.004 ± 0.001
	O/C	0.02 ± 0.01	0.08 ± 0.06	0.07 ± 0.02	0.09 ± 0.02	0.02 ± 0.02
Carbon recovery in solid (%)		78.8 ± 12.7	68.2 ± 6.7	64.0 ± 5.1	69.7 ± 6.2	78.9 ± 17.3
Fixed carbon (wt.%)		66	67	90	85	69
HHV (MJ/kg)		38.5 ± 0.4	32.8 ± 1.6	32.7 ± 0.7	31.5 ± 0.7	36.5 ± 0.8

6.2.7 Perspectives

Overall, the double-stage hydrothermal processing showed to be an interesting way of valorizing PVC waste. With the subcritical stage it was possible to remove 99% of the chlorine present in the virgin PVC under the form of HCl. The produced HCl solution could then be used as reagent for virgin PVC. Simultaneously, nearly all the carbon remains within the solid. This selective removal of chlorine leads to an increase in the heating value of the remaining solid material, thereby enabling substantial energy recovery. It is hence possible to generate a solid that is both denser in energy content and nearly devoid of chlorine, enabling its easier use as feedstock for subsequent technology.

The presence of chlorine is well known for causing significant corrosion issues[218,252,253]. Removing chlorine before any energy valorization process helps protect the equipment, but anticipates the corrosion issue during the dechlorination step, as chlorine is released. The dechlorination step has been also studied through a low-temperature pyrolysis (200-400 °C, dry and inert conditions)[254]. Despite using lower temperatures than pyrolysis, corrosion issues can still observed. To address this problem, sorbents (calcium-based, aluminum-based and composites) have been investigated to capture chlorine[254]. However, this method entrains chlorine in the solid phase, making them unsuitable for use in a pretreatment dechlorination step and more appropriate for direct use in pyrolysis[255].

The advantage of performing dechlorination in hydrothermal environment is that HCl is solubilized in the aqueous phase and thus becomes dilute. In this chapter, using a 20 wt.% concentration of PVC in water and stainless steel reactors, corrosion issues were still observed. However, in the context of dechlorinating mixed plastic waste, the concentration of PVC in water used herein was very high, so a lower concentration of PVC could be beneficial. Moreover, using higher corrosion-resistant materials (nickel-molybdenum alloys, zirconium, tantalum) could further help in limiting corrosion, although at a higher cost[256].

Another significant advantage of performing dechlorination in a hydrothermal environment is the possibility of using solubilized neutralizing agents that counteract the acidity of chlorine, thus preserving the reactor from corrosion. In this chapter, improvements in corrosion after the addition of KOH were not observed. However, further investigations are necessary to better understand why it did not work and how to improve it..

Including the supercritical stage, it was possible to reduce the solid to 29 wt.% of the starting PVC mass, containing approximately 64% of the carbon content of PVC. Simultaneously, gaseous and liquid hydrocarbons were produced, constituting 30% of the carbon content of the initial PVC. It is assumed that the missing carbon in the supercritical step is constituted by light oil rich in aromatic compounds, as no carbon was found in the aqueous phase.

However, the performance of the supercritical stage did not allow for the conversion of much of the solid produced after the subcritical stage. For this reason, the valorization of the dechlorinated solid would be much more effective using other technologies. In particular, if derived from mixed waste, the dechlorinated solid could be valorized energetically without corrosion issue. It is worth noting that no corrosion issues were observed in any of the supercritical steps performed, confirming the possibility of effectively producing an issue-free solid after the subcritical step. Energy valorization is advisable through the introduction of an oxidizer, such as air gasification, given the high amount of fixed carbon in the solid (Figure 74).

6.3 Conclusions

This chapter presented a two-stage hydrothermal processing for the energy valorization of PVC waste. In the first subcritical stage, by operating at 300 °C for 20 min, it was possible to achieve a remarkable 99% removal of chlorine, while retaining 94% of the carbon content in the solid produced. The addition of KOH, as neutralizing additive, during the subcritical stage proved to catalytically favor the substitution mechanism as a dechlorination pathway, albeit hindering high dechlorination efficiency at low operating temperatures. The catalytic activity was confirmed by a reduction in the apparent activation energy (from 186 to 120 kJ/mol) by addition of KOH. At 300 °C, the impact of KOH on performance was less pronounced. Through various analytical techniques (CHNS, Py-GC-MS, FTIR and TGA), the resulting solid was observed to consist mainly of a condensed aromatic structure with aliphatic branches. Following the supercritical stage, the residual solid underwent a reduction to 29 wt.% of the mass of the initial PVC. Concurrently, liquid and gaseous hydrocarbons were produced, though only to a limited extent. Using supercritical HTL for valorizing the dechlorinated solid lead to the production of an oil phase containing a higher share of PAHs and alkylated aromatics and a higher degree of saturation, with respect to pyrolysis products. Overall, the subcritical stage demonstrated its efficiency in producing a nearly chlorine-free solid material with a higher energy density than that of PVC. The dechlorinated solid could then be further processed using other technologies. To implement this on an industrial scale, further advancements are required to address issues related to corrosion, and the incorporation of neutralizing additives could be a potential means to enhance its performance.

Chapter 7

Techno-economic and life-cycle assessment of an HTL plant

7.1 Introduction

The oil phase ('biocrude') obtained after HTL of biomass typically exhibits high viscosity, a moderate heating value (ca. 30 MJ/kg), and a significant residual oxygen content (5-30 wt.%)[65]. To remove heteroatoms and enhance its properties, the biocrude must undergo an upgrading process. This step is usually performed by hydrotreating, which requires hydrogen as a reactant[257]. The hydrogen requirement depends both on the characteristics of the biocrude and on the catalyst and reaction conditions used in the upgrading step[150]. Currently, hydrogen is primarily produced through steam reforming (SR) of natural gas. However, the cost of hydrogen can significantly impact small-scale production facilities[258]. Moreover, considering its reliance a fossil fuel source, there is a growing desire for greener and renewable alternatives.

Another significant cost in an HTL plant is related to the disposal of the hydrothermal liquefaction-derived aqueous phase (HTL-AP)[259]. HTL-AP can contain up to 45% of the feedstock carbon content in various classes of molecules (carboxylic acids, alcohols, ketones, etc.)[163]. Disposing of HTL-AP is not a simple process due to the associated costs and the environmental impacts of continuous fresh water supply. Moreover, the exploitation of residual molecules presents an opportunity, as recently addressed by several review works[260–263].

An innovative approach to valorize the HTL-APR involves aqueous phase reforming (APR). APR is a catalytic reaction conducted under mild operating conditions (225-270 °C and 30-60 bar), typically utilizing noble metal catalysts (typically Pt)[264]. Under these conditions, the dissolved oxygenated compounds, still in the liquid phase, can be converted into hydrogen and carbon dioxide. Operating directly in the aqueous phase eliminates the need for vaporization, resulting in higher energy efficiency compared to conventional steam reforming (SR). In addition, the low temperature range promotes the water gas shift (WGS) reaction, enabling an increased hydrogen yield and a lower carbon monoxide production[265].

The HTL-APR coupling appears as a valuable option to increase the carbon efficiency of the hydrothermal liquefaction, while providing an environmentally friendly source of hydrogen for the upgrading section. For this reason, this chapter describes the design, techno-economic analysis (TEA) and life cycle assessment (LCA) of a combined HTL-APR plant. As economic evaluations are still limited in for HTL plant[266], this analysis may shed light on specific technological bottlenecks and weaknesses that need addressing before progressing to commercial-scale implementation. Furthermore, despite biomass being a renewable source, the sustainability of the technology must be determined, considering potential environmental impacts throughout all production phases.

In this chapter, two different scenarios were investigated, distinguished by the feedstock: corn stover (CS), representative of several lignocellulosic agricultural wastes, and a lignin-rich stream (LRS), being the by-product of a second generation bioethanol industrial plant[267]. The decision to examine two feedstocks stems from the demonstrated influence, as discussed in earlier chapters, of the chosen feedstock on the properties of the aqueous phase and biocrude in HTL. Calculations were derived from a combination of experimental data and information obtained from the literature.

In Paragraph 7.2, the plant is outlined, including the methodology employed for design, economic assessment, and environmental evaluation. Paragraph 7.3 delves into the outcomes of diverse assessments, organized into three subsections. The first one (Paragraph 7.3.1) focuses on detailing the plant's mass and energy balances, coupled with the design of the main units. In Paragraph 7.3.2, the economic evaluation is presented, encompassing various key performance indicators (minimum biofuel selling prices, hydrogen production cost, etc.). A sensitivity analysis was performed to address uncertainties, particularly associated with the lack of precise data with regards to the capital investment due to the low TRL of the examined process. Finally, Paragraph 7.3.3 elucidates the findings of the cradle-to-gate LCA. It covers diverse environmental parameters (global warming, acidification, eutrophication potential, etc.), supplemented by an uncertainty analysis using Monte Carlo simulations. Moreover, it incorporates a sensitivity analysis to assess the impact following variations in different methodological and design choices.

The findings presented in this chapter are derived from two published works[162,268].

7.2 Plant description and methodology

7.2.1 Process description

The main processes involved in the plant are: i) HTL of a wet feedstock, ii) APR of the aqueous phase produced by HTL and iii) hydrotreatment of the biocrude to biofuel. Two scenarios of HTL-APR coupling with different lignocellulosic feedstocks were studied in this work: corn stover (CS) and lignin-rich stream (LRS), whose characterization is reported in Table 12. The basic process scheme is illustrated in Figure 80, with the plant's battery limit extending from feedstock pre-treatment to biofuel production.

Table 12: Main properties of HTL-feedstocks, biocrude and char.

Property	Feedstock		Solid		Biocrude		Biofuel	
	LRS[269]	CS[76]	LRS	CS	LRS	CS	LRS	CS
C (wt.% daf)	55.5	43.6	77.7	68.2	69.3	74.0	90.7	89.6
H (wt.% daf)	6.1	5.8	3.2	4.3	6.9	8.0	9.3	10.4
O (wt.% daf)	37.4	50.0	19.1	25.4	22.8	16.2	-	-
N (wt.% daf)	1.0	0.6	n.a.	2.1	1.0	1.8	-	-
Ash (wt.% dry)	2.6	7.0	2.9	34	0.4	1.0	-	-
Moisture (wt.%)	70.0	5.4	32.0	32.0	5.0	5.0	-	-
LHV (MJ/kg$_{dry}$)	20.0	16.5*	25.7*	28.7*	29.7*	33.2*	40.7*	41.4*

*evaluated with Channiwala and Parikh correlation[95]; daf: dry ash free

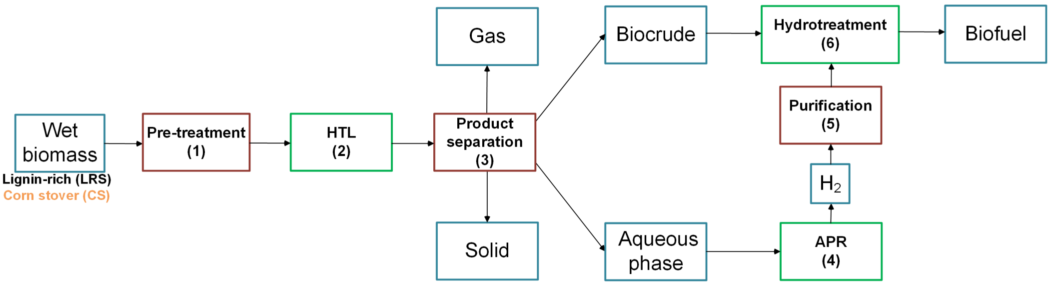

Figure 80: Block flow diagram of the HTL-APR integrated plant. Block numbers in brackets serve identifiers for plant sections.

The capacity of the plant was chosen equal to 20 MW$_{th}$ of LRS (based on its calorific value), corresponding to 12 t$_{wb}$/h of LRS (3.6 t$_{db}$/h) which is consistent with the size of the production of second generation bioethanol plants[270]. The same dry feedstock mass rate was considered for the second case (CS), which is equivalent to 16.5 MW_{th} (due to the different caloric value of the feedstock). This size is coherent with a 50-km radius of harvesting area, according to the average distribution of corn production in Europe[271] (corn/stover production equal to 1:1[272]).

7.2.2 Design

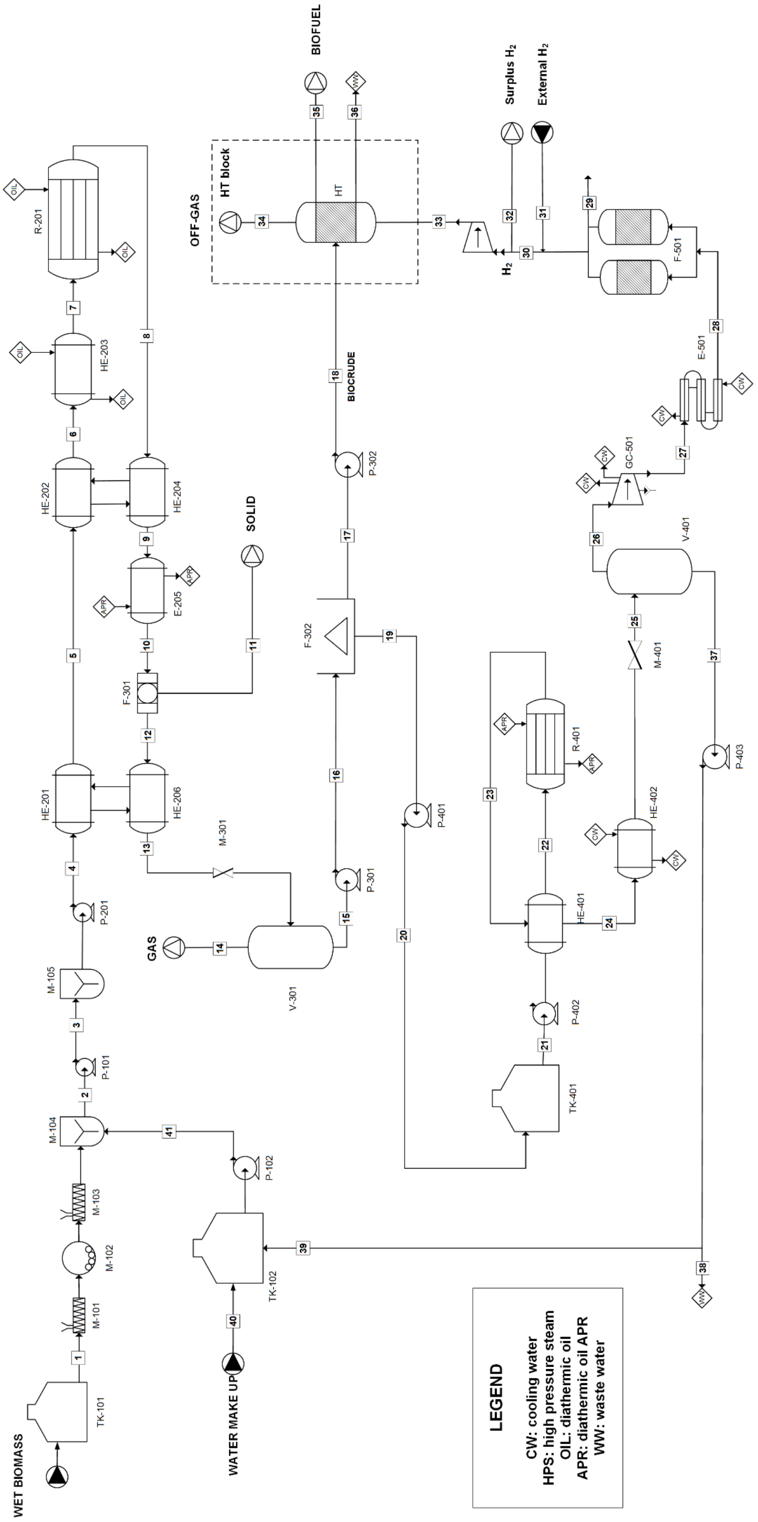

Figure 81: Simplified process flow diagram for the HTL-APR biorefinery (corn stover case).

The model was developed in a Microsoft Excel© spreadsheet where mass and energy balances were performed based on results from experimental work of the research group on LRS-HTL and APR; when own experimental data were not available, results from the literature were used. Based on the balances, the design of the equipment was performed[273,274]. The equipment of the gas purification and upgrading sections (heat exchangers, trim heater and hydrotreatment reactor) were not designed in detail, but their costs were evaluated based on correlations derived from the literature. The preliminary process flow diagram is reported in Figure 81. The equipment list is reported in the appendix (Table A1).

Pre-treatment

HTL is fed by a lignin-rich/corn stover stream being a byproduct of a cellulosic ethanol plant and an agricultural residue, respectively. Due to the high water-content in the LRS case (70% moisture), the plant was assumed to be built next-door to the ethanol plant to avoid dewatering of the LRS matrix and high transport cost. The LRS is therefore temporarily stored, milled, and then mixed with recycled and make-up water.

The corn stover is instead harvested three months per year and is stocked to guarantee a continuous flow rate throughout the whole year. The longer time storage than LRS is possible assuming a higher biological stability guaranteed by the reduced amount of residual moisture (5.4 wt.%[76]). Afterwards, corn stover is milled and mixed with water for the slurry formation. In order to provide a representative scenario of local biomass availability, the corn production in the province of Turin (Piedmont, Italy) was 522 kt in 2019[275]. Since the ratio between corn production and stover is 1:1[272], 522 kt of corn stover were present in Turin province. Therefore approximately 5% of production was needed to meet the plant target capacity, which is a reasonable size that does not pose particular problems in terms of biomass collection and transport logistics.

Hydrothermal liquefaction

The main parameters for the HTL reaction, along with details on product distribution, are outlined in Table 13. Please note that with the term ‘biocrude’ is hereafter defined the raw oil from HTL, while as ‘biofuel’ is defined the upgraded product. For the LRS case, product distribution data were derived from HTL experiments performed by the research group in a batch reactor at 350°C for 10 minutes, with a 10% biomass to water ratio and no additives[276]. Since the gas phase was not characterized, its composition was based on typical literature values[277].

As far as corn stover is concerned, carbon distribution and aqueous phase composition (0.2 wt.% methanol, 0.88 wt.% acetic acid and 1.68 wt.% glycolic acid) were calculated as average values of those experiments conducted by Panisko et al. that had operating condition similar with those used in this work[163]. The distribution among each of the different phases were derived from Mathanker et al.[76], since they were not present in[163]. Gas composition was estimated to be the same as in the LRS case, while ash distribution was determined based on mass balances with inorganic elements, as explained below (‘*Aqueous phase recycling*’ paragraph). Additional information on the properties of biocrude and solid for the two scenarios is available in Table 12.

Table 13: Main reaction conditions and assumptions of the LRS and CS scenarios.

HTL DATA	**LRS**	**Ref**	**CS**	**Ref**
Temperature (°C)	350	276	350	163
Pressure (bar)	200		200	
Solid loading (wt.%)	10%		10%	
	Carbon distribution wt. % (*db*)			
Biocrude	53%	276	49%	76
Aqueous phase	16%		38%	
Gas	15%		10%	
Solid	16%		4%	
APR DATA				
Temperature (°C)	270	278	270	Experimental
Pressure (bar)	60		60	
Catalyst	5%Pt/C		5%Pt/C	
WHSV (kg_C/kg_{cat} h)	0.28		0.40	
Carbon to Gas (CtoG)	20%		48%	
kg H_2/kg C feed	0.037		0.084	
	Gas composition vol.% (*db*)			
H_2	62	278	68	Experimental
CO_2	28		28	
CH_4	9		4	
C_2H_6	1		0	
HT DATA				
Temperature (°C)	400	279	400	279
Pressure (bar)	104		104	
Catalyst	CoMo/alumina		CoMo/alumina	
WHSV ($kg_{biocrude}/kg_{cat}$ h)	0.81		0.81	
	Product distribution			
Biofuel yield*	74.4%	279,280	80.0%	279,280
Water yield*	30.9%		23.5%	
Gas (C1-C6) yield*	2.9%		2.8%	
	Hydrogen consumption			
H_2 to reactor (kg H_2/kg dry biocrude)	0.083	279,280	0.066	279,280
H_2 consumed (kg H_2/kg dry biocrude)	0.042		0.033	
H_2 make-up (kg H_2/kg dry biocrude)	0.048		0.038	

*HT yields are defined as mass of each product (biofuel, water or gas) per mass of dry biocrude. Since H_2 is not considered in the definition, the products sum results higher than 100%.

Product separation

There are four different phases at the outlet of the HTL reactor, therefore an effective product separation is crucial to guarantee a high biofuel yield. In this chapter the proposed product separation consists of: high-temperature and pressure filtration (solid separation), flash separation (gas separation), and centrifugation (liquids separation). Among the by-products, the gas phase contains mainly CO_2 and has negligible calorific value (LHV= 0.27 MJ/kg); the solid is burned to provide a portion of the heat required by the plant, while the aqueous phase is sent to the APR section.

Aqueous phase reforming

APR is performed in a catalytic (5 wt.% Pt/C) fixed bed reactor which converts the carbon-laden water fraction into a gas phase rich in hydrogen by operating at 270 °C and 60 bar. The catalyst amount was calculated assuming the same weight hourly space velocity (WHSV) used in the laboratory scale tests. Its lifetime was assumed equal to 1 year, being this a conservative choice with respect to alternative hypothesis reported in literature[258].

Experimental APR results from the LRS-derived HTL-AP were taken from previous tests performed by the research group[278]. In the CS-derived aqueous phase, APR performances were experimentally evaluated on a synthetic mixture whose composition is in agreement with the one from Panisko et al.[163]. The APR results for LRS and CS cases are reported in Table 13.

Purification

Since the gas phase from APR is a mixture constituted by hydrogen, carbon dioxide, methane etc., it is necessary to separate the desired product from other impurities. For this reason, pressure swing adsorption (PSA) is adopted in this work, assuming for simplicity, 100% hydrogen purity and 85% hydrogen recovery[258]. These assumptions align with the available literature, which indicates that PSA has been the conventional technique for obtaining high-purity hydrogen, especially at a small scale[281]. This stream is utilized for hydrotreating the biocrude in the upgrading section, and any excess quantity is sold as coproduct.

Upgrading

The biocrude cannot be used as drop-in fuel due to the amount of heteroatoms (N, O, S), hence a subsequent upgrading step is required. For this purpose, it was decided to consider only the hydrotreatment step (HT)[277].

Hydrotreatment (HT) step converts biocrude into biofuel by catalytic (CoMo/alumina) hydrogenation at 400 °C and 100 bar of hydrogen[279]. Due to the limited knowledge on upgrading of biocrude from LRS-HTL, the consumption of hydrogen was derived from extrapolation of data from the literature[280]. Specifically, based on the work of PNNL[280] the ratio between the actual hydrogen rate and the amount of stoichiometric hydrogen required to convert all oxygen into water and all nitrogen into ammonia was calculated, resulting equal to 1.36. The resulting hydrogen consumptions were 0.042 (LRS) and 0.033 (CS) kg H_2/kg dry biocrude, resulting similar to values present in the literature[150,277,282]. The hydrogen to be sent to the hydrotreater has been set to two times the amount of hydrogen consumed, as a similar excess is usually designed[280,283]. Moreover, since the excess hydrogen was purified with a PSA unit having a 85% recovery efficiency, the effective hydrogen demand at the HT plant is equal to 1.15 the hydrogen reacting during hydrogenation.

Due to the low TRL of the hydrotreatment step with regards to the biocrude upgrade, a sensitivity analysis was carried out by varying the amount of hydrogen required for the hydrotreatment. This choice allows to take into account the inherent uncertainties related with this technology. Moreover, it is worth noting that after hydrotreatment, the biofuel should be distilled to separate the different fractions, and the heavy residue could be hydrocracked to maximize the lighter distillates. This further step was not evaluated in this chapter, as also done in other works[284,285], because upgrading is not yet well established for biocrude from HTL of lignin-rich residue. Hence, the design of subsequent distillation and hydrocracking would be speculative. Moreover, this choice is justified by the fact that typically the capital cost and hydrogen consumption of a hydrocracking section is limited compared to HT[259,286,287]. To account for the uncertainties related to this assumption, variations in biofuel yield and HT investment cost were investigated in the sensitivity analysis of the economic assessment, as well as in the Monte Carlo simulation for the life cycle assessment.

The carbon yield of subproducts was adapted from[279,280]. In addition to biofuel, an off-gas containing the excess hydrogen is produced. This hydrogen must be separated and purified through PSA to recycle it at the inlet of the reactor. The residual off-gas (LHV=46.6 MJ/kg) is sent to the gas-burning furnace to recover its residual calorific value, while ammonia was assumed to be recovered mostly in the wastewater as reported from the literature[288]. Table 13 summarizes the yields of subproducts from dry biocrude are reported for both cases. The catalyst amount was calculated assuming a weight hourly space velocity (WHSV) equal to 0.81, as suggested by PNNL[279], and with a useful life of 2 years.

When APR could not meet the entire hydrogen demand for biocrude upgrading, a hydrogen generation system was considered to fill the shortfall. In the baseline scenario it was assumed to be comprised of an alkaline electrolysis system[289]. Given that the hydrogen production technology has a significant impact on the final fuel selling price, an alternative process was considered for comparison, i.e., steam reforming of natural gas. In order to carry out its design, technical parameters based on commercial plants were used, and the catalyst was assumed to have a 5-years lifespan[279]. The methodology followed, i.e., designing an on-site hydrogen generation plant rather than considering hydrogen as an operating cost, is commonly performed in literature for similar systems[287,290–292]. This approach takes into account the decentralized nature of biorefineries, which would incur high costs for transportation and delivery if hydrogen were to be derived from a centralized plant. Additionally, it allows for a more precise estimation of the hydrogen price than average data available in databases, thanks to its sensitivity to the plant size.

Aqueous phase recycling

Due to the consistent amount of water required, wastewater at the outlet of the APR was recycled to dilute inlet feedstocks. This recycling improves the sustainability and cost-effectiveness of the process by reducing the supply of fresh water and the disposal of wastewater. For the LRS case, the effect of the recycling was tested through preliminary batch experiments. In the LRS case, the three main inorganic elements were Na, K and Ca, probably in the form of carbonates.

For the CS case, the main inorganic elements present in the aqueous phase (Na, K) were evaluated from Panisko et al.[163]; the inorganic distribution to biocrude and char was assumed to be equal to the one of LRS. The hypothesis is based on the findings of Toufiq Reza et al., which observed that most of the ash content in corn stover can be found in its lignin fraction[293]. In both cases, a large amount of inorganic compounds remains in the aqueous phase and a purge is therefore necessary to avoid their build-up. APR tests were carried out with water containing up to 3000 ppm of Na and no deactivation was observed. To evaluate the purge ratio, it was assumed that the recirculation did not change the inorganic distribution between the phases. As the purge ratio varied, it was possible to calculate the amount of inorganics present in the recycling loop. The amount of recycled water was hence evaluated to not exceed the 3000 ppm of inorganics at the inlet of the APR reactor.

In addition to inorganic compounds, a build-up of organic was also present, especially acetic acid[210]. Therefore, its presence can be considered as ‘inert’ carbon. To this end, the carbon content soluble in the aqueous phase exiting the APR reactor was considered inert throughout the HTL and APR processes. By determining the purge ratio, it became possible to ascertain the quantity of 'inert' carbon within the recycling loop. The amount of fresh water needed to dilute the feedstock was calculated accordingly to the purge ratio.

7.2.3 Economic assessment

Capital costs

The economic analysis was performed considering preliminary estimates, which have a typically accuracy of ±30%, in accordance with the Association for the Advancement of Cost Estimating International (AACE International)[294]. Fixed capital investment was based on the grassroots costs evaluated by the module costing technique described by Turton et al.[295]. Grassroots costs are related to the construction of a new facility and include direct and indirect costs, contingency, fee and auxiliary facilities costs. The module cost technique relates plant costs to the purchased cost of each piece of equipment, based on Guthrie method[296]. If correlations for bare module cost were not present in [295], these were taken from [296] or from extrapolation from other sources. Due to the pandemic situation, the costs were discounted to 2019 through the CEPCI factors ($CEPCI_{1968}$=112; $CEPCI_{2001}$=397; $CEPCI_{2019}$=608) and converted in euros (USD/EUR=1.11).

Purchased cost of each piece of equipment (C_P^0) was evaluated through a polynomial equation having as input the capacity or size parameter (A) of the piece of equipment itself (Eq. (28)). This cost is referred to the purchase of base equipment operating at ambient pressure and made of carbon steel. Bare module cost (C_{BM}) considers all the costs (direct and indirect) required for the installations and depends on material (F_M) and pressure factors (F_P) (Eq. (29)-Eq. (30)).

Silos and mill weren't described by Turton and the compressor size didn't fit into the useful range. Consequently, these equipment costs were evaluated through Guthrie[296]. Guthrie is based on an exponential law using a base cost (K) multiplied by the characteristic size raised to a size exponent (n) (Eq. (31)). Correction factors are a function of material (F_m), pressure (F_p) and design factors (F_d) (Eq. (32)). Evaluation of the bare module cost requires direct field material and labor cost factor ($F_{M\&L}$) and indirect cost factor (F_{IND}). The latter was assumed to be equal to 1.34 whenever it wasn't reported. Taking into account these contributions, Eq. (33) was obtained.

$$log_{10} C_P^0 = K_1 + K_2 \cdot log_{10}(A) + K_3 \cdot [log_{10}(A)]^2 \qquad (28)$$

$$F_{BM} = B_1 + B_2 \cdot F_P \cdot F_M \qquad (29)$$

$$C_{BM} = C_P^0 \cdot F_{BM} \qquad (30)$$

$$C_P^0 = K \cdot A^n \qquad (31)$$

$$F_c = f(F_m, F_p, F_d) \qquad (32)$$

$$C_{BM} = C_P^0 \cdot (F_c + F_{M\&L} \cdot F_{IND} - 1) \qquad (33)$$

PSA bare module costs were evaluated with the correlation described by Sladkovskiy et al. (Eq. (34))[258]. This was based on a 85% hydrogen recovery; input parameter was the hydrogen production rate (G_{H2}), expressed in kg/h.
Filtering system bare module costs were based on data from the NREL[297] (Eq. (35)). The size parameter was the flow rate in gpm of liquid that must be treated.

Hydrotreatment bare module costs were evaluated through Eq. (36). The mass rate (kt/y) of biocrude to be hydrotreated was chosen as the size parameter. The coefficients were evaluated through extrapolation of TEA data reported in literature[286,288]. Steam reforming (SR) plant bare module costs were evaluated through Eq. (37). The mass rate (kt/y) of hydrogen produced was chosen as size parameter. The coefficients were evaluated through extrapolation of data in TEAs reported in the literature[286,288,298]. The bare module cost of the alkaline electrolysis system was assumed equal to 800€/kW of installed power[299] and the system efficiency was set to 56%[289].

Total module cost (C_{TM}) also includes contingencies and fees which were assumed equal to 15% and 3% of the bare module cost, respectively (Eq. (38)). Grassroots cost (C_{GR}) takes into account also the auxiliary costs of construction of the new plant and it was calculated as the total module cost plus 50% of the bare module cost of the piece of equipment at base conditions (C_{BM}^0) (Eq. (39)).

$$C_{PSA} = (447846 + 3407 \cdot G_{H2}^{0.8}) \cdot 1.2 \cdot (608/402) \cdot 0.93 / 1.11 \tag{34}$$

$$C_{FILTER} = 1311000 \cdot (G_{FEED}/3689)^{0.6} \cdot 1.7 \cdot (608/585) \cdot 0.93 / 1.11 \tag{35}$$

$$C_{HT} = (357000 \cdot G_{crude}^{0.7727}) \cdot (608/603) \cdot 0.93 / 1.11 \tag{36}$$

$$C_{H2\,plant} = (4458000 \cdot G_{H2}^{0.70429}) \cdot (608/603) \cdot 0.93 / 1.11 \tag{37}$$

$$C_{TM} = C_{BM} \cdot (1 + Contingency\% + Fee\%) \tag{38}$$

$$C_{GR} = C_{TM} + 50\% \cdot C_{BM}^0 \tag{39}$$

Operating costs

Operating costs were evaluated using the unit costs shown in Table 14. All items, except for the feedstock cost, were assumed to be equal in both simulations.

Table 14: Data for the material & utilities costs.

Item	Price	Unit	Ref.
LRS feedstock (*db*)	60	€/t	300
CS feedstock (*db*)	75	€/t	301
Electric power	0.09	€/kWh	302
Natural gas	0.35	€/Nm^3	303
Cooling power	0.9	€/MWh	284
Make-up water	3.5	€/t	291
Wastewater disposal	0.064	€/kg COD	287

APR catalyst	45	€/kg	258
HT catalyst	28	€/kg	279
SR catalyst	6.54	€/t H_2	279
H_2 selling price	5	€/kg H_2	304

Feedstocks costs were assumed to be 60 €/t for lignin-rich stream and 75 €/t for corn stover, as found in literature[300-301]. Costs for electric power and natural gas were average values present in the EU market in 2019. Regarding the APR catalyst, Sladkovskiy et al. reported the possibility of neglecting the cost of Pt due to its possible recovery at the end of its lifetime[258]. For the evaluation of the overall operating cost, the labor and maintenance costs were added to the material & utilities cost. Labor cost was assumed to be 56 100 €/y per operator and the number of operators was calculated based on the Turton method[295]. Other workers were also added as executives and employees/managers, having costs of 100 000 €/y and 80 000 €/y, respectively. Maintenance was assumed equal to 5% of the sum of fixed capital investment and startup cost every year.

Minimum selling price

The objective of the chapter was to define the minimum selling price (MSP) of the biofuel; this was carried out using the 'Discounted Cash Flow' (DCF) method. The depreciation and plant life were fixed to 20 years and the main set parameters are reported in Table 15. Maintenance cost takes into account both ordinary and extraordinary maintenance due to the long plant life.

Table 15: Economic set parameters.

Parameter	Value
Startup cost	5% of fixed capital investment
Working Hours	8 000 h/y
Depreciation time	20 y
Starting ratio equity/debt ratio	75%/25%
Income tax rate	33%
Internal rate of return (IRR)	0% - 10%

Please note that the figures evaluated in the twenty-year projection profile are real values. It means that they were kept constant throughout the entire life plant, without considering possible variations dependent on inflation trends.

As regards the return on invested capital, two hypotheses were considered:

(1) Contribution of the necessary equity by a public operator, non-profit making, in pursuit of environmental objectives with generation of positive non-economic externalities (IRR=0%).

(2) Contribution of the equity by a private operator, pursuing profit objectives (IRR = 10%).

Two MSPs values were hence herein evaluated, differentiated by internal rate of return (IRR). The use of a MSP with an IRR=0% (hereafter referred to as $MSP^{0\%}$) was justified by the fact that the specificity of the energy sector and the need for public incentives for the ongoing ecological transition may consider the assumption of public support to the initiative. On the other hand, MSP with an IRR=10% (hereafter referred to as $MSP^{10\%}$) is usually used as reference parameter to evaluate biofuel profitability[286,290,292,301,305–307]. Based on this, the $MSP^{0\%}$ was calculated to assess the profitability of the plant and to perform the sensitivity analysis. The $MSP^{10\%}$ was instead evaluated to be consistent with the literature and to allow for comparison with other TEAs based on technology differences rather than different economic management assumptions.

The production of hydrogen used for biocrude upgrading via APR is one of the actual benefits of the coupling of these two processes. Therefore, it is worthwhile to evaluate the hydrogen production cost by this technology. Since the two sections are thermally integrated, it was not possible to quantify it by only considering the APR section. Hence, it was quantified by difference, i.e., by subtracting the contribution of a virtual plant, where the APR section is not implemented, from the overall costs of the integrated HTL-APR plant. The hydrogen production cost was then evaluated as ratio of the difference in costs to the amount of hydrogen that APR can produce with the integrated plant (Eq. (40)). When electrolysis was necessary (LRS scenario), its cost was not taken into account for a safe comparison.

$$H_2\ production\ cost_{APR} = \frac{\sum costs_{HTL+APR} - \sum costs_{\ HTL}}{H_2\ mass\ production\ (APR)} \tag{40}$$

Sensitivity analysis

At the end, a sensitivity analysis was conducted to study the effects of some fundamental parameters (operating costs, hydrotreatment step parameters, investment, plant life, catalyst cost and nominal size) on the biofuel cost. Furthermore, scenarios with different sources of hydrogen (SR plant or alkaline electrolyzer) were compared with the HTL-APR coupling.

Table 16 reports the variations used for the sensitivity analysis. The determination of the feedstocks price is intrinsically complicated by the fact that a market for lignin and corn stover has not yet been established. For this reason, the effect of a change in the cost of LRS and CS was investigated by varying it in a wide range (± 50%). As regard electricity and natural gas cost variations, the minimum and maximum costs from EU countries in 2019 were taken as ranges for the sensitivity.

To assess the impact deriving from the uncertainties in the hydrotreatment step, the amount of hydrogen required for the upgrading and the biofuel yield were varied. The range for the hydrogen required was considered between the lowest and highest values found in the literature for lignocellulosic feedstocks (26-40 g/kg dry biocrude[150,282]). The HT-biofuel yield was changed within ±5%, in accordance with common procedures carried out in similar TEA[282].

The MSP variation was assessed for different plant life, plant size and different total and hydrotreatment-related investment cost. Total investment costs were varied within ±30%, according to the accuracy of the used method[294], while HT investment costs were modified on a wider range (±50%) due to the higher uncertainties. In addition, the influence of catalyst cost on the minimum fuel selling price was assessed, considering a 52-153 €/kg range[308]. The upper value was derived from the work of Baral et al., correcting by the lower metal loading used herein (5%) with respect to the reference (10%). This analysis was carried out to take into account the impact of limitations in the noble metal catalyst recovery ability on the economic profitability of the plant.

The impact on the MSP was also assessed in the case of a 20% solid loading in the inlet slurry. The carbon distribution and elemental composition of the products, as well as the APR reaction parameters, were maintained equal to the 10% solid loading case. This assumption was in agreement with experimental tests performed by the research group (LRS case) and a previous work by Zhu et al.[277] (CS case). In order to take into account the differences in the slurry rheological properties, pumps and heat exchangers for the 20% solid loading case were sized assuming an increase in the slurry viscosity of 10 000 times compared to that of water (used for the 10% case). This assumption was based on slurry viscosity range from PNNL[297].

Table 16: Variations used for the sensitivity analysis.

Item	Min	Max	Unit
Feedstock price	-50%	+50%	%
Electricity price	54	144	€/MWh
Gas natural price	0.23	0.61	€/Nm^3
APR catalyst price	-	153	€/kg
H_2 consumption	26	40	g/kg biocrude
Biofuel yield	-5%	+5%	%
Plant life	15	30	y
Plant size	10	40	MW_{th}
Total investment cost	-30%	+30%	%
HT investment cost	-50%	+50%	%
Solid loading	-	20%	wt.%

As one of the key aspects of this work concerns the production of hydrogen needed for upgrading, the economic impact of replacing the hydrogen derived from the APR section was evaluated. Steam reforming and electrolysis were the two H_2-

producing technologies compared with APR, since they represent respectively the most established way and the most investigated decarbonized option.

7.2.4 Life-cycle assessment

Goal and scope definition

The goal of this life-cycle assessment was to assess the environmental impacts of producing advanced biofuels from LRS or CS feedstocks through a combined HTL-APR plant. An attributional cradle-to-gate LCA was developed, following the approach reported in literature[309]. The system boundaries comprehend the processes from the feedstock collection to the biofuel production (Figure 82), while its utilization is out of the scope of the assessment. Figure 82 shows a simplified block flow diagram for each scenario investigated in this work. The transport and use phase of biofuel were considered only for the global warming (GWP) quantification to enable a comparison with fossil fuels. Since the function of biofuel is to provide energy, 1MJ of biofuel was chosen as functional unit, as recommended by EU RED[310]. Its properties (water and ash content, elemental composition, etc.) are assimilable to those of a diesel, and 43 MJ/kg is considered its lower heating value. The plant location was assumed to be in Europe.

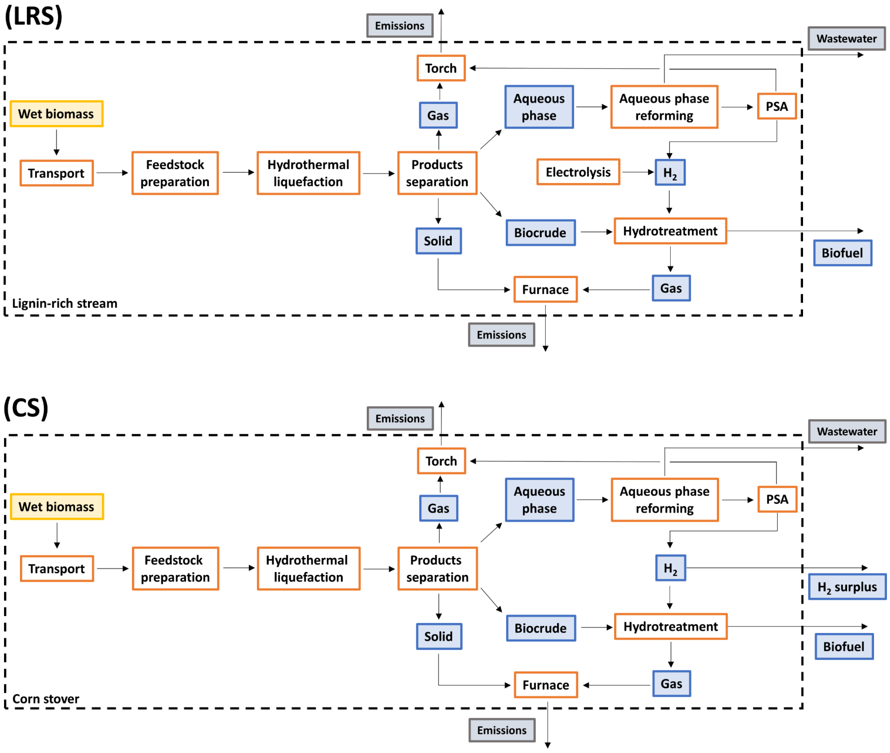

Figure 82: System boundaries of the HTL-APR biorefinery for lignin-rich stream (A) and corn stover (B) feedstock.

When dealing with the LCA of biomass, it is crucial to define its nature: in other words, it should be determined whether it is an energy crop, a residue or a waste[311]. The lignin-rich stream was assumed to be a waste; it is a by-product of a 2nd generation bioethanol plant, and its residual value can be considered zero. On the other hand, corn stover must be considered a residue. It is left on the field after corn harvesting and its value derives from its contribution to soil organic matter[311]. For this reason, land use change aspects, such as the impact deriving from harvesting and replacement of soil nutrients, were accounted in the CS-case[312].

As described below, in the LRS-case the HTL-derived biofuel was the only product, and no allocation was required. In the CS-case, , a surplus hydrogen stream was produced by the APR process, in addition to the HTL-derived biofuel. To account for these two products, different allocation methods were investigated, namely mass, energy and economic-based approaches. However, in all cases the impact related to the hydrogen product was negligible. Under a mass-basis, the hydrogen flowrate was only 0.4% of the biofuel flowrate (2.9 kg/h vs 841 kg/h); under an energy-basis, the hydrogen power was 1% of the biofuel power (being H_2 LHV=120 MJ/kg and biofuel LHV=43 MJ/kg); under an economic-basis, hydrogen counted for 1.1% of the biofuel value (assuming the H_2 selling price as green H_2 – 5 €/kg – and the biofuel selling price as the one derived from the TEA – 1.62 €/kg). For all these reasons, it emerged that the impacts obtained in the CS-case can conservatively be attributed to the biofuel production only. On the other hand, it is worth noting that in the case of the lignin-rich stream, the APR section was not able to provide all the required hydrogen. For this reason, an electrolyzer was assumed to proved the missing quota of hydrogen for the complete upgrading of biocrude.

Cut-off criteria for materials and construction energy were considered to perform the LCA, in accordance with the literature and the ILCD Handbook guidelines. To this end, a cut-off of 1% of total mass was applied; this assumption was confirmed by performing a preliminary assessment (on the materials required for the construction of the equipment, the hydrotreating catalyst and make-up streams) which resulted in an impact of less than 0.5% in each impact category. For this reason, they were not taken into account hereafter. On the other hand, the impact of replacing the APR catalyst (Pt/C) was evaluated due to its higher environmental footprint.

Four impact categories were considered for the environmental characterization:

- Global warming potential (GWP): this impact category has been chosen due to the importance of climate change mitigation in the current European and international policies;
- Acidification potential (AP): it is one of the most investigated impact category in the literature[311]. It refers to the release of acid rain precursors;

- Eutrophication potential (EP): it is due to the discharge of nutrients (e.g., phosphorous and nitrogen) into the environment, which eventually leads to a potential loss of biodiversity;
- Fossil depletion potential (FDP): it is related to the extent to which non-renewable resources are used. Herein, they were considered as reciprocally substitutable fossil fuels (i.e., oil, natural gas and coal) with equal characterization factor. Its evaluation is critical to assess the actual reduction of fossil fuel depletion when considering biofuels.

Therefore, this chapter does not only take into account the environmental burden derived from greenhouse gas emissions, as sometimes reported for other biofuels-related works[313,314], but expands its investigation to other categories which are considered particularly important in addressing the environmental footprint of a biofuel[315]. To facilitate the comparison with impacts from the literature, CML 2001 baseline (version 2016) method was used.

When dealing with biomass, an important discussion point is the assessment of biogenic carbon, which is emitted as CO_2, CO or CH_4 directly attributable to biomass. These emissions might be not considered, as they are derived from the carbon that has been sequestrated during its growth, thus resulting in a net zero impact. However, a consensus on the most appropriate way to consider biogenic carbon in LCA has still not been reached. An issue is the lag time between uptake and release of CO_2, which is particularly severe when dealing with long-rotation period biomass. In this chapter, the climate change impact results are given without taking into account the biogenic carbon emissions, following the ‘0/0 approach’ (neither uptake from the environment nor emissions).

Inventory analysis

The material and energy balances, as well as the design of the main equipment, were based on the results obtained from the design and techno-economic assessment. Table 17 depicts the life cycle inventory related to 1 MJ of biofuel for the corn stover and lignin-rich stream scenarios. In Table 17 are reported the datasets used from GaBi as secondary source. The primary data on biocrude yield, hydrogen production from APR, mass and energy balance were collected from experimental results of the authors[162]. In addition, some assumptions or literature data were necessary to fill specific inventory gaps. In particular:

- The lignin-rich stream was assumed to be a waste, so no environmental burden was associated with it. Corn stover was assumed to be a residue, so impacts deriving from transport and harvesting were taken into account. Biomass transport was considered equal to a 50 km distance covered by truck. The impact due to harvesting was modelled taking into consideration the diesel used for corn stover collection and the use of fertilizer to replace soil nutrients (NPK 15-15-15 from GaBi database)[312];

- For background processes (e.g., thermal and electric energy by European mix), data from GaBI database were used. The cooling power was converted from thermal to electrical energy, as described in technical literature[316]. Natural gas was chosen as the thermal energy source;
- The electric grid mix used in this chapter consisted of various sources: fossil fuels (41.5%), nuclear (27.6%), wind (8.0%), hydro (12.8%) and others (e.g., solar, geothermal, etc.). This distribution is similar to the one reported by the European Commission for the 2019[317];
- The direct CO_2 equivalent flue gas emissions reported in Table 17 account for the combustion of solid and HT-derived off-gas along with the flue gas obtained after torching HTL-gas and PSA off-gas. The breakdown between the different sources is reported in Table 18. The carbon dioxide production from solid and off-gas combustion was calculated based on stoichiometry and complete conversion. It is crucial noting that all these CO_2 represent the biogenic quota, as the carbon was present in the starting feedstocks. The indirect emissions attributable to heating and all other utilities were evaluated separately and are not reported in Table 17 as CO_2 eq;
- The environmental performance of electrolysis for hydrogen production was obtained from mass/energy balances from literature[289]; the environmental performance of steam reforming (SR) when used for hydrogen production was taken from GaBi database;
- The impact of wastewater treatment was assessed by adjusting the parameters in the GaBi model for EU-28 wastewater treatment. This involved setting the COD levels to 18.6 g/L (LRS) and 14.3 g/L (CS), and the total ammonia content to 1.7 g/L (LRS) and 0.9 g/L (CS), as determined by mass balance calculations;
- The catalyst lifetime (platinum-based) was set at 1 year, lower than other assumptions reported in the literature[258], as a conservative measure. The data for platinum impact were taken from the literature based on a 28% platinum recycling[318].

An uncertainty analysis was carried out to evaluate the confidence of the obtained results due to intrinsic uncertainties related to key variables (i.e., biofuel yield, required hydrogen for upgrading, thermal duty, electric duty, APR catalyst demand and wastewater treatment). In order to reach this objective, Monte Carlo simulations with 10 000 iterations were performed by simultaneously modifying the variables with a triangular distribution within a chosen range and the obtained results were depicted by box and whisker plots.

Table 17: Life cycle inventory of 1 MJ biofuel for LRS and CS cases.

Inputs/ Outputs/	Item	LRS-case	CS-case	Unit	Dataset

Emissions					
Inputs					
	Diesel for harvesting	-	0.023	MJ	Diesel mix at refinery (EU-28)
	Fertilizer replacement	-	0.90	g N	NPK 15-15-15 (nitrophosphate route, 15N-15P2O5-15K2O) (EU-28)
	Biomass transport	-	50	km	Truck, Euro 6, 28 - 32t gross weight/22t payload capacity (GLO)
	Feedstock (wb)	0.27	0.11	kg	-
	Process water	0.017	0.26	kg	Process water (EU-28)
	Hydrogen	1.2	-	g	Modelled according to [289] for electrolysis; Hydrogen steam reforming (DE) for SR
	Electricity	0.095	0.025	kWh_{el}	Electricity grid mix (EU-28)
	Heating	0.020	0.098	kWh_{th}	Thermal energy from natural gas (EU-28)
	Cooling	0.094	0.10	kWh_{th}	Modelled according to [316]
	Platinum (APR catalyst)	0.39	0.65	mg	Modelled according to [318]
Output					
	Biofuel	23	23	g	-
	Hydrogen	0.00	0.08	g	-
Direct Emissions					
	CO_2 eq (biogenic)	55.0	37.8	g	-
	Ash	0.40	1.00	g	Municipal solid waste on landfill (EU-28)
	Wastewater	0.22	0.31	kg	Wastewater treatment (EU-28)

Table 18: Breakdown between the sources of biogenic CO_2.

	LRS-case	CS-case
HTL solid (furnace)	25.8	6.4
HT off gas (furnace)	2.6	2.4
HTL gas (torch)	21.9	14.3
PSA off gas (torch)	4.7	14.6
Total	55.0	37.8

7.3 Results and discussion

7.3.1 Design

Mass balance

Table 19 and Figure 83 shows the main inputs and outputs of the plant.

Table 19: Main input and output streams.

Stream	LRS	CS
	Main input (kg/h)	
Feedstock (*wb*)*	12 000	3 805

Feedstock (*db*)*	3 600	3 600
Make-up water	780	9 706
Relevant internal streams (kg/h)		
Water from recycling	23 220	22 489
HTL inlet	36 000	36 000
H_2 required for HT	67	40
H_2 produced from APR	13	43
H_2 missing quota	55	0
Main output (kg/h)		
Biocrude (*db*)	1 406	1 050
Biofuel (*db*)	1047	841
H_2 surplus	0	3
Solid char	619	171
Wastewater	10 169	11 091

* feedstock of the plant (corn stover or lignin-rich stream).

Concerning biocrude production, the two cases exhibited a mass yield (dry biocrude/dry feedstock) of 39.0 wt.% (LRS) and 29.0 wt.% (CS). Subsequently, the biofuel yields post-upgrading were 29.1% (LRS) and 23.4% (CS). The hydrogen yield of the HTL-APR integrated plant was lower with LRS (0.039 Nm^3/kg dry LRS) than with CS (0.131 Nm^3/kg dry CS). The difference was due to the higher organic concentration in the AP for the CS case and to the presence of compounds with higher hydrogen productivity. Moreover, due to the higher oxygen content and mass flow of biocrude, the hydrogen required for upgrading was greater with LRS than with CS. It follows that, in the LRS case APR could only supply 19% of the hydrogen required for hydrotreatment, whereas the HTL-APR coupling with CS was particularly advantageous in that it resulted in a surplus of hydrogen (107% of the amount required), which was assumed to be sold.

A higher solid yield was obtained using LRS, compared with CS, and this stream was not valued as coproduct but instead was energetically exploited in situ. Wastewater purge ratios resulted equal to 0.29 (LRS) and 0.32 (CS). In this way, the amount of inert carbon at APR outlet were 34.8 g C/L (LRS) and 26.7 g C/L (CS) while inorganic compounds remained below 3000 ppm. The amount of water required to dilute the slurry was calculated from purging, promoting the sustainability of the process. The demand for fresh water was limited to 3.3% (LRS) and 30.1% (CS) of the overall water demand.

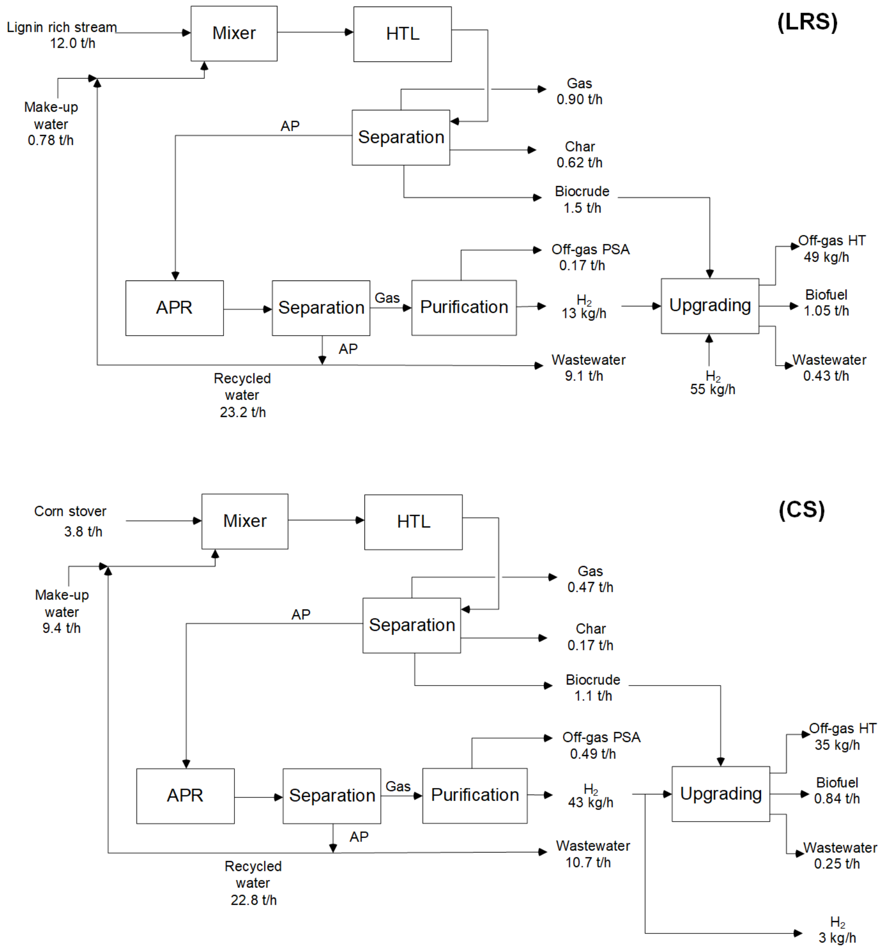

Figure 83: Mass flows for the LRS case (above) and the CS case (below).

Energy balance

The block diagram in Figure 84 shows the energy streams for both cases. Several heat exchangers allow the partial recovery of thermal power from the HTL products stream, resulting in savings of 11.9 MW$_{th}$ (LRS) and 12.6 MW$_{th}$ (CS). After the economizers, the remaining heat is provided by diathermic oil from the furnace. The char combustion in the furnace, allows to save 3.2 MW$_{th}$ (LRS) and 0.8 MW$_{th}$ (CS). The heat required for the APR section is completely provided by the economizer, able to preheat the feed and to cool down the liquid product, and by the thermal integration with the HTL section. Before gas separation and after compression of the product gas (purification section) further heat must be removed. For the LRS plant, an additional amount of heat from the electrolyzer shall be removed (1.1 MW$_{th}$). The upgrading section required 0.2 MW$_{th}$ to heat up the biocrude for hydrotreatment that it is partially provided by the off-gas sent to the furnace, leading to a positive thermal balance of the upgrading section.

The overall energy consumptions are shown in Table 20. The overall required thermal power was similar between the two cases (41 GWh/y for LRS and 40 GWh/y for CS); however, due to a lower production of char and off-gas from upgrading, the net thermal demand provided with natural gas was higher with CS. Cooling power did not differ strongly between the two cases while the discrepancy between the electricity consumption was mainly due to the energy cost (26 GWh/y) of the electrolyzer.

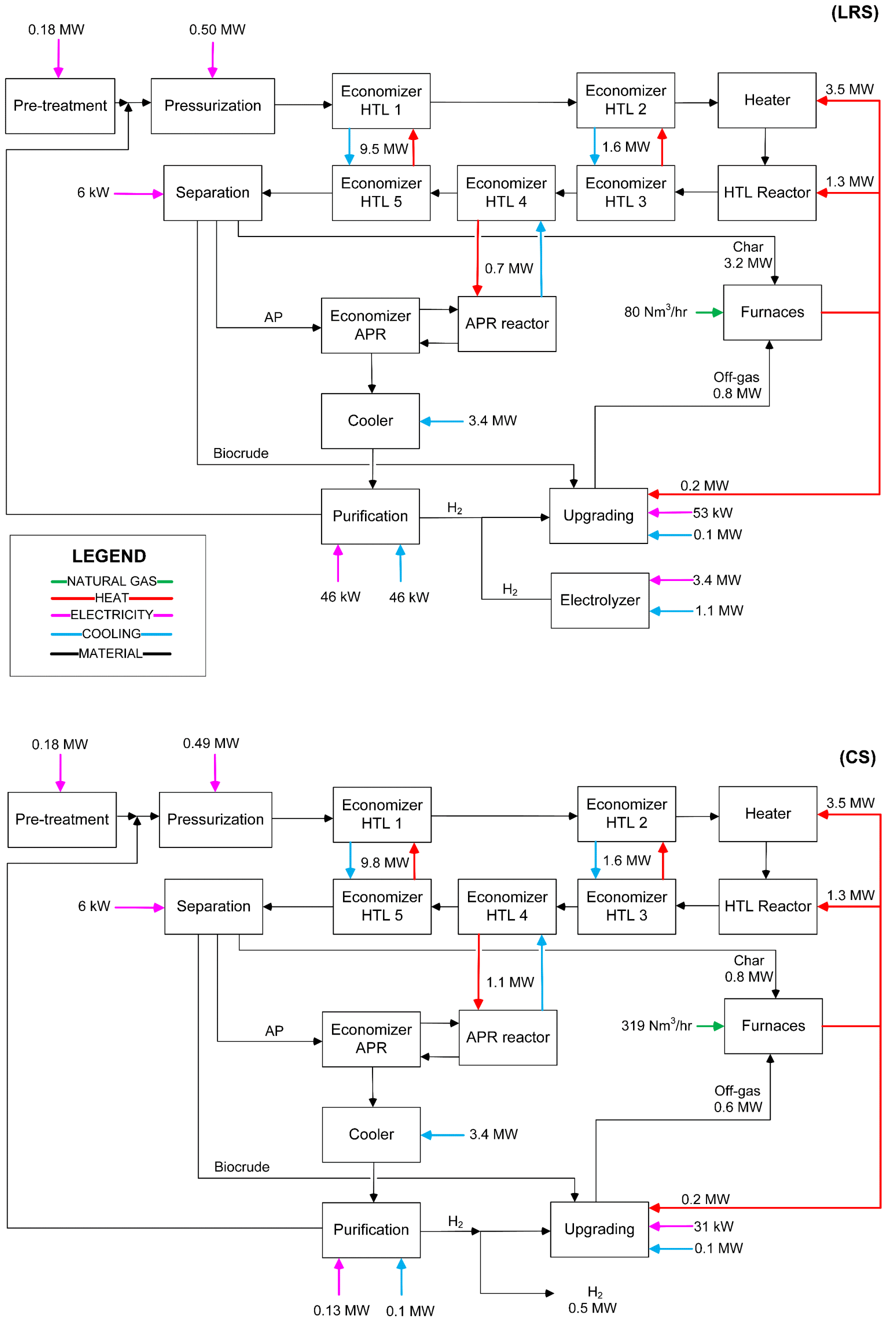

Figure 84: Block diagram and energy streams for the LRS case (above) and the CS case (below).

Table 20: Electric and thermal yearly inputs of the plant.

	LRS	CS
Electric power (GWh)	34.0	7.1
Cooling power (GWh)	33.9	29.9
Natural gas (GWh)	7.1	28.3

7.3.2 Economic analysis

In Table 21 the main sections identified in the biorefinery are summarized, along with the main unit operations. In order to evaluate the economic feasibility of the proposed integrated plant, the main equipment were designed to determine their cost.

Table 21: Plant sections and unit operations.

Section n.	Section name	Unit operations
1	Biomass pre-treatment	Storage, Mixing, Milling
2	Hydrothermal liquefaction	Heating, HTL reaction, Cooling
3	Product separation	Flash evaporation, Filtration, Centrifugation
4	Aqueous phase reforming	Heating, APR reaction, Flash
5	Purification	Compression, Cooling, PSA
6	Upgrading	Hydrotreatment, H_2 production, Electrolyzer*

*Implemented only for the LRS case.

The overall costs are summarized in Table 22. The details of capital and operating costs are detailed below.

Capital costs

Fixed capital investments were equal to 26.8 M€ and 22.2 M€, for LRS and CS case, respectively. The distributions of these costs between the sections of the plant are reported in Figure 85, while the breakdown by equipment is reported in the appendix (Figure A1). The HTL section was the most expensive of the plant due to the high number of heat exchangers operating at high pressure (LRS: 24%; CS: 29% of the overall fixed capital cost), to the hose pump P-201 (LRS: 8.1%; CS: 9.7%) and, secondly to the HTL reactor (LRS: 5.4%; CS: 6.5%). APR was also quite demanding from the economic point of view (LRS: 15%; CS: 16% of the overall cost) and its impact mainly derived from the heat exchangers (LRS: 7.2%; CS: 6.2%) and the APR reactor (LRS: 4.1%; CS: 6.0%). Biomass pre-treatment had almost no impact on costs, as well as the product separation section.

Cost differences between the LRS and the CS case were mainly due to the purification and upgrading sections: 30% of the fixed capital investment for the LRS case were allocated to the upgrading section because of the electrolyzer (16% of the overall cost), which is needed to supply the missing hydrogen. On the other hand, in the CS case the purification section cost was almost double of the LRS case due to the higher amount of hydrogen produced from APR.

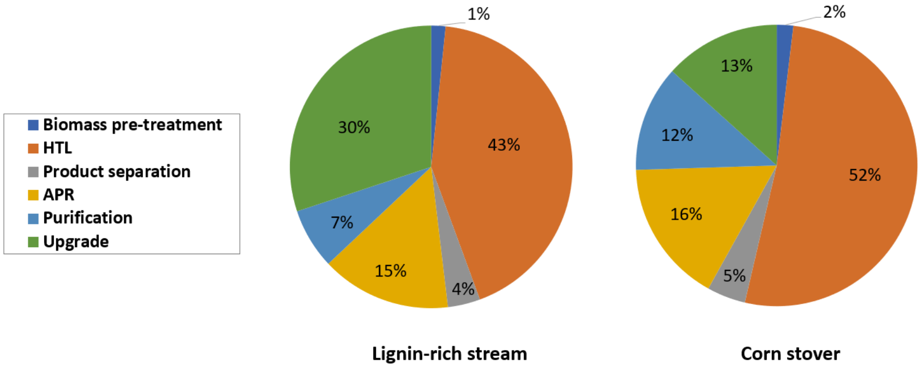

Figure 85: Grassroot costs breakdown between sections, with LRS case (left) and CS case (right).

Operating costs

Operating costs accounted for 8.2 M€/y and 6.7 M€/y for the LRS and the CS case, respectively. As can be seen from Figure 86, one of the two highest costs was related to the purchase of the feedstock. In the LRS case, the highest cost was due to electricity, especially related to the electrolyzer. Maintenance had the same impact in both cases (17% of the overall operating costs) while labor had the same cost but different share. The number of operators required per shift was 3, and the number of total operators required was 14 plus 1 executive and 2 employees/managers. In the CS case, natural gas accounted for 13%, due to the higher energy input required, and water make-up accounted for 4%, due to the low moisture of the feedstock. Wastewater disposal was modest in both cases (6%), while catalysts and cooling power costs had very low impacts. Within the CS case, the credit from the sale of the produced hydrogen was subtracted from the material & utilities costs, resulting in a slightly lower net cost (6.6 M€/y).

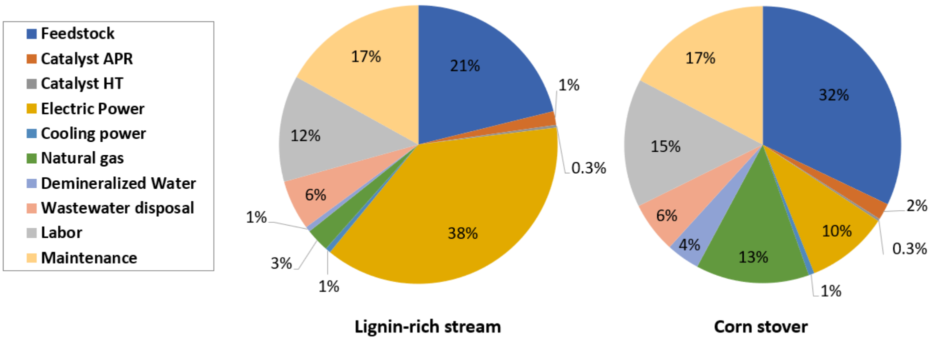

Figure 86: Operating costs, with LRS case (left) and CS case (right).

Minimum selling prices and economic indicators

The resulting MSPs$^{0\%}$ of the biofuels were 1.23 €/kg (LRS) and 1.27 €/kg (CS). Assuming a distillation cut similar to diesel (LHV=43 MJ/kg), the gasoline equivalent prices were 3.43 €/GGE (LRS) and 3.54 €/GGE (CS). The MSPs$^{10\%}$ were 1.57 €/kg (4.40 €/GGE) and 1.63 €/kg (4.54 €/GGE) for the LRS case and the

CS case, respectively, which are within the range of existing TEAs. In Table 22 the main economic parameters are reported.

Table 22: Economic parameters and main indicators for LRS and CS case.

	LRS	CS
Fixed capital investment (M€)	26.8	22.2
Start-up cost (M€)	1.3	1.1
Total investment cost (M€)	28.2	23.3
Maintenance cost (M€/y)	1.4	1.2
Material cost (raw material, catalyst, water) (M€/y)	2.5	3.0
Utilities cost (M€/y)	3.3	1.5
General cost (M€/y)	0.6	0.6
Labor cost (M€/y)	1.0	1.0
H_2 credit (M€/y)	0	0.12
$MSP^{0\%}$ (€/kg)	1.23	1.27
$MSP^{10\%}$ (€/kg)	1.57	1.62

The hydrogen production costs were estimated at 7.7 €/kg (LRS) and 1.5 €/kg (CS). The costs attributable to the APR section were mostly dependent on the amount of aqueous stream to be treated, which was approximately the same for both cases. Hence, the higher profitability of the CS case was ascribed to its higher hydrogen production rate. APR competitiveness therefore strongly depends on the carbon concentration and hydrogen productivity of the organic compounds present in the aqueous phase.

Compared to the literature, both these values were significantly lower than the hydrogen produced by APR of sorbitol syrup (11.7 €/kg)[258], which was heavily penalized by the high cost of the feedstock that constituted up to 91.8 % of the overall costs. In this work, APR was instead carried out on a low value stream. In addition, the HTL-APR coupling also allowed the reduction of the COD of the HTL water, resulting in lower disposal costs and higher profitability. Khodabandehloo et al. assessed the economic performance of APR from a by-product of glycerol stream from biodiesel production[319]. Glycerol was assumed to have a residual value of 45 €/kg, and the resulting hydrogen production cost was estimated to be 6.7 €/kg. Although slightly lower than the LRS case, this value was much higher than in the CS case.

The cost of producing hydrogen from steam reforming (SR) and electrolysis was also calculated as benchmark. These values were obtained by means of correlations, reported in Paragraph 7.2.3, based on the flow rates required by the two cases. The resulting costs were 2.7-2.9 €/kg for SR and 6.4-6.5 €/kg for electrolysis, which fell within the ranges known for these two technologies: 1.3-3.6 €/kg for steam methane reforming[320] and 3-9 €/kg for electrolysis using different electricity sources[321]. Although the hydrogen requirement in this chapter fell within the lower operability limit of the typical SR plant, the use of a centralized upgrading plant, where biocrudes are collected from multiple HTL plants, could be economically beneficial if SR is adopted. On the other hand, with APR this lower limit does not exist and hence this technology can be a valid solution for HTL plants with in-situ upgrading. The comparison with other technologies for hydrogen production will be investigated more in detail below .

Economic sensitivity analysis

The $MSP^{0\%}$'s variations, related to the parameter described in Paragraph 7.2.3, are reported in Figure 87. As seen in the figure, the main factor affecting both cases was plant size: a reduction to 10 MW in nominal capacity would lead to a large increase in MSP (+21% LRS, +26% CS). On the other hand, an opposite increase to 30 MW would result in a less pronounced decrease (-6.8% LRS, -9.5% CS). However, a bigger plant would require adequate biomass availability.

Figure 87: $MSP^{0\%}$ changes as consequence of the sensitivity analysis performed for the lignin-rich stream (above) and corn stover (below) scenario.

The second most impacting item on the MSP$^{0\%}$ of the LRS-derived biofuel was the electricity price (-12%/+17%). This is attributable to the high amount of electricity required by electrolysis. However, the dependence on electricity is not to be traced directly to the HTL-APR integration, but to the missing quota of hydrogen that APR was not able to provide. In fact, an HTL-APR plant capable of being self-sufficient in the production of hydrogen limits the strong influence that electricity has on the selling price of the biofuel. This is corroborated by the lower MSP variations observed for electricity price variation for the CS-case (-3.1%/+4.4%).

The increase of solid loading to 20 wt.% led to a reduction in the capital and operating costs in both cases, resulting in a significant decrease of 9.6% (LRS) and 11% (CS) in both MSPs$^{0\%}$. This is attributable to the fact that with a double solid loading the flow rate of the biofuel produced is kept constant while the mass flow to be treated is halved. However, with state-of-the-art technology it is difficult to pump slurry with 20% of solid[83]. This problem is strictly linked to the biomass feature and is currently receiving great attention in order to evaluate, on the different types of substrates, the optimal solution (pre-treatments, basic additives, biocrude recycling). This result confirmed a commendable improvement of the economic performance of a plant operating at a higher solid concentration, but further investigations are necessary to support its technical feasibility.

Feedstock price variation changed the LRS-MSP$^{0\%}$ within ±8.3% while changed the CS-MSP$^{0\%}$ within ±13%; despite it was important in both cases, the variation was particularly evident for the CS case because of the high share of the feedstock in the operating costs. Also, the impact of the cost of natural gas was higher with the CS case than in the LRS case because of the almost thermal self-sufficiency of the latter. Natural gas cost variation had the smallest impact among all the parameters studied for the LRS case (-0.7%/+1.6%) while was the fifth most impacting parameter for the CS case (-3.5%/+7.6%). Catalyst cost increase led to very low variations (+3.0% LRS, +5.1% CS), especially when referring to the high value used for sensitivity.

The hydrogen requirement for the hydrotreatment step for the LRS-derived biocrude was higher than values reported in the literature. In addition, the value of 26 g/kg, chosen as the minimum value for sensitivity, was lower than the required stoichiometric value (31 g/kg): the latter was therefore used as the minimum value for sensitivity. The decrease in hydrogen requirement led to a consistent decrease in MSP$^{0\%}$ (-7.9%) for the LRS case. On the other hand, the variation in hydrogen consumption for the CS case led to a lower variation in MSP$^{0\%}$ (-3.2%/+3.9%). However, for the upper limit value of the analysis (40 g/kg), it was necessary to introduce the electrolyzer to produce the 12% of hydrogen required that APR was no more able to produce.

In both cases the variation in biofuel yield during HT (±5%) led to MSP variations (-4.7/+5.2%) proportional to the increase/decrease of biofuel produced.

Among the uncertainties for investment costs and plant life, the total investment cost has the biggest impact: ±30% variation led to ±8.1% (LRS) and ±8.2% (CS) change in the MSPs$^{0\%}$. Different assumptions for the plant life also impact the MSPs$^{0\%}$ (-5.0%/+5.3% for LRS and -5.1%/+5.3% for CS) while ±50% variations in the HT investment cost had a very low effect on the MSPs$^{0\%}$.

In order to evaluate the competitiveness of the APR implementation, different plant configurations for the hydrogen supply are described in Figure 88, along with the MSP$^{0\%}$ variations with respect to the base configuration.

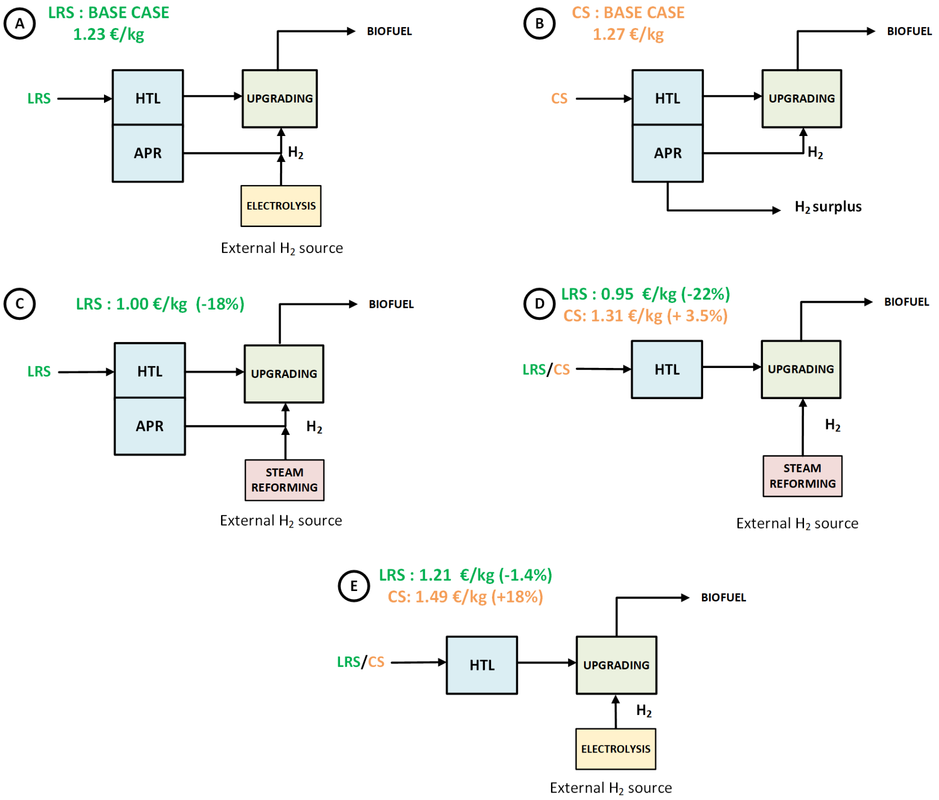

Figure 88: Plant configurations for hydrogen supply. (A) APR+electrolysis, (B) APR alone, (C) APR+SR, (D) SR alone, (E) Electrolysis alone, (F) No upgrading. The percentage values refer to the variation of the MSP$^{0\%}$ of the considered configuration compared to the respective base case ((A) for LRS and (B) for CS).

Looking at the LRS case, an external hydrogen source was always required because APR can produce only 19% of the hydrogen needed for upgrading. Compared to the production of the remaining 81% via electrolysis (Figure 88-A), the use of SR was economically very advantageous (Figure 88-C) as the MSP$^{0\%}$ was reduced by 18%. The resulting MSPs$^{0\%}$ in configuration E (only electrolyzer) and D (only reforming) turned out to be lower than with APR. The economic advantage of using SR and electrolyzer instead of APR derives from their lower hydrogen production cost.

For the CS case, the integrated HTL-APR plant (Figure 88-B) was able to produce 107% of the hydrogen required by the upgrading section. In this case, the replacement of the APR section with electrolyzer (Figure 88-E) or SR (Figure 88-D) led to an increase of MSP$^{0\%}$ (+18% and +3.5%, respectively). These results confirmed the lower H_2 production cost through HTL-APR (1.5 €/kg) compared to the other technologies. The economic performance of the HTL-APR plant was further improved by the fact that a surplus of hydrogen can be sold, thus increasing the revenue.

MSPs$^{0\%}$ for the LRS-derived biofuels were much lower than the CS-derived ones if conventional H_2-producing technologies were used: 1.21 vs 1.49 €/kg with electrolysis and 0.95 vs 1.31 €/kg with steam reforming. This was mostly due to the higher biofuel productivity with LRS, despite LRS-derived biocrude was more oxygenated and hence required higher upgrading expenses. However, the difference between MSPs$^{0\%}$ of the two cases with the integrated HTL-APR plants (case A and B) was almost levelled; this was due to the high H_2 productivity (107% of the hydrogen required) through APR of the residual aqueous phase from HTL of CS. For this reason, while HTL plants are more profitable with feedstocks or operating conditions which allows higher biocrude yield and quality, good carbon yield in the aqueous phase and good hydrogen yield (kg H_2/kg C feed) are required to make the HTL-APR integration attractive.

7.3.3 Life-cycle assessment

Impact assessment and interpretation

In Table 23 the chosen impact categories for the entire HTL-APR biorefinery are summarized for the two evaluated scenarios; the main contributions of each impact category are presented in Figure 89. It is important to emphasize that the results reported in this paragraph are highly dependent on the methodological choices[322] depicted above, i.e., 1 MJ of biofuel as functional unit, *cradle-to-gate* system boundaries, single product, exclusion of biogenic carbon emissions. The end of this paragraph will be devoted to exploring this last aspect in more detail.

Table 23: Environmental impacts of the HTL-APR plant for LRS and CS cases (1 MJ biofuel).

Environmental impact	Unit	LRS	CS
Global warming potential	g CO_2 eq/MJ	56.1	58.4
Fossil depletion potential	MJ eq/MJ	0.64	0.83
Acidification potential	mg SO_2 eq/MJ	380	486
Eutrophication potential	mg PO_4^{3-} eq/MJ	52.1	51.8

Figure 89-A shows that GHG emissions were similar between the two cases, although there were differences in the distribution among the various impact items. Regarding the cumulative LRS-GWP, electrolysis was responsible for 56% of the overall impact, while the second highest impact was due to catalyst replacement (17%), which is platinum-based. Electricity (for mixing, pumping and centrifugation) and thermal energy accounted for 14% and 8%, respectively. The electricity grid mix used in this chapter resembled the average share found in the

EU and consisted mainly of fossil sources. It derives that the hypothesis on the location of the plant strongly affected the results of this assessment. In this sense, Ögmundarson et al. showed that electricity-demanding facilities are hardly determined by the regional mix[323]. The necessity of using electricity brings an environmental burden unless renewable energy sources are strongly deployed. Further evaluations on this topic are reported at the end of this paragraph.

Platinum had a significant impact on GWP (as well as on each other impact category). As mentioned above, it derives from the assumption here used of a conservative lifetime, equal to 1 year, which is lower than other assumptions reported in the literature[258]. Furthermore, it must be recalled that a 28% recycling of platinum was assumed. There are few works in the literature that address the impact of catalyst in the LCA of biofuels, and it is sometimes considered negligible[324]. On the other hand, it must be highlighted that a noble metal catalyst, such as the one used for APR, strongly affects the environmental performance, due to the complex, costly and energy-intensive mining process. This is a hot topic in the research and development stage, calling for the formulation of catalysts free from noble metals.

Concerning the CS-case, thermal energy represented 40% of its total GWP impact, with the remaining 27% and 18% attributed to platinum and electricity, respectively. The higher thermal duty was due to the lower production of char (during HTL) and alkanes (during upgrading). These by-products are burned to provide a fraction of the heating energy required by the biorefinery. In the CS-plant was thus required a higher supply of natural gas that causes the discussed difference with respect to the LRS-plant. The supply of heat by natural gas ensured a low impact (240 g CO_2 eq/kWh) with respect to other fossil sources such as heavy fuel oil (320 g CO_2 eq/kWh) and coal (380 g CO_2 eq/kWh). 8% of the CS-impact was also attributable to corn stover harvesting and transport to the plant.

The fossil depletion potential was equal to 0.64 (LRS) and 0.83 (CS) MJ eq/MJ (Figure 89-B). This indicates that for every MJ of biofuel produced, 64% and 83%, respectively, was attributable to fossil resources. The most impacting item for the LRS-case was electrolysis (52%), primarily due to the fossil fuels used in electricity production. On the other hand, thermal power was the most impacting item for the CS-case (48%), due to its high thermal demand compared to the LRS-case. Platinum was also quite impacting (20% and 25% for LRS and CS, respectively), as well as electricity (13% for both cases).

The acidification potential was higher for the CS-case (Figure 89-C), primarily stemming from the replacement of the platinum catalyst (66% and 85% for LRS and CS, respectively). This was attributable to the environmental impact of platinum extraction and purification[325]. The higher SO_2 eq observed for platinum in the CS-case was attributable to its higher platinum/biofuel ratio (338 mg Pt/kg biofuel vs. 557 mg Pt/kg biofuel). Only in the LRS-case the impact of electrolysis was also present, accounting for 24% of the overall impact. This is due to the SO_2 emissions derived from fossil fuel-based thermoelectrical plants[326]. The impacts due to electricity and thermal energy were limited and were both due to the sulfur content present in fossil fuels.

Finally, the eutrophication potential resulted very similar in the two cases, and wastewater treatment had the highest impact in both of them (66% and 62% for LRS and CS, respectively) (Figure 89-D). This was due to the chemical oxygen demand (COD) and total nitrogen (TN) left in the wastewater to be treated. Platinum (11% and 19% for LRS and CS, respectively) and electrolysis (16% for LRS) also had remarkable impact. The latter was attributed to the emissions of nitrogen oxides emissions due to the presence of nitrogen (i.e., fuel NO_x) and the elevated temperatures reached during the combustion process (i.e., thermal NO_x) of fossil fuels required for electricity generation. For the CS-case, the impact of nitrogen fertilizer to be replaced due to corn stover removal from field amounted to 6%, while electricity to 5%, as well as thermal energy. As for the impact of harvesting, it is worthy of attention that this outcome was affected by the chosen system boundary (i.e., starting from the cradle) and the decision of taking into account the land use change derived from the removal of the stover. For the LRS-case, electricity accounted for 4%. In the end, the transport of the feedstock (CS) from the collection point to the biorefinery was found to be negligible for each impact category under the hypothesis reported in Paragraph 7.2.4.

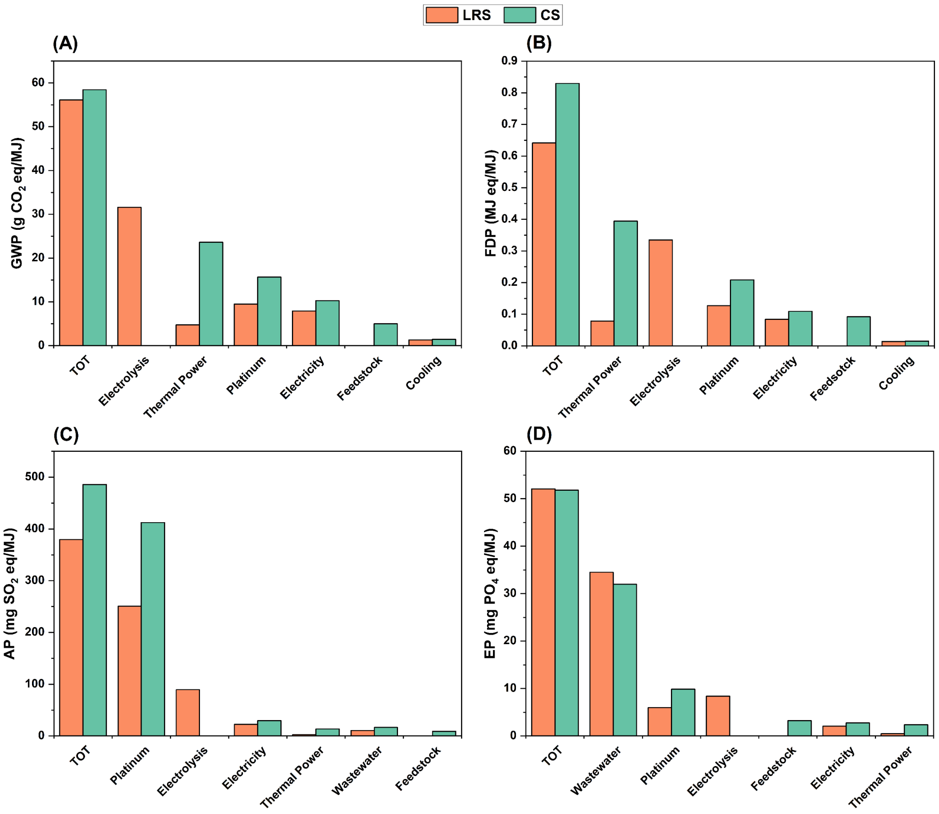

Figure 89: Distribution of GWP (A), FDP (B), AP (C) and EP (D) among the main processes. Please note that the sum of impacts of harvesting and transport of the biomass is reported as ‘feedstock’.

Uncertainty analysis

Since HTL and APR are promising yet still emerging technologies, LCA results may be affected by process uncertainties and lack of reliable, which becomes available only when commercial plants are in operation[327]. Despite these challenges, its capacity to estimate environmental impacts at the design stage makes LCA an effective tool, provided that uncertainties are appropriately reported[328]. Different types of uncertainties can be detected during LCA, including those associated with systematic errors, model, non-linear processes, parameters, etc.[329]. In this section, the focus was placed on the last category. In addressing these uncertainties, a Monte Carlo simulation was employed to examine the potential variations in key variables identified in the preceding paragraph. The assigned uncertainties were ±15% for electricity, thermal power and wastewater, ±30% for platinum demand, ±10% for biofuel yield from hydrotreatment and ±20% for hydrogen demand at hydrotreatment. These uncertainties often stem from the accuracy level of the design method and the intrinsic TRL of the process block. Moreover, the uncertainty study was also directed towards the study of the catalyst impact though its importance has been often overlooked[330]. Please note that, in the CS-case, particular attention must be paid to the methodology used for the hydrogen demand for hydrotreatment. In fact, APR would be able to provide hydrogen up to a +7% variation; for larger uncertainties, the use of an electrolyzer was assumed.

The Monte Carlo simulation results are given in Figure 90 for each impact category and case study. With regards to GWP (Figure 90-A), the percentage deviations ranged from -13 to +11% for LRS and from -11 to +9% for CS. The greater variation for the former could be attributed to its higher dependence on the hydrogen requirement. The FDP for corn stover (Figure 90-B) was always higher than that of the lignin-rich stream, even considering the 5th (0.75 MJ eq/MJ) and 95th percentile (0.72 MJ eq/MJ), respectively. With regards to AP (Figure 90-C), the percentage deviations ranged from -15 to +16% for LRS and from -18 to +19% for CS. The greater variation for the latter could be ascribed to its higher dependency on the platinum consumption, which was the variable with the highest variation in this analysis (±30%). Finally, Figure 90-D depicts the uncertainties related to the EP, for which similar variations were found for both feedstocks (±11%). This result was attributed to the similar impact distribution between the items for both cases, wastewater treatment and platinum being similarly responsible for eutrophication.

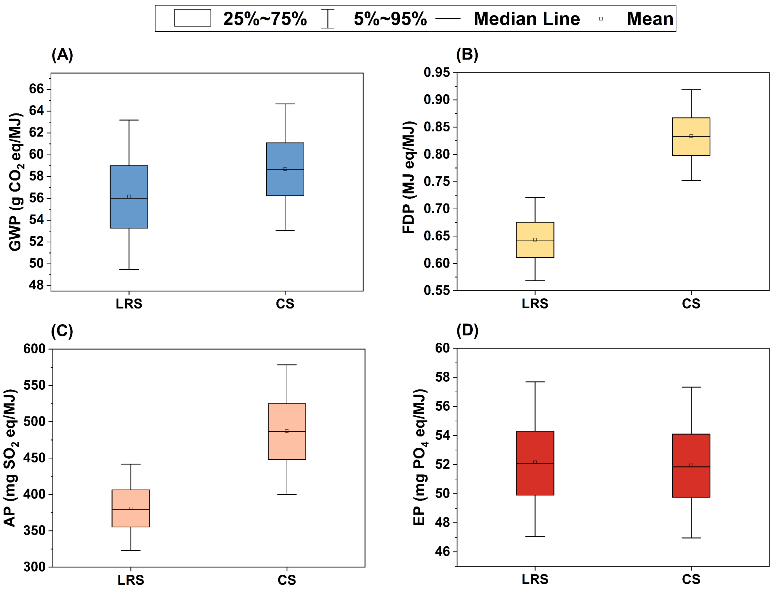

Figure 90: Uncertainty results of the four impact categories for the two feedstocks scenarios investigated.

Sensitivity analysis

From the observed results, most of the environmental burden was attributed to the electrolysis in the LRS-case, while it was more distributed in the CS-case. In the next paragraphs, a sensitivity analysis is presented to consider: (i) the non-biogenic nature of biomass; (ii) the influence of different sources of electrical and thermal energy; (iii) alternative plant configurations for hydrogen supply.

Non-biogenic carbon

As reported in the methodology section, the global warming potential of the HTL-APR biorefinery was evaluated following the '0/0 approach', that is, considering biomass as a carbon-neutral energy resource. However, an agreement on the way to treat biogenic carbon is still not reached in LCA[331]. This uncertainty arises because the CO_2 emissions from biomass combustion remain in the atmosphere and can affect the greenhouse effect's delicate balance. Therefore, this paragraph presents the GWP including biogenic carbon.

Figure 91 shows how the GWP changes with the addition of biogenic carbon, according to the values reported in Table 18. In the LRS-case, 27 g CO_2 eq/MJ biofuel are related to the torch emissions, and 28 g CO_2 eq/MJ biofuel are attributed to the furnace. The former are caused by the CO_2-rich gas phases derived from HTL and PSA, which do not have sufficient heating value to justify their use in a furnace but cannot be released into the atmosphere due to the presence of harmful greenhouse gas (e.g., methane). The latter is attributed to the burning of char and HT-derived gas phase to recover heat. As a result, the cumulative GWP increases from 56 to 111 g CO_2 eq/MJ biofuel (+98%). In the CS-case, the GWP also increases from 58 to 96 g CO_2 eq/MJ biofuel (+64%). It can be observed that a lower impact (8.8 g CO_2 eq/MJ) is due to the furnace section in the CS-case, owing to the lower amount of char combusted, while the amount of gas phase from HTL and APR is approximately the same as in the LRS-case.

These values represent the actual release of CO_2 eq into the atmosphere, but they should be considered as a worst-case scenario for the environmental assessment of biomass processing, as no information is provided regarding the source of carbon. Since the feedstocks examined in the present case studies are residues/waste from fast-growing biomass, their embedded carbon was previously absorbed by the plant as CO_2 from the environment. If the feedstock carbon would be accounted as CO_2 credit, from mass balances it would theoretically amount to 162 and 159 g CO_2 eq/MJ. This would hence result in an overall negative *cradle-to-gate* CO_2 eq emission, according to a '-1/1 approach' that does not take into account the fuel use.

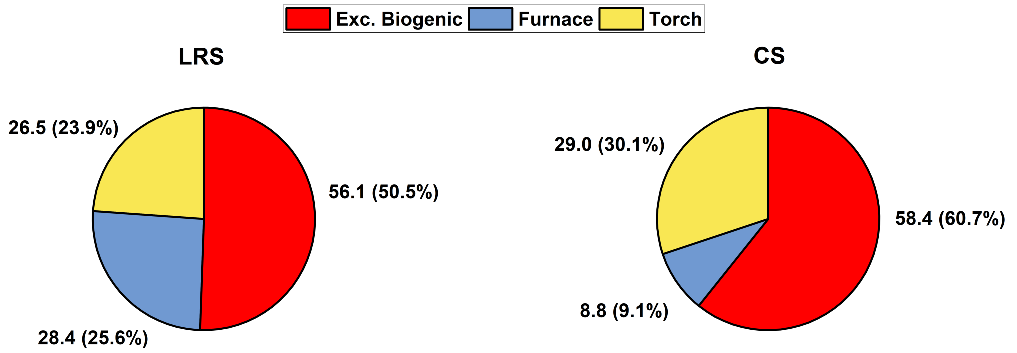

Figure 91: Influence of biogenic carbon on cumulative GWP for the LRS-case (left) and CS-case (right). The numbers are referred to the g CO_2 eq/MJ biofuel, while the percentage with respect to the total value is reported in brackets.

Energy sources

As reported above, the electrolysis unit (in the LRS-case) and the heating unit (in the CS-case) had a significant impact on the overall global warming potential. This was not directly correlated with the running of the electrolysis itself, but rather to the source of electricity used to carry out the water splitting. For this reason, it is interesting to evaluate greener and renewable options. To this end, wind, photovoltaic, hydro and biomass-based electricity, as well as biomass-based heating system were evaluated (Figure 92).

Each of the renewable sources led to a decrease in the GWP. As for electricity, in the LRS-case it ranged from a 71% reduction with hydropower and wind to a 42% reduction with biogas. On the other hand, the CS-case was less influenced by the change in electricity, with the reduction of the impact ranging between 8 and 16%. This result was a direct consequence of the GWP related to the production of 1 kg of hydrogen. In literature it was reported that wind-based electrolysis is generally the best method, from an environmental point of view, followed by hydroelectricity[332]. In this work, the GWP related to electrolysis via grid mix resulted equal to 26 kg CO_2/kg H_2, similar to values reported in the literature[332]. This value was even higher than the H_2 production through natural gas-based steam reforming. An in-depth comparison will be performed below. It is interesting to observe that by employing renewable sources for electricity production, the LRS-case became more environmentally sustainable than the CS-case. This is because the latter, being self-sufficient in terms of hydrogen production, had a much lower electricity demand and hence was less affected by the type of electricity used.

The greatest reduction in impact (34%) for the CS-case was reached when fossil thermal energy was substituted using direct biomass combustion to produce the necessary heat, followed by thermal valorization of biogas (23%). In these cases, the environmental burden of the LRS-case decreased only slightly (6-8%) because of its lower thermal energy demand.

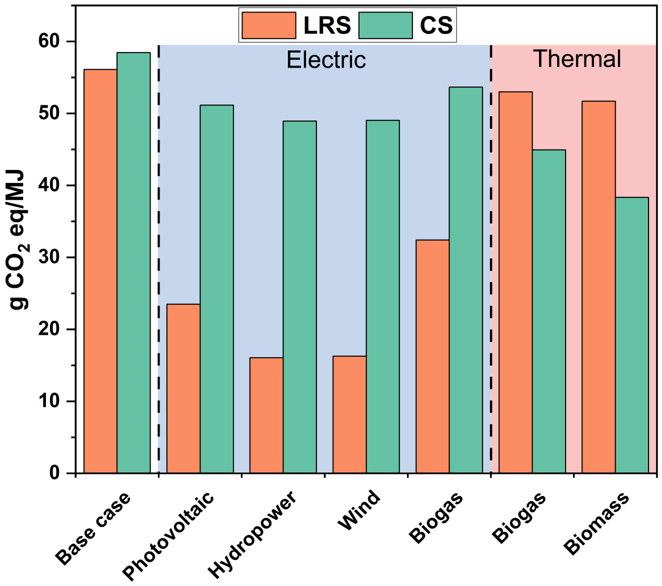

Figure 92: Influence of electricity and thermal energy source on the GWP of the HTL-APR plant for the two investigated scenarios.

Hydrogen sources

In this paragraph, the comparison in terms of GWP of different hydrogen sources is presented and the results are summarized in Figure 93. The base case for LRS and CS is reported in Figure 93-A and Figure 93-B, respectively.

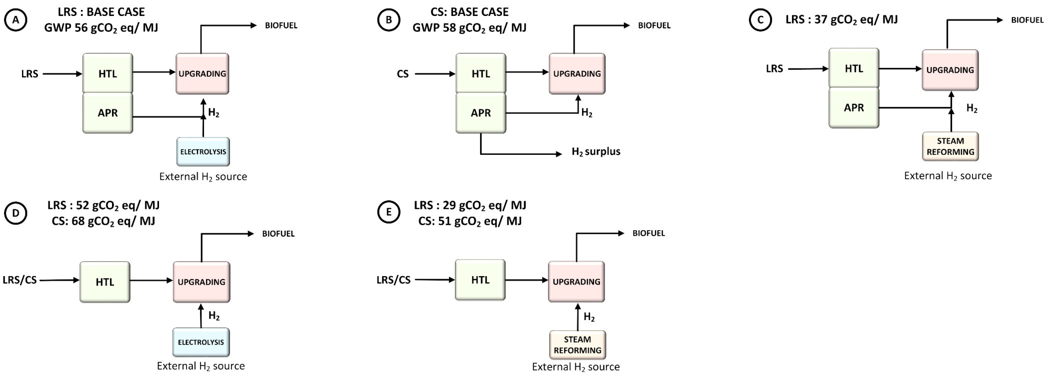

Figure 93: Influence of hydrogen source on the GWP of the HTL-APR biorefinery for the two investigated scenarios.

In Figure 93-C, the substitution of electrolysis by steam reforming was hypothesized to provide the make-up hydrogen necessary for the LRS scenario. This option reduces the environmental impact by 33% (37 g CO_2 eq/MJ) due to the lower GHG emissions of such technology (11 g CO_2 eq/g H_2 vs 26 g CO_2 eq/g H_2 from electrolyzer)[333]. In fact, electrolyzer can be a greener option than conventional steam reforming to provide hydrogen only if the source of electricity is renewable. If electrolysis is employed to provide the entire hydrogen requirement of the upgrading step and no APR section is assumed (Figure 93-D), the GWP decreases by 7% in the LRS-case (52 g CO_2 eq/MJ) and increases by 17% in the CS-case (68 g CO_2 eq/MJ). Figure 93-E shows the case in which steam reforming is used for providing all the hydrogen. This option would decrease the LRS base case by 48% (29 g CO_2 eq/MJ) and the CS base case by 12% (51 g CO_2 eq/MJ). These differences can be traced back to the impact of APR.

To estimate the GWP impact per amount of hydrogen produced from the APR section, a particular calculation was performed. Due to the strong thermal integration between HTL and APR sections in the HTL-APR plant, it was not possible to estimate the GWP attributable to the APR-alone section by directly creating the model on GABI. In fact, the thermal power necessary for heating the inlet of the APR reactor is completely given by the integration and hence the GWP evaluated for an APR stand-alone plant would be higher than the one in this study. Instead, it could be assessed by difference between the impact of the HTL-APR plant and that of the HTL plant. To do so, the GWP of the HTL-alone configuration was subtracted to the the GWP of the HTL-APR (minus the contribution from the electrolysis). The removal of the electrolysis contribution is necessary to evaluate the GWP related to the APR only. The amount of CO_2 eq was then normalized by the amount of hydrogen produced. The resulting values were 39 g CO_2 eq/g H_2 for the LRS-case and 13.8 g CO_2 eq/g H_2 for the CS-case.

Overall, the implementation of APR allows to reduce the GWP of the CS-case with respect to electrolysis, while it is higher in the other scenarios. However, it must be noted that, unlike steam reforming, APR of HTL wastewater complies with the development of a circular economy, which can contribute to the societal pursuit of energy independence. Furthemore, APR does not suffer from the intrisic fluctuations related to the use of renewable energies devoted to water electrolysis.

The analysis conducted here clearly suggests that the APR environmental footprint is highly dependent on the impact of platinum, as 83% of the GWP of APR is related to the platinum-based catalyst. For this reason, it is stressed the necessity of developing effective non-noble metals catalysts for APR implementation on a long-term scale. Nevertheless, it should be cited that a conservative assumption was used here, i.e. that 72% of the platinum derived from new mining, while the remaining 28% was recovered through recycling techniques. However, since the spent catalysts would be returned to the producer and hence regenerated, the precious metal would be fully recovered, with a significant advantage on an environmental (and economic) perspective[334]. With the assumption of using 100% recycled platinum, the APR impact would decrease to 8.0 g CO_2 eq/g H_2 for LRS and 3.0 g CO_2 eq/g H_2 for CS, resulting lower than electrolysis and steam reforming in both cases.

Comparison with literature

Cradle-to-gate

As reported in many LCA works, a fair comparison with other results reported in the scientific literature is not an easy task due to the varying choices (e.g., about the functional unit, system boundaries or allocation) which can have a significant effect on the results. As suggested by Wiloso et al. for bioethanol production, clear and shared guidelines should be established to evaluate the environmental impact of biofuel production thanks to new technologies, and HTL can serve as an example[311].

Table 24 compares the environmental impact of 1 MJ of biofuel derived from an HTL-APR biorefinery with 1 MJ fuel from alternative biomass-based processes (fast pyrolysis biofuel[335,336], bioethanol from fermentation, bio-oil from fast pyrolysis with supercritical ethanol upgrading, and jet fuel from gasification of corn stover[337]). The impacts related to the harvesting, transport and processing stages (i.e., excluding the use of the fuel) were derived, so that these figures could be considered coherent with the ones reported herein. Please note that with the poplar fast pyrolysis plant, the GWP was not used as reference because it included the CO_2 uptake, making it not comparable with the present work.

In the fast pyrolysis of poplar[335], AP was mainly attributed to the pyrolysis plant, particularly its electric demand. FDP was mostly accredited to the need of natural gas to produce the hydrogen for bio-oil upgrading, while 47% of the EP was attribute to direct and indirect emissions derived from the agriculture of poplar, which was not a residue or waste but was cultivated specifically for this purpose. For this reason, the fertilizer expenses directly impacted the biofuel, increasing its EP from 39 mg PO_4^{3-} eq to 73 mg PO_4^{3-} eq, leading to a higher EP compared to the biofuels from waste/residue of this chapter. The decrease in EP and AP was indeed observed if corn stover is used as feedstock of fast pyrolysis[336]. The GWP was comparable to those obtained in this chapter, but it mostly derived from the upgrading section due to the higher hydrogen demand of pyrolysis biocrude compared to HTL biocrude[336].

In [337], three technologies were directly compared. For all technologies, the fossil-derived electricity contributed to GWP, AP and EP. The AP was found as one of the most critical categories because of NO_x and SO_2 emissions during the combustion processes involving biomass (such as lignin by-product during fermentation and bio-char from pyrolysis). GWP of fast pyrolysis was substantially higher than gasification and fermentation and it is explained by the supercritical ethanol upgrading which used fossil hydrogen (derived from natural gas) and fossil ethanol (derived from ethylene hydrolysis). The other impact categories were higher for fermentation due to the lower fuel yield and the consumption of chemicals during the operation. Unlike the present study, Sun et al. took into account the impact derived by the stover by allocating the impact of corn cultivation between corn and corn stover on an economic basis[337]. However, this choice can vary the results according to the market price of the waste, which is not yet stable[338].

Table 24: Comparison of impact categories of the HTL-APR biorefineries with alternative biofuels (1 MJ biofuel).

	HTL-APR (LRS)	HTL-APR (CS)	Fast pyrolysis (poplar)[335]	Fast pyrolysis (CS)[336]	Fast pyrolysis - supercritical ethanol upgrading (CS)[337]	Gasification-FT* (CS)[337]	Fermentation* (CS)[337]
GWP 100 year (g CO_2 eq)	56	58	-*	54	63	19	18
FDP (MJ eq)	0.64	0.83	0.81	-	-	-	-
AP (g SO_2 eq)	0.38	0.49	0.25	0.18	0.85	0.34	1.14
EP (mg PO_4^{3-} eq)	52	52	73	24	151	34	604

* Not taken into account because of different assumptions for CO_2 uptake and biogenic carbon emissions used.

The GWP of fast pyrolysis was comparable to those obtained in this chapter while gasification and fermentation showed significantly lower values. As reported above, this result was mainly attributed to the impact related to the need for electricity for hydrogen production (LRS) and external heating (CS). Changing the electricity and heat sources helped reduce the GWP for both cases, making them more comparable to other biofuels. The eutrophication and acidification potentials for both cases were higher than fast pyrolysis from a similar feedstock[336], while fermentation had higher values. Regarding the FDP, the value obtained in the CS-case was slightly higher compared to the fast pyrolysis of poplar, while the LRS-case was significantly lower. The main contributors to the FDPs in this chapter were electrolysis and thermal demand, while the electricity used in the pyrolysis step was mainly for drying the biomass.

Well-to-wheels

Finally, it was necessary to compare the GWP with an equivalent fossil fuel. In this case, it was generally recommended to use a *'well-to-wheels'* system boundary, so that the growth and utilization stages (i.e. fuel combustion in the engine) are included[335]. To evaluate the *well-to-wheels* GWP, the GHG emission deriving from the biofuel usage must be added, as well as transport to the fuel station. The total GHG emissions due to combustion phase were evaluated by referring not only to CO_2 exhaust emissions, but also by taking into account the emissions of methane (CH_4) and nitrous oxide (N_2O)[339]. However, the CO_2 produced during the use of the biofuel can be considered zero, being biogenic CO_2. Thus, the impact of combustion in terms of CO_2 eq can be calculated as the sums of CH_4 and N_2O, resulting in 0.98 g CO_2 eq/MJ fuel[339]. With regard to the transport of the biofuel, a distance to be covered by truck of 15 km was assumed[340], and the resulting impact was limited (0.03 g CO_2 eq/MJ fuel). The *well-to-wheels* GWP hence resulted equal to 57.1 and 59.4 g CO_2 eq/MJ for LRS and CS, respectively.

In Figure 94 the *well-to-wheels* GWP for the previously presented biofuels is reported, as well as the reference value for fossil diesel (89.1 g CO_2 eq/MJ fuel)[338]. It is crucial to note that in Figure 94, the GWPs are reported using a *well-to-wheels* approach instead of the cradle-to-gate approach reported in Table 24. The GWP of the HTL-APR plant resulted higher than those of fermentation and gasification ans similar to that of pyrolysis, even when comparing them within a *well-to-wheels* boundary system. Compared to fossil diesel, the HTL-APR technology showed better performances (-37%), highlighting the environmental benefit of such integration. A further GWP reduction compared to fossil diesel can be obtained if a change in the electricity or in the heat source is adopted, as reported above. In fact, using electricity from hydropower allowed a reduction of 80% for the LRS-case, while a reduction of 55% is reached for the CS-case with thermal power from biomass. In this way, this technology could achieve the 65% reduction in greenhouse gases with biofuels compared with fossil equivalents indicated by the Renewable Energy Directive (RED II)[11].

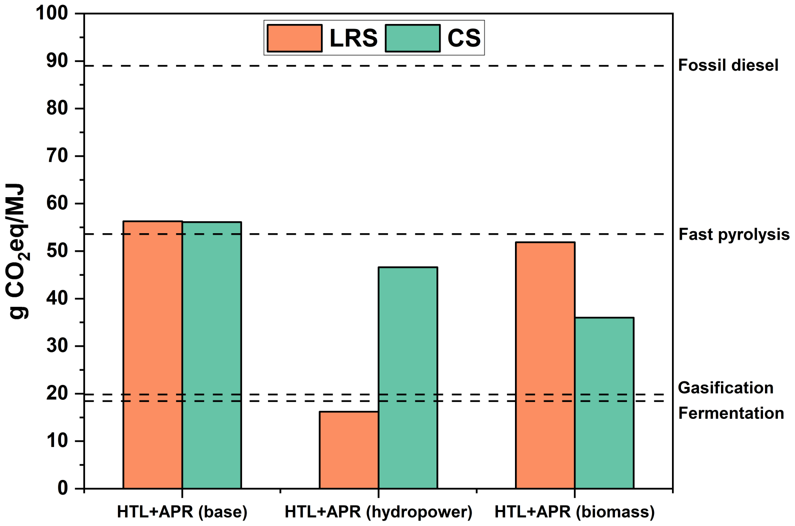

Figure 94: Comparison of global warming potential *well-to-wheels* between HTL-APR and alternative technologies[336,337] (1 MJ biofuel).

7.4 Conclusion

This chapter investigated a novel conceptual design, techno-economic and life cycle assessment of an HTL-APR integrated plant. Two different feedstocks were compared, maintaining the same mass flow rate and 10 wt.% of solid loading: a lignin-rich stream (LRS, 20 MW input) and corn stover (CS, 16.5 MW input).

The economic assessment resulted in a minimum selling price (MSP) with a 0% internal rate of return (IRR) of 1.27 €/kg for CS and 1.23 €/kg for LRS. In both cases the MSP was consistently affected by the feedstock cost. In addition, electricity significantly influenced the LRS-case, mainly due to the high electricity demand for electrolysis, whereas natural gas and total investment costs uncertainties consistently impacted the CS-case.

The global warming potential was similar between the two cases (approximately 57 CO_2 eq/MJ), but the sources of emissions were different. The results emphasize the dramatic impact of electrolysis, and hence electricity, in the LRS-case, which consequently outlines the challenge of low-carbon electricity demand and the advantage of APR implementation. Furthermore, the environmental burden resulting from platinum use that noble metal-based catalysts should be avoided if a more sustainable process is desired. With regard to the other impact categories investigated, the corn-stover case had a 28% higher potential for acidification and fossil depletion, mainly driven by electricity, thermal energy and catalyst. The sensitivity analysis showed that the use of renewable electricity (wind and hydro) reduced the GWP of the LRS-case by 71%, while renewable thermal energy decreased the GWP of the CS-case by 34%.

The addition of an APR section to the HTL plant proved great economic potential, especially for the corn stover case. The hydrogen production costs were 7.7 €/kg (LRS) and 1.5 €/kg (CS). The compellingly low values of the latter was attributed to APR, being able to produce 107% of the hydrogen required for biocrude upgrading. This indicates that APR can be a useful process for producing greener hydrogen, but its effectiveness is strongly related to the feedstock. In fact, LRS and CS showed different compositions of biocrude (lower hydrogen demand for CS-derived biocrude) and hydrogen productivity from the aqueous phase.

In conclusion, hydrothermal liquefaction has been affirmed as an effective technology for biofuel production, with APR demonstrating significant potential for coupling. Notably, the advantages arising from this coupling are intricately tied to the feedstock utilized. Identified synergies, such as APR of HTL-wastewater, and bottlenecks, such as the fossil share of electricity and the use of noble metal catalysts, were highlighted. Addressing these factors can ultimately facilitate the decarbonization of the transport sector.

Conclusions

The urgent challenges posed by fossil fuel depletion and global warming necessitate the exploration of sustainable methods for biofuel production from waste and/or their chemical recycling. While much remains to be understood, hydrothermal liquefaction (HTL) holds the potential to be a valuable solution. This thesis aimed to enhance the understanding of chemical reactions and interactions in HTL, utilizing both biomass and plastic as feedstocks.

Focusing on biomass HTL, monomeric compounds (glucose, glycine, oleic acid) were employed to simulate the more complex bio-polymers constituting biomass. Oleic acid showed limited reactivity and only a slight interaction with glycine, resulting in the production of oleylamine. Conversely, glucose and glycine produced a plethora of compounds when reacting independently, while, their joint reaction revealed strong interactions, causing significant deviations from their normal pathways. This interaction was primarily attributed to the Maillard reaction leading to increased oil production at higher temperatures and higher solid and gas phases at lower temperatures. An innovative experimental campaign based on consecutive reactions provided insight into the relationships among the phases. Notably, the interaction between glucose and glycine was found to be centered on the formation of solid melanoidin-like compounds, which degrade at high temperatures, forming nitrogen-containing aromatics that constitute the oil phase.

Subsequently, HTL of bio-polymers (cellulose, ovalbumin, and triolein) and real biomass was studied, focusing on the impact of the heating rate. Understanding the heating rate is crucial for real biomass and bio-polymers, as it can influence overall reaction selectivity through variations in the hydrolysis rate to monomers and the decomposition rate of these monomers and intermediates to the final products. Experiments showed that with long reaction times, the heating rate effect had limited effects, while significant changes were observed at shorter times. The variations in heating rate were explained by changes in the kinetic advancement of the reaction, with only minor differences were attributed to a direct influence of heating rate on reactive mechanisms.

Beyond biomass, synthetic polymers constitute a crucial waste category that demands attention. Particularly challenging are multilayer plastic film that cannot be recycled through current recycling technology. Their valorization through a sequential hydrothermal dechlorination-liquefaction process was studied in this work. By leveraging the different reactivity of subcritical water with polyolefins and polycondensation polymers, the study achieved targeted hydrolysis. Operating at 325 °C for 20 min with a 20 wt.% solid loading using a real PET-LLDPE film, only the PET layer underwent hydrolysis, leaving a solid residue composed solely of PE. The recovery of 94% terephthalic acid, a PET monomer, with a purity of 78%, presents an opportunity for further upgrading and use in the production of virgin PET, thereby reducing reliance on fossil resources. Subsequently, the PE residue served as feedstock for a supercritical reaction step, resulting in its complete conversion into gas-oily paraffinic hydrocarbons, which offer potential as feedstock for steam cracking, contributing to the production of olefins for the petrochemical industry.

PVC stands out as another crucial plastic polymer due to the challenges it presents, given the corrosivity and toxicity of the hydrochloric acid and dioxin it generates. This hampers the effective valorization of mixed post-consumer plastic waste, as PVC is commonly present. To address this issue, the feasibility of generating a chlorine-free solid for subsequent valorization in a hydrothermal environment was assessed. Almost complete dechlorination of PVC occurred in water at 300 °C in just 20 minutes, resulting in a solid residue with a 94% carbon yield, 86% energy recovery, and an aromatic structure. The dechlorination mechanisms were investigated, and the changes in reaction mechanisms after addition of the basic additive KOH were highlighted. The subcritical stage thus demonstrated its efficiency in producing a nearly chlorine-free solid material with a higher energy density than that of PVC. The dechlorinated solid could then undergo further processing using other technologies. One possibility, which involved testing HTL in supercritical conditions, allowed for its partial conversion into hydrocarbons containing 30% of the initial PVC's carbon content.

In the end, the industrial implementation of an HTL plant was assessed from both techno-economic (TEA) and life-cycle (LCA) perspectives. The study focused on the coupling between an HTL plant and an aqueous phase reforming (APR) section, as possible way to valorize the HTL-derived aqueous phase. APR facilitates the catalytic conversion of the residual oxygenated compounds present in the aqueous phase into hydrogen, which can be used for the in-situ upgrading of the biocrude into drop-in biofuel. Two case studies were evaluated based on two different lignocellulosic feedstocks. The resulting minimum selling price for the biofuel ranged within 1.23-1.27 €/kg, while the global warming potentials (GWP) ranged within 41-47 g CO_2 eq/MJ biofuel, representing a substantial reduction compared to fossil diesel. Interestingly, the implementation of APR was particularly profitable with CS, as it produced 107% of the hydrogen required for biocrude upgrading. This indicates that HTL-APR can be a useful process for producing greener hydrogen, but its effectiveness is strongly related to the feedstock performance during HTL.

References

1. Dey, R. & Lewis, S. C. Natural disasters linked to climate change. *Impacts Clim. Chang. A Compr. Study Phys. Biophys. Soc. Polit. Issues* 177–193 (2021) doi:10.1016/B978-0-12-822373-4.00004-5.

2. Framing, Context, and Methods. in *Climate Change 2021 – The Physical Science Basis* 147–286 (Cambridge University Press, 2023). doi:10.1017/9781009157896.003.

3. Breidenich, C., Magraw, D., Rowley, A. & Rubin, J. W. The Kyoto Protocol to the United Nations Framework Convention on Climate Change. *Am. J. Int. Law* **92**, 315–331 (1998).

4. *Report of the Conference of the Parties on its sixteenth session, held in Cancun from 29 November to 10 December 2010. Framework Convention on Climate Change* (2011) doi:10.4135/9781412971867.n129.

5. *The Paris Agreement*. (2016).

6. Edenhofer, O. *et al. IPCC, 2014: Climate Change 2014: Mitigation of Climate Change. Contribution of Working Group III to the Fifth Assessment Report of the Intergovernmental Panel on Climate Change. Cambridge University Press* (2014).

7. Energy Institute. *Statistical Review of World Energy 2023 (72nd edition)*. (2023).

8. Global Monitoring Laboratory-Earth System Research Laboratories. (2023).

9. BP. *Statistical Review of World Energy 2021 (70th edition)*. (2021).

10. European Parliament. *Directive 2009/28/EC of the European Parliament and of the Council of 23 April 2009 on the promotion of the use of energy from renewable sources and amending and subsequently repealing Directives 2001/77/EC and 2003/30/EC. Official Journal of the European Union* (2009).

11. European Parliament. *Directive (EU) 2018/2001 of the European Parliament and of the Council of 11 December 2018 on the promotion of the use of energy from renewable sources (recast). Official Journal of the European Union* (2018).

12. European Parliament. *Directive (EU) 2023/2413 of the European Parliament and of the Council of 18 October 2023 amending Directive (EU) 2018/2001, Regulation (EU) 2018/1999 and Directive 98/70/EC as regards the promotion of the use of energy from renewable sources, and repeali*. (2023).

13. Renewable energy statistics (Eurostat). https://ec.europa.eu/eurostat/statistics-explained/index.php?title=Renewable_energy_statistics.

14. Rudnik, E. Compostable Polymer Materials. in *Handbook of Biopolymers and Biodegradable Plastics* 189–211 (Elsevier, 2013). doi:10.1016/B978-1-4557-2834-3.00010-0.

15. Gibson, L. J. The hierarchical structure and mechanics of plant materials. *J. R. Soc. Interface* **9**, 2749–2766 (2012).

16. Kumar, N. & Dixit, A. Management of biomass. in *Nanotechnology for Rural Development* 97–140 (Elsevier, 2021). doi:10.1016/B978-0-12-824352-7.00004-9.

17. Millam, S. Developments in Transgenic Biology and the Genetic Engineering of Useful Traits. in *Potato Biology and Biotechnology* 669–686 (Elsevier, 2007). doi:10.1016/B978-044451018-1/50072-5.

18. Pawar, R. *et al.* Polysaccharides as carriers of bioactive agents for medical applications. in *Natural-Based Polymers for Biomedical Applications* 3–53 (Elsevier, 2008). doi:10.1533/9781845694814.1.3.

19. Zeqiraj, E. *et al.* Structural basis for the recruitment of glycogen synthase by glycogenin. *Proc. Natl. Acad. Sci.* **111**, (2014).

20. Bezborodkina, N. N., Chestnova, A. Y., Vorobev, M. L. & Kudryavtsev, B. N. Spatial Structure of Glycogen Molecules in Cells. *Biochem.* **83**, 467–482 (2018).

21. Lau, D. C. W. Utilization of sewage sludge as a resource for protein extraction and recovery. *Conserv. Recycl.* **4**, 193–200 (1981).

22. Timorshina, S., Popova, E. & Osmolovskiy, A. Sustainable Applications of Animal Waste Proteins. *Polymers (Basel).* **14**, 1601 (2022).

23. Tomii, K. Protein Properties. in *Encyclopedia of Bioinformatics and Computational Biology* 28–33 (Elsevier, 2019). doi:10.1016/B978-0-12-809633-8.20266-5.

24. Maloy, S. Amino Acids. in *Brenner's Encyclopedia of Genetics* 108–110 (Elsevier, 2013). doi:10.1016/B978-0-12-374984-0.00051-6.

25. Sparkman, O. D., Penton, Z. E. & Kitson, F. G. Amino Acids. in *Gas Chromatography and Mass Spectrometry: A Practical Guide* 265–271 (Elsevier, 2011). doi:10.1016/B978-0-12-373628-4.00012-5.

26. Fahy, E. *et al.* Update of the LIPID MAPS comprehensive classification system for lipids. *J. Lipid Res.* **50**, S9–S14 (2009).

27. Srivastava, L. M. Seed Food Reserves and Their Accumulation. in *Plant Growth and Development* 503–520 (Elsevier, 2002). doi:10.1016/B978-0-12-660570-9.50178-7.

28. Turchini, G. M., Wing-Keong, N. & Tocher, D. R. Terrestrial Animal Fats. in *Fish Oil Replacement and Alternative Lipid Sources in Aquaculture Feeds* 551 (Taylor & Francis, 2010).

29. Lembke, P. & Schubert, A. Introduction to Fish Oil Oxidation, Oxidation Prevention, and Oxidation Correction. in *Omega-3 Fatty Acids in Brain and Neurological Health* 455–460 (Elsevier, 2014). doi:10.1016/B978-0-12-410527-0.00037-5.

30. Lu, Y. *et al.* Structural Characterization of Lignin and Its Degradation Products with Spectroscopic Methods. *J. Spectrosc.* **2017**, 1–15 (2017).

31. Structure and Characteristics of Lignin. in *Lignin Chemistry and Applications* 25–50 (Elsevier, 2019). doi:10.1016/B978-0-12-813941-7.00002-3.

32. Chio, C., Sain, M. & Qin, W. Lignin utilization: A review of lignin depolymerization from various aspects. *Renew. Sustain. Energy Rev.* **107**, 232–249 (2019).

33. Shanmugam, V. *et al.* Polymer Recycling in Additive Manufacturing: an Opportunity for the Circular Economy. *Mater. Circ. Econ.* **2**, 0–11 (2020).

34. Geyer, R., Jambeck, J. R. & Law, K. L. Production, use, and fate of all plastics ever made. *Sci. Adv.* **3**, 3–8 (2017).

35. Li, H. *et al.* Expanding plastics recycling technologies: chemical aspects, technology status and challenges. *Green Chem.* **24**, 8899–9002 (2022).

36. Van Geem, K. M. Plastic waste recycling is gaining momentum. *Science* **381**, 607–608 (2023).

37. Garcia-Gutierrez, P. *et al. Environmental and Economic Assessment of Management of Plastic Packaging Waste*. (2023) doi:10.2760/0472.

38. Mathanker, A. *et al.* A review of hydrothermal liquefaction of biomass for biofuels production with a special focus on the effect of process parameters, co-solvents and extraction solvents. *Energies* **14**, 4916 (2021).

39. Mishra, R. K., Kumar, V., Kumar, P. & Mohanty, K. Hydrothermal liquefaction of biomass for bio-crude production: A review on feedstocks, chemical compositions, operating parameters, reaction kinetics, techno-economic study, and life cycle assessment. *Fuel* **316**, 123377 (2022).

40. Pecchi, M., Cascioli, A., Maag, A. R., Goldfarb, J. L. & Baratieri, M. Uncovering the transition between hydrothermal carbonization and liquefaction using differential scanning calorimetry. *Fuel Process. Technol.* **235**, 107349 (2022).

41. Lachos-Perez, D., César Torres-Mayanga, P., Abaide, E. R., Zabot, G. L. & De Castilhos, F. Hydrothermal carbonization and Liquefaction: differences, progress, challenges, and opportunities. *Bioresour. Technol.* **343**, 126084 (2022).

42. Peterson, A. A. *et al.* Thermochemical biofuel production in hydrothermal media: A review of sub- and supercritical water technologies. *Energy Environ. Sci.* **1**, 32 (2008).

43. Toor, S. S., Rosendahl, L. & Rudolf, A. Hydrothermal liquefaction of biomass: A review of subcritical water technologies. *Energy* **36**, 2328–2342 (2011).

44. Akiya, N. & Savage, P. E. Roles of water for chemical reactions in high-temperature water. *Chem. Rev.* **102**, 2725–2750 (2002).

45. Gollakota, A. R. K., Kishore, N. & Gu, S. A review on hydrothermal liquefaction of biomass. *Renew. Sustain. Energy Rev.* **81**, 1378–1392 (2018).

46. Berl, E. Origin of Asphalts, Oil, Natural Gas and Bituminous Coal. *Science* **80**, 227–228 (1934).

47. Berl, E. The Origin of Natural Oil. *Science* **81**, 18–18 (1935).

48. Berl, E. Production of Oil from Plant Material. *Science* **99**, 309–312 (1944).

49. Basar, I. A., Liu, H., Carrere, H., Trably, E. & Eskicioglu, C. A review on key design and operational parameters to optimize and develop hydrothermal liquefaction of biomass for biorefinery applications. *Green Chem.* **23**, 1404–1446 (2021).

50. Bassoli, S. C., da Fonseca, Y. A., Wandurraga, H. J. L., Baeta, B. E. L. & de Souza Amaral, M. Research progress, trends, and future prospects on hydrothermal liquefaction of algae for biocrude production: a bibliometric analysis. *Biomass Convers. Biorefin.* (2023) doi:10.1007/s13399-023-03905-7.

51. Elliott, D. C. *et al.* Process development for hydrothermal liquefaction of algae feedstocks in a continuous-flow reactor. *Algal Res.* **2**, 445–454 (2013).

52. Anastasakis, K., Biller, P., Madsen, R., Glasius, M. & Johannsen, I. Continuous Hydrothermal Liquefaction of Biomass in a Novel Pilot Plant with Heat Recovery and Hydraulic Oscillation. *Energies* **11**, 2695 (2018).

53. Pedersen, T. H. *et al.* Continuous hydrothermal co-liquefaction of aspen wood and glycerol with water phase recirculation. *Appl. Energy* **162**, 1034–

1041 (2016).

54. Jazrawi, C. *et al.* Pilot plant testing of continuous hydrothermal liquefaction of microalgae. *Algal Res.* **2**, 268–277 (2013).

55. Suesse, A. R., Norton, G. A. & Van Leeuwen, J. Pilot-Scale Continuous-Flow Hydrothermal Liquefaction of Filamentous Fungi. *Energy Fuels* **30**, 7379–7386 (2016).

56. Genifuel website. https://genifuel.com/.

57. Commercial-Scale Demonstration Plant. https://steeperenergy.com/commercialization-journey/commercial-scale-demo-plant/.

58. Jensen, C. U., Guerrero, J. K. R., Karatzos, S., Olofsson, G. & Iversen, S. B. Hydrofaction^{TM} of forestry residues to drop-in renewable transportation fuels. in *Direct Thermochemical Liquefaction for Energy Applications* 319–345 (Elsevier, 2018). doi:10.1016/B978-0-08-101029-7.00009-6.

59. Licella Pty Ltd. Corporate Website. doi:https://www.licella.com/.

60. Biller, P. & Ross, A. B. Potential yields and properties of oil from the hydrothermal liquefaction of microalgae with different biochemical content. *Bioresour. Technol.* **102**, 215–225 (2011).

61. Déniel, M., Haarlemmer, G., Roubaud, A., Weiss-Hortala, E. & Fages, J. Hydrothermal liquefaction of blackcurrant pomace and model molecules: understanding of reaction mechanisms. *Sustain. Energy Fuels* **1**, 555–582 (2017).

62. dos Passos, J. S., Glasius, M. & Biller, P. Screening of common synthetic polymers for depolymerization by subcritical hydrothermal liquefaction. *Process Saf. Environ. Prot.* **139**, 371–379 (2020).

63. Seshasayee, M. S. & Savage, P. E. Oil from plastic via hydrothermal liquefaction: Production and characterization. *Appl. Energy* **278**, 115673 (2020).

64. Gholami, Z., Gholami, F., Tišler, Z. & Vakili, M. A review on the production of light olefins using steam cracking of hydrocarbons. *Energies* **14**, 1–24 (2021).

65. Lu, J., Watson, J., Liu, Z. & Wu, Y. Elemental migration and transformation during hydrothermal liquefaction of biomass. *J. Hazard. Mater.* **423**, 126961 (2022).

66. Fan, Q., Fu, P., Song, C. & Fan, Y. Valorization of waste biomass through hydrothermal liquefaction: A review with focus on linking hydrothermal factors to products characteristics. *Ind. Crops Prod.* **191**, 116017 (2023).

67. Akhtar, J. & Amin, N. A. S. A review on process conditions for optimum bio-oil yield in hydrothermal liquefaction of biomass. *Renew. Sustain. Energy Rev.* **15**, 1615–1624 (2011).

68. Yan, S., Xia, D., Lai, N. C., Jiang, B. & Liu, X. New insight into the synergistic reactions involved in the hydrothermal co-liquefaction of synthetic polymer wastes by molecular dynamics and DFT methods. *J. Hazard. Mater.* **449**, 131032 (2023).

69. Xue, Y. *et al.* A review on the operating conditions of producing bio- oil from hydrothermal liquefaction of biomass. *Arch. Thermodyn.* **33**, 23–40 (2012).

70. Borazjani, Z., Azin, R. & Osfouri, S. Kinetics studies and performance analysis of algae hydrothermal liquefaction process. *Biomass Convers. Biorefin.* (2023) doi:10.1007/s13399-023-04067-2.

71. Faeth, J. L., Valdez, P. J. & Savage, P. E. Fast Hydrothermal Liquefaction of Nannochloropsis sp. To Produce Biocrude. *Energy & Fuels* **27**, 1391–1398 (2013).

72. Qian, L., Wang, S. & Savage, P. E. Fast and isothermal hydrothermal liquefaction of sludge at different severities: Reaction products, pathways, and kinetics. *Appl. Energy* **260**, 114312 (2020).

73. Gollakota, A. & Savage, P. E. Hydrothermal Liquefaction of Model Food Waste Biomolecules and Ternary Mixtures under Isothermal and Fast Conditions. *ACS Sustain. Chem. Eng.* **6**, 9018–9027 (2018).

74. Ni, J. *et al.* A review on fast hydrothermal liquefaction of biomass. *Fuel* **327**, 125135 (2022).

75. Zhang, S. *et al.* Effect of operating parameters on hydrothermal liquefaction of corn straw and its life cycle assessment. *Environ. Sci. Pollut. Res.* **27**, 6362–6374 (2020).

76. Mathanker, A., Pudasainee, D., Kumar, A. & Gupta, R. Hydrothermal liquefaction of lignocellulosic biomass feedstock to produce biofuels: Parametric study and products characterization. *Fuel* **271**, 117534 (2020).

77. Yang, L. *et al.* Hydrothermal liquefaction of spent coffee grounds in water medium for bio-oil production. *Biomass Bioenergy* **86**, 191–198 (2016).

78. Tekin, K., Akalin, M. K. & Karagöz, S. The effects of water tolerant Lewis acids on the hydrothermal liquefaction of lignocellulosic biomass. *J. Energy Inst.* **89**, 627–635 (2016).

79. Kabyemela, B. M., Takigawa, M., Adschiri, T., Malaluan, R. M. & Arai, K. Mechanism and Kinetics of Cellobiose Decomposition in Sub- and Supercritical Water. *Ind. Eng. Chem. Res.* **37**, 357–361 (1998).

80. Singh, R., Balagurumurthy, B., Prakash, A. & Bhaskar, T. Catalytic hydrothermal liquefaction of water hyacinth. *Bioresour. Technol.* **178**, 157–165 (2015).

81. Yin, S., Dolan, R., Harris, M. & Tan, Z. Subcritical hydrothermal liquefaction of cattle manure to bio-oil: Effects of conversion parameters on bio-oil yield and characterization of bio-oil. *Bioresour. Technol.* **101**, 3657–3664 (2010).

82. Liu, H. M., Li, M. F. & Sun, R. C. Hydrothermal liquefaction of cornstalk: 7-Lump distribution and characterization of products. *Bioresour. Technol.* **128**, 58–64 (2013).

83. Dãrãban, I. M., Rosendahl, L. A., Pedersen, T. H. & Iversen, S. B. Pretreatment methods to obtain pumpable high solid loading wood-water slurries for continuous hydrothermal liquefaction systems. *Biomass Bioenergy* **81**, 437–443 (2015).

84. Berglin, E., Enderlin, C. & Schmidt, A. Review and Assessment of Commercial Vendors / Options for Feeding and Pumping Biomass Slurries for Hydrothermal Liquefaction. *Pnnl* **21981**, 1–35 (2012).

85. Hietala, D. C., Faeth, J. L. & Savage, P. E. A quantitative kinetic model for the fast and isothermal hydrothermal liquefaction of Nannochloropsis sp. *Bioresour. Technol.* **214**, 102–111 (2016).

86. Mathimani, T. & Mallick, N. A review on the hydrothermal processing of microalgal biomass to bio-oil - Knowledge gaps and recent advances. *J. Clean. Prod.* **217**, 69–84 (2019).

87. Overend, R. P. & Chornet, E. Fractionation of lignocellulosics by steam-aqueous pretreatments. *Philos. Trans. R. Soc. London. Ser. A, Math. Phys. Sci.* **321**, 523–536 (1987).

88. Chum, H. L., Johnson, D. K., Black, S. K. & Overend, R. P. Pretreatment-Catalyst effects and the combined severity parameter. *Appl. Biochem. Biotechnol.* **24–25**, 1–14 (1990).

89. Ruiz, H. A., Rodríguez-Jasso, R. M., Fernandes, B. D., Vicente, A. A. & Teixeira, J. A. Hydrothermal processing, as an alternative for upgrading agriculture residues and marine biomass according to the biorefinery concept: A review. *Renew. Sustain. Energy Rev.* **21**, 35–51 (2013).

90. Castello, D., Pedersen, T. & Rosendahl, L. Continuous Hydrothermal Liquefaction of Biomass: A Critical Review. *Energies* **11**, 3165 (2018).

91. Cheng, F., Cui, Z., Mallick, K., Nirmalakhandan, N. & Brewer, C. E. Hydrothermal liquefaction of high- and low-lipid algae: Mass and energy balances. *Bioresour. Technol.* **258**, 158–167 (2018).

92. Prestigiacomo, C., Laudicina, V. A., Siragusa, A., Scialdone, O. & Galia, A. Hydrothermal liquefaction of waste biomass in stirred reactors: One step forward to the integral valorization of municipal sludge. *Energy* **201**, 117606 (2020).

93. Prestigiacomo, C., Scialdone, O. & Galia, A. Hydrothermal liquefaction of wet biomass in batch reactors: Critical assessment of the role of operating parameters as a function of the nature of the feedstock. *Journal of Supercritical Fluids* vol. 189 105689 (2022).

94. Agostini, I. *et al.* Recovery of Terephthalic Acid from Densified Post-consumer Plastic Mix by HTL Process. *Molecules* **27**, 7112 (2022).

95. Channiwala, S. A. & Parikh, P. P. A unified correlation for estimating HHV of solid, liquid and gaseous fuels. *Fuel* **81**, 1051–1063 (2002).

96. Simonne, A. H., Simonne, E. H., Eitenmiller, R. R., Mills, H. A. & Cresman, C. P. Could the Dumas Method Replace the Kjeldahl Digestion for Nitrogen and Crude Protein Determinations in Foods? *J. Sci. Food Agric.* **73**, 39–45 (1997).

97. Matayeva, A. & Biller, P. Hydrothermal liquefaction of post-consumer mixed textile waste for recovery of bio-oil and terephthalic acid. *Resour. Conserv. Recycl.* **185**, 106502 (2022).

98. Kotnik, P., Čolnik, M., Finšgar, M., Knez, Ž. & Škerget, M. Determination of C1C6 hydrocarbons in gaseous plastic degradation products by GC–MS method. *Polym. Degrad. Stab.* **182**, 109386 (2020).

99. Zhang, X. Applications of kinetic methods in thermal analysis: A review. *Eng. Sci.* **14**, 1–13 (2021).

100. FAO. *Global food losses and food waste-Extent, causes and prevention*. (2011).

101. FAO. *The State of Food and Agriculture*. (2019).

102. Minowa, T., Inoue, S., Hanaoka, T. & Matsumura, Y. Hydrothermal reaction of glucose and glycine as model compounds of biomass. *Nihon Enerugi Gakkaishi/Journal Japan Inst. Energy* **83**, 794–798 (2004).

103. Fan, Y., Hornung, U., Dahmen, N. & Kruse, A. Hydrothermal liquefaction of protein-containing biomass: study of model compounds for Maillard reactions. *Biomass Convers. Biorefin.* **8**, 909–923 (2018).

104. Peterson, A. A., Lachance, R. P. & Tester, J. W. Kinetic evidence of the maillard reaction in hydrothermal biomass processing: Glucose-glycine interactions in high-temperature, high-pressure water. *Ind. Eng. Chem. Res.* **49**, 2107–2117 (2010).

105. Teri, G., Luo, L. & Savage, P. E. Hydrothermal treatment of protein,

polysaccharide, and lipids alone and in mixtures. *Energy Fuels* **28**, 7501–7509 (2014).

106. Zhang, C., Tang, X., Sheng, L. & Yang, X. Enhancing the performance of Co-hydrothermal liquefaction for mixed algae strains by the Maillard reaction. *Green Chem.* **18**, 2542–2553 (2016).

107. Lu, J., Liu, Z., Zhang, Y. & Savage, P. E. Synergistic and Antagonistic Interactions during Hydrothermal Liquefaction of Soybean Oil, Soy Protein, Cellulose, Xylose, and Lignin. *ACS Sustain. Chem. Eng.* **6**, 14501–14509 (2018).

108. Lu, J., Fan, G., Yang, M. & Wu, Y. Origin of carbon in the bio-oil from hydrothermal liquefaction of protein and glucose via isotopic labeling. *Fuel* **308**, 121941 (2022).

109. Sheehan, J. D. & Savage, P. E. Molecular and Lumped Products from Hydrothermal Liquefaction of Bovine Serum Albumin. *ACS Sustain. Chem. Eng.* **5**, 10967–10975 (2017).

110. Gautam, R. & Vinu, R. Reaction engineering and kinetics of algae conversion to biofuels and chemicals: Via pyrolysis and hydrothermal liquefaction. *React. Chem. Eng.* **5**, 1320–1373 (2020).

111. Obeid, R. *et al.* Reaction kinetics and characterisation of species in renewable crude from hydrothermal liquefaction of monomers to represent organic fractions of biomass feedstocks. *Chem. Eng. J.* **389**, 124397 (2020).

112. Tito, E., Pipitone, G., Monteverde Videla, A. H. A., Bensaid, S. & Pirone, R. Exploring HTL pathways in carbohydrate–protein mixture: a study on glucose–glycine interaction. *Biomass Convers. Biorefin.* **13**, 16385–16404 (2023).

113. Minowa, T., Fang, Z., Ogi, T. & Várhegyi, G. Decomposition of cellulose and glucose in hot-compressed water under catalyst-free conditions. *Journal of Chemical Engineering of Japan* vol. 31 131–134 (1998).

114. Promdej, C. & Matsumura, Y. Temperature effect on hydrothermal decomposition of glucose in sub- and supercritical water. *Ind. Eng. Chem. Res.* **50**, 8492–8497 (2011).

115. Kruse, A., Krupka, A., Schwarzkopf, V., Gamard, C. & Henningsen, T. Influence of proteins on the hydrothermal gasification and liquefaction of biomass. 1. Comparison of different feedstocks. *Ind. Eng. Chem. Res.* **44**, 3013–3020 (2005).

116. Kabyemela, B. M., Adschiri, T., Malaluan, R. M. & Arai, K. Glucose and fructose decomposition in subcritical and supercritical water: Detailed reaction pathway, mechanisms, and kinetics. *Ind. Eng. Chem. Res.* **38**, 2888–

2895 (1999).

117. Gomes, F. N. D. C., Pereira, L. R., Ribeiro, N. F. P. & Souza, M. M. V. M. Production of 5-hydroxymethylfurfural (HMF) via fructose dehydration: Effect of solvent and salting-out. *Brazilian J. Chem. Eng.* **32**, 119–126 (2015).

118. Jakob, A., Grilc, M., Teržan, J. & Likozar, B. Solubility Temperature Dependence of Bio-Based Levulinic Acid, Furfural, and Hydroxymethylfurfural in Water, Nonpolar, Polar Aprotic and Protic Solvents. *Processes* **9**, 924 (2021).

119. Aida, T. M. *et al.* Dehydration of d-glucose in high temperature water at pressures up to 80 MPa. *J. Supercrit. Fluids* **40**, 381–388 (2007).

120. Rasmussen, H., Sørensen, H. R. & Meyer, A. S. Formation of degradation compounds from lignocellulosic biomass in the biorefinery: Sugar reaction mechanisms. *Carbohydr. Res.* **385**, 45–57 (2014).

121. Patil, S. K. R., Heltzel, J. & Lund, C. R. F. Comparison of structural features of humins formed catalytically from glucose, fructose, and 5-hydroxymethylfurfuraldehyde. *Energy Fuels* **26**, 5281–5293 (2012).

122. Van Zandvoort, I. *et al.* Formation, molecular structure, and morphology of humins in biomass conversion: Influence of feedstock and processing conditions. *ChemSusChem* **6**, 1745–1758 (2013).

123. Maruani, V., Narayanin-Richenapin, S., Framery, E. & Andrioletti, B. Acidic Hydrothermal Dehydration of d -Glucose into Humins: Identification and Characterization of Intermediates. *ACS Sustain. Chem. Eng.* **6**, 13487–13493 (2018).

124. Rasrendra, C. B. *et al.* Experimental studies on the pyrolysis of humins from the acid-catalysed dehydration of C6-sugars. *J. Anal. Appl. Pyrolysis* **104**, 299–307 (2013).

125. Hong, C. *et al.* Effects of aqueous phase circulation and catalysts on hydrothermal liquefaction (HTL) of penicillin residue (PR): Characteristics of the aqueous phase, solid residue and bio oil. *Sci. Total Environ.* **776**, (2021).

126. Luijkx, G. C. A., van Rantwijk, F. & van Bekkum, H. Formation of 1,2,4-benzenetriol by hydrothermal treatment of carbohydrates. *Recl. des Trav. Chim. des Pays-Bas* **110**, 343–344 (1991).

127. Abdelmoez, W., Yoshida, H. & Nakahasi, T. Pathways of amino acid transformation and decomposition in saturated subcritical water conditions. *Int. J. Chem. React. Eng.* **8**, (2010).

128. Cox, J. S. & Seward, T. M. The reaction kinetics of alanine and glycine under hydrothermal conditions. *Geochim. Cosmochim. Acta* **71**, 2264–2284

(2007).

129. Qiu, Y. *et al.* Biocrude Oil Production through the Maillard Reaction between Leucine and Glucose during Hydrothermal Liquefaction. *Energy Fuels* **33**, 8758–8765 (2019).

130. Klingler, D., Berg, J. & Vogel, H. Hydrothermal reactions of alanine and glycine in sub- and supercritical water. *J. Supercrit. Fluids* **43**, 112–119 (2007).

131. Madsen, R. B. *et al.* Predicting the Chemical Composition of Aqueous Phase from Hydrothermal Liquefaction of Model Compounds and Biomasses. *Energy Fuels* **30**, 10470–10483 (2016).

132. Dote, Y., Inoue, S., Ogi, T. & Yokoyama, S. Y. Distribution of nitrogen to oil products from liquefaction of amino acids. *Bioresour. Technol.* **64**, 157–160 (1998).

133. Rogalinski, T., Liu, K., Albrecht, T. & Brunner, G. Hydrolysis kinetics of biopolymers in subcritical water. *J. Supercrit. Fluids* **46**, 335–341 (2008).

134. Shin, H. Y., Ryu, J. H., Park, S. Y. & Bae, S. Y. Thermal stability of fatty acids in subcritical water. *J. Anal. Appl. Pyrolysis* **98**, 250–253 (2012).

135. Fu, J., Lu, X. & Savage, P. E. Hydrothermal Decarboxylation and Hydrogenation of Fatty Acids over Pt/C. *ChemSusChem* **4**, 481–486 (2011).

136. Allen, R. R. & Johnston, P. V. The isomerization of fats during hydrogenation and the metabolism of the component fatty acids. *J. Am. Oil Chem. Soc.* **37**, 16–18 (1960).

137. Ledoux, M., Juanéda, P. & Sébédio, J. Trans fatty acids: Definition and occurrence in foods. *Eur. J. Lipid Sci. Technol.* **109**, 891–900 (2007).

138. Fang, X. & Schmidt-Rohr, K. Fate of the amino acid in glucose-glycine melanoidins investigated by solid-state nuclear magnetic resonance (NMR). *J. Agric. Food Chem.* **57**, 10701–10711 (2009).

139. Yaylayan, V. A. Recent Advances in the Chemistry of Strecker Degradation and Amadori Rearrangement: Implications to Aroma and Color Formation. *Food Sci. Technol. Res.* **9**, 1–6 (2003).

140. Wang, Z. Reaction mechanisms of hydrothermal liquefaction of model. (2011).

141. Inoue, S., Noguchi, M., Hanaoka, T. & Minowa, T. Organic compounds formed by thermochemical degradation of glucose-glycine melanoidins using hot compressed water. *J. Chem. Eng. Japan* **37**, 915–919 (2004).

142. Yaylayan, V. A. & Kaminsky, E. Isolation and structural analysis of Maillard

polymers: Caramel and melanoidin formation in glycine/glucose model system. *Food Chem.* **63**, 25–31 (1998).

143. Torri, C., Garcia Alba, L., Samorì, C., Fabbri, D. & Brilman, D. W. F. Hydrothermal treatment (HTT) of microalgae: Detailed molecular characterization of HTT oil in view of HTT mechanism elucidation. *Energy Fuels* **26**, 658–671 (2012).

144. Mahadevan Subramanya, S. & Savage, P. E. Identifying and Modeling Interactions between Biomass Components during Hydrothermal Liquefaction in Sub-, Near-, and Supercritical Water. *ACS Sustain. Chem. Eng.* **9**, 13874–13882 (2021).

145. Changi, S. M., Faeth, J. L., Mo, N. & Savage, P. E. Hydrothermal Reactions of Biomolecules Relevant for Microalgae Liquefaction. *Ind. Eng. Chem. Res.* **54**, 11733–11758 (2015).

146. Wang, H. Y., Qian, H. & Yao, W. R. Melanoidins produced by the Maillard reaction: Structure and biological activity. *Food Chem.* **128**, 573–584 (2011).

147. Adams, A., Tehrani, K. A., Keršien, M., Venskutonis, R. & De Kimpe, N. Characterization of model melanoidins by the thermal degradation profile. *J. Agric. Food Chem.* **51**, 4338–4343 (2003).

148. Chiaberge, S. *et al.* Amides in bio-oil by hydrothermal liquefaction of organic wastes: A mass spectrometric study of the thermochemical reaction products of binary mixtures of amino acids and fatty acids. *Energy Fuels* **27**, 5287–5297 (2013).

149. Simoneit, B. R. T., Rushdi, A. I., bin Abas, M. R. & Didyk, B. M. Alkyl Amides and Nitriles as Novel Tracers for Biomass Burning. *Environ. Sci. Technol.* **37**, 16–21 (2003).

150. Castello, D., Haider, M. S. & Rosendahl, L. A. Catalytic upgrading of hydrothermal liquefaction biocrudes: Different challenges for different feedstocks. *Renew. Energy* **141**, 420–430 (2019).

151. Chacon-Parra, A. D., Hall, P. A., Lewis, D. M., Glasius, M. & Van Eyk, P. J. Elucidating the Maillard Reaction Mechanism in the Hydrothermal Liquefaction of Binary Model Compound Mixtures and Spirulina. *ACS Sustain. Chem. Eng.* **10**, 10989–11003 (2022).

152. Liu, S. *et al.* Advances in understanding the humins: Formation, prevention and application. *Appl. Energy Combust. Sci.* **10**, 100062 (2022).

153. Yang, J. *et al.* Advanced models for the prediction of product yield in hydrothermal liquefaction via a mixture design of biomass model components coupled with process variables. *Appl. Energy* **233–234**, 906–915 (2019).

154. Brand, S., Hardi, F., Kim, J. & Suh, D. J. Effect of heating rate on biomass liquefaction: Differences between subcritical water and supercritical ethanol. *Energy* **68**, 420–427 (2014).

155. Tran, K.-Q. *et al.* Fast Hydrothermal Liquefaction of Native and Torrefied Wood. *Energy Procedia* **105**, 218–223 (2017).

156. Kamio, E., Takahashi, S., Noda, H., Fukuhara, C. & Okamura, T. Effect of heating rate on liquefaction of cellulose by hot compressed water. *Chem. Eng. J.* **137**, 328–338 (2008).

157. Tito, E. *et al.* Understanding the effect of heating rate on hydrothermal liquefaction: A comprehensive investigation from model compounds to a real food waste. *Bioresour. Technol.* **396**, 130446 (2024).

158. Sasaki, M. *et al.* Cellulose hydrolysis in subcritical and supercritical water. *J. Supercrit. Fluids* **13**, 261–268 (1998).

159. Velasco Calderón, J. C., Arora, J. S. & Mushrif, S. H. Mechanistic Investigation into the Formation of Humins in Acid-Catalyzed Biomass Reactions. *ACS Omega* **7**, 44786–44795 (2022).

160. Toor, S. S. *et al.* Hydrothermal liquefaction of biomass: A review of subcritical water technologies. *Energy* **36**, 2328–2342 (2011).

161. Chay Pak Ting, B. P., Pouliot, Y., Gauthier, S. F. & Mine, Y. Fractionation of egg proteins and peptides for nutraceutical applications. in *Separation, Extraction and Concentration Processes in the Food, Beverage and Nutraceutical Industries* 595–618 (Elsevier, 2013). doi:10.1533/9780857090751.2.595.

162. Tito, E. *et al.* Conceptual design and techno-economic assessment of coupled hydrothermal liquefaction and aqueous phase reforming of lignocellulosic residues. *J. Environ. Chem. Eng.* **11**, 109076 (2023).

163. Panisko, E., Wietsma, T., Lemmon, T., Albrecht, K. & Howe, D. Characterization of the aqueous fractions from hydrotreatment and hydrothermal liquefaction of lignocellulosic feedstocks. *Biomass Bioenergy* **74**, 162–171 (2015).

164. Rizzo, A. M. & Chiaramonti, D. Blending of Hydrothermal Liquefaction Biocrude with Residual Marine Fuel: An Experimental Assessment. *Energies* **15**, 450 (2022).

165. Aida, T. M., Oshima, M. & Smith, R. L. Controlled Conversion of Proteins into High-Molecular-Weight Peptides without Additives with High-Temperature Water and Fast Heating Rates. *ACS Sustain. Chem. Eng.* **5**, 7709–7715 (2017).

166. Sakata, K., Kitadai, N. & Yokoyama, T. Effects of pH and temperature on dimerization rate of glycine: Evaluation of favorable environmental conditions for chemical evolution of life. *Geochim. Cosmochim. Acta* **74**, 6841–6851 (2010).

167. Madsen, R. B., Zhang, H., Biller, P., Goldstein, A. H. & Glasius, M. Characterizing Semivolatile Organic Compounds of Biocrude from Hydrothermal Liquefaction of Biomass. *Energy Fuels* **31**, 4122–4134 (2017).

168. Déniel, M., Haarlemmer, G., Roubaud, A., Weiss-Hortala, E. & Fages, J. Energy valorisation of food processing residues and model compounds by hydrothermal liquefaction. *Renew. Sustain. Energy Rev.* **54**, 1632–1652 (2016).

169. Motavaf, B. & Savage, P. E. Effect of Process Variables on Food Waste Valorization via Hydrothermal Liquefaction. *ACS ES&T Eng.* **1**, 363–374 (2021).

170. Aierzhati, A. *et al.* Experimental and model enhancement of food waste hydrothermal liquefaction with combined effects of biochemical composition and reaction conditions. *Bioresour. Technol.* **284**, 139–147 (2019).

171. Ncube, L. K., Ude, A. U., Ogunmuyiwa, E. N., Zulkifli, R. & Beas, I. N. An overview of plasticwaste generation and management in food packaging industries. *Recycling* **6**, 1–25 (2021).

172. Marsh, K. S. Polymer and Plastic Packaging. in *Reference Module in Food Science* (Elsevier, 2016). doi:10.1016/b978-0-08-100596-5.03379-5.

173. Marsh, K. & Bugusu, B. Food packaging - Roles, materials, and environmental issues: Scientific status summary. *J. Food Sci.* **72**, (2007).

174. Ellen MacArthur Foundation. *The New Plastics Economy: Catalysing Action*. https://ellenmacarthurfoundation.org/the-new-plastics-economy-catalysing-action (2015).

175. Butler, T. I. & Morris, B. A. PE-Based Multilayer Film Structures. in *Multilayer Flexible Packaging: Second Edition* 281–310 (2016). doi:10.1016/B978-0-323-37100-1.00017-X.

176. Soares, C. T. de M., Ek, M., Östmark, E., Gällstedt, M. & Karlsson, S. Recycling of multi-material multilayer plastic packaging: Current trends and future scenarios. *Resour. Conserv. Recycl.* **176**, 105905 (2022).

177. Cabrera, G., Li, J., Maazouz, A. & Lamnawar, K. A Journey from Processing to Recycling of Multilayer Waste Films: A Review of Main Challenges and Prospects. *Polymers (Basel).* **14**, (2022).

178. Walker, T. W. *et al.* Recycling of multilayer plastic packaging materials by

solvent-targeted recovery and precipitation. *Sci. Adv.* **6**, 1–10 (2020).

179. Li, S., Cañete Vela, I., Järvinen, M. & Seemann, M. Polyethylene terephthalate (PET) recycling via steam gasification – The effect of operating conditions on gas and tar composition. *Waste Manag.* **130**, 117–126 (2021).

180. Artetxe, M. *et al.* Operating Conditions for the Pyrolysis of Poly-(ethylene terephthalate) in a Conical Spouted-Bed Reactor. *Ind. Eng. Chem. Res.* **49**, 2064–2069 (2010).

181. Çepelioğulları, Ö. & Pütün, A. E. Utilization of Two Different Types of Plastic Wastes from Daily and Industrial Life. *J. Selcuk Univ. Nat. Appl. Sci.* 694–706 (2013).

182. Marco, I. de *et al.* Recycling polymeric wastes by means of pyrolysis. *J. Chem. Technol. Biotechnol.* **77**, 817–824 (2002).

183. Gendell, A. & Lahme, V. *Feedstock Quality Guidelines for Pyrolysis of Plastic Waste Report for the Alliance to End Plastic Waste Prepared by.* www.endplasticwaste.org (2022).

184. Jin, K., Vozka, P., Kilaz, G., Chen, W.-T. & Wang, N.-H. L. Conversion of polyethylene waste into clean fuels and waxes via hydrothermal processing (HTP). *Fuel* **273**, 117726 (2020).

185. Čolnik, M., Kotnik, P., Knez, Ž. & Škerget, M. Hydrothermal decomposition of polyethylene waste to hydrocarbons rich oil. *J. Supercrit. Fluids* **169**, 105136 (2021).

186. Goto, M. Chemical recycling of plastics using sub- and supercritical fluids. *J. Supercrit. Fluids* **47**, 500–507 (2009).

187. Čolnik, M., Knez, Ž. & Škerget, M. Sub- and supercritical water for chemical recycling of polyethylene terephthalate waste. *Chem. Eng. Sci.* **233**, 116389 (2021).

188. Roosen, M. *et al.* Detailed Analysis of the Composition of Selected Plastic Packaging Waste Products and Its Implications for Mechanical and Thermochemical Recycling. *Environ. Sci. Technol.* **54**, 13282–13293 (2020).

189. Tito, E., dos Passos, J. S., Bensaid, S., Pirone, R. & Biller, P. Multilayer plastic film chemical recycling via sequential hydrothermal liquefaction. *Resour. Conserv. Recycl.* **197**, 107067 (2023).

190. Latifa, B., Zohra, F. F. & Said, H. Study of Raw and Recycled Polyethylene Terephthalate by Meaning of TGA and Computer Simulation. *Adv. Polym. Technol.* **2020**, 1–7 (2020).

191. Dubdub, I. & Al-Yaari, M. Pyrolysis of Low Density Polyethylene: Kinetic

Study Using TGA Data and ANN Prediction. *Polymers (Basel).* **12**, 891 (2020).

192. Mancini, S. D. & Zanin, M. Optimization of neutral hydrolysis reaction of post-consumer PET for chemical recycling. *Prog. Rubber, Plast. Recycl. Technol.* **20**, 117–132 (2004).

193. Yamamoto, S., Aoki, M. & Yamagata, M. Recovery of monomers from polyethylene terephthalate by hydrolysis under pressure. *R D Kobe Seiko Giho* **46**, 60–63 (1996).

194. Zhou, J. H., Shen, G. Z., Zhu, J. & Yuan, W. K. Terephthalic acid hydropurification over Pd/C catalyst. *Stud. Surf. Sci. Catal.* **159**, 293–296 (2006).

195. Tomás, R. A. F., Bordado, J. C. M. & Gomes, J. F. P. P-xylene oxidation to terephthalic acid: A literature review oriented toward process optimization and development. *Chem. Rev.* **113**, 7421–7469 (2013).

196. Tomás, R. A. F., Bordado, J. C. M., Gomes, J. F. P. & Sheehan, R. J. Terephthalic Acid, Dimethyl Terephthalate, and Isophthalic Acid. *Ullmann's Encycl. Ind. Chem.* 1–17 (2024) doi:10.1002/14356007.a26_193.pub3.

197. Silverstein, R. M., Webster, F. X. & Kiemle, D. J. *Spectrometric Identification of Organic Compounds (seventh edition). Analytical Chemistry* vol. 21 (1949).

198. Yang, Z., Peng, H., Wang, W. & Liu, T. Kinetics of Neutral Hydrolytic Depolymerization of PET (Polyethylene Terephthalate) Waste at Higher Temperature and Autogenious Pressures. *J. Appl. Polym. Sci.* **116**, 2658–2667 (2010).

199. Zhao, P. *et al.* Supercritical water co-liquefaction of LLDPE and PP into oil: Properties and synergy. *Sustain. Energy Fuels* **5**, 575–583 (2021).

200. Lu, T., Jan, K. & Chen, W.-T. Hydrothermal liquefaction of pretreated polyethylene-based ocean-bound plastic waste in supercritical water. *J. Energy Inst.* **105**, 282–292 (2022).

201. Chen, W. T., Jin, K. & Linda Wang, N. H. Use of Supercritical Water for the Liquefaction of Polypropylene into Oil. *ACS Sustain. Chem. Eng.* **7**, 3749–3758 (2019).

202. *Ullmann's Encyclopedia of Industrial Chemistry. Ullmann's Encyclopedia of Industrial Chemistry* (Wiley, 2003). doi:10.1002/14356007.

203. Mirghani, M. E. S. & Che Man, Y. B. Determination of hexane residues in vegetable oils with FTIR spectroscopy. *JAOCS, J. Am. Oil Chem. Soc.* **80**, 619–623 (2003).

204. Bucci, R., Girelli, A. M., Tafani, S. & Tarola, A. M. Oils and grease

determination by FT-IR and n-hexane as extraction solvent. *J. Anal. Chem.* **70**, 316–319 (2015).

205. Kusenberg, M. *et al.* Assessing the feasibility of chemical recycling via steam cracking of untreated plastic waste pyrolysis oils: Feedstock impurities, product yields and coke formation. *Waste Manag.* **141**, 104–114 (2022).

206. Kusenberg, M. *et al.* A comprehensive experimental investigation of plastic waste pyrolysis oil quality and its dependence on the plastic waste composition. *Fuel Process. Technol.* **227**, 107090 (2022).

207. Kusenberg, M. *et al.* Maximizing olefin production via steam cracking of distilled pyrolysis oils from difficult-to-recycle municipal plastic waste and marine litter. *Sci. Total Environ.* **838**, 156092 (2022).

208. Takebayashi, Y., Sue, K., Yoda, S., Hakuta, Y. & Furuya, T. Solubility of terephthalic acid in subcritical water. *J. Chem. Eng. Data* **57**, 1810–1816 (2012).

209. Dhale, A. D., Myrant, L. K., Chopade, S. P., Jackson, J. E. & Miller, D. J. Propylene glycol and ethylene glycol recovery from aqueous solution via reactive distillation. *Chem. Eng. Sci.* **59**, 2881–2890 (2004).

210. Pipitone, G. *et al.* Towards the sustainable hydrogen production by catalytic conversion of C-laden biorefinery aqueous streams. *Chem. Eng. J.* **377**, (2019).

211. *Plastics-The Facts 2022*. (2020).

212. Edo, C., Fernández-Piñas, F. & Rosal, R. Microplastics identification and quantification in the composted Organic Fraction of Municipal Solid Waste. *Sci. Total Environ.* **813**, 151902 (2022).

213. Schwarzböck, T., Van Eygen, E., Rechberger, H. & Fellner, J. Determining the amount of waste plastics in the feed of Austrian waste-to-energy facilities. *Waste Manag. Res.* **35**, 207–216 (2017).

214. Sorell, G. The role of chlorine in high temperature corrosion in waste-to-energy plants. *Mater. High Temp.* **14**, 207–220 (1997).

215. López, A., De Marco, I., Caballero, B. M., Laresgoiti, M. F. & Adrados, A. Dechlorination of fuels in pyrolysis of PVC containing plastic wastes. *Fuel Process. Technol.* **92**, 253–260 (2011).

216. Poerschmann, J., Weiner, B., Woszidlo, S., Koehler, R. & Kopinke, F. D. Hydrothermal carbonization of poly(vinyl chloride). *Chemosphere* **119**, 682–689 (2015).

217. Lu, J., Ma, S. & Gao, J. Study on the pressurized hydrolysis dechlorination

of PVC. *Energy Fuels* **16**, 1251–1255 (2002).

218. Salimi, M., Pedersen, T. H. & Rosendahl, L. Optimizing hydrothermal dechlorination of PVC in a SS-316 reactor: From chemistry knowledge to material considerations. *J. Environ. Chem. Eng.* **11**, 109783 (2023).

219. Ling, M. *et al.* Hydrothermal treatment of polyvinyl chloride: Reactors, dechlorination chemistry, application, and challenges. *Chemosphere* **316**, 137718 (2023).

220. Zhu, Z., Toor, S. S., Rosendahl, L., Yu, D. & Chen, G. Influence of alkali catalyst on product yield and properties via hydrothermal liquefaction of barley straw. *Energy* **80**, 284–292 (2015).

221. Gandon-Ros, G., Soler, A., Aracil, I. & Gómez-Rico, M. F. Dechlorination of polyvinyl chloride electric wires by hydrothermal treatment using K2CO3 in subcritical water. *Waste Manag.* **102**, 204–211 (2020).

222. Zhao, P., Li, T., Yan, W. & Yuan, L. Dechlorination of PVC wastes by hydrothermal treatment using alkaline additives. *Environ. Technol.* **39**, 977–985 (2018).

223. Tito, E. *et al.* Sequential hydrothermal dechlorination and liquefaction of PVC. *Energy Convers. Manag.* **304**, 118228 (2024).

224. Takeshita, Y., Kato, K., Takahashi, K., Sato, Y. & Nishi, S. Basic study on treatment of waste polyvinyl chloride plastics by hydrothermal decomposition in subcritical and supercritical regions. *J. Supercrit. Fluids* **31**, 185–193 (2004).

225. Lu, J., Ma, S., Gao, J., Freitas, J. C. C. & Bonagamba, T. J. Study on Characterization of Pyrolysis and Hydrolysis Products of Poly(vinyl chloride) Waste. *J. Appl. Polym. Sci.* **90**, 3252–3259 (2003).

226. Nagai, Y., Smith, R. L., Inomata, H. & Arai, K. Direct observation of polyvinylchloride degradation in water at temperatures up to 500°C and at pressures up to 700 MPa. *J. Appl. Polym. Sci.* **106**, 1075–1086 (2007).

227. Yoshioka, T., Kameda, T., Ieshige, M. & Okuwaki, A. Dechlorination behaviour of flexible poly(vinyl chloride) in NaOH/EG solution. *Polym. Degrad. Stab.* **93**, 1822–1825 (2008).

228. Lu, J. *et al.* Practical dechlorination of polyvinyl chloride wastes in NaOH/ethylene glycol using an up-scale ball mill reactor and validation by discrete element method simulations. *Waste Manag.* **99**, 31–41 (2019).

229. Yao, Z. & Ma, X. A new approach to transforming PVC waste into energy via combined hydrothermal carbonization and fast pyrolysis. *Energy* **141**, 1156–1165 (2017).

230. Ma, D. *et al.* Dechlorination of polyvinyl chloride by hydrothermal treatment

with cupric ion. *Process Saf. Environ. Prot.* **146**, 108–117 (2021).

231. Bodîrlău, R., Teacă, C. A. & Spiridon, I. Preparation and characterization of composites comprising modified hardwood and wood polymers/poly(vinyl chloride). *BioResources* **4**, 1285–1304 (2009).

232. Coltro, L., Pitta, J. B. & Madaleno, E. Performance evaluation of new plasticizers for stretch PVC films. *Polym. Test.* **32**, 272–278 (2013).

233. Sau, S., Pandit, S. & Kundu, S. Crosslinked poly (vinyl alcohol): Structural, optical and mechanical properties. *Surfaces and Interfaces* **25**, 101198 (2021).

234. Nandiyanto, A. B. D., Oktiani, R. & Ragadhita, R. How to read and interpret ftir spectroscope of organic material. *Indones. J. Sci. Technol.* **4**, 97–118 (2019).

235. Yang, J. *et al.* Insight into the pyrolysis behavior of polyvinyl chloride using in situ pyrolysis time-of-flight mass spectrometry: Aromatization mechanism and Cl evolution. *Fuel* **331**, 125994 (2023).

236. Wang, Z., Wei, R., Wang, X., He, J. & Wang, J. Pyrolysis and combustion of polyvinyl chloride (PVC) sheath for new and aged cables via thermogravimetric analysis-fourier transform infrared (TG-FTIR) and calorimeter. *Materials (Basel).* **11**, (2018).

237. Hou, X. *et al.* Role of normal/cyclo-alkane in hydrocarbons pyrolysis process and product distribution. *J. Anal. Appl. Pyrolysis* **156**, 105130 (2021).

238. Cypres, R. Aromatic hydrocarbons formation during coal pyrolysis. *Fuel Process. Technol.* **15**, 1–15 (1987).

239. Fabbri, D., Torri, C. & Spokas, K. A. Analytical pyrolysis of synthetic chars derived from biomass with potential agronomic application (biochar). Relationships with impacts on microbial carbon dioxide production. *J. Anal. Appl. Pyrolysis* **93**, 77–84 (2012).

240. Zhou, J., Liu, G., Wang, S., Zhang, H. & Xu, F. TG-FTIR and Py-GC/MS study of the pyrolysis mechanism and composition of volatiles from flash pyrolysis of PVC. *J. Energy Inst.* **93**, 2362–2370 (2020).

241. Hashimoto, K., Suga, S., Wakayama, Y. & Funazukuri, T. Hydrothermal dechlorination of PVC in the presence of ammonia. *J. Mater. Sci.* **43**, 2457–2462 (2008).

242. Li, Z., Niu, S., Liu, J. & Wang, Y. Solid fuel production from co-hydrothermal carbonization of polyvinyl chloride and corncob: Higher dechlorination efficiency and process water recycling. *Sci. Total Environ.* **843**, 157082 (2022).

243. Shin, S.-M., Yoshioka, T. & Okuwaki, A. Dehydrochlorination behavior of flexible PVC pellets in NaOH solutions at elevated temperature. *J. Appl. Polym. Sci.* **67**, 2171–2177 (1998).

244. Yang, M., Zhao, P., Cui, X., Geng, F. & Guo, Q. Kinetics study on hydrothermal dechlorination of poly(vinyl chloride) by in-situ sampling. *Environ. Technol. Innov.* **23**, 101703 (2021).

245. Xiu, F. R., Lu, Y. & Qi, Y. DEHP degradation and dechlorination of polyvinyl chloride waste in subcritical water with alkali and ethanol: A comparative study. *Chemosphere* **249**, 126138 (2020).

246. Čolnik, M., Kotnik, P., Knez, Ž. & Škerget, M. Degradation of Polyvinyl Chloride (PVC) Waste with Supercritical Water. *Processes* **10**, 1–14 (2022).

247. Fisch, M. H. & Bacaloglu, R. Mechanism of poly(vinyl chloride) stabilisation. *Plast. Rubber Compos. Process. Appl.* **28**, 119–124 (1999).

248. Mukherjee, A. K. & Gupta, A. Structure and dehydrochlorination of poly(vinyl chloride). *J. Macromol. Sci. Part C* **20**, 309–331 (1981).

249. Bockisch, C., Lorance, E. D., Hartnett, H. E., Shock, E. L. & Gould, I. R. Kinetics and Mechanisms of Dehydration of Secondary Alcohols under Hydrothermal Conditions. *ACS Earth Sp. Chem.* **2**, 821–832 (2018).

250. Zhao, P., Li, Z., Li, T., Yan, W. & Ge, S. The study of nickel effect on the hydrothermal dechlorination of PVC. *J. Clean. Prod.* **152**, 38–46 (2017).

251. Li, T., Zhao, P., Lei, M. & Li, Z. Understanding Hydrothermal Dechlorination of PVC by Focusing on the Operating Conditions and Hydrochar Characteristics. *Appl. Sci.* **7**, 256 (2017).

252. Khaing, K., Yuchen, A., Jianqiang, C. & David, Z. Effect of Temperature on Corrosion Behaviour of Fe – Cr Alloys in Wet - CO 2 With and Without HCl Gases. *Oxid. Met.* **97**, 371–400 (2022).

253. Lu, P. *et al.* Review on fate of chlorine during thermal processing of solid wastes. *J. Environ. Sci.* **78**, 13–28 (2018).

254. Giglio, E. *et al.* Critical issues for the deployment of plastic waste pyrolysis. *Catal. Sci. Technol.* **13**, 5799–5820 (2023).

255. Perondi, D. *et al.* The role of CaO and its influence on chlorine during the thermochemical conversion of shredder residue. *Process Saf. Environ. Prot.* **122**, 58–67 (2019).

256. Davies, M. *Alloy Selection for Service in Chlorine, Hydrogen Chloride and Hydrochloric Acid: A Guide to the Use of Nickel-Containing Alloys*. (2022).

257. Ramirez, J. A., Brown, R. J. & Rainey, T. J. A review of hydrothermal liquefaction bio-crude properties and prospects for upgrading to transportation fuels. *Energies* **8**, 6765–6794 (2015).

258. Sladkovskiy, D. A. *et al.* Process design and techno-economical analysis of hydrogen production by aqueous phase reforming of sorbitol. *Chem. Eng. Res. Des.* **134**, 104–116 (2018).

259. Snowden-Swan, L. *et al.* Wet Waste Hydrothermal Liquefaction and Biocrude Upgrading to Hydrocarbon Fuels: 2021 State of Technology. *Pacific Northwest Natl. Lab.* (2022).

260. Leng, L. *et al.* Bioenergy recovery from wastewater produced by hydrothermal processing biomass: Progress, challenges, and opportunities. *Sci. Total Environ.* **748**, 142383 (2020).

261. Swetha, A. *et al.* Review on hydrothermal liquefaction aqueous phase as a valuable resource for biofuels , bio-hydrogen and valuable bio-chemicals recovery. *Chemosphere* **283**, 131248 (2021).

262. Sundarrajan, P. *et al.* Insights into valuing the aqueous phase derived from hydrothermal liquefaction. *Renew. Sustain. Energy Rev.* **144**, 111019 (2021).

263. Watson, J. *et al.* Valorization of hydrothermal liquefaction aqueous phase: pathways towards commercial viability. *Prog. Energy Combust. Sci.* **77**, 100819 (2020).

264. Di Fraia, A. *et al.* Coupling hydrothermal liquefaction and aqueous phase reforming for integrated production of biocrude and renewable H2. *AIChE J.* **69**, 1–14 (2023).

265. Coronado, I. *et al.* A review of catalytic aqueous-phase reforming of oxygenated hydrocarbons derived from biorefinery water fractions. *Int. J. Hydrog. Energy* **41**, 11003–11032 (2016).

266. Cao, L. *et al.* Hydrothermal liquefaction of agricultural and forestry wastes: state-of-the-art review and future prospects. *Bioresour. Technol.* **245**, 1184–1193 (2017).

267. Solimene, R. *et al.* Devolatilization and fragmentation of solid lignin-rich residues from bioethanol production in lab-scale fluidized bed reactors. *Chem. Eng. Trans.* **50**, 79–84 (2016).

268. Zoppi, G. *et al.* Life cycle assessment of the biofuel production from lignocellulosic biomass in a hydrothermal liquefaction – aqueous phase reforming integrated biorefinery. *Renew. Energy* **206**, 375–385 (2023).

269. Miliotti, E. *et al.* Lignocellulosic ethanol biorefinery: Valorization of lignin-rich stream through hydrothermal liquefaction. *Energies* **12**, (2019).

270. Chiaramonti, D., Giovannini, A., Pescarolo, S. & Nistri, R. *2° Generation Bioethanol The world ' s largest demo plant ready to be transferred all over the world - A Handbook - Part II.* (2013).

271. Foreign Agricultural Service. Europe: Corn production (2010-2014 Average).

272. Menardo, S., Airoldi, G., Cacciatore, V. & Balsari, P. Potential biogas and methane yield of maize stover fractions and evaluation of some possible stover harvest chains. *Biosyst. Eng.* **129**, 352–359 (2015).

273. Perry, R. H. & Green, D. W. *Perry's Engineers' Handbook. Perry's Engineers' Handbook* (1997).

274. Kern, D. Q. *Process Heat Transfer*. (Elsevier, 2007). doi:10.1016/B978-0-12-373588-1.X5000-1.

275. Tab. 02.18 Superficie coltivata e produzione di cereali in Piemonte per provincia - Anno 2019.

276. Miliotti, E. *et al.* Lignocellulosic ethanol biorefinery: Valorization of lignin-rich stream through hydrothermal liquefaction. *Energies* **12**, (2019).

277. Zhu, Y., Biddy, M. J., Jones, S. B., Elliott, D. C. & Schmidt, A. J. Techno-economic analysis of liquid fuel production from woody biomass via hydrothermal liquefaction (HTL) and upgrading. *Appl. Energy* **129**, 384–394 (2014).

278. Pipitone, G. *et al.* Aqueous phase reforming of the residual waters derived from lignin-rich hydrothermal liquefaction: investigation of representative organic compounds and actual biorefinery streams. *Catal. Today* **345**, 237–250 (2020).

279. Snowden-Swan, L. J. *et al.* Conceptual Biorefinery Design and Research Targeted for 2022: Hydrothermal Liquefaction Processing of Wet Waste to Fuels. *Pnnl-27186* **27186**, 1–40 (2017).

280. Tews, I. *et al.* Biomass direct liquefaction options: technoeconomic and life cycle assessment. *Pacific Northwest Natl. Lab.* 62 (2014).

281. Lin, L. *et al.* Techno-economic analysis and comprehensive optimization of an on-site hydrogen refuelling station system using ammonia: hybrid hydrogen purification with both high H2 purity and high recovery. *Sustain. Energy Fuels* **4**, 3006–3017 (2020).

282. Collett, J. R. *et al.* Renewable diesel via hydrothermal liquefaction of oleaginous yeast and residual lignin from bioconversion of corn stover. *Appl. Energy* **233–234**, 840–853 (2019).

283. Jones, S. *et al.* *Process design and economics for the conversion of lignocellulosic biomass to hydrocarbon fuels: Fast pyrolysis and hydrotreating bio-oil pathway. Energy* http://www.pnnl.gov/main/publications/external/technical_reports/PNNL-23053.pdf%5Cnhttp://www.nrel.gov/docs/fy14osti/61178.pdf (2013).

284. Masoumi, S. & Dalai, A. K. Techno-economic and life cycle analysis of biofuel production via hydrothermal liquefaction of microalgae in a methanol-water system and catalytic hydrotreatment using hydrochar as a catalyst support. *Biomass Bioenergy* **151**, 106168 (2021).

285. Hoffmann, J., Rudra, S., Toor, S. S., Holm-Nielsen, J. B. & Rosendahl, L. A. Conceptual design of an integrated hydrothermal liquefaction and biogas plant for sustainable bioenergy production. *Bioresour. Technol.* **129**, 402–410 (2013).

286. Gu, X. *et al.* Comparative techno-economic analysis of algal biofuel production via hydrothermal liquefaction: One stage versus two stages. *Appl. Energy* **259**, 114115 (2020).

287. Zhu, Y., Albrecht, K. O., Elliott, D. C., Hallen, R. T. & Jones, S. B. Development of hydrothermal liquefaction and upgrading technologies for lipid-extracted algae conversion to liquid fuels. *Algal Res.* **2**, 455–464 (2013).

288. Jones, S., Zhu, Y., Anderson, D., Hallen, R. T. & Elliott, D. C. Process Design and Economics for the Conversion of Algal Biomass to Hydrocarbons : Whole Algae Hydrothermal Liquefaction and Upgrading. *Pnnl* 1–69 (2014).

289. Sánchez, M., Amores, E., Abad, D., Rodríguez, L. & Clemente-Jul, C. Aspen Plus model of an alkaline electrolysis system for hydrogen production. *Int. J. Hydrog. Energy* **45**, 3916–3929 (2020).

290. Zhu, Y. *et al.* Techno-economic analysis of alternative aqueous phase treatment methods for microalgae hydrothermal liquefaction and biocrude upgrading system. *Algal Res.* **39**, 101467 (2019).

291. Magdeldin, M., Kohl, T. & Järvinen, M. Techno-economic assessment of the by-products contribution from non-catalytic hydrothermal liquefaction of lignocellulose residues. *Energy* **137**, 679–695 (2017).

292. Brown, T. R., Thilakaratne, R., Brown, R. C. & Hu, G. Techno-economic analysis of biomass to transportation fuels and electricity via fast pyrolysis and hydroprocessing. *Fuel* **106**, 463–469 (2013).

293. Reza, M. T., Emerson, R., Uddin, M. H., Gresham, G. & Coronella, C. J. Ash reduction of corn stover by mild hydrothermal preprocessing. *Biomass Convers. Biorefin.* **5**, 21–31 (2015).

294. Towler, G. & Sinnott, R. K. *Chemical Engineering Design - Principles, Practice and Economics of Plant and Process Design (2nd Edition). Elsevier* (2013).

295. Turton, R., Bailie, R. C., Whiting, W. B., Shaeiwitz, J. A. & Bhattacharyya,

D. *Analysis, synthesis, and design of chemical processes, 4th edition*. *Choice Reviews Online* (Pearson, 2012). doi:10.5860/choice.36-0974.

296. Guthrie, K. M. *Capital cost estimating*. *Chemical Engineering* vol. 76 (1969).

297. Knorr, D., Lukas, J. & Schoen, P. Production of Advanced Biofuels via Liquefaction. Hydrothermal Liquefaction Reactor Design. vol. 303 www.nrel.gov/publications. (2013).

298. Shi, Q. *et al.* Clinical and familial characteristics of ten Chinese patients with fatal family insomnia. *Biomed. Environ. Sci.* **25**, 471–475 (2012).

299. Salomone, F. *et al.* Techno-economic modelling of a Power-to-Gas system based on SOEC electrolysis and CO2 methanation in a RES-based electric grid. *Chem. Eng. J.* **377**, 120233 (2019).

300. Funkenbusch, L. T. *et al.* Technoeconomic assessment of hydrothermal liquefaction oil from lignin with catalytic upgrading for renewable fuel and chemical production. *Wiley Interdiscip. Rev.: Energy Environ.* **8**, 1–12 (2019).

301. Swanson, R. M., Platon, A., Satrio, J. A. & Brown, R. C. Techno-economic analysis of biomass-to-liquids production based on gasification. *Fuel* **89**, S11–S19 (2010).

302. Alves, B. Prices of electricity for industries with a consumption of 20,000 to 70,000 MWh in the European Union from 2008 to 2020. *Statista* https://www.statista.com/statistics/1046683/industry-electricity-prices-european-union-eu-28/ (2021).

303. Sönnichsen, N. Industrial natural gas prices in the European Union from 2008 to 2020, by consumption. *Statista* https://www.statista.com/statistics/1047070/natural-gas-price-european-union/ (2021).

304. Agyekum, E. B., Nutakor, C., Agwa, A. M. & Kamel, S. A Critical Review of Renewable Hydrogen Production Methods: Factors Affecting Their Scale-Up and Its Role in Future Energy Generation. *Membranes (Basel).* **12**, (2022).

305. Nie, Y. & Bi, X. T. Techno-economic assessment of transportation biofuels from hydrothermal liquefaction of forest residues in British Columbia. *Energy* **153**, 464–475 (2018).

306. Wright, M. M., Daugaard, D. E., Satrio, J. A. & Brown, R. C. Techno-economic analysis of biomass fast pyrolysis to transportation fuels. *Fuel* **89**, S2–S10 (2010).

307. Ramirez, J. A. & Rainey, T. J. Comparative techno-economic analysis of biofuel production through gasification , thermal liquefaction and pyrolysis

of sugarcane bagasse. *J. Clean. Prod.* **229**, 513–527 (2019).

308. Baral, N. R. *et al.* Production Cost and Carbon Footprint of Biomass-Derived Dimethylcyclooctane as a High-Performance Jet Fuel Blendstock. *ACS Sustain. Chem. Eng.* **9**, 11872–11882 (2021).

309. Gutiérrez Ortiz, F. J., Alonso-Fariñas, B., Campanario, F. J. & Kruse, A. Life cycle assessment of the Fischer-Tropsch biofuels production by supercritical water reforming of the bio-oil aqueous phase. *Energy* **210**, (2020).

310. European Commision. *Directive 2009-28-EC on the promotion of the use of energy from renewable sources. Paper Knowledge . Toward a Media History of Documents* (2014).

311. Wiloso, E. I., Heijungs, R. & De Snoo, G. R. LCA of second generation bioethanol: A review and some issues to be resolved for good LCA practice. *Renew. Sustain. Energy Rev.* **16**, 5295–5308 (2012).

312. Dang, Q., Yu, C. & Luo, Z. Environmental life cycle assessment of bio-fuel production via fast pyrolysis of corn stover and hydroprocessing. *Fuel* **131**, 36–42 (2014).

313. Lam, M. K., Lee, K. T. & Mohamed, A. R. Life cycle assessment for the production of biodiesel: A case study in Malaysia for palm oil versus jatropha oil. *Biofuels Bioprod. Biorefin.* **3**, 601–612 (2009).

314. Yee, K. F., Tan, K. T., Abdullah, A. Z. & Lee, K. T. Life cycle assessment of palm biodiesel: Revealing facts and benefits for sustainability. *Appl. Energy* **86**, S189–S196 (2009).

315. Czyrnek-Delêtre, M. M., Smyth, B. M. & Murphy, J. D. Beyond carbon and energy: The challenge in setting guidelines for life cycle assessment of biofuel systems. *Renew. Energy* **105**, 436–448 (2017).

316. Sinnott, R. K., Coulson, J. M. & Richardson, J. F. *Chemical Engineering Volume 6 - Design. ELSEVIER - Coulson & Richardson's Chemical Engineering series* (1983).

317. Net electricity generation, EU27, 2019.

318. International Platinum Group Metals Association. *The Life Cycle Assessment of Platinum Group Metals*. https://ipa-news.de/assets/sustainability/2021-08-02_IPA LCA Fact Sheet.pdf (2017).

319. Khodabandehloo, M., Larimi, A. & Khorasheh, F. Comparative process modeling and techno-economic evaluation of renewable hydrogen production by glycerol reforming in aqueous and gaseous phases. *Energy Convers. Manag.* **225**, 113483 (2020).

320. Yukesh Kannah, R. *et al.* Techno-economic assessment of various hydrogen

production methods – A review. *Bioresour. Technol.* **319**, 124175 (2021).

321. *Hydrogen Production Costs 2021.* https://assets.publishing.service.gov.uk/government/uploads/system/uploads/attachment_data/file/1011506/Hydrogen_Production_Costs_2021.pdf (2021).

322. Van Der Voet, E., Lifset, R. J. & Luo, L. Life-cycle assessment of biofuels, convergence and divergence. *Biofuels* **1**, 435–449 (2010).

323. Ögmundarson, Ó., Sukumara, S., Laurent, A. & Fantke, P. Environmental hotspots of lactic acid production systems. *Glob. Change Biol. Bioenergy* **12**, 19–38 (2020).

324. Snowden-Swan, L. J., Spies, K. A., Lee, G. J. & Zhu, Y. Life cycle greenhouse gas emissions analysis of catalysts for hydrotreating of fast pyrolysis bio-oil. *Biomass Bioenergy* **86**, 136–145 (2016).

325. Duclos, L. *et al.* Environmental assessment of proton exchange membrane fuel cell platinum catalyst recycling. *J. Clean. Prod.* **142**, 2618–2628 (2017).

326. Acar, C. & Dincer, I. *Hydrogen Production*. *Comprehensive Energy Systems* vols 3–5 (2018).

327. Hetherington, A. C., Borrion, A. L., Griffiths, O. G. & McManus, M. C. Use of LCA as a development tool within early research: Challenges and issues across different sectors. *Int. J. Life Cycle Assess.* **19**, 130–143 (2014).

328. Finnveden, G. *et al.* Recent developments in Life Cycle Assessment. *J. Environ. Manage.* **91**, 1–21 (2009).

329. Barahmand, Z. & Eikeland, M. S. Life Cycle Assessment under Uncertainty: A Scoping Review. *World* **3**, 692–717 (2022).

330. Benavides, P. T., Cronauer, D. C., Adom, F., Wang, Z. & Dunn, J. B. The influence of catalysts on biofuel life cycle analysis (LCA). *Sustain. Mater. Technol.* **11**, 53–59 (2017).

331. Liu, W. *et al.* Analysis of the Global Warming Potential of Biogenic CO2 Emission in Life Cycle Assessments. *Sci. Rep.* **7**, 1–8 (2017).

332. Bhandari, R., Trudewind, C. A. & Zapp, P. Life cycle assessment of hydrogen production via electrolysis - A review. *J. Clean. Prod.* **85**, 151–163 (2014).

333. Bhandari, R., Trudewind, C. A. & Zap, P. *Life Cycle Assessment of Hydrogen Production Methods-A Review Contribution to ElyGrid Project*.

334. Gunukula, S. & Anex, R. P. Techno-economic analysis of multiple bio-based routes to adipic acid. *Biofuels Bioprod. Biorefin.* **11**, (2017).

335. Peters, J. F., Iribarren, D. & Dufour, J. Simulation and life cycle assessment

of biofuel production via fast pyrolysis and hydroupgrading. *Fuel* **139**, 441–456 (2015).

336. Vienescu, D. N., Wang, J., Le Gresley, A. & Nixon, J. D. A life cycle assessment of options for producing synthetic fuel via pyrolysis. *Bioresour. Technol.* **249**, 626–634 (2018).

337. Sun, H. *et al.* Comparative life cycle assessment (LCA) of biofuel production via corn stover: fermentation to ethanol, pyrolysis to bio-oil, and gasification to jet fuel. *Biomass Convers. Biorefin.* **13**, 12809–12821 (2023).

338. Edwards, R., Mahieu, V., Griesemann, J. C., Larivé, J. F. & Rickeard, D. J. *Well-to-Wheels Analysis of Future Automotive Fuels and Power Trains in the European Context - Report, Version 3c. SAE Technical Papers* (2004) doi:10.4271/2004-01-1924.

339. Huss, A. and Weingerl, P. *EC Tank-to-Wheel report v5: Passenger cars.* (2020) doi:10.2760/557004.

340. Tsalidis, G. A. *et al.* An LCA-based evaluation of biomass to transportation fuel production and utilization pathways in a large port's context. *Int. J. Energy Environ. Eng.* **8**, 175–187 (2017).